# Photoionization of Nitrogen-Containing Reactive Molecules with Synchrotron Radiation

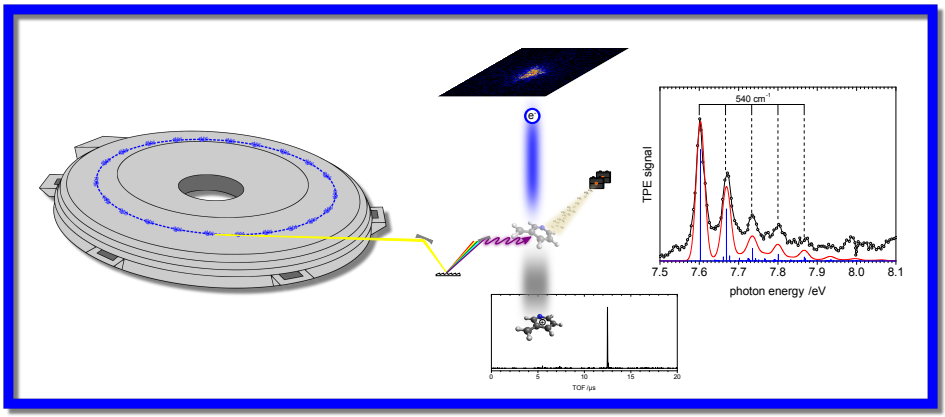


Dissertation zur Erlangung des naturwissenschaftlichen Doktorgrades der Julius-Maximilians-Universität Würzburg

vorgelegt von
Fabian Holzmeier
geboren in Würzburg

Würzburg, November 2015

Eingereicht bei der Fakultät für Chemie und Pharmazie am 09. November 2015

Gutachter der schriftlichen Arbeit

1. Gutachter: Prof. Dr. Ingo Fischer

2. Gutachter: Prof. Dr. Richard P. Tuckett

Prüfer des öffentlichen Promotionskolloquiums

1. Prüfer: Prof. Dr. Ingo Fischer

2. Prüfer: Prof. Dr. Christoph Lambert

3. Prüfer: Prof. Dr. Tobias Hertel

4. Prüfer: Prof. Dr. Volker Engel

5. Prüfer: Prof. Dr. Maik Finze

Datum des öffentlichen Promotionskolloquiums: 22. Februar 2016

Doktorurkunde ausgehändigt am _____

# Contents

# List of Publications

Parts of this thesis have been previously published in the following peer-reviewed journal articles. For all reproduced material the permission for reprint was granted by the respective publishing company holding the copyright of the articles.

(1) F. Holzmeier, I. Wagner, I. Fischer, A. Bodi, P. Hemberger, **Pyrolysis of 3-Methoxypyridine - Detection and Characterization of the Pyrrolyl Radical by Threshold Photoelectron Spectroscopy**, submitted for publication.

(2) F. Holzmeier, M. Lang, I. Fischer, P. Hemberger, **The threshold photoelectron spectrum of cyanovinylacetylene leads to an upward revision of the ionization energy**, *Chem. Phys. Lett.*, 2015, **638**, 201-204.

(3) F. Holzmeier, M. Lang, I. Fischer, X. Tang, B. Cunha de Miranda, C. Romanzin, C. Alcaraz, P. Hemberger, **Threshold photoelectron spectroscopy of unstable N-containing compounds: Resolution of $\Delta$K subbands in $HNCO^+$ and vibrational resolution in $NCO^+$**, *J. Chem. Phys.*, 2015, **142**, 184306.

(4) F. Holzmeier, M. Lang, P. Hemberger, I. Fischer, **Improved Ionization Energies for the Two Isomers of Phenylpropargyl Radica**l, *ChemPhys Chem*, 2014, **15**, 3489-3492.

(5) F. Holzmeier, M. Lang, P. Hemberger, A. Bodi, M. Schäfer, R. D. Dewhurst, H. Braunschweig, I. Fischer, **Photoionization and Pyrolysis of a 1,4-Azaborinine: Retro-Hydroboration in the Cation and Identification of Novel Organoboron Ring Systems**, *Chem. Eur. J.*, 2014, **20**, 9683-9692.

Further publications that are not content of the present work:

(6) F. Holzmeier, M. Lang, I. Fischer, P. Hemberger, G. A. Garcia, X. Tang, J.-C. Loison, **Assignment of high-lying bending mode levels in the threshold photoelectron spectrum of $NH_2$: a comparison between pyrolysis and fluorine-atom abstraction radical sources**, *Phys. Chem. Chem. Phys.*, 2015, **29**, 19507-19614.

(7) M. Lang, F. Holzmeier, P. Hemberger, I. Fischer, **Threshold Photoelectron Spectra of Combustion Relevant $C_4H_5$ and $C_4H_7$ Isomers**, *J. Phys. Chem. A*, 2015, **17**, 3995-4000.

(8) M. Lang, F. Holzmeier, I. Fischer, P. Hemberger, **Decomposition of Diazomeldrum's Acid: A Threshold Photoelectron Spectroscopy Study**, *J. Phys. Chem. A*, 2014, **118**, 11235-11243.

(9) F. Holzmeier, M. Lang, K. Hader, P. Hemberger, I. Fischer, **$H_2CN^+$ and $HCNH^+$: New insight into the structure and dynamics from mass-selected threshold photoelectron spectra**, *J. Chem. Phys.*, 2013, **138**, 214310.

(10) M. Lang, F. Holzmeier, I. Fischer, P. Hemberger, **Threshold Photoionization of Fluorenyl, Benzhydryl, Diphenylmethylene, and Their Dimers**, *J. Phys. Chem. A*, 2013, **117**, 5260-5268.

# List of Abbreviations

| | |
|---|---|
| AE | appearance energy |
| AECD | auxiliary emission control device |
| CCD | charge-coupled device |
| CI | configuration interaction |
| CW | continuous wave |
| DFT | density functional theory |
| DPI | dissociative photoionization |
| EC | experimental chamber |
| EPA | Environmental Protection Agency |
| EXAFS | extended x-ray absorption fine structure |
| FC | Franck-Condon |
| FEL | free electron laser |
| FWHM | full width at half maximum |
| HOMO | highest occupied molecular orbital |
| ICCT | International Council on Clean Transportation |
| IE | ionization energy |
| IR | infrared |
| IVR | intramolecular vibrational redistribution |
| (i)PEPICO | (imaging) photoelectron photoion coincidence |
| LCAO | linear combination of atomic orbitals |
| MCP | microchannel plate |
| MCSCF | multi-configurational self consistent field |

| | |
|---|---|
| m/z | mass to charge |
| NEXAFS | near edge x-ray absorption fine structure |
| NMR | nuclear magnetic resonance |
| PAH | polycyclic aromatic hydrocarbons |
| PFI-ZEKE | pulsed field ionization - zero kinetic energy |
| PIE | photoionization efficiency |
| PIMS | photoionization mass spectrometry |
| RAC | rigid activated complex |
| $RAPRENO_x$ | rapid reduction of nitrogen oxides |
| RRKM | Rice Ramsperger Kassel Marcus |
| SASE | self-amplified spontaneous emission |
| SC | source chamber |
| SLS | Swiss Light Source |
| SOLEIL | Source Optimisée de Lumière d'Énergie Intermédiaire du LURE |
| SPES | slow photoelectron spectroscopy |
| (S)SACM | (simplified) statistical adiabatic channel model |
| SXR | soft x-ray radiation |
| TOF | time of flight |
| (T)PES | (threshold) photoelectron spectroscopy |
| VMI | velocity map imaging |
| VUV | vacuum ultraviolet |
| XES | x-ray emission spectroscopy |
| XPS | x-ray photoelectron spectroscopy |
| 1PPR | 1-phenyl-propargyl |
| 3PPR | 3-phenyl-propargyl |

# 1. Introduction

Following investigations of the US Environmental Protection Agency (EPA), the German car manufacturer Volkswagen admitted in September 2015 to have installed auxiliary emission control devices (AECDs), which were only activated when a software sensed that the vehicle was being tested, in eleven million diesel passenger cars.[1] These AECDs had not been described in the certificate of conformity application submitted to the EPA in order to manipulate the nitrogen oxide $NO_x$ emission under testing conditions and therefore meet the standards of the EPA (max. $NO_x$ emission: $32\,mg\,km^{-1}$). $NO_x$ are considered harmful to the environment, a health threat and can poison catalysts.[2] The nitrogen oxide emission of passenger vehicles is therefore progressively regulated also in the European Union. The Euro 6 Standard for all diesel cars built after September 2015 for example allows a maximum $NO_x$ emission of $80\,mg\,km^{-1}$.[3] The Volkswagen manipulations and a recent report by the International Council on Clean Transportation (ICCT)[4] show that it is a major challenge for the manufacturers to build diesel engines that meet the requested criteria. One reason for that is the complexity of combustion processes, in which a plethora of chemical species coexist and therefore numerous reaction pathways are possible.[5,6] Understanding these reactions and, in the best case, controlling them is therefore difficult. The outcome of the elapsing chemical reactions is significantly influenced by chemical intermediates. A chemical intermediate is defined in the IUPAC gold book as a molecular entity with a lifetime appreciably longer than a molecular vibration,

which reacts further yielding directly or indirectly the products of a chemical reaction.[7] In other words, an intermediate is a thermodynamically stable product formed from the educts in a stepwise chemical reaction sequence. The formation of such a reactive species is followed by one or several further reaction steps giving the final product species. The physical and chemical properties of intermediates, which often are challenging to isolate due to their short lifetimes, constitute consequently an important role for understanding combustion.[8,9] While some intermediates are closed-shell molecules, in particular radicals and carbenes play important roles in combustion processes. Radicals have unpaired electrons and carbenes are electron deficient due to a free electron pair. These types of molecules possess hence a strong driving force to compensate their electron deficiency. As most of the common fuels consist predominantly of hydrocarbon structures, the combustion research has so far been focused on the associated chemistry, which leads to the formation of soot as unwanted by-product.[10,11] As shown above, it is also important to consider nitrogen-containing fuel ingredients since these lead to $NO_x$. This field of research has so far been explored less profoundly. Important groundwork on combustion intermediates that contain nitrogen atoms, i.e. their isolated generation and spectroscopic characterization, is therefore presented in this thesis.

Combustion is the chemical reaction of a solid, liquid, or gaseous fuel with an oxidizing agent (usually aerial oxygen), during which energy is released in the form of heat and/or light. Controlled combustion is used for energy conversion, e.g. in transport, aviation, and electricity generation.[12] Fossil fuels, i.e. natural gas, crude oil, and coal, covered 81.7 % of the worldwide energy demand in 2013.[13] They evolve from organic material (natural gas and crude oil: plankton, coal: terrestrial plants) that was hermetically sealed by mud and buried under other heavy layers of earth. Heat and high pressure lead to a chemical transformation of this biomass to fossil fuels over millions of years.

Since the time of formation of fossil fuels is so long, they are considered as non-renewable energy sources. By contrast, biofuels are referred to as renewable fuels because they do not originate from prehistoric biomass conversion, but are gathered from recently living biological materials like rapeseed, soy, cereal grain, sugar cane and beet, wood or agricultural waste.[12] While fossil fuels contain mostly hydrocarbons, the chemical variability in biomass is much greater. The nitrogen content in fuels is important for combustion research because it is almost completely converted to $NO_x$ (NO and $NO_2$). The reaction of nitric oxide NO or nitrogen dioxide $NO_2$ with atmospheric water, for example, yields nitric acid $HNO_3$, which leads to acid rain.[14] In addition, $NO_x$ participates in the generation of photochemical smog and can be converted in secondary reactions to nitrous oxide $N_2O$, a greenhouse gas.[15,16] Fuel nitrogen occurs in a comparable quantity range of 0-5.5 % both in fossil fuels as well as in biofuels as illustrated in fig. 1.1. The percentage of nitrogen in biofuels is essentially dependent on the use of fertilizers for growing the energy crop.[12]

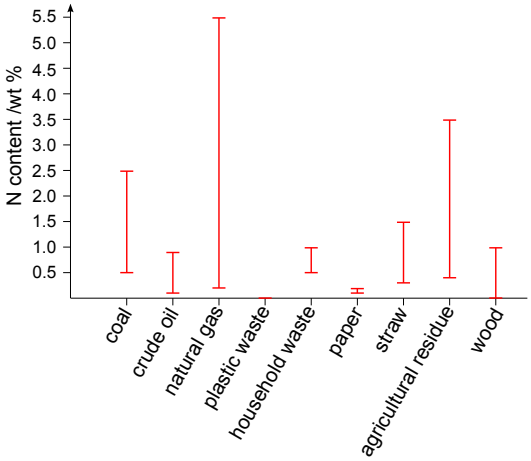


Figure 1.1.: Typical nitrogen content in selected fuels. Data taken from ref.[2].

In fossil fuels, nitrogen is predominantly bound in five-membered (pyrrolic) and six-membered (pyridinic) heterocycles,[17–22] while in biomass, it occurs mainly in the form of proteins, but also in heterocyclic structures such as DNA, RNA, alkaloids, porphyrin, or chlorophyll.[23,24] There are three chemical mechanisms for $NO_x$ formation during combustion: "Thermal" NO formation, "prompt" NO formation and conversion of fuel-nitrogen. The "thermal" NO formation mechanism is also relevant for fuels that do not contain nitrogen since atmospheric nitrogen is oxidized by released atomic oxygen:[25]

$$O + N_2 \rightleftharpoons NO + N \tag{1.1}$$

$$N + O_2 \rightleftharpoons NO + O \tag{1.2}$$

$$N + OH \rightleftharpoons NO + H \tag{1.3}$$

Since the initiating step (1.1) has a high activation barrier, this NO formation process is only relevant for temperatures above 1800 K.[2] "Prompt" NO formation arises from the reaction of hydrocarbon intermediates like the CH radical with molecular nitrogen and is especially relevant for fuel rich combustion conditions.[25]

$$CH + N_2 \rightleftharpoons NCN + H \tag{1.4}$$

The reaction product NCN may then be oxidized to NO. The majority of NO during combustion, however, originates from the conversion of organically bound nitrogen in the fuel. As stated above, nitrogen in fossil fuels are often found in pyrrolic and pyridinic structures. The pyrolysis of pyrrole[26–28] and pyridine,[29–31] which can therefore be seen as prototype systems for nitrogen-containing structures found in fuels, has been investigated to draw conclusions on the occurring chemical processes during combustion. Fig. 1.2 shows a reaction path diagram for possible mechanisms in the pyrrole pyrolysis based on the intermediates identified in flame experiments.[27,28]

In this figure, it stands out that many radicals are involved in the complex

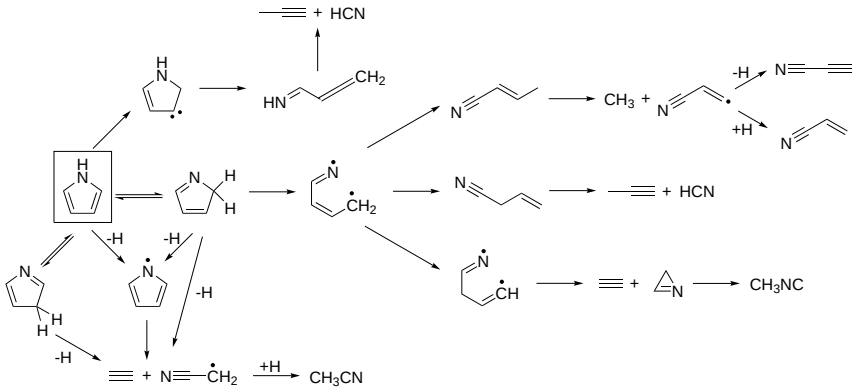


Figure 1.2.: The reaction path diagram for the pyrolytic decomposition of the coal model system pyrrole shows the complexity of combustion processes. [27,28]

decomposition of nitrogen-containing heterocycles. Radicals are therefore assumed to play important roles in the nitrogen conversion mechanisms during coal pyrolysis. [32] Nitrogen bound in pyrrolic and pyridinic structures is almost exclusively converted to HCN. [2,20,24] At a lower percentage, the formation of $NH_3$ is observed in the pyrolytic conversion of fuel prototype compounds. Due to the higher content of aminic bound nitrogen in biofuels, more $NH_3$ is released during biofuel incineration. [12] Both volatile combustion products, HCN and $NH_3$, are undesired, since they are oxidized to nitric oxide as illustrated in the scheme of fig. 1.3. In addition, HCN is a highly toxic gas.

Reliable models on the combustion processes based on experimental data are necessary to identify the ongoing reactions, determine the kinetics and to be ultimately able to regulate the combustion and make it more efficient. An established technique to investigate the chemical composition of flames on-line is photoionization mass spectrometry (PIMS). [34,35] Electromagnetic radiation in the vacuum ultraviolet (VUV) can ionize molecules, i.e. eject an electron

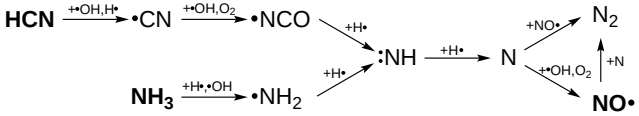


Figure 1.3.: Reaction path diagram for the conversion of HCN and $NH_3$ to NO.[33] On top of the reaction arrows, possible reactants are given.

from an occupied orbital, which leads to the formation of a cation. The mass to charge ratio of the generated ion can be determined by mass spectrometry, which is a first hint for the identification of a species in a flame. The minimum photon energy, at which an ion signal is detected, is the ionization energy (IE). The IE is characteristic for a certain molecule as it constitutes, within the approximations of Koopmans' theorem,[36] the binding energy of an electron in the highest occupied molecular orbital (HOMO). It can be determined by scanning the photon energy of a tunable light source, e.g. a synchrotron, and observing the onset of the ion signal. The ionization onset of a certain mass to charge (m/z) ratio enables in many cases the unambiguous assignment of an observed peak in the mass spectrum to a certain compound. If the absolute photoionization cross section, i.e. the probability for the ionization event as a function of the photon energy, is known, the ion yield even is a direct measure of the concentration of the observed species. It is therefore possible to determine the stoichiometric composition of a flame. In some cases, the data obtained from PIMS are not sufficient to make a definitive assignment. Especially for larger molecules, there often exist several isomers with close lying IEs, which makes an assignment to a specific isomer difficult. Additional information on the species and its behavior upon ionization from more structure-sensitive experiments are therefore required. Removing an electron from a bonding (antibonding) molecular orbital, weakens (strengthens) the chemical bond. The bonding distance is therefore elongated (shortened) upon

ionization. This leads to an excitation of the corresponding vibrational mode in the cation, which can be resolved in photoelectron spectra (see sec. 2.3). The spectral resolution and therefore the accuracy of the ionization energy in photoelectron spectroscopy (PES) is also higher than in PIMS because the ionization energy is determined not only by an onset of the ion yield curve, but, in many cases, by a sharp peak in the PE spectrum. Photoelectron photoion coincidence (PEPICO) experiments, which combine mass spectrometry and PES and have recently been applied to flames,[37–39] yield three criteria for an unambiguous identification of a chemical species: the m/z ratio, the ionization energy, and the vibrational structure of the cation. However, it is often still difficult to distinguish molecules with a similar composition in flames, especially isomers, as they have the same m/z ratio and often similar chemical properties. It is therefore worthwhile to selectively generate a species which is assumed to be involved in combustion processes and compare the isolated data to the ones from flame experiments. As the lifetimes of the species involved in combustion are often very short, this is a challenging task.

Closed-shell intermediates are usually stable enough to be stored under inert conditions and cryogenic temperatures (e.g. isocyanic acid HNCO, section 5.1). By contrast, radicals and carbenes have to be generated *in situ* and very low particle densities have to be maintained to avoid recombination. Techniques for the generation of open-shell intermediates from suitable precursor molecules are electrical discharge,[40] hydrogen abstraction reactions,[41–43] photolysis,[44] and pyrolysis.[45,46] Pyrolysis, i.e. the cleavage of a chemical bond by heat, offers a high selectivity as the temperature can be easily adjusted in a way that only the thermodynamically most labile bond in the precursor molecule is broken. In addition, the precursor can often be completely converted to the desired intermediate by pyrolysis and the radical or carbene yield is in general much higher than for the other techniques. This enables experiments with low sensitivity and accelerates data acquisition. *In*

*situ* generation and high dilution of a reactive intermediate in an inert carrier gas makes it thus possible to study these species as isolated molecules in the gas phase. Previous work in our group dealt with the generation and characterization of hydrocarbon radicals employing threshold photoelectron spectroscopy.[47–53] Hydrocarbon chemistry is very important to understand the chemical processes leading to the formation of polycyclic aromatic hydrocarbons (PAH), which are soot precursors.[54–59] With the growing importance of biofuels[60–62] and a great relevance in atmospheric chemistry,[63] oxygen containing intermediates have aroused the attention of several research groups. Reactive nitrogen-containing organic molecules are not only important in the context of combustion chemistry, but are also of interest in interstellar chemical reactions as has been reviewed by Ehrenfreund and Charnley.[64] The largest moon of Saturn, Titan, has a dense atmosphere, which is rich of nitrogen and Titan is hence considered the celestial body which is most similar to the earth. The chemistry involving nitrogen in Titan's atmosphere has therefore been investigated in detail.[65] Nevertheless, reliable photoionization data on this class of molecules is sparse. That is why the main topic of this thesis is the selective generation of nitrogen-containing combustion intermediates, which are identified and characterized by threshold photoelectron spectroscopy employing VUV synchrotron radiation.

The theoretical principles of spectroscopic techniques for photoionization experiments, which are important to understand the presented results, are described in chapter 2. An overview on how these principles and techniques are realized is given in chapter 3, which deals with the experimental setups of the presented studies and the employed computational methods. As shown in one of the previous paragraphs, absolute photoionization cross sections constitute an important information for postulating combustion mechanisms. A discussion on using the iPEPICO setup at the Swiss Light Source (SLS) storage ring to determine absolute photoionization cross sections therefore follows in

chapter 4 for the example of the hydrocarbon carbene cyclopropenylidene, *c*-$C_3H_2$. Nitrogen-containing intermediates, whose importance in combustion has been emphasized at the beginning of the introduction, are addressed in chapter 5. Here, the results on the photoionization experiments on several nitrogen-containing closed and open shell intermediates are presented. The section on isocyanic acid HNCO comprises also a discussion of the inner shell spectroscopy, i.e. the excitation or ionization of 1s core orbital electrons, in the subsection 5.1.2. As will be discussed in more detail later in this thesis, inner shell spectroscopy can be employed as a highly localized probe for time-resolved experiments on nuclear and electronic dynamics.[66] In addition, it can also be applied to combustion studies on flames.[67] The thesis's focus will be shifted in chapter 6 towards heterocylces containing both boron and nitrogen atoms. In this part of the thesis, it is shown on the example of 1,4-di-*tert*-butyl-1,4-azaborinine that photoionization is also a suitable tool to get important insight into the electronic properties of those molecules. Boron atoms in organic molecules are usually $sp^2$-hybridized and have thus an empty $p_z$-orbital. The electron deficiency can be compensated through $\pi$-conjugation, which causes that many boron-containing systems have unique optoelectronic properties.[68–79] The interest in boron-doped $\pi$-conjugated materials has increased significantly over the last few years.[80–83] In addition, unraveling dissociative photoionization (DPI) pathways reveals interesting information on bonding properties in boron-containing molecules and complexes.[84] At last, the most important findings of the experimental work presented in this thesis are summarized in the conclusion in chapter 7.

# 2. Spectroscopic Techniques

## 2.1. Monochromatic Synchrotron Radiation

Generation of monochromatic radiation in the VUV, which is needed for valence shell photoionization, is challenging. The VUV spectral region ranges from 200 nm (6.2 eV) to 104 nm (11.9 eV). At energies above 200 nm molecular oxygen absorbs the electromagnetic radiation and 104 nm is the cut-off wavelength of Lithium Fluoride. Hence, the optical elements usually used in laser spectroscopy are only suitable to a limited spectral range. VUV laser radiation can be generated by non-linear processes in gases (4 wave mixing, sum or difference frequency mixing).[85] By contrast, synchrotron radiation offers a continuous spectral range covering the infrared (IR) up to hard X-ray radiation and is therefore ideally suited as a light source for spectroscopy of valence and even inner shell electrons (soft X-ray radiation).[86]

### 2.1.1. Generation and Properties of Synchrotron Radiation

Charged particles that are exposed to an electric or magnetic force emit electromagnetic radiation as described in Maxwell's equations.[87] Ivanenko and Pomerantschuk predicted that an intense and broad spectrum of electromagnetic radiation is emitted when electrons at relativistic speed are transversely accelerated.[88] This so-called synchrotron radiation was first observed in 1947 by Elder *et al.* at the General Electric Synchrotron in Schenectady, New

York.[89] As synchrotrons were primarily used for high-energy physics experiments and synchrotron radiation was therefore seen as an unwanted by-product and energy-loss channel, it was not before the late 1960s that there were wide-spread experiments with synchrotron radiation after dedicated storage rings had been built.[90] In these storage rings, electrons pass magnetic devices while circulating at relativistic speed in a closed orbit. This leads to the emittance of synchrotron radiation. The radiant power $P_{SR}$ can be described as:[86]

$$P_{SR} = \frac{cq^2E^4}{6\pi\epsilon_0 r^2(mc^2)^4} \tag{2.1}$$

In this equation, $c$ is the speed of light, $q$ the particle's charge, $E$ its energy, $\epsilon_0$ the vacuum permittivity, $r$ the radius of the orbit on which the charged particle is traveling, and $m$ the mass of the particle. In theory, all kind of charged particles emit synchrotron radiation. But as the radiant power scales inversely with the fourth power of the mass, electrons (or sometimes also positrons) are commonly used to generate synchrotron radiation. Electron storage rings consist of an electron source, a linear accelerator and a booster ring to pre-accelerate the electrons and the storage ring with magnetic devices, at which the radiation is generated. When emitting electromagnetic radiation, the electrons lose energy which is compensated in radio frequency cavities. These are located in between the magnetic devices. The basic arrangement of these elements is depicted in fig. 2.1.

It is essential that the storage ring is kept under a high vacuum ($<10^{-8}$ mbar) to minimize electron loss due to collisions with residual gas molecules. Permanent bending magnets are used to force the electrons on the circular orbit of the storage ring and simultaneously to generate synchrotron radiation. The radiation emitted from bending magnets comprises a broad spectrum of electromagnetic radiation (IR - X-ray) and is horizontally polarized in the electron's plane of motion. Outside the orbit plane, the synchrotron light is elliptically polarized. An increased photon flux can be achieved when magnetic

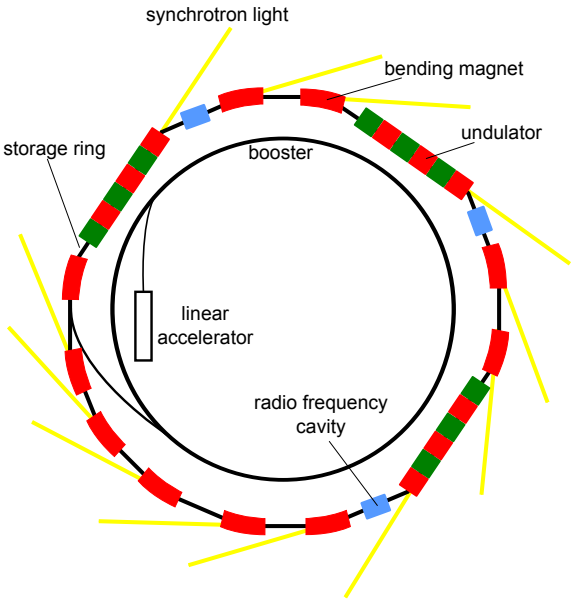


Figure 2.1.: Basic build-up of an electron storage ring for the generation of synchrotron radiation.

insertion devices with periodically alternating magnetic fields are inserted in the linear sections of the storage ring. The electron beam oscillates inside those devices, which leads to the emittance of higher collimated light. Hence, a quasi-continuous spectrum with a high flux density is obtained in so-called wigglers. Undulators have essentially the same build-up as wigglers, but force the electron beam on a wave motion with a lower amplitude. This leads to interference effects of the radiation cones emitted at each of the changes of direction in the undulator and a very intense, narrow band (and the corresponding higher harmonics) is obtained.[86] Fig. 2.2 shows a schematic illustration of a wiggler or undulator and a sketch, from which the interference conditions in an undulator can be derived.

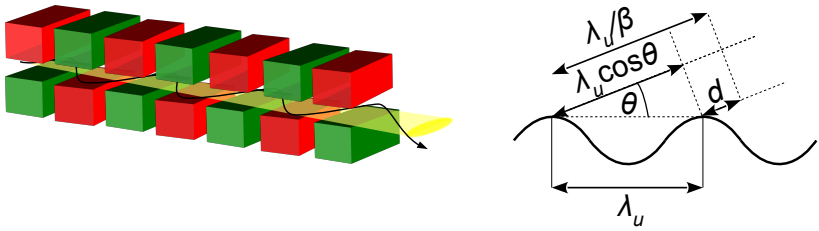


Figure 2.2.: Build-up of wigglers and undulators (left). The interference of wave fronts in an undulator depends on the undulator parameter, the wavelength, and the observation angle (right, adapted from ref. [86]).

The time that is needed for the electrons to cover one sweep $\lambda_u$ in the periodic magnetic field, the undulator period, is $\lambda_u/c\beta_z$. $c\beta_z$ is the mean logitudinal drift velocity, with $\beta_z$ being the relativistic speed $v_z/c$. During this time, the wave front of the radiation emitted under the angle $\theta$ travels $\lambda_u/\beta_z$. The path difference between this wave front and the one of the next period must be a multiple of the wavelength $n \cdot \lambda$ for constructive interference to be observed under the angle $\theta$:

$$d = \lambda_u/\beta_z - \lambda_u \cos\theta = n \cdot \lambda \tag{2.2}$$

The wavelength of the synchrotron radiation which is intensified in an undulator is therefore defined as: [86]

$$\lambda_n = \frac{\lambda_u}{2n\gamma^2}(1 + K^2 + \gamma^2\theta^2) \tag{2.3}$$

In this equation, $\gamma$ is the particle energy in units of its rest energy $E_e/m_0c^2 = 1/\sqrt{1-\beta_z^2}$, $n$ the order of the interference maximum, and $K$ the undula-

tor parameter. The undulator parameter $K$ describes the deflection of the electron beam inside the insertion device.

$$K = \frac{eB\lambda_u}{2\pi mc} \tag{2.4}$$

$e$ is the electron charge and $B$ the magnetic field. The wavelength hence varies with the observation angle $\theta$ and the shortest wavelength is observed in the center of the radiation cone. As obvious from equations (2.4) and (2.3), the spectrum of the emitted synchrotron radiation of an undulator can be tuned by changing the undulator parameter $K$. This is usually done by varying the gap between the two sets of permanent magnets, which changes the magnetic field $B$. Synchrotron light from an undulator is linearly polarized. By longitudinal shifting of the magnetic elements of an undulator, elliptically polarized light, or, for a shift of $\lambda_u/4$, circularly polarized light, can be realized. Undulators with which the polarization of the synchrotron radiation can be varied are called Sasaki type undulators.[91]

Synchrotron radiation provides a continuous spectrum of intense, collimated, electromagnetic radiation with a well defined polarization. The photon energy can be easily selected by the use of monochromators. In addition, it has a quasi-continuous time structure (several hundred MHz) since the electrons circulate in bunches in the storage ring. One electron bunch usually contains about $10^{10}$ charged particles and spreads over several centimeters, which leads to photon pulses with a duration of 10-100 ps.[86] The number of bunches circling in the storage ring and its circumference define the time structure of the photon pulses. Modern synchrotron facilities are most of the time operated in the so called top-up mode, in which the storage ring is seeded with the maximum number of electron bunches and therefore a quasi-continuous photon beam is generated (repetition rate of several hundreds MHz).

### 2.1.2. Swiss Light Source and Synchrotron SOLEIL

The experiments of this thesis were conducted at two state of the art electron storage rings located in central Europe: the Swiss Light Source and the Synchrotron SOLEIL. The Swiss Light Source is a storage ring with a circumference of 288 nm located in Villigen, Switzerland, operating at an electron energy of 2.4 GeV with a top-up mode ring current of 400 mA. The first synchrotron experiments were commissioned in 2001. A linear accelerator pre-accelerates the electrons to 100 MeV, which are then further accelerated to the final energy of 2.4 GeV in a booster with a circumference of 270 m. After injection into the storage ring, the electrons are held on the orbit by 36 bending magnets. Energy loss is compensated by radio frequency transmitters operated at 500 MHz. Nine undulator beamlines and eight beamlines located at bending magnets are currently operated.

Experiments at Synchrotron SOLEIL were commissioned in 2006. The acronym SOLEIL stands for Source Optimisée de Lumière à Energie Intermédiaire du LURE (Laboratoire d'Utilisation du Rayonnement Electromagnétique). The storage ring has a circumference of 354 m and hosts 26 beamlines for experiments. The electrons are pre-accelerated in a similar way as at the SLS and the storage ring is operating at an electron energy of 2.75 GeV and a 430 mA current. Bending magnets and undulators provide the synchrotron radiation.

### 2.1.3. Monochromators

Even when an undulator is used, the bandwidth of the emitted synchrotron radiation is too broad for high resolution spectroscopic experiments. Therefore, monochromators have to be utilized to select a distinct photon energy. As there is no opaque material for wavelengths in the VUV and X-ray region, gratings serve as dispersive elements. The mode of operation of such gratings relies again on interference effects. Constructive interference occurs when the

path difference $d$ is a multiple of the wavelength $\lambda$ as illustrated in fig. 2.3. The following condition can be set up: [92]

$$d = m\lambda = a(\sin\alpha - \sin\beta) \tag{2.5}$$

$a$ is the distance between two grooves and $\alpha$ and $\beta$ are the incident and emergent angle relative to the grating normal. Different wavelengths are thus spatially expanded and can be selected. The resolving power of such an reflecting diffraction grating $\lambda/\Delta\lambda$ is directly related to the number of lines that are exposed to the incident radiation.

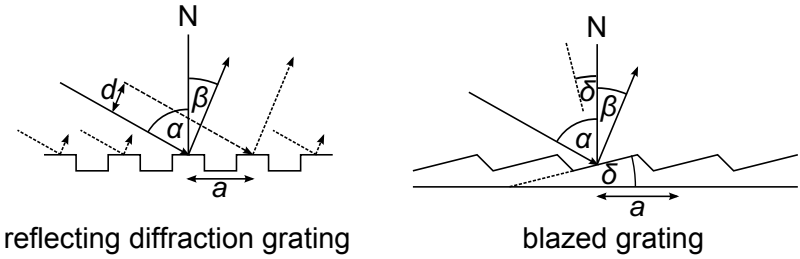


Figure 2.3.: Reflecting diffraction grating and blazed grating. Figure adapted from ref. [92].

However, the majority of the light is simply reflected on the grating surface and therefore concentrated in zeroth order. The utilization of a blazed grating enables to concentrate energy into a given diffraction order. Such a grating also has an equidistant line spacing, but the cross-section of the grating has a step structure with a saw tooth shape (see fig. 2.3). The steps are tilted at the blaze angle $\delta$. The diffraction angles are not influenced by the shape of the grating. Reflection, by contrast, has now to be considered relative to the blaze normal, which is also tilted at the angle $\delta$ to the grating normal $N$. Reflection occurs then under the angle $\alpha - \delta$, which is now a different angle compared to a common reflecting diffraction grating. For a certain wavelength, eq. (2.5)

is valid for the first order if $\alpha - \delta = \beta + \delta$. The reflected beam emerges then under the same angle relative to $N$ as the diffracted beam. This wavelength is consequently intensified by constructive interference with the reflected light.

## 2.2. Photoionization

A molecule $AB$ can be ionized upon interaction with electromagnetic radiation $h\nu$ of sufficiently high energy and a cation $AB^+$ and an electron $e^-$ are generated.

$$AB + h\nu \rightarrow AB^+ + e^- \tag{2.6}$$

An ion and electron signal are detected when the photon energy is greater than the binding energy of the electron. The minimum energy which is necessary to ionize a molecule is called ionization energy, which lies around 10 eV for most organic molecules. Consequently, VUV radiation is necessary to induce such a process. The ionization energy of radicals is in general lower than for closed shell molecules because the unpaired electron destabilizes the initial state in comparison to a closed shell state, while the final cationic state for radicals is more stable since it is a closed shell state and not a radical cation. The ionization energy of a molecule can be determined by scanning the photon energy and detecting the ions in a mass spectrometer. This technique is called photoionization mass spectrometry. The ionization energy is defined as the onset of the ion signal when plotted against the photon energy. The ion signal steadily increases above the ionization signal as it is directly related to the ionization probability, i.e. the absolute photoionization cross section. As will be discussed below, analysis of the electrons in (threshold) photoelectron spectroscopy yields a significantly higher accuracy.

There are also indirect processes called autoionization, which lead to the generation of cations and electrons. Autoionization in molecules can be divided in three classes: electronic, vibrational, and rotational autoionization. In these processes, photons with an energy higher than the first ionization threshold excite an electron into a high Rydberg orbital. The molecule with $N$ electrons is hence excited into a highly excited, quasi-bound, discrete neutral state. The resulting configuration can then be described as an electronically,

vibrationally or rotationally excited core state with $N-1$ electrons and a loosely bound electron in an orbital just below the ionization continuum. Relaxation of the core state to a lower electronic, vibrational or rotational state transfers the core's electronic, vibrational or rotational energy to the Rydberg electron, which consequently reaches the ionization continuum and a cation in the ground state is generated. Autoionization can analogically be observed for higher excited states, i.e. the resulting cation is also an excited state. The electronic autoionization of oxygen is sketched in fig. 2.4 utilizing a simplified picture, in which a generalization of Koopman's theorem for all orbital energies is assumed.

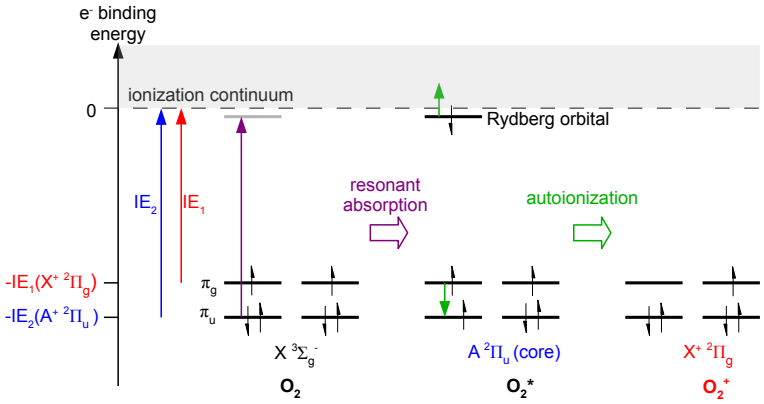


Figure 2.4.: Electronic autoionization in molecular oxygen. Resonant absorption of a photon with an energy higher than the first ionization energy of $O_2$ leads to a neutral, highly excited Rydberg state with an electronically excited ion core and a loosely-bound electron in a Rydberg orbital. Relaxation of the core transfers energy to the Rydberg electron, which is subsequently excited above the ionization threshold. Figure adapted from ref. [93].

## 2.3. Photoelectron Spectroscopy

### 2.3.1. Conventional Ultraviolet Photoelectron Spectroscopy

When an atom or molecule is ionized by ultraviolet light, the excess energy distributes between kinetic energy of the ion, internal (vibrational, rotational) energy of the ion and electron kinetic energy. The former can in good approximation be neglected due to conservation of momentum as the mass of the ion exceeds the electron mass by orders of magnitude. In photoelectron spectroscopy, the electron kinetic energy distribution is measured for a constant photon energy $h\nu$. Hence, information on the ion's internal energy is obtained. The energy necessary to remove an electron from an atom or molecule depends on the binding energy of an electron in the respective orbital. For ionization out of valence orbitals, which contain the most weakly bound electrons, electromagnetic radiation in the vacuum ultraviolet is needed. Monochromatic light sources providing reasonable intensities in this spectral region were not available until the 1960s, when noble gas resonance lamps were developed. The most common VUV light sources are helium resonance lamps. He atoms are excited by high voltage discharge and relax back to the ground state by emitting electromagnetic radiation in the VUV. The most intense line in the emission spectrum is referred to as the HeI$\alpha$ line, which corresponds to the transition $^1\mathrm{S}(1\mathrm{s}^2) \leftarrow {}^1\mathrm{P}(1\mathrm{s}^1 2\mathrm{p}^1)$ at 21.218 eV (58.4 nm). The valence orbitals of the majority of molecules can be ionized with HeI$\alpha$ radiation. To determine the molecule's ionization energy and vibrational or rotational structure of the ion generated by HeI$\alpha$ radiation, the kinetic energy of the electron is analyzed. This is usually done utilizing an electric field in a hemispherical deflection analyzer. The spectrometer consists of two concentric hemispherical electrodes, of which the inner electrode is charged with a positive potential and the outer one with a negative potential of the same magnitude. The incoming electrons are thus deflected in different paths according to their initial

velocities. As the electron kinetic energy resolution $E/\Delta E$ depends on the absolute kinetic energy of the electrons, a set of electrostatic lenses is used to decelerate the electrons and therefore increase the spectral resolution. As visible in fig. 2.5, only electrons with a certain velocity can enter the analyzer through the entrance slit and follow the right trajectory so that they leave the analyzer through the exit slit and reach the detector, which measures the electron current. This energy is referred to as the pass energy. Electrons which enter the analyzer, but have a different velocity and therefore trajectory, collide with the wall and are lost. By scanning the voltage applied to the hemispheres and measuring the respective electron current, an electron kinetic energy spectrum is recorded. Alternatively, the voltages of the electrostatic lenses can be tuned to decelerate kinetic electrons to match the pass energy. The difference between the VUV photon energy and the kinetic energy of the detected electron corresponds to the energy which is needed to ionize an electron out of a certain rovibronic state. The resolution of such a spectrometer is limited by the size of the entrance and exit slits. Reducing the slit size improves the resolution, but is detrimental to the sensitivity. Thus, a compromise has to be made resulting usually in a resolution of 10-30 meV. While it is enough to resolve the majority of the vibrational bands in most molecules, with the exception of several very small ones, rotational structure of the ion cannot be analyzed employing conventional photoelectron spectroscopy in the VUV.

Different variations of PES have been developed. In Penning ionization electron spectroscopy, metastable excited atoms inelastically collide with the target molecules and therefore induce ionization. Vibrational states in the Franck-Condon (FC) gap are in some cases also accessible employing Penning ionization since the molecule can be resonantly excited to an autoionizing Rydberg state.[94] In negative photoionization spectroscopy (photodetachment), anions are ionized to investigate the electron affinity and structure of the neu-

tral molecule. The anions are usually produced in electrical discharge. As a much lower photon energy (usually in the visible spectral range) is necessary to remove an electron from an anion, neutral and cationic side-products of the discharge do not perturb the photodetachment spectrum.

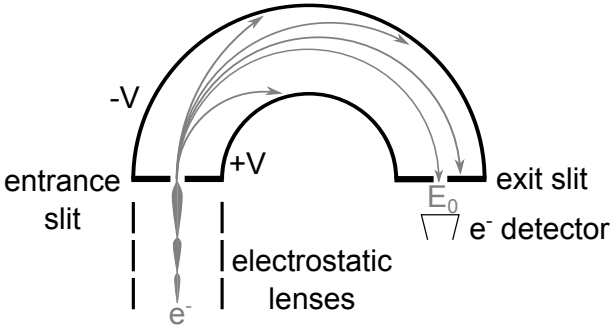


Figure 2.5.: Schematic view of a hemispherical analyzer as used in conventional photoelectron spectroscopy. The electrons are focused through the entrance slit by electrostatic lenses. The potentials on the inner and outer hemisphere deflect the electrons' pathways according to their kinetic energy such that only electrons with the energy $E_0$ can pass the exit slit and are detected.

### 2.3.2. Threshold Photoelectron Spectroscopy

Besides the restricted resolution, conventional photoelectron spectroscopy has the disadvantage that the cross section of a certain electronic or vibrational state depends also on the excess energy. Hence, some states might not be detected employing a single photon energy like in PES. This can be overcome when the photon energy is scanned, which necessitates the use of a monochromatic light source, and the electron analyzer is adjusted such that only electrons with a single kinetic energy are detected. Frequencies can be measured much more accurately than the kinetic excess energy of the pho-

toelectrons, which increases the resolution. By scanning the photon energy, resonant transitions into autoionizing states can be probed, in addition, which can add intensity to cationic states with low Franck-Condon factors. While experiments have been performed at constant non-zero electron energies,[95] most conveniently photoelectrons with zero kinetic energy are analyzed. This is called threshold photoelectron spectroscopy (TPES).

Discriminating threshold photoelectrons (TPE) against kinetic electrons demands a more complex design of the experimental setup. The first TPE spectrum was recorded in 1967 by Villarejo *et al.*,[96] who preaccelerated the electrons and then used an electrostatic analyzer to discriminate against kinetic electrons. As this technique did not increase the resolution compared to conventional photoelectron spectroscopy, Schlag and co-workers developed the so-called steradiancy analysis, where the energetic electrons are discriminated by their ejection angle.[97,98] Here, the generated electrons are first accelerated in an electrostatic field and are then allowed to drift in a long flight tube. Those electrons with no or only a small kinetic energy can pass the flight tube and reach the detector, while those electrons with transverse velocity components hit the wall of the flight tube. A very uniform extraction field is needed to achieve a high TPE resolution, which is best ensured for low electrostatic fields of about $4\,\mathrm{V\,cm^{-1}}$. Employing this technique, an electron kinetic energy resolution of 30 meV was realized.[97,98] Berkowitz and co-workers modified this approach by utilizing an electrostatic condenser, in which the electrons were accelerated parallel to the condenser plates.[99] Disks pierced with many parallel, cylindrical channels were inserted in the central region of the latter, which ensures that electrons with nonzero transverse velocity components cannot pass the condenser plate, while low kinetic energy electrons can and are thus detected by an electron channel multiplier. The energy resolution for the threshold photoelectrons for this setup mainly depends on the diameters and lengths of the cylindrical channels. Simultaneous

detection of the ions, which are accelerated in the opposite direction of the electrons, enables to use the photoion yield curves to calibrate the monochromator on autoionization resonances. In addition, coincidence experiments, in which the two particles originating from the same ionization event are correlated (see 2.5.1), can be performed. However, higher extraction fields are necessary for the ions, which is detrimental to the electron resolution. Another big disadvantage of all these methods is that they suffer from contamination of hot electrons, which only have a transverse velocity component and therefore are not deflected. These are detected alongside the threshold electrons and increase the background signal. Techniques to eliminate this background were thus developed. One possibility is to distinguish threshold and hot electrons by their time of flight.[100] While hot electrons with nonzero transverse velocity components can again be discriminated by their ejection angle, hot electrons with only a transverse velocity component arrive either earlier or later at the detector than threshold electrons. Wiley-McLaren space focusing conditions[101] ensure that the time of flight for the electrons is independent from their initial position. Employing this technique, hot electrons with energies greater than 20 meV can be successfully eliminated. However, 40 % of the true threshold electrons are lost and the extraction field has to be even smaller ($\ll 1\,\mathrm{V\,cm^{-1}}$) to differentiate energetic and threshold electrons by their time of flight. In addition, the experiment can only be performed utilizing a pulsed tunable photon source with a low repetition rate. Synchrotron facilities of the third generation are nowadays seldom operated in single-bunch mode, which is required for such experiments. For pulsed lasers, another very efficient technique for threshold photoionization with a resolution of up to $1\,\mathrm{cm^{-1}}$ (0.1 meV) was developed: PFI-ZEKE (pulsed field ionization zero kinetic energy).[102,103] Employing this technique, highly excited Rydberg states are prepared by the interaction of the molecule with a laser pulse and are subsequently field ionized by an electrical extraction field. The application of this technique is mainly limited by the range and tunability of laser light sources.

A milestone for the development of more efficient TPES techniques was the development of velocity map imaging (VMI) by Eppink and Parker. [104] Upon ionization, electrons with the same velocity spread from a punctual ionization origin uniformly in all spatial dimensions on so called Newton spheres. Large apertures are utilized in VMI as an electrostatic lens in the extraction field assembly instead of grid electrodes as depicted in fig. 2.6. Hence, particles with transverse velocity components are no longer scattered or deflected on the grid electrodes and the complete Newton sphere can be mapped in a two-dimensional image with a position sensitive detector.

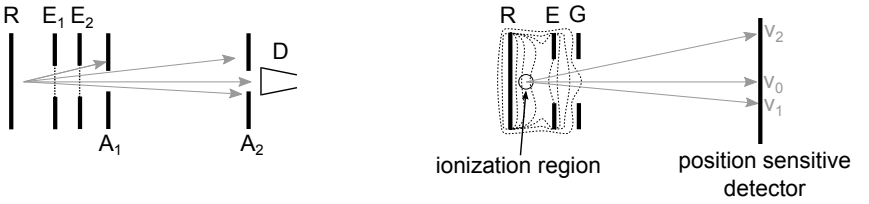


Figure 2.6.: Steradiancy analyzer with Wiley-McLaren set up (left; R: repeller; $E_1$, $E_2$: extraction grid electrodes; $A_1$, $A_2$: apertures; D: detector) and VMI extraction field assembly (right; R: repeller; E: extractor; G: ground electrode). The dashed lines depict the equipotential surfaces of the electrostatic lens. The velocities of the charged particles can be spatially resolved ($v_0 < v_1 < v_2$).

As the light/molecular beam interaction region comprises a certain volume, electrons with the same velocity are generated at different origins. It has to be ensured, however, that all particles with the same velocity are detected on the same spot on the detectors to obtain a defined image. Using large apertures leads to a very inhomogeneous electrostatic field between the repeller and extractor electrode, which is depicted by the curved equipotential surface lines in fig. 2.6 and can be exploited for focusing the electrons. A high negative voltage on the repeller can be employed that the electron cloud is collapsed in one dimension along the extraction axis. This is also called

'pancaking'. The shape of the equipotential surfaces between the electrodes can be influenced by varying the ratio between extractor and repeller voltage $V_E/V_R$. Like this, electrons in the pancake-shaped distribution with the same velocity see different effective potentials and can be focused onto the same spot on the detector. Threshold electrons arrive at the center of the detector, while hot electrons with nonzero transverse components are imaged as concentric rings around the central TPE spot. The radii are proportional to the kinetic electrons' velocities perpendicular to the extraction field. This focusing is significantly more efficient for low-energetic electrons than for high-energetic ones. TPES can thus be obtained with a very high resolution, which is mainly limited by the monochromator resolution.[105] A huge advantage of VMI compared to discrimination against energetic electrons by their angular distribution is that in VMI significantly higher extraction fields can be employed (typically 20-150 $\mathrm{V\,cm^{-1}}$). Hence, efficient ion extraction and high photoelectron resolution is no longer contradictory. However, the VMI technique still suffers from contamination of energetic electrons which initially have a trajectory parallel to the extraction field. Assuming that all electrons are ejected isotropically, which is valid for all larger molecules because they have high densities of states, the contribution of energetic electrons can be considered by a simple subtraction scheme of different regions of the electron image. Next to the central spot for the threshold electrons, a region in which only energetic electrons are assumed to arrive is analyzed. Sztáray and Baer suggested an approach, in which the respective electrons are selected by a mask in front of the micro channel plate (MCP) detector, which is divided into two sections.[106] The threshold electrons are detected in a central circle and electrons with kinetic energies greater than 38 meV are detected in a ring. By subtracting the ring signal, weighted by a constant empirical factor, from the circle signal, hot electron contributions are efficiently suppressed. For anisotropic electron distributions, the empirical factor has to be altered depending on the $\beta$-parameter, which describes the anisotropy of the ejected

electrons. The latest evolution of this technique foregoes the usage of a mask, but uses a position sensitive detector.[107] Like this, the full electron 2D image is available. A high electron energy resolution is usually achieved by the employment of delay line anodes. The buildup of such a detector is sketched in fig. 2.7. It consists of two curved wires, which are rotated by 90° to each other to form a grid. An incoming electron provokes a current in those wires and the arrival times of the induced electric current at the respective ends of these wires is registered. The differences between the arrival times $x_1$, $x_2$, $y_1$, $y_2$ yield the position of the electron on the detector. Delay line anodes are able to handle the high count rates of synchrotron experiments in contrast to the setups usually employed in VMI laser experiments, which consist of a phosphor screen and a CCD camera. The hot electron subtraction scheme can also be applied for the VMI setup. Here, the size of the selected regions can be varied according to the demands of signal intensity and desired TPE resolution and does not omit energetic electrons of a certain energy range as in the previous setup. This collection scheme for threshold photoelectrons has proven to be easily applicable and offers a high resolution. However, an empirical factor has to be used and a fully isotropic electron distribution is assumed.

### 2.3.3. Slow Photoelectron Spectroscopy

Recording the two-dimensional energy distribution of the ejected electrons employing VMI (see sec. 2.3.2) opens another pathway to discriminate against hot electrons since the image contains the complete information on the three-dimensional energy distribution of the electrons. However, reconstructing the distribution is challenging. Introducing the arrival time as the third dimension is theoretically possible, but difficult to implement for electrons, as a very high temporal resolution is necessary due to their short times of flight. In addition, this would again only be possible when light sources, generating light

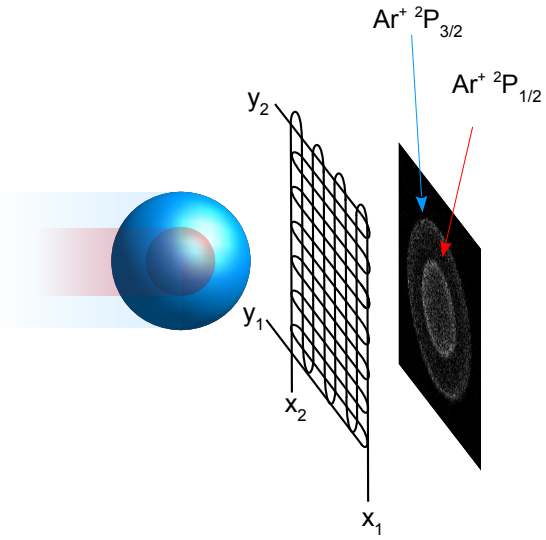


Figure 2.7.: Two Newton spheres evolve when ionizing Ar with 16.0 eV corresponding to the $Ar^+$ $^2P_{3/2}$ (IE=15.759 eV) and $^2P_{1/2}$ (IE=15.937 eV) spin orbit states. A two-dimensional map of the image of the Newton spheres can be mapped employing a delay line anode. The position of the registered electron can be deduced from the delay between the electric pulses at $x_1/x_2$ and $y_1/y_2$.

pulses at a lower repetition rate than the quasi-continuous time structure of electron storage rings, are utilized. Garcia *et al.* bypassed these difficulties by developing a sophisticated algorithm called pBasex to reconstruct the original Newton sphere by fitting a set of basis functions with a known inverse Abel integral.[108] As the Abel transformation of the images goes along with a loss of electron signal, signal/noise ratio would be significantly reduced in comparison to the established TPES method discussed in the previous section. A new experimental method to analyze the photoelectron signal was thus

developed, which is reported to even increase signal/noise ratio and is also able to resolve more spectral features than TPES.[109,110] When Abel-transforming a photoelectron image for a certain photon energy and radially integrating the reconstructed Newton sphere, the photoelectron spectrum can be obtained by plotting the electron signal against the kinetic energy of the electrons. Plotting the photoelectron spectra as a function of the photon energy results in a two-dimensional matrix, in which different cationic levels are mapped as diagonal, parallel lines, since the electron energy increases with the photon energy.

$$E_{kin}(e^-) = h\nu - IE_{rve} \tag{2.7}$$

Here $E_{kin}(e^-)$ is the kinetic energy of the ejected electron, $h\nu$ the photon energy and $IE_{rve}$ the energy for a resonant transition to a certain rovibronic level. The projection of this 2D matrix onto the photon energy axis yields the resonant photoelectron spectrum equivalent to a photoionization efficiency (PIE) curve. By contrast, a highly resolved photoelectron spectrum, in which also non-threshold electrons up to a certain kinetic energy are considered and which is therefore called slow photoelectron spectrum (SPES), is obtained when the electron signal is summed up along the parallel diagonals. The 2D map can be transformed by subtracting the kinetic energy from the photon energy as, according to eq. (2.7), the resonant excitation energy to the corresponding level can thus be obtained. In the resulting matrix the transitions to the different cationic levels are plotted as parallel lines perpendicular to the photon energy axis. Projection over this axis from 0 to X meV electron energy thus yields the SPES spectrum. For X=5 meV the TPE spectrum equivalent to the circle/ring method is obtained, although here, hot electron contributions do not have to be considered statistically. However, a worse signal/noise ratio is expected for the Abel-inverted TPES scheme. Statistics can be improved by summing up the 2D cuts up to a certain electron kinetic energy. As discussed in the previous section, the resolution in VMI is better

for lower kinetic energies of the detected particle. Therefore, as can be seen in fig. 2.8, the vertical lines broaden for higher electron energies.

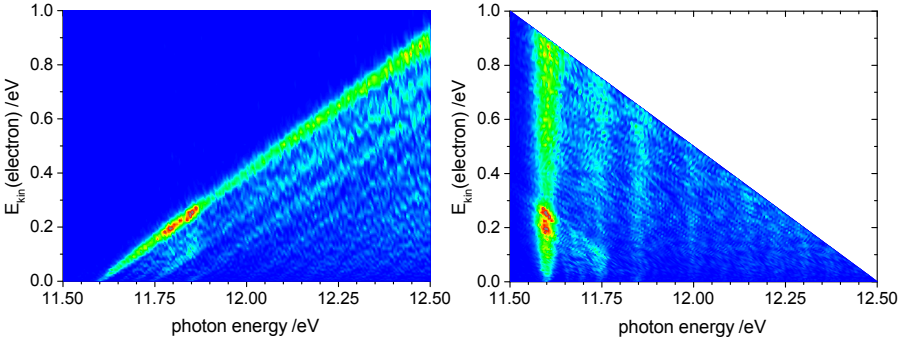


Figure 2.8.: Two-dimensional photoionization matrix for the example of HNCO (see also sec. 5.1). The vibrational levels of HNCO form parallel lines as the difference between photon energy and electron kinetic energy is constant (left). The bright spots at 11.79 and 11.85 eV can be assigned to autoionization resonances. By subtracting the electron energy from the photon energy, the photoelectron signal for the respective level can then be easily summed up by projection over the photon energy axis and a SPES spectrum is obtained.

Upper limits between 50 [111] and 170 meV [110] have proven to be a good trade-off between signal/noise ratio and resolution. In addition, SPES enables to resolve also transitions to vibrational levels in the Franck-Condon gap, which are accessible via autoionizing neutral states. This has been illustrated for the example of $Ar_2$ clusters. [110] The SPES 2D matrix and a comparison of the SPES spectrum with a TPE spectrum from the same experimental data is shown in fig. 2.9. It is obvious that the SPES spectrum (blue), for which the upper limit of the electron energy was chosen 170 meV, shows a much richer vibrational structure than the TPE spectrum (green). The bonding distance in the $Ar_2$ ground state is about 3.7 Å, which is reduced to 2.4 Å in $Ar_2^+$. The

vertical transition to the cation corresponds thus to an excitation in the tenth vibrational level of $Ar_2^+$. The 0-0 transition is hence well outside the Franck-Condon region and a direct determination for the adiabatic ionization energy of $Ar_2$ clusters is not possible with TPES. As in SPES electrons far from the ionization threshold are also considered, transitions to vibrational levels with low quantum numbers are observed and the adiabatic IE was determined to be 14.4564±0.0008 eV. Vibrational levels with low FC factors can be better resolved in SPES due to better statistics, but also vibrational levels in the FC gap are accessible via autoionization resonances, which can be seen in fig. 2.9 as bright spots. The autoionization resonance at 14.960 eV for example increases significantly the intensity of the levels $\nu_{11}^+$ to $\nu_{14}^+$, which are only very weak in the TPE spectrum.

SPES is therefore a powerful tool to obtain highly resolved photoelectron spectra without any empirical parameters like in the circle/ring TPE method. Vibrational levels outside the Franck-Condon limits can be detected due to autoionization resonances which produce non-threshold photoelectrons. This is especially relevant for very small molecules, which have a low density of autoionizing states. In addition, SPES increases the signal/noise ratio. This point, however, strongly depends on the precision with which the complete Newton spheres can be reconstructed. The better the quality of the two-dimensional image, the better the reconstruction algorithm works and good statistics in the SPES matrix can be achieved. The images occasionally suffer from blind spots because of defunct MCPs or sample debris on the MCPs. This might be the reason why in the experiments presented in this thesis no significant increase in signal/noise was obtained when comparing SPES with TPES. The data treatment for SPES is already well implemented and documented in the manual of the Igor extension of the DESIRS beamline of Synchrotron SOLEIL. A manual for obtaining SPES from raw data recorded at the Swiss Light Source can be found in appendix E.

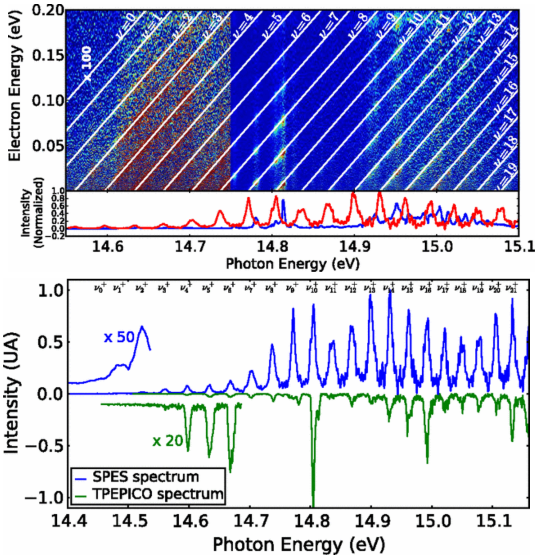


Figure 2.9.: Top: 2D SPES matrix for $Ar_2$ with the SPES spectrum (red line) and the electron yield (blue line) plotted at the bottom. Bottom: The comparison of the SPES spectrum (blue line) and the TPE spectrum (green line) shows that vibrational states in the Franck-Condon gap can be resolved with SPES. Figure reprinted from ref.[110]. Copyright (2015) by the American Physical Society.

## 2.4. Rovibronic Photoionization Transitions

As discussed in the previous sections, vibrational structure of the cation can be resolved by threshold and slow photoelectron spectroscopy. Comparing the observed band positions relative to the ionization origin with wavenumbers obtained from quantum chemical computations for the cationic structures enables to assign a band to a certain vibrational mode or a combination of several modes. The relative intensities of these transitions is determined by the corresponding Franck-Condon factors. The Franck-Condon principle works within the Born-Oppenheimer approximation and therefore neglects the motion of the nuclei for an electronic transition. Consequently, the transition probability from a neutral state described by the wavefunction $\Psi$ to a cationic final state described by $\Psi' = \Psi^+ \cdot \epsilon$, where $\Psi^+$ is the wavefunction of the cationic state and $\epsilon$ is the wavefunction of the ejected electron, is:[112,113]

$$\begin{aligned} < \Psi|\mu|\Psi' > \quad &= \quad < \Psi_K|\Psi_K^+ >< \Psi_{el}|\mu|\Psi_{el}^+\epsilon > \\ &\quad + < \Psi_{el}|\Psi_{el}^+\epsilon >< \Psi_K|\mu_K|\Psi_K^+ > \end{aligned} \tag{2.8}$$

Here, $\mu$ is the electric dipole operator. The second summand of eq. (2.8) is zero because the electronic wavefunctions are orthonormal and therefore identical for all allowed electronic transitions, i.e. $< \Psi_{el}|\mu|\Psi_{el}^+\epsilon > \neq 0$. $< \Psi_{el}|\mu|\Psi_{el}^+\epsilon >$ represents the selection rule for the dipole transition. The overlap of the nuclear vibrational wavefunctions of the initial and final state $< \Psi_K|\Psi_K^+ >$ are defined as the Franck-Condon integral. The square of this integral's absolute value is directly proportional to the intensity of a spectral transition. The intensities of vibrational bands can easily be simulated by a Franck-Condon analysis. In some cases, especially for small molecules, even rotational structure can be resolved employing TPES. The simulation of rovibronic photoionization transitions requires a profound analysis of the photoionization selection rules as will be discussed in the following sections.

### 2.4.1. Molecular Rotations

Molecules are classified in four groups according to their geometries for analyzing rotation: linear molecules, symmetric rotators, asymmetric rotators, and spherical rotators.[112] The classification results from the moments of inertia along the molecule's principal axes. The moment of inertia $I$ for any axis comprising the center of gravity is defined as:

$$I = \sum_i m_i r_i^2 \tag{2.9}$$

$m_i$ is the atomic mass and $r_i$ the distance from the atom to the axis. By definition, the axis with the smallest moment of inertia is the $a$-axis, while the one with the greatest moment of inertia is referred to as the $c$-axis. $a$ and $c$-axis are perpendicular, while the $b$-axis is in turn perpendicular to the former two axis. The three respective moments of inertia $I_a$, $I_b$, $I_c$ are defined as the principal moments of inertia, with

$$I_a \leq I_b \leq I_c \tag{2.10}$$

The energy of rotational levels is usually quantified in dependence on the rotational constants $A$, $B$, $C$ in $\mathrm{cm}^{-1}$which are inverse proportional to the moments of inertia $I_a$, $I_b$, $I_c$:

$$A = \frac{h}{8\pi c^2 I_a} \tag{2.11}$$

Here, $h$ is the Planck's constant and $c$ the speed of light. The rotational constants $B$ and $C$ are defined analogously. For a linear molecule, the moment of inertia along the bond axis is zero and the moments of inertia of all axis perpendicular to the former are the same, i.e. $A = 0$ and $B = C$.

In a symmetric-top molecule, which can be described as a symmetric rotator,

the moments of inertia along two of the principal axis are the same. Two cases can be distinguished. For a prolate symmetric rotator, $B$ and $C$ are equal ($A > B = C$) and for an oblate symmetric rotator $A$ and $B$ are equal ($A = B > C$). An example of a prolate symmetric top molecule is methyl iodide, in which the $a$ axis runs along the iodine carbon bond, while benzene is an oblate symmetric top molecule with the $c$ axis perpendicular to the molecule plane. In an asymmetric top molecule, all three rotational constants are different, i.e. $A \neq B \neq C$, whereas molecules with three equivalent rotational constants ($A = B = C$, e.g. methane) can be described as spherical rotators.

To calculate the rotational energy levels, the rotational Schrödinger equation is solved:[114]

$$\frac{1}{\hbar^2}(A\hat{J_a}^2 + B\hat{J_b}^2 + C\hat{J_c}^2)\Phi_{rot}(\theta,\phi,\chi) = E_{rot}\Phi_{rot}(\theta,\phi,\chi) \tag{2.12}$$

Here, $\hat{J_a}$, $\hat{J_b}$, $\hat{J_c}$ are the projections of the angular momentum operator $\hat{J}$ on the three prinicpal inertial axes of the molecule. The square of the rovibronic angular momentum operator is defined as the following:

$$\hat{J}^2 = \hat{J_a}^2 + \hat{J_b}^2 + \hat{J_c}^2 \tag{2.13}$$

The eigenvalues of these operators can be computed as

$$\hat{J}^2\Phi_{rve} = J(J+1)\hbar^2\Phi_{rve} \tag{2.14}$$

with the angular momentum quantum number $J$ defined for integer values from 0 to $J$ and

$$\hat{J}_\zeta\Phi_{rve} = m_J\hbar\Phi_{rve} \tag{2.15}$$

with the projection quantum number $m_J$ for the projection of $\hat{J}$ on any space fixed axis $\zeta$. $m_J$ has $2J+1$ integer values ranging from $-J$ to $J$. As $\hat{J}_\zeta$ and

$\hat{J}_z$, the projection of $\hat{J}$ on the molecule fixed $z$ axis, commute with each other, the eigenvalue of $\hat{J}_z$ is $k\hbar$ with the molecule fixed projection quantum number $k$.

The rotational Schrödinger equation (2.12) for a prolate symmetric top can be written as:

$$\frac{1}{\hbar^2}[A\hat{J_a}^2 + B(\hat{J_b}^2 + \hat{J_c}^2)]\Phi_{rot} = E_{rot}\Phi_{rot} \tag{2.16}$$

Using the type I$^r$ convention, which defines the $a$ axis as the $z$ axis, results in the rotational eigenvalue for a prolate symmetric top:[112]

$$E_{rot} = BJ(J+1) + (A-B)k^2 \tag{2.17}$$

For an oblate symmetric top molecule in the type III$^r$ convention ($c$ axis = $z$ axis), the following eigenvalue is obtained:[112]

$$E_{rot} = BJ(J+1) - (B-C)k^2 \tag{2.18}$$

For a spherical top molecule the eigenvalue is only dependent on the angular momentum quantum number $J$:[112]

$$E_{rot} = BJ(J+1) \tag{2.19}$$

The rotational eigenfunctions for all symmetric top and spherical top molecules are the same and do not involve the rotational constants. As they depend on the three quantum numbers $J$, $k$, $m$ the so-called symmetric top wavefunctions can be written as $|J,k,m\rangle$. The eigenenergy only depends on the quantum numbers $J$ and $K = |k|$.[114]

For an asymmetric top molecule, the Hamiltonian matrix therefore has to be set up in a basis of symmetric top wavefunctions for solving the rigid rotor rotational Schrödinger equation. Diagonalization of this matrix yields the

wavefunctions and eigenenergies. The asymmetric top wavefunctions are linear combinations of symmetric top wavefunctions. The respective coefficients are functions of the rotational constants $A$, $B$, $C$. In the type $\mathrm{I^r}$ convention, the Hamiltonian for an asymmetric top can be rewritten:[114]

$$\begin{aligned}\hat{H}_{rot} &= \frac{1}{\hbar^2}(A\hat{J_z}^2 + B\hat{J_x}^2 + C\hat{J_y}^2) && (2.20)\\ &= \frac{1}{\hbar^2}\{[(B+C)/2]\,\hat{J}^2 + [A-(B+C)/2]\,\hat{J_z}^2 \\ &\quad + [(B-C)/4]\left[(\hat{J_m^+})^2 + (\hat{J_m^-})^2\right]\} && (2.21)\end{aligned}$$

Here, $\hat{J_m^{\pm}}$ are the angular momentum ladder operators. The diagonal elements of the Hamiltonian matrix are:[114]

$$\left\langle J,k,m|\hat{H}_{rot}|J,k,m\right\rangle = [(B+C)/2]\,J(J+1) + [A-(B+C)/2]\,k^2 \quad (2.22)$$

It can be shown that only those off-diagonal elements coupling $|J,k,m\rangle$ with $\langle J,k\pm 2,m|$ possess values different from zero.[115] For an asymmetric rotor near the prolate top limit, i.e. $B \approx C$, the off-diagonal elements in a type $\mathrm{I^r}$ basis ($k$=$k_a$) are small and can be neglected. Hence, the eigenenergies are in good approximation given by eq. (2.22). For nearly oblate asymmetric rotors in a type $\mathrm{III^r}$ basis ($k$=$k_c$) the energy levels can be derived in an analogous way yielding the following eigenenergy:[114]

$$E_{rot}(J,k) = [(A+B)/2]J(J+1) + [C-(A+B)/2]k^2 \quad (2.23)$$

The asymmetry of a molecule is given by the parameter $\kappa$:[114]

$$\kappa = \frac{2B-A-C}{A-C} \quad (2.24)$$

In the most asymmetric case, $\kappa$ is zero, while for a prolate top molecule $\kappa = -1$

and +1 for an oblate top. Energy levels in an asymmetric top are usually designated $J_{K_a K_c}$ with $K_a = |k_a|$ and $K_c = |k_c|$ being the labels indicating with which prolate and oblate levels the former are correlated. The energy levels for the limiting cases of a prolate, an oblate and an asymmetric top and their correlation is depicted in figure 2.10. Asymmetric top wavefunctions cannot generally be assumed to be eigenfunctions of the angular momentum operator $\hat{J}_a$ or $\hat{J}_c$. That is why $K_a$ and $K_c$ are no good quantum numbers, but only labels. [114]

### 2.4.2. Photoionization Selection Rules

Photoionization can be described as the interaction of an electromagnetic field, represented by the electric dipole moment operator $\mu$, with a neutral molecule denoted by the rovibronic wavefunction $\Psi$. As a result, a cation and a photoelectron are prepared. The final state can be described by the product of the two independent rovibronic wavefunctions $\Psi^+$ and $\epsilon$ as coupling of the latter two particles can be neglected in the long range part of the electron-core potential. [113] The photoionization process can therefore be described as:

$$\left\langle \Psi^+ \epsilon | \mu | \Psi \right\rangle \tag{2.25}$$

The rovibronic wavefunction for the photoelectron can be expressed in dependence of the angular momentum quantum number $l$ of the outgoing partial wave. [116] As Signorell and Merkt have shown, [113] photoionization symmetry selection rules can be derived using group theory. The rovibronic symmetry of a state is characterized by the irreducible representation $\Gamma$. While the neutral and cationic state can be easily classified in their molecular symmetry group, the irreducible representation for the ejected photoelectron depends on the orbital angular momentum quantum number $l$ of the orbital out of which the electron is ejected. For even $l$ values, the photoelectron wavefunc-

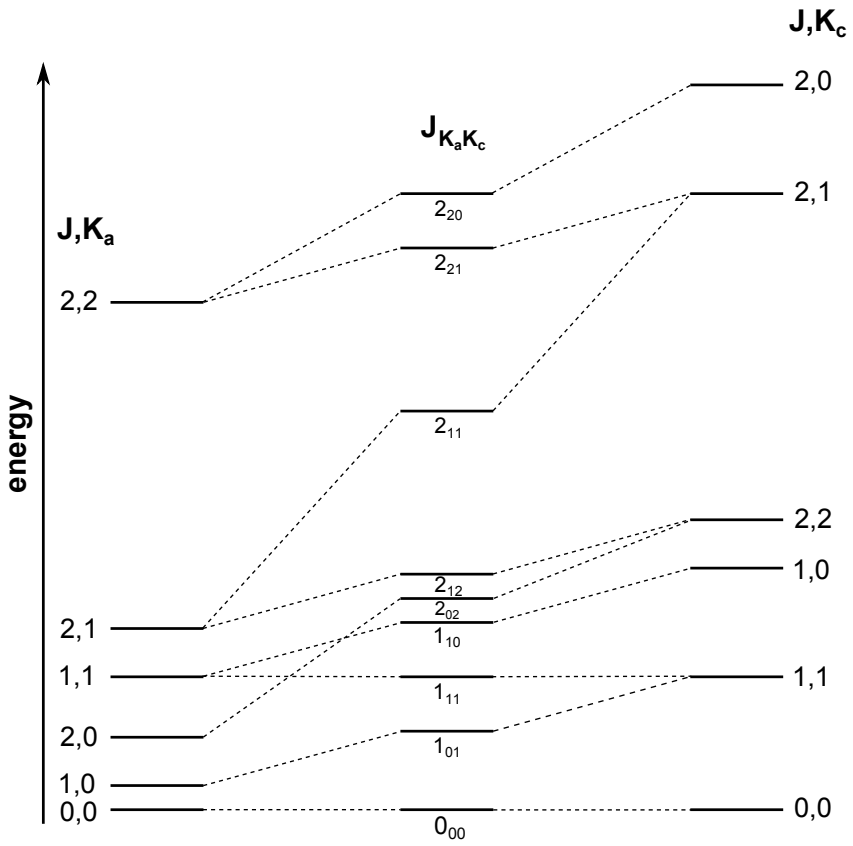


Figure 2.10.: Energy levels for $J$=0,1,2 for a prolate symmetric top molecule (left, A>B=C, $\kappa = -1$), an oblate symmetric top (right, A=B>C, $\kappa = +1$) and an asymmetric top molecule (middle, A>B=$\frac{A+C}{2}$>C, $\kappa = 0$) and their correlation. Figure adapted from [114].

tion transforms as the totally symmetric representation $\Gamma^{(s)}$ and for odd $l$ as the totally antisymmetric representation $\Gamma^*$. The totally antisymmetric representation is defined as the irreducible representation which is antisymmetric under all symmetry operations containing the space-fixed conversion $E^*$.[117] $E^*$ reverses the sign of all spatial coordinates in the space-fixed origin.[118] For example, the totally antisymmetric representation in the point group $C_{2v}$ is $A_2$, for $D_{3h}$ it is $A_1^{"}$, and $A_{1u}$ for $D_{6h}$.[113] As parity and nuclear spin symmetry must be conserved, the general rovibronic selection rule for a single-photon electric dipole transition states that the cross product of the final and initial state's representation must contain the antisymmetric represention. Hence, the following general photoionization selection rule can be derived:[113]

$$\Gamma_{e^-} \otimes \Gamma_{rve}^{+} \otimes \Gamma_{rve}^{"} \supset \Gamma^* \tag{2.26}$$

Here, the $\Gamma_{rve}^{+}$ and $\Gamma_{rve}^{"}$ symbolize the irreducible symmetry representation of the cation's and the neutral molecule's rovibronic state. Therefore two selection rules depending on the angular momentum quantum number $l$ of the photoelectron's partial wave can be introduced:[113]

$$\Gamma_{rve}^{+} \otimes \Gamma_{rve}^{"} \supset \Gamma^* \text{ for } l \text{ even} \tag{2.27}$$

$$\Gamma_{rve}^{+} \otimes \Gamma_{rve}^{"} \supset \Gamma^{(s)} \text{ for } l \text{ odd} \tag{2.28}$$

An additional restriction for photoionization in a single-photon process is introduced by the conservation of the total angular momentum $\overrightarrow{J}$,[119]

$$\Delta J = J^+ - J" = -l - \frac{3}{2}, -l - \frac{1}{2}, ..., l + \frac{3}{2} \tag{2.29}$$

where $J^+$ and $J"$ stand for the total angular momentum quantum numbers for the cation and the neutral molecule. $l$ is once again the orbital angular momentum quantum number of the photoelectron partial wave. For atoms,

$l$ can be predicted from the angular momentum quantum number $l$" of the ionized atomic orbital and the selection rule for single-photon processes $\Delta l = \pm 1$.

$$l = l" \pm 1 \tag{2.30}$$

This orbital ionization model assumes that the photon angular momentum characteristics are entirely transferred to the photoelectron.[120] In molecules, the partial wave can usually not be reduced to a single $l$ value. However, it has been shown that using an orbital ionization model for describing photoionization processes is a good approximation. Here, the angular momentum of the molecular orbital is assumed to be coupled to the one of the photoelectron partial wave. If the molecular orbital out of which is ionized resembles an atomic orbital, it can be described by a single $l$-value. But in general $l$-mixing cannot be disregarded.

### 2.4.3. Rovibronic Intensities in Photoelectron Spectra

A model for calculating rovibronic line intensities in photoelectron spectra of diatomic molecules has been developed by Buckingham, Orr and Sichel in 1970.[116] This model was later extended to asymmetric top molecules by Willitsch and Merkt.[121] In the following, all parameters and quantum numbers denoted with " refer to the neutral molecule and those denoted with $^+$ refer to the cation. As shown in eq. (2.31), the wavefunction of the orbital $\alpha$" out of which an electron is ejected can be deconstructed in a single-center expansion into its angular momentum components $l$" and $\lambda$", the projection of $l$" on the molecular axis. $\lambda$" is given as the number and symmetry of nodal planes of the orbital containing the molecular axis.[122] For near-prolate asymmetric top molecules, the molecular axis is the $a$ inertial axis, while for

near-oblate asymmetric tops, it is the $c$ axis.[121]

$$\phi_{\alpha"} = \sum_{|\lambda"|\leq l"}^{\infty} C_{l"\lambda"}^{\alpha"} R_{\alpha"\lambda"}(r) Y_{l",\lambda"}(\theta,\varphi) \tag{2.31}$$

Here $C_{l"\lambda"}^{\alpha"}$ are the single-center expansion coefficients, $R_{\alpha"\lambda"}(r)$ the radial functions and $Y_{l",\lambda"}(\theta,\varphi)$ the spherical harmonics. If the ionized orbital can be described by a single $l"$ in the framework of the orbital ionization model, the only expansion coefficients different from zero will be those containing the properties of the orbital out of which the electron is ejected $C_{l\pm|\lambda|}^{\alpha"}$. As already stated in section 2.4.1, the asymmetric top wavefunctions are not necessarily eigenfunctions of the angular momentum operators $\hat{J}_a$ and $\hat{J}_c$. That is why the asymmetric top wavefunctions $|N, K_a, K_c\rangle$ are expanded in the basis of symmetric top functions $|N, k, m\rangle$.

$$|N, K_a, K_c\rangle = \sum_k c_k^{NK_aK_c} |N, k\rangle \tag{2.32}$$

$N$ is the quantum number for the total angular momentum without spin and $c_k^{NK_aK_c}$ are the expansion coefficients. For an asymmetric top molecule near the prolate limit, this expansion coefficient has a nonzero value in good approximation only for $k = \pm K_a$, while for a near-oblate asymmetric top this is the case for $k = \pm K_c$. Using these approximations, it is possible to calculate the ionization cross section $\sigma$ at a certain energy $E$:[121,123]

$$\begin{aligned} \sigma_{tot}(E) \quad \propto \quad & \rho" |\langle \nu^+ | \nu" \rangle|^2 \sum_{|\lambda"|\leq l"} \frac{1}{2l"+1} Q(l") |C_{l"\lambda"}^{\alpha"}|^2 \\ & \times \left[ l" |F_{\alpha" l"}^{E,l"-1}|^2 + (l"+1) |F_{\alpha" l"}^{E,l"+1}|^2 \right] \end{aligned} \tag{2.33}$$

$$\text{with} \quad Q(l") = (2N^+ + 1) \left[ \sum_{k^+ k"} (-1)^{k^+} c_{k^+}^{NK_aK_c} c_{k"}^{NK_aK_c} \begin{pmatrix} N^+ & l" & N" \\ -k^+ & \lambda" & k" \end{pmatrix} \right]^2$$

In eq. (2.33), a Boltzmann weighting factor $\rho$" of the neutral's state initial rovibronic level is included:

$$\rho" = \chi" \exp\left\{-\frac{E"}{k_B T}\right\}(2N" + 1) \tag{2.34}$$

$\chi$" denotes the spin-statistical weight, $E$" the relative energy with respect to the lowest level and $k_B$ is the Boltzmann's constant. $|\langle \nu^+ | \nu" \rangle|^2$ determines the vibrational intensities and can be approximated by the product of the Franck-Condon factors of all normal modes. $F^{El}_{\alpha" l"}$ stands for the radial transition integral:

$$F^{El}_{\alpha" l"} = \int_0^\infty R_l(E, r) R_{\alpha" l"}(r) r^2 \mathrm{d}r \tag{2.35}$$

with $R_l(E, r)$ being the radial part of the photoelectron partial wave. If the orbital out of which the electron is ejected can be mainly represented by one atomic orbital, the term in the brackets of eq. (2.33) is constant and can be taken as unity. The sum running over $k^+$ and $k$" in $Q(l")$ is only relevant for asymmetric top molecules. The $3j$-symbol in $Q(l")$ couples the angular momenta of the neutral state with those of the cationic state. The selection rules of Wigner $3j$-symbols define further restrictions for the photoionization selection rules:

$$|\Delta N| = |N^+ - N"| \leq l" \tag{2.36}$$

$$\Delta k = k^+ - k" = \lambda" \tag{2.37}$$

This orbital ionization model for calculating rovibronic photoionization intensities has proven to yield convincing agreement with experiments in a number of studies mainly employing the PFI-ZEKE technique.[120,124–127] However, as the model utilizes some approximation, there are limitations for the applicability. The model will only stay valid if the electronic wavefunction of the

neutral and cationic state can be described by a single Slater-determinant. The model neglects that configurational mixing can introduce additional electronic angular momentum components into the electronic wavefunction. In addition, the frozen-core Hartree-Fock approximation is assumed, i.e. the geometry of the single molecular orbital which is supposed to be the only one, out of which ionization occurs, does not change upon ionization. If configuration interaction has a significant influence on the neutral or/and cationic state, transitions conflicting with the model selection rules will occur. However, these deficiencies can be compensated by introducing additional $B^{\alpha"}_{l"\lambda"}$ parameters. Thus, information on the degree of configurational mixing can be obtained. The model's main limitation is that interaction between the photoelectron and the dynamics of the ion-core is completely neglected. Coupling between different ionization channels mediated by the electron-ion core interaction at short range is therefore not included in the model. This coupling is for example important in some PFI-ZEKE experiments where autoionization processes and scattering of the Rydberg-electron on the ion-core can occur.[121]

## 2.5. Dissociative Photoionization

The excess energy in photoionization processes is distributed between the kinetic energy of the electron $E_{kin}(e^-)$ and the internal energy of the generated cation $E_{int}(ion)$.

$$h\nu = IE + E_{int}(ion) + E_{kin}(e^-) \tag{2.38}$$

If the internal ion energy exceeds a barrier for dissociation in the molecular ion, the molecule dissociatively ionizes to a daughter ion and a neutral fragment. The energy at which this dissociative process sets in is called appearance energy (AE). Appearance energies reveal information on bonding properties in the cation as they relate to the corresponding bond dissociation energy if there is no reverse barrier for the dissociation. For dissociation mechanisms proceeding via a tightly bound transition state, the appearance energy corresponds to the activation barrier for the bond breaking in the cation. In addition, appearance energies can be used to derive heats of formation for stable and unstable species. The AE of the fragment $A^+$ from dissociative photoionization reaction $AB + h\nu \rightarrow A^+ + B$ is associated with the following thermochemical cycle:

$$AE = \Delta_f H^0[A^+] + \Delta_f H^0[B] - \Delta_f H^0[AB] \tag{2.39}$$

Knowing the appearance energy and two of the heats of formation $\Delta_f H^0$, the third one can easily be derived. Ions and electrons from the same photoionization event can be correlated in photoelectron photoion coincidence experiments. As discussed in sec. 2.3, the ionization energy of the molecule and the kinetic energy of the electrons can be determined by photoelectron spectroscopy. Assigning a parent or daughter ion signal to the electron from the same ionization event, enables to simply derive the internal energy of the cation according to eq. (2.38).

### 2.5.1. PEPICO

Photoelectron photoion coincidence combines the information from photoelectron spectroscopy and mass spectrometry. Electrons and cations are accelerated in opposite directions by a small electric field to obtain a high electron energy resolution. In the first coincidence experiment by Brehm and von Puttkamer [128] a fixed energy line source was used to measure ions in coincidence with energetic electrons. The electrons were energy selected by a countervoltage and the electron pulse was delayed to account for the longer times of flight of the cations. The electron signal triggered the mass spectrometer, which opened for a time window of 0.1 to 1.6 µs to detect the corresponding ion signal. An electron can therefore be related to the cation of the same ionization event, which is detected in the corresponding time of flight window. In a similar way, the ion yield of a certain mass to charge ratio can be measured as a function of the electron kinetic energy. It is however possible that, by coincidence, a cation with a different mass to charge ratio is detected in the active time window of the mass spectrometer as it possesses excess translational energy. Such an event is called a false coincidence. The challenge in PEPICO experiments is hence to distinguish between true and false coincidences. The number of false coincidences is directly proportional to the total ionization rate and the time window for the coincidence signal. [129] That is why the goal of coincidence experiments is to keep the total ionization rate low and optimize the collection efficiency. The high pulse energy of a VUV ns-laser usually operated at 10 Hz would generate many electron-ion pairs that cannot be distinguished. The high repetition rate (several hundred MHz), low pulse energy and easy tunability make synchrotron radiation the ideal light source for PEPICO. The data acquisition schemes of early PEPICO experiments have an inefficient collection since no further ionization events can be detected in the time between the electron start signal and the ion stop signal. A sophisticated multiple start/multiple stop data acquisition

scheme was therefore developed to increase the collection efficiency especially for synchrotron experiments with higher ionization rates.[130] A master clock assigns time stamps to each event that is registered either on the electron or the ion detector. Employing statistics, the electrons and ions can be related to each other. As all start and stop signals are considered, the background signal from false coincidences is constant in the whole time of flight (TOF) range. It can therefore be easily subtracted.[107] The collection efficiency for threshold photoelectrons is nearly 100 %. Hence, the false coincidence signal in threshold PEPICO (TPEPICO) or, when an imaging electron detector is utilized, imaging PEPICO (iPEPICO) can be minimized. In addition, a very high electron energy resolution can be achieved with TPES, which results in a high resolution of the internal ion energy according to eq. (2.38). PEPICO is employed to obtain mass-selected TPE spectra, which is useful in pyrolysis experiments to distinguish precursor signal, signal from different pyrolysis products and possibly sample contamination. The main application of PEPICO is however to unravel dissociative photoionization.

### 2.5.2. Statistical Rate Theory

Statistical rate theory can be applied on the interpretation of PEPICO data on dissociative photoionization. DPI occurs when there is enough energy in the cation to reach the transition state leading to dissociation. Transition state theory makes the basic assumptions that the Born-Oppenheimer approximation is valid, nuclear motion can be described classically, and that crossing the transition state once leads inevitably to the products.[92] Statistical rate theory adds the presuppositions that the rate constant of the dissociation reaction depends only on the total energy and total angular momentum of the system and not where the energy is initially located. In addition, a microcanonical ensemble is assumed to be maintained as the molecule dissociates. Intramolecular vibrational energy redistribution (IVR) is consequently fast. A

microcanonical ensemble can be represented by a system of non-coupled harmonic oscillators. Employing statistical rate theory, the rate constant $k(E)$ for a dissociation of an ion with the internal energy $E$ can be determined and consequently the minimum energy for which the rate constant is unequal zero, i.e. the transition state's energy. In DPI this is the difference between the appearance energy of the fragment ion and the ionization energy of the parent molecule $AE - IE$, which will be referred to as $E_0$ in the following.

The approach by Rice, Ramsperger, Kassel, and Marcus (RRKM) [131] is most commonly used in statistical rate theory. In this theory, one out of the $(3N-6)$ non-coupled harmonic oscillators represents the critical mode that leads to dissociation. IVR, which is assumed to elapse on a time scale much faster than the dissociation, leads to deposition of energy in this critical mode. The molecule or ion dissociates when enough energy to surmount the activation barrier has been deposited in that mode. The rate constant therefore depends on the number of channels in the system in the internal energy interval from 0 to $E$, the density of states $\rho(E)$, and the total number of open channels in the transition state at the energy $E - E_0$, the sum of states $N^{\ddagger}(E - E_0)$:

$$k(E) = \frac{\sigma N^{\ddagger}(E - E_0)}{h\rho(E)} \tag{2.40}$$

In this equation, $h$ is Planck's constant and $\sigma$ a degeneracy factor respecting equal reaction pathways. The vibrational density of states can be easily derived, when the harmonic frequencies are known for example from quantum chemical computations, with the direct count algorithm by Beyer and Swineheart. [132] The sum of states can either be obtained by numerical integration of the density of states or employing a modification of the Beyer/Swineheart algorithm developed by Stein and Rabinovitch. [133] Upon dissociation, two vibrational modes of the reactant are converted to translational modes in the product and another two or three to rotational product modes for linear and

non-linear fragments, respectively. These modes are referred to as transitional modes. RRKM theory assumes fixed vibrational frequencies for calculating the transition state's sum of states and the transitional modes are therefore not taken into account when calculating $N^{\ddagger}(E - E_0)$. This approach works very well for dissociative photoionization pathways involving a tightly bound transition state since the activation is the rate-determining step.

Many dissociations, however, proceed along a purely attractive potential energy curve. The force constants for the transitional modes decrease along the reaction coordinate and disappear as these modes turn into pure rotations and translations.[134] Such processes can be better described in the statistical adiabatic channel model (SACM).[135] SACM makes the assumption that the set of quantum numbers for energized molecules is statistically distributed and the vibrational quantum levels remain the same along the reaction path. Vibronic potential energy curves do hence not cross, i.e. they are adiabatic curves. Quite counterintuitive, diabatic potential energy surfaces are constructed in SACM. The part of the potential curve, which corresponds to the conserved modes, i.e. long bond lengths, is approximated by the potential of the separated fragments. If the energy for the diabatic curve on the product side is higher than the internal energy of the dissociating system, the rate constant for that diabatic state $k(E, \nu)$ will be zero. If it is lower, a relation similar to the RRKM rate can be constructed:[129]

$$k(E, \nu) = \frac{1}{h\rho(E)} \tag{2.41}$$

Here, $\nu$ is the vibrational quantum number. The total rate constant is then given as the sum of all initial molecular states with sufficient energy to pass the barriers along the diabatic potential curves. The formula for the rate constant differs therefore only in the numerator for RRKM and SACM. Moreover, SACM includes centrifugal barriers along the reaction coordinate and hence angular momentum is conserved, contrary to RRKM.[129] The energies of the

two respective modes in the molecular and product state are correlated in SACM and are assumed to vary smoothly along the reaction path. This is considered by introducing a 1-parameter interpolation function. The potential energy curve along the reaction coordinate can be described by a Morse potential for dissociations without a reverse barrier, which causes a second parameter. Large molecules possess many vibronic channels,which must be considered in SACM. A simplified form of SACM (SSACM) was developed for that reason, which only uses a single parameter, i.e. the quotient of the two SACM parameters.[136] However, the application of SSACM to large molecules comprises still difficulties. If a reverse barrier exists for the dissociation, the modes in the transition state need to be considered in SACM, which makes it very similar to standard RRKM.[129]

### 2.5.3. Data Modeling

Plotting the relative abundances of the TPE signal detected in coincidence with a certain mass to charge ratio as a function of the photon energy reveals the breakdown diagram. The signal of the parent ion disappears upon dissociative photoionization with the signal of a daughter ion simultaneously rising. The photon energy $AE$ at which the barrier to dissociation in the ion $E_0 = AE - IE$ can be overcome is referred to as appearance energy. The appearance energy coincides with the energy of disappearance of the parent ion signal for dissociations with fast rate constants. The parent ion breakdown curve at 0 K, i.e. all dissociating ions are in the rovibronic ground state, describes a step function, which is 1 below the appearance energy and 0 at higher energies. The breakdown curve of the daughter ion describes the complementary behavior. Heated parent molecules, which are in a higher rovibronic state, dissociate already at lower photon energies as illustrated in fig. 2.11, which is why a thermal shift to lower photon energies is observed in the breakdown diagram for the onset of the daughter ion. Assuming that the

probability of threshold ionization is uniform across the neutral molecule's energy distribution, the internal energy distribution of the neutral can be transposed onto the ion manifold.[134] The neutral's energy distribution $P(E)$ can be computed for a temperature $T$ with the Boltzmann formula:

$$P(E) = \frac{\rho(E)\exp(-E/k_B T)}{\int_0^\infty \rho(E)\exp(-\mathrm{E}/\mathrm{k_B T})} \tag{2.42}$$

$\rho(E)$ is the density of states, which can be calculated from experimental or computed vibrational frequencies and rotational constants, and $k_B$ is the Boltzmann constant. The abundance of the parent and daughter ion signal in the breakdown diagram $BD_P(E)$ and $BD_D(E)$ as a function of the photon energy $h\nu$ for a fast dissociation is then given for photon energies below the appearance energy as:

$$BD_P(h\nu) = \int_0^{AE-h\nu} P(E)\mathrm{d}E; \quad BD_D(h\nu) = \int_{AE-h\nu}^{\infty} P(E)\mathrm{d}E \tag{2.43}$$

For photon energies above the appearance energy, it is:

$$BD_P(h\nu) = 0; \quad BD_D(h\nu) = 1 \tag{2.44}$$

If the first daughter ion undergoes further fragmentation in a sequential dissociation step, the energy distribution of the dissociating ion, i.e. the first daughter ion, has to be used in eq. (2.43) and (2.44). Contrary to the first dissociating (parent) ion, which is energy selected by the coincidence conditions and has the internal energy $E$, the excess energy in the second dissociating (first daughter) ion distributes between the ion and the neutral fragment. The internal energy distribution of the second dissociating ion gets therefore significantly broader and ranges from 0 to $E - E_0$. The probability for a first daughter ion $F^+$ produced with an internal energy $E_i$ at a total excess energy

$E - E_0$ can be calculated with the following formula:[137]

$$P(E_i, E - E_0) = \frac{\rho_{F^+}(E_i) \int_0^{E-E_0-E_i} \rho_N(x)\rho_{tr}(E - E_0 - E_i - x)\mathrm{d}x}{\int_0^{E-E_0} \rho_{F^+}(y)(\int_0^{E-E_0-y} \rho_N(x)\rho_{tr}(E - E_0 - y - x)\mathrm{d}x)\mathrm{d}y} \tag{2.45}$$

$\rho_N$ and $\rho_{tr}$ are the densities of states of the neutral fragment and the translational density of states, respectively.

If the dissociation is slow ($k(E) \lesssim 10^7\,\mathrm{s}^{-1}$), the rate constant of the reaction has to be considered. As discussed above, rate constants can be computed employing statistical rate theory using eq. (2.40). A kinetic shift of the breakdown curves to higher photon energies is observed for slow dissociative photoionization reactions as some ions, even though they possess enough internal energy to overcome the barrier to dissociation, do not dissociate on the time scale of the experiment and are still detected as parent ions. The rate constant must therefore be included in the calculation of the breakdown curve:[134]

$$BD_P(h\nu) = \int_0^{AE-h\nu} P(E)\mathrm{d}E + \int_{AE-h\nu}^{\infty} P(E)\exp(-k(E)\tau_{max})\mathrm{d}E \tag{2.46}$$

Here, $k(E)$ is the rate constant and $\tau_{max}$ the maximum time of flight of a dissociating ion to be detected as a fragment ion. The daughter ion abundance can be calculated complementary. The dissociation rate is also important for parallel competing dissociation channels of an ion as it defines the branching ratio. The branching ratio of two parallel dissociation channels can be calculated employing the rate expression from eq. (2.40):[138]

$$\frac{BD_{D1}(h\nu)}{BD_{D2}(h\nu)} = \frac{k_{D1}(E)}{k_{D2}(E)} = \frac{N_1^{\ddagger}(E - E_0(D1))}{N_2^{\ddagger}(E - E_0(D2))} \tag{2.47}$$

Here, $N_1^{\ddagger}$ and $N_2^{\ddagger}$ are the transition states' sums of states leading to dissociation above the thermodynamic dissociation limit of $E_0(D1)$ and $E_0(D2)$.

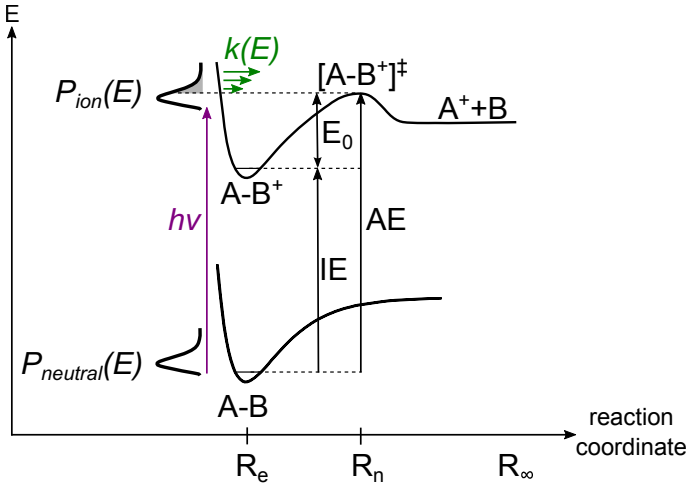


Figure 2.11.: Potential energy curves along the reaction coordinate of a dissociative photoionization involving a tightly bound transition state. The energy $AE$ is necessary to overcome the barrier leading to dissociation from the neutral ground state. The observation of the fragment ion's appearance depends on the photon energy $h\nu$, the internal energy distribution $P(E)$, i.e. the temperature, and the rate constant for the dissociation $k(E)$.

Information on the dissociation rate can be extracted from the peak shape of the daughter ion in the TOF distribution. When the dissociation of the ion happens while passing the acceleration region of the mass spectrometer, a daughter ion signal will be detected, but at a slightly higher time of flight. The daughter ion signal peak will therefore feature an exponential decay to higher flight times depending on the dissociation rate. Modeling the experimental TOF distribution reveals therefore information on the rate constant as a function of the photon energy, which is in turn needed to model the breakdown diagram using eq. (2.46). The peak shape of the daughter ion can

be computed with the following formula:[134]

$$Fr_i(h\nu) = \int_{AE-h\nu}^{\infty} P(E)(\exp(-k(E)\tau(TOF_i)) - \exp(-k(E)\tau(TOF_{i+1})))\mathrm{d}E \tag{2.48}$$

The TOF distribution is divided in $i$ TOF bins. $Fr_i(h\nu)$ is the normalized height of the fragment ion peak in channel $i$ and $\tau(TOF_i)$ this channel's dissociation time, which is obtained by numerical inversion of the $TOF(\tau)$ function.

The appearance energy for a fragment ion can be obtained by fitting $k(E)$ in eq. (2.48) to match the experimental TOF distributions for different photon energies and extrapolating the rate constant as a function of the ion internal energy to the barrier leading to dissociation $AE$. It has been pointed out in sec. 2.5.2 that RRKM and SSACM differ essentially in the way the sum of states of the transition state leading to dissociation is calculated. $k(E)$ is therefore fitted in different ways for these two theories. The transitional modes in RRKM, i.e. the five lowest frequencies for non-linear fragments, the four lowest ones for linear fragments, and the two lowest frequencies for atomic fragments, are scaled by a uniform factor to fit $k(E)$ to obtain a good match of the modeled and experimental TOF distributions. SSACM, by contrast, uses an energy-dependent rigidity factor to consider the "rigidity" or "tightness" of the transition state.[136] The purpose of this factor is to improve the part of the potential energy surface in which the transitional modes are converted into rotations of the separated fragments. The potential energy surface plays an essential role in the way the dissociation rate is computed in SSACM (*vide supra*). Simultaneously, the calculated breakdown diagram is fitted to the experimental data by varying the appearance energy $AE = E_0 + IE$ in eq. (2.46). When a good fit of the experimental TOF distributions and breakdown curves is reached, the appearance energy is obtained. For barrierless dissociations, the difference between appearance and ionization

energy is the bond dissociation energy in the cation. Fitting a breakdown diagram is also a reliable way to determine the temperature of the molecules in the gas phase because the shape of the breakdown curves depends on the temperature according to eq. (2.46) and (2.42).

## 2.6. Molecular Inner Shell Spectroscopy

While valence orbitals are usually diffuse and therefore characterize the chemical properties of the entire molecule, inner shell orbitals are highly localized. The binding energies of electrons in inner shell orbital are element specific and in the range of several hundred electron volts for first and second row elements. Spectroscopy on these orbitals hence requires higher photon energies in the domain of soft x-ray radiation (100 eV - 5 keV). X-ray radiation can be generated in x-ray tubes, in which electrons are accelerated towards an anode by a high voltage of several kilovolts. The electrons collide with the anode material and can transfer energy to electrons of inner shell orbitals, which are excited to higher levels. X-ray radiation is emitted when electrons relax to the vacancy of the lower level. The frequency $\nu$ of the irradiated light is element specific and can be derived from Moseley's law which includes the effective nuclear charge $Z_{eff}^2$.

$$\nu = f_R Z_{eff}^2 (\frac{1}{n_1^2} - \frac{1}{n_2^2}) \tag{2.49}$$

In this formula, $f_R$ is the reduced Rydberg frequency, $n_1$is the principal quantum number of the inner level and $n_2$ of the outer level. Light from 1s$\leftarrow$2s transitions, i.e. from the L shell to the K shell, is referred to as K$\alpha$ radiation. The most common monochromatic x-ray sources are Al-K$\alpha$ with an energy of 1486.6 eV and Mg-K$\alpha$ at 1253.6 eV. Synchrotron radiation represents by contrast a tunable x-ray source enabling a variety of spectroscopic techniques. X-ray spectroscopy, i.e. excitation or ionization of inner shell electrons, is mainly applied for the characterization of solid states. Although x-ray radiation penetrates a sample deeply, x-ray photoelectron spectroscopy, for example, only reveals information on the surface up to a depth of 10-30 Å. The ejected photoelectrons of atoms at greater depths lose energy by collisions with other atoms of the solid and thus only contribute to a background signal in the photoelectron spectrum. As information on the chemical surroundings,

bonding distances and oxidation levels can be revealed employing inner shell spectroscopy, it is also applied to molecules in the gas phase. The following sections deal with x-ray absorption and x-ray photoelectron spectroscopy, as well as spectroscopic techniques probing multiple electron transitions, like x-ray emission and Auger electron spectroscopy.

### 2.6.1. X-ray Absorption and Photoelectron Spectroscopy

Interaction of a molecule with soft x-ray radiation can either lead to excitation or ionization of an inner-shell bound electron. As core electrons occupy orbitals, which can in first approximation be regarded as atomic orbitals, the nomenclature of these orbitals is transferred from atomic systems, i.e. K for 1s, L for 2s/2p, and M for 3s/3p/3d orbitals. In x-ray absorption spectroscopy, a core-bound electron of a molecule $M$ is resonantly excited by soft x-ray radiation into an unoccupied valence orbital $V$ below the ionization potential and a core-excited molecule $M^*$ is generated.

$$M + h\nu_{res} \rightarrow M^*(1s^{-1}V^{+1}) \tag{2.50}$$

This process is sketched in the left scheme of fig. 2.12. The absorption probability is rather high [66] and the absorption coefficient $a$ follows the Lambert-Beer law, where $c$ is the concentration, $l$ the path length of the absorbing sample and $I$ and $I_0$ are the resulting and incoming light intensity:

$$a \cdot c \cdot l = \lg(\frac{I}{I_0}) \tag{2.51}$$

In near edge X-ray absorption fine structure (NEXAFS) spectroscopy, the absorption of a sample is recorded as a function of the photon energy. [139] A strong absorption is observed for resonant transitions of a core electron into an unoccupied valence orbital. The probed core excited state relaxes usually

through an electronic decay and a cation is produced (*vide infra*). The absorption can therefore easily be measured by recording the ion signal as a function of the excitation energy. The absorption intensity depends on the transition strength between the core electron and an unoccupied molecular valence state. This is, within the LCAO (linear combination of atomic orbitals) approximation, proportional to the atomic orbital coefficient of the molecular valence orbital. NEXAFS spectroscopy yields information on the nature of virtual molecular orbitals and enables probing of highly local electronic properties of valence electronic states. At the so-called K-absorption-edge, the ionization continuum is reached and a sharp onset with a slowly decreasing flank is observed in the absorption spectrum. The K-edge flanks exhibit often modulated fine structure, which arises from back scatter of the ejected core electron on the chemical surroundings. This is exploited in extended X-ray absorption fine structure (EXAFS) spectroscopy and yields for example information on bonding distances.[112]

If the molecule is core-ionized, this will result in a core-excited cationic state $M^+$ and an ejected photoelectron $e^-$:

$$M + h\nu \rightarrow M^+(1s^{-1}) + e^- \tag{2.52}$$

Analyzing the kinetic energy of the ejected electron in X-ray photoelectron spectroscopy (XPS) enables to determine the ionization energy of the core orbital from the difference of the photon energy and the kinetic energy of the electron. The recoil energy of the cation can be neglected as the molecular ion mass exceeds the electron's one by several orders of magnitude. This technique is depicted in the right scheme of fig. 2.12. In analogy to atoms, the ionization energy of a certain shell is greater, the higher the charge number of the nucleus. In addition, it is dependent on the direct surroundings of the core orbital, which leads to a chemical shift similar to NMR spectroscopy. The chemical shift in X-ray photoelectron spectra is linked to the electron density

of the valence electrons. Hence, the shift can be explained by the electronegativity of the neighboring atoms. Electronegative substituents decrease the electron density. The core electrons are consequently more tightly bound on the nucleus and the ionization energy increases. The chemical shift $\Delta E$ for an atom $A$ with the principal quantum number $n$ and the angular quantum number $l$ of a molecule $M$ can be derived as follows:[112]

$$\Delta E_{nl} = [E_{nl}(M^+) - E_{nl}(M)] - [E_{nl}(A^+) - E(A)] \tag{2.53}$$

Utilizing the approximation of Koopmans' theorem, the chemical shift can be derived from computed orbital energies $\epsilon$:

$$\Delta E_{nl} \cong -\epsilon_{nl}(M) + \epsilon_{nl}(A) \tag{2.54}$$

The chemical shift in XPS hence provides information on the chemical environment of a core ionized atomic orbital, which makes it possible to employ this technique for structural analysis of molecules and solid states. If the resolution of the electron spectrometer is sufficient, even vibrational structure can be resolved in X-ray photoelectron spectra. Removing a core electron influences the bonding of the other electrons, which may lead to a significant structural distortion and therefore vibrational structure is observed in the spectrum.

The final states in eq. (2.50) and (2.52) are highly unstable and relax on a fast timescale. The deactivation of a core excited neutral or cationic state can either proceed via nuclear motion in a radiating process or via radiation-less electronic decay.

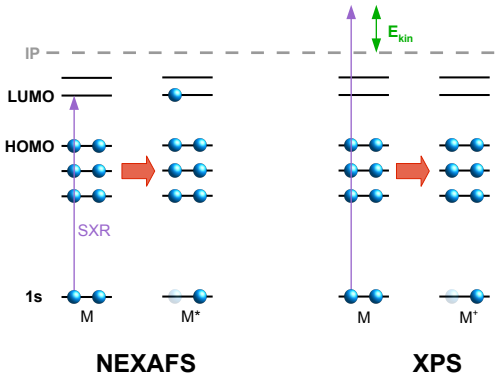


Figure 2.12.: Schemes of spectroscopic techniques exploiting interaction with soft x-ray radiation (SXR). In NEXAFS spectroscopy a core electron is resonantly absorbed by an unoccupied molecular orbital, while in XPS the ionization of a core electron is probed.

### 2.6.2. X-ray Emission and Auger Electron Spectroscopy

Core excited molecules can relax through nuclear motion, i.e. molecular vibration and/or dissociation.[66] In such processes, the energy is released as electromagnetic radiation in the soft x-ray regime. As depicted on the left of fig. 2.13, the deactivation can be monitored employing x-ray emission spectroscopy (XES). X-ray emission is, however, only of minor importance since electronic relaxation precedes molecular dissociation in most cases.[66] Photoemission follows the Einstein rate for spontaneous decay. By contrast, the timescale in which electronic relaxation occurs is tenth of femtoseconds for neutral and ionic core excited states. The core hole in a cationic state, which is generated by interaction of a molecule with soft x-ray radiation of an energy that exceeds the ionization energy of the core orbital, can be filled by a

valence electron from the orbital $V_1$. The released energy is transferred to a second valence electron of the same or a different valence orbital $V_2$, which will then be ejected into the ionization continuum. The kinetic energy of this so-called Auger electron $E_{kin}(Auger)$, which is independent of the irradiated photon energy, can be derived from the binding energies of the core electron $E_{core}$ and the binding energies of the two valence electrons $E_{V_1}$ and $E_{V_2}$ by neglecting the electron interaction.

$$E_{kin}(Auger) = E_{core} - E_{V_1} - E_{V_2} \tag{2.55}$$

As the influence of the chemical surroundings on the core electron and valence electron binding energy is approximately equal, a chemical shift can also be observed for Auger processes in analogy to XPS. This two-electron process, which is depicted in the middle scheme of fig. 2.13, results in a doubly charged cationic state and is called normal or non-resonant Auger. The deactivation of the core excited cation can be described as follows:

$$M^+(1s^{-1}) \rightarrow M^{++}(V_1^{-1}V_2^{-1}) + e^-(Auger) \tag{2.56}$$

The terminology of such a normal Auger transition is typically $KL_{V_1}L_{V_2}$, in which $K$ stands for the core orbital out of which an electron was initially removed, $L_{V_1}$ indicates the orbital of the electron that fills the core hole, and $L_{V_2}$ stands for the orbital in which a second vacancy is produced. In a normal Auger process the photoelectron of the primary core electron ionizing step can also transfer energy to a second electron, which is also ejected. Such a mechanism is termed 'shake-off'. [112]

For a core excited neutral state, there is a similar deactivation mechanism, in which an Auger electron is generated. This resonant Auger process is depicted on the right of fig. 2.13. In analogy to normal Auger, the core hole is filled by an electron from a valence orbital and an electron from the same or a second

valence orbital is ejected as an Auger electron. If the electron which fills the core orbital is the one that has been excited by the soft x-ray excitation in the primary step (eq. (2.50)), the deactivation mechanism is called participator resonant Auger decay. If it is a different electron, the decay is referred to as spectator resonant Auger. The kinetic energy of the released Auger electron is directly related to the remaining singly-charged electronic and rovibronic quantum state $V'^{-1}$.

$$E_{kin}(Auger) = h\nu_{res} - E_{el}(V'^{-1}) - E_{vib}(V'^{-1}) - E_{rot}(V'^{-1}) \tag{2.57}$$

The resolution of Auger spectra is not only limited by instrumental factors, but also by natural broadening of spectral lines. This is also termed lifetime broadening as, according to Heisenberg's uncertainty principle, it is directly related to the lifetime of a quantum state:

$$\Delta E \Delta t \geq \hbar \tag{2.58}$$

$\Delta E$ is the energy uncertainty, $\Delta t$ the lifetime, and $\hbar$ the reduced Planck's constant. As highly excited states are prepared in inner-shell spectroscopy, which decay on a femtosecond timescale, the natural broadening in the recorded spectra can be as high as 100 meV.[66] Other causes for spectral broadening are the intensity and monochromaticity (resonant Auger) of the exciting radiation and the resolution and collection efficiency of the spectrometer. Thermal motion of a gas phase sample can lead to Doppler broadening, while postcollision interaction and ion recoil effects also contribute to the line width.[66] In addition, the high density of electronic states - for normal Auger processes the configurations of dicationic states scale with the square of the number of valence orbitals, which multiply in most cases due to multiplicity splitting - leads to spectral overlap of many transitions, which makes it difficult to assign bands in Auger spectra, especially because of the lack of strict selection rules.

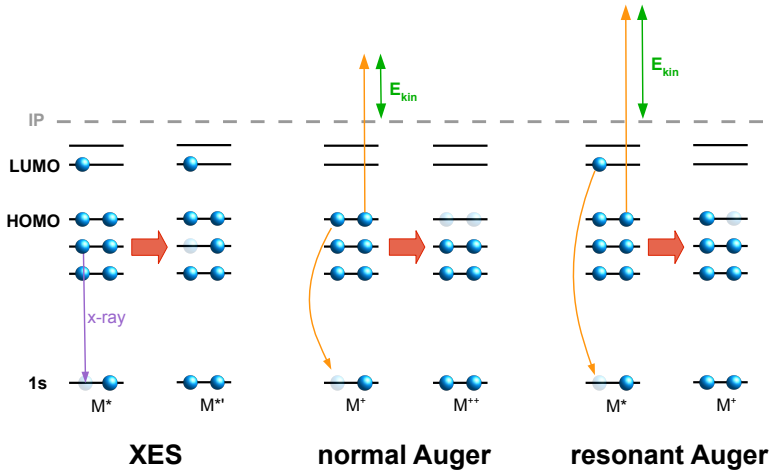


Figure 2.13.: Deactivation schemes for core-excited molecules and ions. Radiationless relaxation of the core excited state can lead to a doubly charged cation (normal Auger) or a singly charged cation (resonant Auger). These deactivation processes are competed by a relaxation mechanism in which a x-ray photon is emitted. The latter process can be observed employing x-ray emission spectroscopy (XES).

Extrinsic and intrinsic processes, like shake-up, shake-off, double Auger transitions, autoionization or inelastic scattering leads to even broader spectral lines.[140] Auger spectra of first row elements usually show three separated regions, which can be assigned to three classes for double hole Auger states. Those are characterized by outer-outer, outer-inner, and inner-inner valence orbital vacancies. Tightly bound valence orbitals which have a high fraction of 2s character are referred to as inner orbitals. The binding energy of those orbitals is around 30 eV, i.e. significantly higher than for the highest occupied

molecular orbitals, which is around 10 eV for most organic species. These three non-overlapping energy regions in normal Auger spectra show different characteristics in terms of the relaxation energy, electron correlation, transition amplitudes, and vibrational broadening.[140] The sharpest bands are observed for the outer-outer region at high kinetic energies. Electrons in the inner valence orbitals are more tightly bound. Removal of an inner valence electron thus leads to a larger structural change and therefore to broad bands due to vibrational structure or dissociation. An assignment of the observed bands in Auger spectra to certain final dicationic states is difficult because of all of those reasons and gets harder the bigger the molecule is. However, quantum chemistry can be employed to compute states and transition strengths, although at a high computational cost.

Auger decay is usually approximated as decoupled from the core ionization in the primary step. Therefore, only the core hole state and the final dicationic state are considered. As ab initio methods would require calculating all initial and final states, multiconfiguration self consistent field (MCSCF) or configuration interaction (CI) can only be applied for small systems, usually not larger than triatomics, due to computational cost. By contrast, Green's function techniques are capable of directly calculating ionization or excitation spectra,[141] i.e. the calculation of the wavefunction and energy of each individual final state is not necessary. Computed double ionization spectra yield the relative energy of the observed transitions. The intensity of these transitions in an Auger spectrum are defined by the matrix element between the highly localized initial core hole state and the final dicationic state. As a consequence, the spatial distribution of the two-hole density in the doubly ionized final state is very important. Considering these approximations, ADC(2), a second order Green's function scheme based on the Algebraic Diagrammatic Construction formalism developed by Tarantelli and co-workers, reduces the Auger decay to a symmetric eigenvalue problem in the space of the dicationic

configurations.[142] The solution yields the double ionization energies and the spectroscopic factors. Subtracting the double ionization energies from the core ionization potential then yields the Auger electron energies. The intensities are determined in a two hole population analysis of the ADC(2) eigenvectors. This has been successfully applied for example in the assignment of the normal Auger spectrum of acetaldehyde[143] and thymine.[144]

Auger electron spectroscopy offers element selectivity and very high local sensitivity as the very narrow core orbital is included in the spatial integral of the matrix element. In addition, it is independent of the irradiated photon energy.[66] Therefore it can be used as an efficient probe in femtosecond time-resolved spectroscopy on photoexcited molecular states employing free electron laser (FEL) sources. The monochromatic electromagnetic radiation of a FEL, which is referred to as fourth generation synchrotron radiation, is generated by self amplified spontaneous emission (SASE) and hence suffers from spectral shot-to-shot jitter.[145] This does not influence the kinetic energy of the Auger electrons, though. Electronic relaxation of a photoexcited state changes the valence orbital occupation and, as these orbitals are also involved in the Auger decay, different orbitals can be probed by Auger decays at different core hole sites. Besides time-resolved spectroscopy, inner shell spectroscopy techniques can also be employed to investigate combustion processes in flames. As has been shown recently by D. Osborn and co-workers, inner shell spectroscopy is a suitable tool to identify species in flames on-line, which holds several advantages over valence shell photoionization:[67] In the far edge region, it is possible to probe all molecules containing a certain element with an equal sensitivity, i.e. there is no molecule-specific cross section to be considered. It is thus possible to spatially map the concentration of an element. Employing NEXAFS spectroscopy, by contrast, specific molecules can be probed. Doppler broadening in the spectra is negligible because line widths are primarily set by the natural line width and the instrumental re-

sponse. In addition, when investigating carbonaceous species, the interference of non-carbon containing species, like $H_2O$ or $O_2$, can be totally excluded. The chemical shift in XPS or Auger spectroscopy can also be used complementary to PIMS studies to disentangle the contribution of two isomers with similar IEs.

# 3. Experiment

## 3.1. Pyrolysis Source

The following section describes the experimental procedure for the generation of a reactive intermediate in a continuous wave (CW) molecular beam at the VUV X04DB endstation of the Swiss Light Source as all pyrolysis experiments presented in this thesis were conducted there. Liquid precursor molecules with a sufficiently high vapor pressure ($> 3$ mbar) are transferred into the gas phase by bubbling a stream of argon through the liquid sample stored in a closed container outside the vacuum apparatus. The absolute background pressure of the Ar carrier gas is typically in the range of 2-4 bar, which enables to produce dilutions of 1-10 % of the precursor in the molecular beam. The molecular beam containing the sample is piped to the pyrolysis source, which consists basically of a gas feeding tube built into a DN 200 ISO-K vacuum flange (Ø 240 mm) and can be connected directly to the source chamber of the endstation's vacuum apparatus. The pressure in the source's tube is controlled by a needle valve or a mass flow controller. The flow of the gas is typically chosen to be between 20 and 70 sccm. The gas tube is connected to a 5.08 cm long 1/4" closed tubing (i.d. 5.33 mm) with a 150 µm orifice (Lenox LASER SS-1/4-TUBE), through which the molecular beam is expanded into the vacuum. The tubing orifice is placed in a copper block with a water feed through and the pyrolysis tube is directly attached to the tubing's orifice. The water circulation in the copper block can either be used

in cooling mode to prevent the gas supply tube from heating, which might be crucial for thermally unstable precursors, or in heating mode to transfer solids and liquid samples with low vapor pressures, which can be placed inside the orifice tubing, into the gas phase. Glass wool soaked with the liquid sample has proven to work efficiently for low-volatile precursors and re-condensation or re-sublimation is avoided by placing the sample very close to the pyrolysis region. The temperature of the water circuit is controlled by a chiller (Huber Minichiller), which can be operated in the temperature range between -20°C and +80°C (water has to be replaced by a cryogenic agent for the low temperature range). Pyrolysis takes place in an electrically heated silicon carbide (SiC) tube. This reactor invented by P. Chen and co-workers [46] consists of a SiC tube (HEXOLOY® SG, Saint-Gobain Ceramics) of about 30 mm length and an inner diameter of about 1 mm. Two electrical contacts are attached to the pyrolysis tube, which enables to heat the pyrolysis zone between the two contacts, which is typically 15 mm long. SiC is a refractory semiconductor with an inverted temperature coefficient of resistance. This ensures a minimal temperature gradient along the length of the heated zone, which is important to prevent for example radical recombination in lower temperature regions. In addition, SiC has a high thermal conductivity. Consequently, the thermal gradient between the inside and outside walls of the tube is also minimal. A type C thermocouple connected to the outside of the tube therefore provides a reliable temperature measurement of the pyrolytic conditions. Temperatures between 25 and 950°C can thus be realized in the pyrolysis region for SiC tubes with resistances of 20-100 Ω as used in these experiments. As the molecular beam has to pass the pyrolysis tube after expansion into the vacuum, no real supersonic molecular beam, in which the molecules would be cooled to several Kelvin, forms under these experimental conditions. The molecular beam properties in a Chen nozzle type microtubular reactor have been reviewed by J.W. Daily and co-workers. [146] The major findings for a molecular beam as used in the experiments presented in this thesis is discussed in more detail in

sec. 4.1. The front part of the used pyrolysis source is illustrated in fig. 3.1.

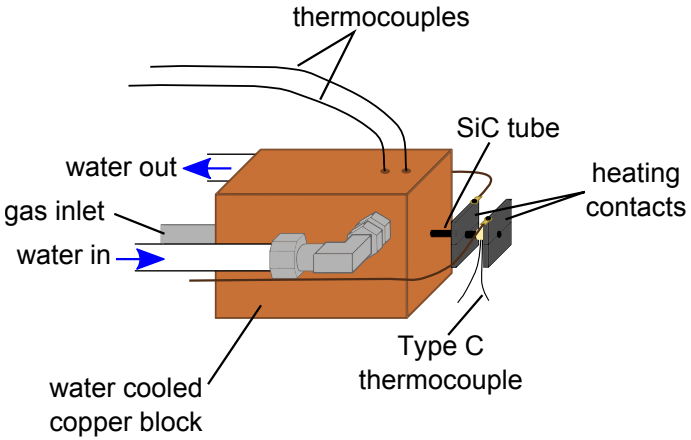


Figure 3.1.: Build-up of the pyrolysis source to generate reactive intermediates in a molecular beam.

## 3.2. Synchrotron SOLEIL DESIRS beamline

DESIRS is an acronym of the experiments that the VUV beamline at synchrotron SOLEIL is dedicated to: Dichroïsme et Spectroscopie par Interaction avec le Rayonnement Synchrotron (dichroism and spectroscopy by the interaction with synchrotron radiation). The beamline's spectrum spans nearly the complete VUV range from 5 to 40 eV. The scientific focus of the DESIRS beamline lies on very-high-resolution spectroscopy on small molecules, spectroscopy, fragmentation and reactivity of state- and/or mass-selected molecular ions, photoionization dynamics and excitation and relaxation in solids. Synchrotron radiation is provided by an HU640 undulator called OPHELIE2 (Onduleur Plan/Hélicoïdal du LURE à Induction Electromagnétique 2),[147] a further development of the undulator used at the VUV beamline of the Super

ACO LURE synchrotron (decomissioned in 2006). The undulator is 10.4 m long, has 14 magnetic periods with a period length of $\lambda_u$=640 mm and is able to produce synchrotron radiation from 5 to 40 eV. A pure electromagnetic scheme is utilized to produce synchrotron radiation with a controlled polarization (linear, elliptical or circular). Therefore, three sets of pure air coils are incorporated, of which one set generates a horizontal magnetic field. Air core coils do not have a ferromagnetic core, which allows operation at higher frequencies since energy losses occur in ferromagnetic coils. The other two sets or coils are shifted by $\lambda_u/4$ along the longitudinal direction and produce the vertical magnetic field with a continuously tunable longitudinal phase shift with respect to the horizontal magnetic field.[148] The horizontal and vertical magnetic field can be independently tuned and it is hence possible to produce fully calibrated quasi-perfect horizontally, vertically and circularly polarized synchrotron radiation in the VUV. The undulator provides photons to three independent endstation at the DESIRS beamline. White light can be fed into the fourier-transform spectrometer (FTS) branch for high-resolution VUV absorption spectroscopy.[149] In addition, two monochromated branches can be fed by OPHELIE2, the molecular beam endstation SAPHIRS (Spectroscopie d'Agrégats Photo-Ionisés par le Rayonnement Synchrotron) and the branch B, on which different experimental chambers from external users can be installed. The optical setup of the DESIRS beamline is depicted in fig. 3.2. Details on the optics can be found elsewhere.[148] Briefly, the synchrotron radiation emitted by the undulator is deflected by the mirrors M1 and M2 to minimize the heat load down stream because these mirrors do not transmit above 60 eV. Ionizing radiation is absorbed by a tungsten block. M2 focuses the light into a triple differentially pumped gas filter filled with Ne, Ar, Kr or Xe to suppress high harmonics of the undulator. The beam width is narrowed by a 4 blades aperture A, before the beam path is vertically elevated by the M3/M4 mirror pair. The beam is deflected by the same incidence and using the same reflecting material as on the M1/M2 mirror pair and the ini-

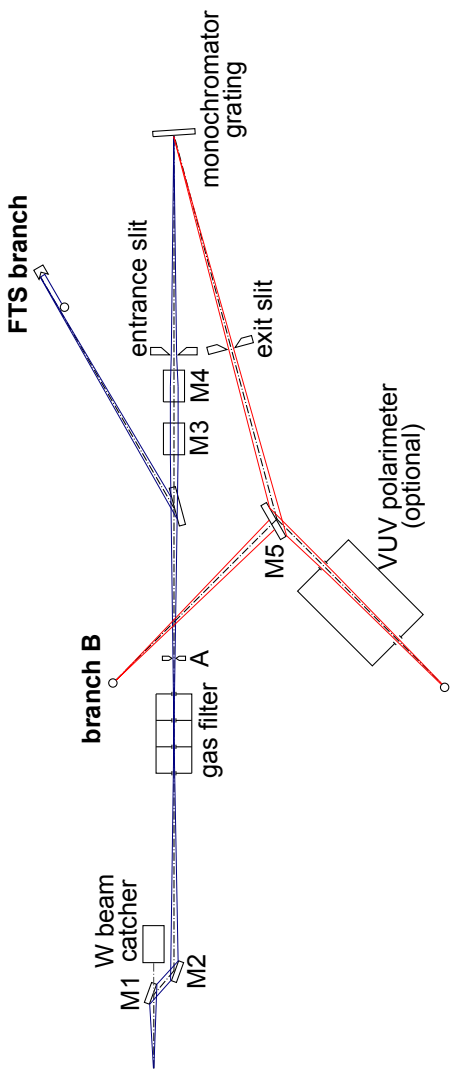


Figure 3.2.: Optics of the DESIRS beamline at Synchrotron SOLEIL (see text for description). Figure adapted from ref.[148].

tial polarization of the light is therefore conserved. Alternatively, a toroidal mirror can be inserted to focus the light onto the FTS branch. For feeding the monochromated branches, M4 refocuses the light onto the entrance slit of a 6.65 m long normal incidence monochromator. Four different spherical gratings with 200, 400, 2400, or 4300 lines $mm^{-1}$ can be utilized to diffract the synchrotron radiation. In the experiment presented in this thesis, the 200 lines $mm^{-1}$ grating was employed exclusively, offering a photon energy resolution of $E/\Delta E = 10^4$ at a photon flux of about $10^{12}$ photons$\cdot s^{-1}$. The photon beam is steered towards either the SAPHIRS branch or the B branch of the beamline by the toroidal mirror M5. A VUV polarimeter can be inserted into the beam path leading to the SAPHIRS endstation, but was not utilized in the presented experiment.

The SAPHIRS endstation at the DESIRS beamline consists of two vacuum chambers, the source chamber and the experimental chamber as depicted in fig. 3.3.[150]

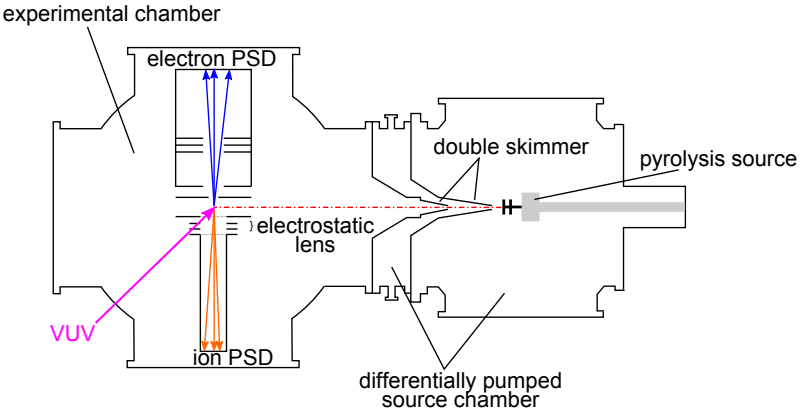


Figure 3.3.: SAPHIRS endstation with DELICIOUS III spectrometer at the DESIRS beamline.

The pyrolysis source is flanged directly onto the source chamber, which is connected to the experimental chamber, where the ionization takes place. Both chambers are evacuated by two 1000 $l\,s^{-1}$ turbomolecular pumps each. A differentially pumped double skimmer chamber (2 conical copper skimmers, Ø 1 mm) was recently built into the source chamber. This increased the maximum working pressure in the main source chambers to tens of millibars, which is especially suited for on-line spectroscopy in flames.[38] Passing these two skimmers, the coldest part of the molecular beam is directed to the ionization region in the main chamber. The centerpiece of the SAPHIRS endstation is the DELICIOUS III (Dichroism and Electron/Ion Coincidence in Ionization Using Synchrotron) double imaging PEPICO spectrometer.[151–153] Electrons and ions are extracted in opposite directions perpendicular to the molecular beam. The repeller voltage in the shown experiment was chosen 500 V (extraction field 250 $V\,cm^{-1}$). Electrons were detected with a commercial Roentdek DLD80 delay-line anode, while a modified Wiley-McLaren TOF spectrometer coupled with a delay-line anode[154] was used as a position sensitive detector (PSD) for the cations. The ion spectrometer optics include an electrostatic lens, with which the ions can be focused on the detector plane. The two-dimensional position of the ions on the detector plane and the measured time of flight reveals then the full 3D particle momentum distribution. This setting is called 3D momentum focusing mode. In addition, this mode enables to separate ions originating from the molecular beam from background ions from residual gas because the molecular beam ions carry a translational momentum along the beam axis, which is mapped onto the detector (see also sec. 5.1.1.3). In the time focusing mode, the electrostatic lens is turned off and a homogeneous electric field is generated in the second Wiley-McLaren acceleration area. The different ionization origins are thus not compensated, but an increased mass resolution is obtained. Electrons and ions from the same ionization event are correlated employing a multiple start/multiple stop coincidence scheme and false coincidences are considered as described in sec. 2.5.1.

Mass-selected threshold or slow photoelectron spectra (sec. 2.3.2 and 2.3.3) are obtained by using the Igor data analysis extension provided by the beamline. As the photon energy is usually calibrated on literature TPE spectra of $O_2$, $N_2$ or $H_2O$, the Stark effect does not have to be explicitly considered in the determination of IEs.

## 3.3. Swiss Light Source VUV X04DB beamline

Synchrotron radiation at the Swiss Light Source VUV beamline is provided by a bending magnet (port X04DB). The magnet's radius is 5.73 m and the magnetic field is 1.4 T. Details on the beamline layout can be found in the literature [155] and have been described in a recent PhD thesis. [156] In brief, the photon beam is collimated onto one of three monochromator gratings (150, 600, and 1200 lines $mm^{-1}$), which can be selected on a turntable-type construction. [157] Unless stated otherwise in the following discussions of TPE spectra, the 150 lines $mm^{-1}$ ($E/\Delta E=10^3$, $5{\cdot}10^{11}$ photons$\cdot s^{-1}$ at 8 eV) grating was utilized. The monochromatized radiation is then refocused into a rare gas filter operated with a mixture of Ne/Ar/Kr (8 eV < E < 14 eV) or pure Ne (10.5 eV < E < 21 eV) to suppress second order radiation. A $MgF_2$ window, which transmits only electromagnetic radiation below 11.0 eV, can be inserted into the optical path in front of the gas filter. The synchrotron radiation is then passed through the gas filter's exit slit into the vacuum apparatus, which has essentially the same buildup as the SAPHIRS endstation described in the preceding section. The pyrolysis source described in sec. 3.1 can be directly connected to the endstation's source chamber and the molecular beam is passed into the ionization region through a 1 mm conical skimmer. Both source (SC) and experimental chamber (EC) are each pumped by one turbomolecular pump (SC: 1600 l $s^{-1}$ Pfeiffer TPH 1201 UP, EC: 500 l $s^{-1}$ Pfeiffer TMH 521 YP) and one cryopump (SC: 5000 l $s^{-1}$ Leybold COOLVAC 5000

CK, EC: 1500 $l\,s^{-1}$ COOLVAC 1500 CL). Electrons and ions are extracted by a 120 $V\,cm^{-1}$ electric field in the iPEPICO spectrometer,[107] which consists of a Wiley-McLaren TOF mass spectrometer (Jordan C-726) for ion detection and a Roentdek DLD40 delay line anode for electron velocity map imaging. The mass spectrometer can be replaced by another Roentdek DLD 40 position sensitive detector in the $i^2$PEPICO setup, with which not only the ion times of flight can be resolved, but also their spatial distribution.[157] An effusive inlet system can be used for letting the sample molecule directly flow into the ionization chamber. The gas flow can be controlled by a needle valve. This inlet system is used for investigating dissociative photoionization of stable molecules as the temperature of the sample (298 K) is then exactly known. Data acquisition and analysis at the Swiss Light Source experiment are handled in a similar way as at the DESIRS beamline and are thus not discussed in more detail. Slow photon electron spectra can also be obtained at the SLS beamline. A manual on the data treatment is given in the appendix E. Photon energy calibration is performed using the 11s', 12s', and 13s' Argon autoionization resonances in first and second order. The observation of autoionization resonances is only dependent on the photon energy and not influenced by a Stark effect due to the extraction field. Previous studies have shown that the employed 120 $V\,cm^{-1}$ electric extraction field leads to a Stark shift of the observed signal to lower photon energies of up to 8 meV, but cannot be assigned to one precise value.[158,159] The Stark shift must hence be considered in the error bar of ionization and appearance energies determined from TPE spectra.

## 3.4. Synchrotron SOLEIL PLEIADES beamline

Photoionization experiments in the soft x-ray spectral range can be performed at the PLEIADES (Polarized Light source for Electron and Ion Analysis from Diluted Excited Species) beamline of Synchrotron SOLEIL. An Apple II HU80 permanent magnet undulator and an HU256 electromagnetic undulator provide synchrotron radiation between 10 eV and 1 keV to three branches. The 1.6 m long Apple II undulator consists of 38 sets of NbFeB magnet blocks, which are aligned to produce a symmetric vertical magnetic field in longitudinal direction. The undulator period length is $\lambda_u$(HU80)=80 mm and the minimal magnetic gap is 15 mm. The electrons pass twelve complete periods of $\lambda_u$(HU256)=256 mm in the HU256 electromagnetic undulator. The coils are arranged with a horizontal gap of 56 mm and a vertical gap of 16 mm and a maximum magnetic field of 0.3 T (0.43 T) can be obtained in horizontal (vertical) direction. Synchrotron light of horizontal, vertical, linear tilted, circular and elliptic polarization of photon energies as low as 55 eV is obtained from the Apple II undulator, while horizontally and circularly polarized radiation above 10 eV can be generated in the electromagnetic undulator. The synchrotron radiation is passed to an in-house designed Peterson plane grating monochromator, for which four gratings (400, 600, 1600, and 2400 lines $mm^{-1}$) with varied line spacing and varied groove depths can be selected to keep the monochromator's efficiency optimal.[160] The monochromatized radiation is focused onto the exit slits and then passed to one of the beamline's three branches. Three endstations are permanently installed on the PLEIADES beamline as depicted in fig. 3.4:[161] a station for positive and negative ion photoionization studies (MAIA), an energy and angle Auger electron/ion coincidence setup (EPICEA) and a high resolution wide-angle lens electron spectrometer (VG Scienta R4000). The Auger spectra of HNCO (sec. 5.1.2) were recorded using this hemispherical analyzer (cf. fig. 2.5). Electrons are accepted in an angle up to 16° and deflected by 180° in a radius of

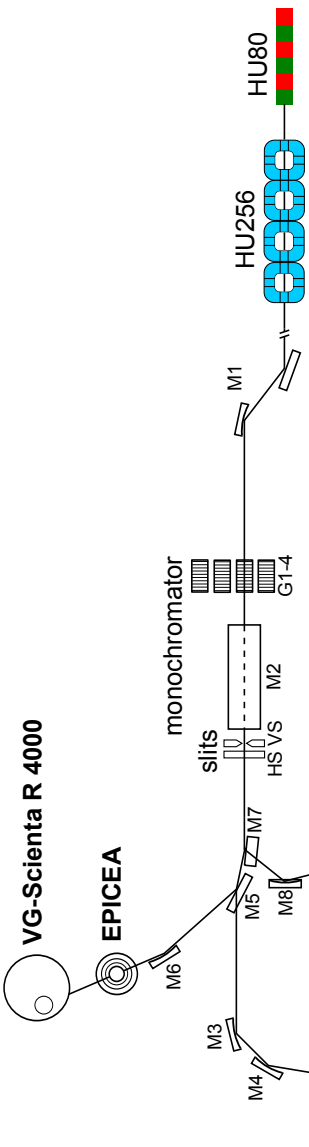


Figure 3.4.: Layout of the PLEIADES soft X-ray beamline. (M1-8: toroidal mirrors, G1-4: four monochromator gratings, HS/VS: horizontal/vertical exit slits)

200 mm to the 2D CCD-MCP detector system in this spectrometer. For the spectra presented in this thesis a pass energy of 50 eV and a slit width of 0.3 mm were chosen. The spectrometer's resolution is 37.5 meV for these settings. Gaseous samples are fed into the interaction region with the soft x-ray radiation in a differentially pumped gas cell, which prohibits the formation of plasma potentials, which would perturb the spectra.[160] Plasma potential are space charges, which can be produced in photoionization experiments since the very large velocity difference between electrons and ions generated upon photoionization can lead to an excess of positive ions in the excitation region.[162] The recorded Auger and NEXAFS spectra were calibrated on the literature spectra of $CO_2$[163,164] and $N_2$.[165,166]

## 3.5. Computational Methods

Quantum chemistry was employed to help interpret the experimental data. Using the Gaussian09 suite of programs[167] geometries, harmonic vibrational frequencies, rotational constants and total energies of all relevant structures were computed. The composite method CBS-QB3 features a high accuracy for computed thermochemical data.[168,169] This method first performs a density functional theory (DFT) geometry optimization on the B3LYP/6-311G(2d,d,p) level. The basis set, which is also referred to as CBSB7, includes p-polarization functions for hydrogen atoms to obtain better transition state structures for hydrogen transfers.[168] Harmonic vibrational frequencies are then computed on the same level of theory and the zero-point energy is computed with CBS-QB3 employing a scale factor of 0.99. The accuracy of the total energy is then improved by single point calculations on MP2/CBSB3 (= 6-311+G(3d2f,2df,2p)), MP4(SDQ)/CBSB4 (= 6-31+G(d(f),p)), and finally on the CCSD(T)/6-31+G(d') level of theory. An extrapolation to the basis set limit is performed with the MP2 method. The total CBS-QB3 energy

$E_{CBS-QB3}$ is then derived:

$$\begin{aligned} E_{CBS-QB3} &= E_{MP2} + \Delta E_{MP4} + \Delta E_{CCSD(T)} + \Delta E_{ZPE} \\ &\quad + \Delta E_{CBS} + \Delta E_{emp} + \Delta E_{int} \end{aligned} \tag{3.1}$$

In this equation, $\Delta E_{MP4}$ and $\Delta E_{CCSD(T)}$ are the energy differences of the respective level with the next lower one. $\Delta E_{ZPE}$ is the zero-point energy correction, $\Delta E_{CBS}$ accounts for the basis set truncation error on the MP2 energy, $\Delta E_{emp}$ is an empirical correction term, and the $\Delta E_{int}$ term considers an error due to spin contamination. As will be shown in the results section of this thesis, ionization energies derived by subtracting the neutral molecule's CBS-QB3 energy from the cation's one agree usually very well with the experimentally determined ionization energies. Appearance energies $AE_{0K}$ of cationic daughter fragments in dissociative photoionization processes can be derived in a similar way for DPI channels without a reverse barrier:

$$AE(AB;\, A^+) = E_{CBS-QB3}(A^+) + E_{CBS-QB3}(B) - E_{CBS-QB3}(AB) \tag{3.2}$$

If relaxed scans of the dissociation coordinate reveal a barrier, transition states can also be optimized on CBS-QB3 level of theory and the appearance energy can then be derived from the energy difference between this transition state and the neutral parent molecule. Time-dependent DFT was employed in some contexts to compute transition energies to and geometries and frequencies of electronically excited cationic states. All computations were performed either on the Linux-Cluster of the Leibniz-Rechenzentrum der Bayerischen Akademie der Wissenschaften (LRZ) in Munich or at the Merlin 4 HPC cluster at the Paul-Scherrer-Institut in Villigen.

Franck-Condon simulations based on the computed structural data and harmonic frequencies were performed to compare experimental and simulated photoelectron spectra and helped assigning the ionization energies and the

vibrational transitions. The CBS-QB3 wavenumbers were scaled with a factor of 0.967 unless stated otherwise.[170] In this study, the programs FCfit v2.8.20[171] developed in the group of M. Schmitt (Heinrich-Heine Universität Düsseldorf) and ezSpectrum[172] by A. Krylov and co-workers (University of Southern California) were used. The spectra of linear molecules can only be computed with ezSpectrum. The source code for the simulation of the rovibronic transitions in the TPES of HNCO (sec. 5.1.1) was developed specifically for the analysis and cannot be transferred to other system without further modification.

The program MinimalPEPICO v194i[134] utilizes computed frequencies and rotational constants for the calculation of densities and numbers of states, which are needed to model breakdown diagrams and TOF distributions by statistical rate theory (see sec. 2.5.2 for details). Both rigid activated complex (RAC) RRKM and SSACM are implemented in this program and it is possible to model fast, slow, sequential, parallel and all different combinations of these four dissociation pathways.

# 4. Determination of Photoionization Cross Sections

As outlined in the introduction, photoionization is a suitable probe for the identification of combustion intermediates in flames. However, quantitative data are needed for measuring absolute species concentrations in flames, which enables modeling reaction mechanisms and rates. Therefore absolute photoionization cross sections have to be determined. The photoionization cross section $\sigma$ is directly proportional to the measured ion signal $S$:

$$S \propto P\sigma[A]l \tag{4.1}$$

In this equation, $P$ is the photon flux, $[A]$ the concentration of the investigated species and $l$ the interaction length. Cross sections are usually given in the area unit barn [b] or megabarn [Mb] (1Mb=$10^{-22}$ m$^2$). As the interaction length is a constant for a particular experimental setup, absolute photoionization cross sections at a certain photon energy can be easily determined by comparing the ion signal normalized on the photon flux of a binary mixture with exactly defined concentrations of an analyte and a reference species with a well-known absolute photoionization cross section. Like this, absolute photoionization cross sections of numerous hydrocarbon species relevant in combustion processes have been determined.[55,173,174] A more elaborate approach has to be made, however, for reactive intermediates' photoionization cross sections because binary mixtures of those with a reference species can-

not be easily fabricated. Only few cross sections for radicals and carbenes are known so far for that reason.[175–180] Pyrolytic generation of radicals has proven to be a suitable method to investigate photoionization cross sections, provided that the cross section of the other pyrolysis products and/or of the precursor itself and their concentrations are exactly known. This was for example exploited in the investigation of the cross section of the methyl radical, which was produced from the corresponding iodide.[176] There exist two pyrolysis channels for methyl iodide: one leading to methyl and an iodine atom and a second one leading to methylene and HI. The relative concentration of the methyl radical can then be derived from the difference between the depletion of the precursor signal and the growth of the HI signal, for which the absolute photoionization cross section have been reported previously.[181,182] To avoid such a subtraction scheme, it is desirable to find a precursor, which can be cleaved into the reactive intermediate and a second fragment with a known cross section without any other side products. An example of such a system is depicted in fig. 4.1: Spiro(cycloprop[2]ene-1,3'-tetracyclo[3.2.0.0$^{2,7}$.0$^{4,6}$]heptane), a quadricyclane, can be pyrolyzed and yields selectively the cyclopropenylidene carbene and benzene.[183,184]

Cyclopropenylidene has a high thermodynamic stability and exists therefore in high abundance in the interstellar space, e.g. in the radiogalaxy Centaurio A (NGC 5128).[185] It is the most stable one of the three $C_3H_2$ isomers: cyclopropenylidene $c$-$C_3H_2$, propargylene HCCCH, and propadienylidene $H_2CCC$. The electronic ground state is a singlet state with the lone pair located in a $\sigma$-orbital. Hence, there are two $\pi$-electrons in the ring system, which is why the carbene is defined as aromatic.[185] Due to its high dipole moment it can be easily identified by microwave spectroscopy in the interstellar space.[186] As cyclopropenylidene is kinetically instable, it is assumed to play a central role in fundamental interstellar reactions.[187,188] In addition, cyclopropenylidene was identified as a combustion intermediate in cyclopentene/oxygen flames.[189]

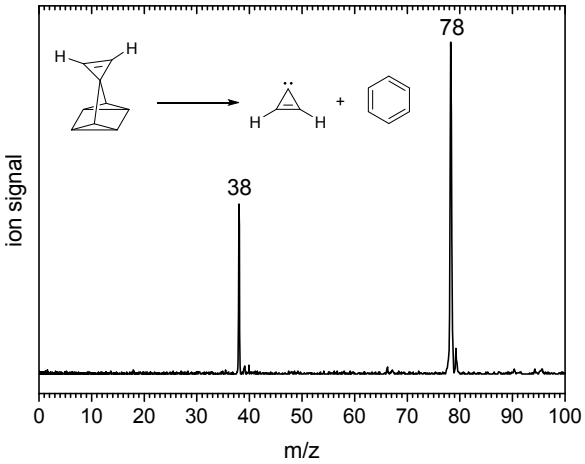


Figure 4.1.: Pyrolysis of the quadricyclane precursor on the left yields selectively cyclopropenylidene (m/z=38) and benzene (m/z=78). The mass spectrum was recorded at E=9.5 eV and a pyrolysis temperature of 470°C.

This makes the knowledge of an absolute photoionization cross section of $c$-$C_3H_2$ desirable as it enables to determine absolute mole fractions in the flame and hence model combustion processes by the derived reaction rates. The photoionization of cyclopropenylidene has already been thoroughly investigated by conventional photoelectron spectroscopy [190] and TPEPICO. [191] The ionization energy was determined to be IE=9.17 eV. In previous pyrolysis experiments, chloro-cyclopropene was used as a precursor, from which HCl is cleaved upon pyrolysis. [191–193] This precursor holds several disadvantages because side products from the synthesis as well as produced during pyrolysis complicates data analysis. A determination of the low-energy photoionization cross section of cyclopropenylidene, i.e. around the ionization threshold, is impossible since the ionization energy of the corresponding pyrolysis fragment HCl, from which's cross section cyclopropenylidene's one would have to be de-

rived, is significantly higher than for *c*-$C_3H_2$ (IE=12.79 eV[194]). A different precursor, with which this problem can be circumvented, is the quadricyclane (*vide supra*). This precursor was suggested and tested in matrix by Reisenauer *et al.*[183] Recently, an improved synthetic route was reported, which enables to synthesize the quadricylclane in high enough quantities to run demanding gas phase experiments.[184]

The synthesis of the quadricylclane precursor for the following experiment was performed in the group of Prof. Dr. Anke Krüger (Institute of Organic Chemistry, University of Würzburg). In this work, the absolute photoionization cross section of cyclopropenylidene was determined by relating it to the cross section of benzene, which is generated in the same stoichiometry by pyrolysis of the quadricylclane precursor. The ratio of $C_3H_2$ ion signal to benzene ion signal is then given by the following relationship:

$$\frac{S_{C_3H_2}}{S_{C_6H_6}} = \frac{[C_3H_2]}{[C_6H_6]} \frac{\sigma_i^{C_3H_2}}{\sigma_i^{C_6H_6}} \frac{A_{C_3H_2}}{A_{C_6H_6}} \tag{4.2}$$

Here, $\sigma_i$ is the absolute photoionization cross section. The concentrations $[C_3H_2]$ and $[C_6H_6]$ are equal, as discussed above. $A$ is an apparatus function. While most of the elements for this apparatus function cancel out in the fraction of eq. (4.2), it also contains a mass-dependent element, the so-called mass discrimination factor of a species $x$, which will be denoted as $F_x$ in the following discussion.

## 4.1. Mass Discrimination Factor

The mass discrimination in a gas phase photoionization experiment is directly related to the properties of the molecular beam. A molecular beam is generated when a gas under high pressure is expanded into a low-pressure region through a small orifice. As this involves no heat transfer, the enthalpy is con-

served and the expansion is therefore an adiabatic process.[85] Fast atoms or molecules of the expanded gas collide during the expansion with slower atoms or molecules in front of them and transfer translational energy, which leads to a narrowed speed distribution and translational cooling. Like that, supersonic gas velocities and therefore strong cooling to only a few Kelvin may be achieved in the beam. As the translational temperature decreases with the distances from the expansion nozzle, vibrational and rotational energy flows to the translational modes. Consequently, molecules are also vibrationally and rotationally cooled, but to different temperatures, as the relaxation rates differ.[129] The presence of background gas in the low-pressure region, i.e. randomly moving molecules, leads to interaction with the directed jet molecules. The core of the expanding beam is not affected by the background gas, but the molecules in the jet boundary undergo many collisions, which slow down the expansion and so-called barrel shock waves on the jet boundaries and the Mach disk perpendicular to the flow direction form.[195] This leads to an enrichment of light molecules in the jet.[196] This pressure diffusion within the barrel shock region can be suppressed, when a skimmer is placed downstream of the first Mach disk and therefore only the core of the expanding beam, which shows no interaction with the background gas molecules, passes to the ionization region. Pressure diffusion in the jet, however, leads to enrichment of heavier species in the centerline and can only be neglected for turbulent flows. Recent studies of J. W. Daily, G. B. Ellison and co-workers showed that the flow inside and at the end of a SiC reactor, like it was used in all experiments presented in this thesis, is not turbulent.[146] A second cause for mass discrimination is Mach-number focusing downstream of the skimmer.[196] The translational velocity $u$ of a species in a molecular beam scales with $\frac{1}{\sqrt{m}}$:

$$u = \sqrt{\frac{2k_B T}{m}} \tag{4.3}$$

$m$ is the molecular mass, $k_B$ the Boltzmann constant and $T$ the translational temperature. The velocity along the beam axis is the same for all species. Perpendicular to the molecular beam, however, the transverse velocity will be higher for lighter species, which leads to an enrichment of heavier molecules in the molecular beam. Therefore, the ionization probability for heavier molecules is higher than for lighter species, which has to be taken into consideration when determining absolute photoionization cross sections. This is reflected in the apparatus function and is called mass discrimination factor.

The description above relates to a molecular beam, which can in good approximation be described by laminar flow dynamics. In fluid mechanics fluids are considered to be continuous, i.e. the composition of the fluid of discrete molecules is neglected. The Knudsen number $Kn$, which is defined as the ratio of the molecular mean free path to a characteristic length, which in the case of the pyrolysis source is the length of the SiC reactor tube, decides whether the continuous limit holds.[146] For Knudsen numbers <0.1, a flow can be described as continuous. For $Kn < 0.01$, laminar flow characteristics can be assumed, i.e. a flow of highly ordered particles moving in parallel lines. The flow in a supersonic molecular beam can be described as a laminar flow. If $Kn \geq 1$, the flow will be much more disordered. Due to lower densities, collisions between particles become rare and the atoms and molecules scatter randomly between the walls. The flow is then referred to as free-molecule or molecular flow. The region of $0.01 < Kn < 1$ constitutes a transition region from laminar to molecular flow. As the discussion on the causes of a mass discrimination above alludes to a supersonic molecular beam, the question arises to what extent such an effect has to be expected for the experimental setup used at the SLS . The CW flow of gas combined with a pyrolysis tube produces a beam which should be in between a 'real' supersonic molecular beam and an effusive beam. Recently, a detailed study of the flow in a SiC pyrolysis reactor was published.[146] Simulations on different flow character-

istics were run for helium in a SiC tube with a wall temperature of 1500 K for different flow rates. As expected, the velocity of the molecules increases with increasing flow rates, but sonic conditions are reached near the end of the SiC tube even at the lowest flow rate of 100 sccm. Fig. 4.2 shows a plot of the Knudsen number versus the axial distance from the expansion orifice for 100, 200, and 280 sccm. It becomes obvious that the 100 sccm curve leaves the true laminar flow region at significantly shorter axial distances than the other two reference curves corresponding to higher flows. Typical mass flow rates in the performed SLS experiments were in the region between 25 and 70 sccm, i.e. significantly lower than either of the three modeled flow rates. Consequently, the laminar flow characteristics of the molecular beam should be much lower and the beam should therefore resemble more an effusive beam. That means that the effect of mass discrimination is expected to be much less pronounced than for experiments with a pulsed molecular beam. Nevertheless, this hypothesis was tested by experimental data.

Binary mixtures of five compounds (NO, acetone, benzene, cyclohexane, ethyl bromide) $A$ with propene, for all of which accurate values for the photoionization cross section exist,[55,197–200] were prepared. 30 mbar of the analyte and 600 mbar of a mixture of propene in nitrogen (5 %) were prepared in a 3 l stainless steel cylinder and 2370 mbar of argon was added to obtain a defined gas mixture which contains 1 % of the analyte and propene, respectively. The ratio of the ion signal was then analyzed for different photon energies under similar conditions for which the experiment on cyclopropenylidene had been performed (T(pyro)=460°C, p(EC)=$4{\cdot}10^{-6}$ mbar, p(sample)=1.7 bar). It has to be considered in the selection of the analytes that the position sensitive electron detector at the SLS beamline only records electrons up to a maximum kinetic energy of about 1 eV. The photon energies have to be chosen accordingly, i.e. IE<$h\nu$<IE+1 eV. Ideally, the analyte has a similar ionization energy as the reference substance (propene) to ensure that an energy range

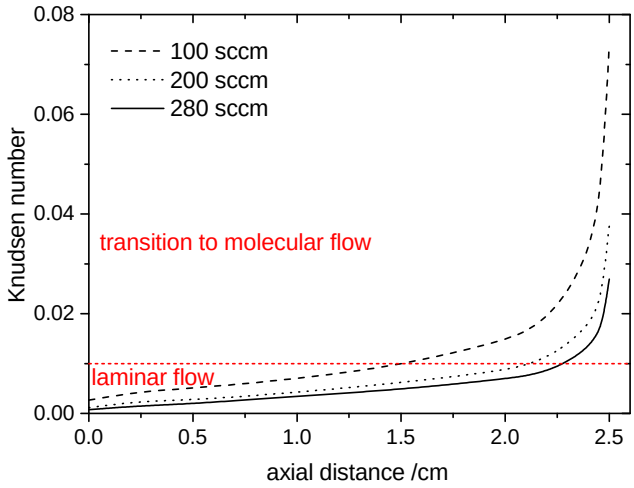


Figure 4.2.: Knudsen number of CW beams at different flow rates as a function of the axial distance from the expansion orifice. Figure adapted from ref. [146].

as large as possible can be measured. The ion signal ratio is given by the following relationship:

$$\frac{S_A}{S_P} = [\frac{P_A}{P_P}][\frac{\sigma_i^A(E)}{\sigma_i^P(E)}][\frac{F_A}{F_P}] \tag{4.4}$$

In this equation, $S$ is the ion signal of the analyte ($A$) and propene ($P$), $\sigma_i(E)$ is the absolute photoionization cross section, and $F_A$ and $F_P$ are the mass discrimination factors, and $P_A$ and $P_P$ the partial pressures.. The mass discrimination factors for NO (m/z=30), acetone (m/z=58), benzene (m/z=78) and cyclohexane (m/z=82) were determined relative to propene at six different photon energies (9.8-10.05 eV), while for ethyl bromide (m/z=108/110) the

ion signal ratio was only determined at 10.5 eV because the ionization energy of ethyl bromide (10.3 eV) is 0.57 eV higher than propene's one. The obtained mass discrimination factors are depicted in fig. 4.3.

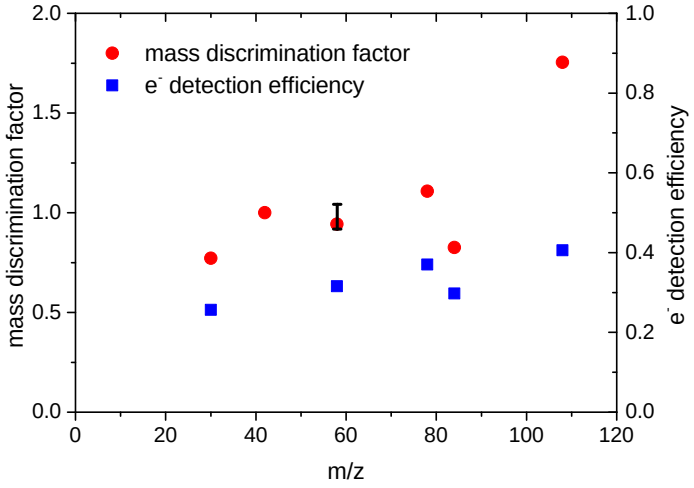


Figure 4.3.: Mass discrimination factor and electron detection efficiency for NO (m/z=30), propene (m/z=42), acetone (m/z=58), benzene (m/z=78), cyclohexane (m/z=82), and ethyl bromide (m/z=108/110). The black bar shows the range of dispersion for the mass discrimination factor of acetone for different pyrolysis conditions.

The mass discrimination factor for a molecular beam enriched with heavy species, as expected for a beam with predominent laminar flow character, increases with the molecular weight. In such a case, the curve progression can be fitted by a monotonically increasing growth function which equals 1 for the mass of propene (m/z=42). The experimentally determined mass discrimination factors, however, deviate from this model since for example the factors

for acetone (m/z=58) and cyclohexane (m/z=78) have values lower than 1, but should be enriched in the beam in comparison to propene. However, the obtained mass discrimination factors are associated with rather large error bars. The propene gas mixture contained 5.0±0.1 % of propene in nitrogen. The analytes were used in purity grades >99.9 %. A Baratron gauge with an accuracy of 0.2 % was utilized for the preparation of the binary mixtures. The uncertainty in the tabulated absolute photoionization cross sections, which is stated as 20 % in the cited literature (*vide infra*), though is the greatest source of error. The overall relative error for the derived mass discrimination factors therefore accumulates to 42.4 %. The fact that in the literature mass discrimination factor curves following the expected progression are reported for pulsed[176] and high flow rate CW molecular beams,[55,174] indicates that the accuracy in the photoionization cross sections should be sufficient for an analysis of mass discrimination factors. The mass discrimination factors determined in the SLS experiment could be reproduced with different batches, which is why observational errors can be excluded. Interestingly, the electron detection efficiency shows a similar dependency from the m/z ratio as the mass discrimination factor. This is also presented in fig. 4.3. The electron detection efficiency can be derived by dividing the sum of the analyte's and propene's coincidence electron signal by the overall electron signal. The detection efficiency for propene is the same for all binary mixtures at a certain photon energy. Thus, the electron detection efficiency reflects the relative detection efficiency of the analyte, which could vary for example because of blind spots on the delay-line anode. These characteristics transfer also to the derivation of mass discrimination factors and might explain the deviation from the expected result. As shown in fig. 4.3, mass discrimination factor and electron detection efficiency show a similar dependance on the m/z ratio. Additionally, the characteristics of the molecular beam were altered by varying the pyrolysis temperature and the background pressure of the gas mixture. No systematic impact on the mass discrimination factor on acetone was observed

for this set of experiments because the obtained ratio of mass discrimination factors disperses randomly about $\frac{F_{acetone}}{F_{propene}} = 0.9647^{+0.0776}_{-0.0459}$ (see fig. 4.3). This leads to the conclusion that the effect of the mass discrimination factor on the ionization probability of a species in the utilized molecular beam is very small. The molecular beam has rather effusive character, which is additionally supported by relatively high vibrational temperatures visible in the TPE spectra (*vide infra*), for which enrichment of heavy species in the beam can be in good approximation neglected. In the following, the mass discrimination factor is therefore assumed constant for all m/z ratios.

## 4.2. Photoionization Cross Section of Cyclopropenylidene

As stated above, cyclopropenylidene can be efficiently generated by pyrolysis of the quadricylclane depicted in fig. 4.1 and benzene is generated as a side product in stoichiometric quantities. The corresponding PIE curves were recorded from 8.8 to 9.8 eV in photon energy steps of 10 meV and an acquisition time of 360 s per data point. The pyrolysis temperature was 465 °C. The PIE curves were normalized on the photon flux. The absolute photoionization cross section of cyclopropenylidene was derived by transposing eq. (4.2). The ratios of the concentrations and apparatus functions containing the mass discrimination factors were assumed as unity. The absolute photoionization cross section of benzene was obtained by comparison of the experimental data with the literature.[55,199] Fig. 4.4 depicts the absolute photoionization cross sections of benzene and cyclopropenylidene and the literature cross section curve of benzene for comparison.

The ionization energy for benzene is 9.24 eV[201] and for cyclopropenylidene 9.17 eV.[191] The PIE curves show clear steps in signal intensity at these respective energies. A deviation from the literature curve between 9.0 and

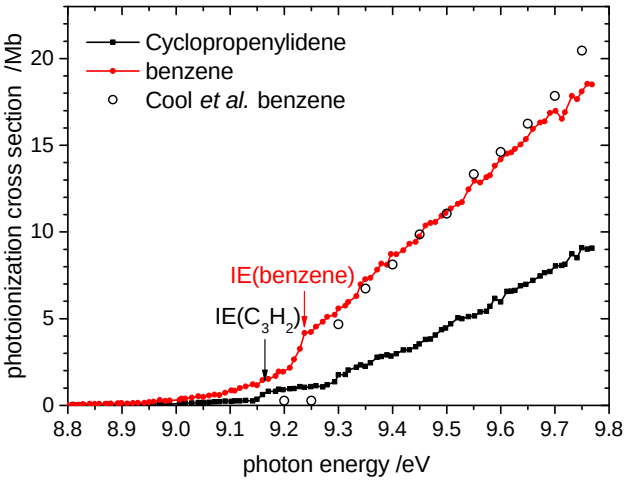


Figure 4.4.: Absolute photoionization cross sections for benzene and cyclopropenylidene. The literature cross section for benzene [55] (open circles) is given for comparison.

9.3 eV is observed in the PIE curve of benzene, though. This can be ascribed to thermal effects as benzene is produced vibrationally hot in the pyrolysis and the molecular beam characteristics do not lead to an effective vibrational cooling. The reference curve has been recorded for vibrationally cold benzene by contrast. The temperature effect can also be observed in the corresponding mass-selected TPE spectra of benzene and cyclopropenylidene shown in fig. 4.5, which show clear signs of hot and sequence bands below the adiabatic ionization energy. Franck-Condon simulations for transitions from the neutral ground state at a vibrational temperature of 470°C to the ionic ground state show an excellent agreement with the experimental spectra. The observation that there are almost no cooling effects of the molecular beam confirms that

the beam characteristics are far from a laminar flow and the assumptions which lead to neglecting the mass discrimination factor seem therefore valid.

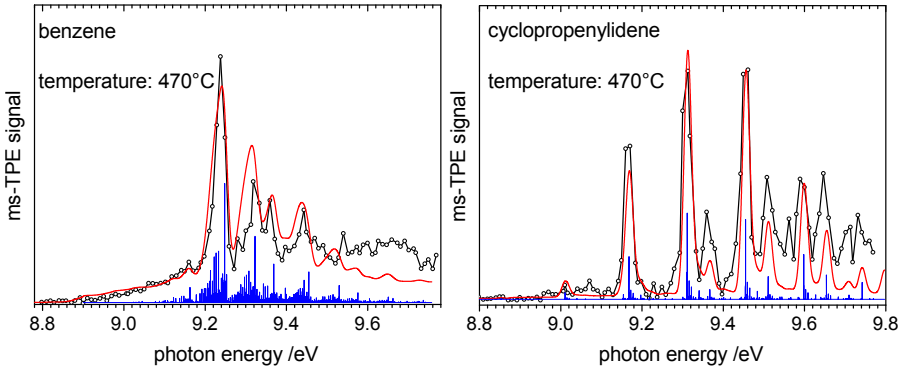


Figure 4.5.: Franck-Condon simulations for the TPE spectra of benzene (left) and cyclopropenylidene (right) for a vibrational temperature of 470°C.

The error in the absolute photoionization cross section of benzene, which was used to derive the cross section of cyclopropenylidene,[199] is given as 20 %. Further sources of error are the data analysis, i.e. the integration limits for the respective mass peaks and the subtraction of false coincidences, the scaling of the recorded benzene PIE signal to the literature photoionization cross section, and the disregard of mass discrimination effects. Therefore, an overall relative error of 30 % has to be assumed for the absolute photoionization cross section of cyclopropenylidene. The absolute photoionization cross section curve of cyclopropenylidene between 8.8 and 9.8 eV is again depicted in fig. 4.6, in which the 30 % margin of error is also highlighted. A tabulated list of the cross section of $c$-$C_3H_2$ can be found in the appendix C. Note that the non-zero values for the photoionization cross section below the ionization energy of 9.17 eV are ascribed to thermal effects from the pyrolysis.

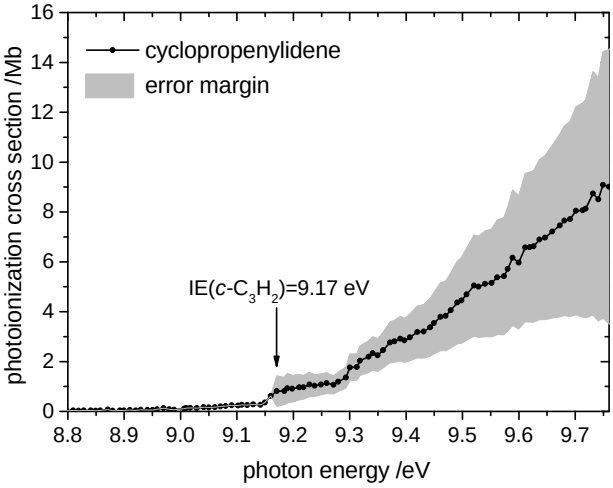


Figure 4.6.: Absolute photoionization cross section of cyclopropenylidene. The grey region depicts a 30 % margin of error.

## 4.3. Summary Photoionization Cross Sections

Absolute photoionization cross sections of reactive intermediates, like radicals and carbenes, generated by flash pyrolysis can be easily derived when the cross sections of the other pyrolysis fragments and the stoichiometry are known. The pyrolysis experiment at the SLS does not comprise a mass-dependent apparatus function, which would have to be considered in the derivation scheme. The molecular beam produced under standard experimental conditions in the pyrolysis source is in good approximation effusive. Therefore, enrichment of heavier species in the beam because of pressure diffusion and Mach-number focusing is below the detection limit, unlike in a supersonic molecular beam. The absolute photoionization cross section of cyclopropenylidene, which is

produced from a quadricyclane precursor in the same quantity as the well-investigated benzene molecule, was determined in the ionization onset region between 8.8 and 9.8 eV. The uncertainty for the reported photoionization cross section is 30 %, which traces back mainly to the high error associated with the reference cross section of benzene.

# 5. Photoionization of Nitrogen-Containing Intermediates

## 5.1. Isocyanic Acid HNCO

With the RAPRENO$_x$ process (**R**obert **A**. **P**erry or **rap**id **re**duction of **n**itrogen **ox**ides), an efficient pathway has been developed to remove toxic NO$_x$ from exhaust gases in combustion.[202–205] In this process, cyanuric acid is admixed to the fuel because it releases isocyanic acid upon thermal decomposition. Reactions of HNCO with other combustion products lead to reaction sequences, in which nitrogen oxides, like NO, are very efficiently reduced. The presumed mechanistic pathways are sketched in fig. 5.1. HNCO is, in addition, an intermediate in the NO$_x$ reduction process in which AdBlue® (ISO 22241-1 / AUS 32), an aqueous urea solution, is injected in the exhaust stream of diesel vehicles.[206] Urea undergoes thermal decomposition to ammonia and HNCO, the latter of which is subsequently hydrolyzed yielding another equivalent of ammonia and $CO_2$. Ammonia then reduces selectively the nitrogen oxides in the exhaust stream to nitrogen and water. Furthermore, HNCO has been observed in the interstellar space.[207]

For all of these reasons, isocyanic acid has been investigated spectroscopically in a number of experiments. Many studies were focused on the photodissoci-

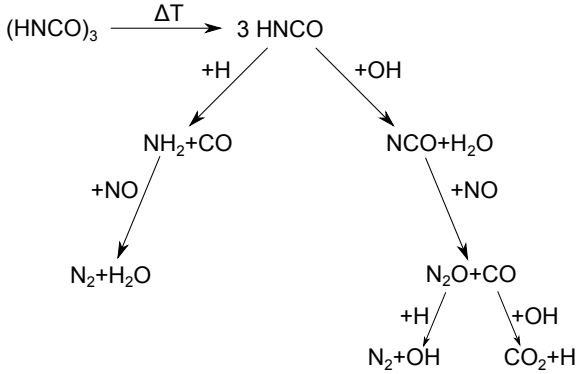


Figure 5.1.: Mechanism of the RAPRENO$_x$ process. Figure adapted from ref. [6].

ation of HNCO since there are pathways to two nitrogen-containing radicals, NH and NCO. [208,209] In fact, these experiments lead to the invention of the ion imaging technique by D. Chandler and co-workers. [210,211] Up to today, the photodissociation of HNCO has been frequently re-investigated by evolutions of this technique. [212–216] The structure of the molecule was studied in IR and microwave experiments [217–219] and was determined to be planar with $C_s$ symmetry. Several studies also focused on photoionization processes. [216,220–224] The ionization energy of HNCO was first measured by photoionization mass spectrometry in 1968 and a value of 11.60 eV was obtained. [220] To get a more profound understanding of the HNCO molecular orbitals and the electronic and vibrational structure of the cation, conventional VUV photoelectron spectroscopy was employed. [225–227] Using the He(I$\alpha$) discharge line at 21.22 eV, four band systems belonging to different electronic states of $HNCO^+$ could be resolved. In the first conventional PES study by Eland *et al.* the ionization energy was determined to be 11.60±0.01 eV and the three stretching mode fundamentals of the cationic ground state with wavenumbers of 1050, 2020, and 3222 $cm^{-1}$ were assigned. [225] For the first excited state, a vertical excitation

energy of 11.39±0.10 eV was reported and a progression with 565 $cm^{-1}$ was observed. Structures in the PES at 15.54 and 16.7 eV were assigned to higher electronic states. Follow-up experiments focused on comparing the spectrum to the ones of related compounds, like $CH_3NCO$, $SiH_3NCO$, $GeH_3NCO$, and $Me_3SiNCO$,[226] and the dissociation of energy-selected $HNCO^+$ ions[227] using the same technique and validated the reported energies and assignments of vibrational bands for HNCO. Dissociative photoionization of HNCO was investigated employing photoionization mass spectrometry.[220,228,229] More recently, a PEPICO experiment employing He($2\alpha$) light at 40.81 eV was performed and twelve dissociation channels were observed in the cation and the corresponding appearance energies were reported.[227] An extensive theoretical investigation of the $HNCO^+$ ion was also included.

In this thesis, valence shell photoionization of HNCO utilizing threshold photoelectron spectroscopy is reported. This technique enables recording highly resolved spectra and thus a better understanding of the HNCO ion's electronic, vibrational and even rotational structure. Furthermore, inner-shell spectroscopy was employed to investigate photoexcitation and photoionization processes of core orbitals. As will be discussed in more detail in the respective section, inner-shell spectroscopy of HNCO is relevant for understanding experiments in which the photodissociation of thymine was investigated.

### 5.1.1. Valence Shell Photoionization of HNCO

Valence shell photoionization of isocyanic acid was conducted at the DESIRS VUV beamline of Synchrotron SOLEIL, France. Mass-selected threshold photoelectron spectra were recorded utilizing the $i^2$PEPICO endstation DELICIOUS III. Isocyanic acid was freshly prepared by heating a mixture of potassium isocyanate and stearic acid as described in sec. B.1. Fig. 5.2 shows the mass-selected TPES of isocyanic acid for an energy range from 11.5 to 16.0 eV. The spectrum consists of different overlapping scans as the sample

consumption did not allow to record a continuous spectrum over the complete energy range. For the low energy part from 11.5 to 12.0 eV, a step size of 2 meV and an acquisition time of 30 s was employed, while 10 meV steps were chosen from 12.0 to 14.5 eV. Above 14.5 eV, the step size was increased to 20 meV. For the latter two parts, each data point was averaged for 60 s. Threshold photoelectrons with a kinetic energy up to 2.5 meV were selected for the first part of the spectrum, while a threshold of 5 meV was employed for higher energies.

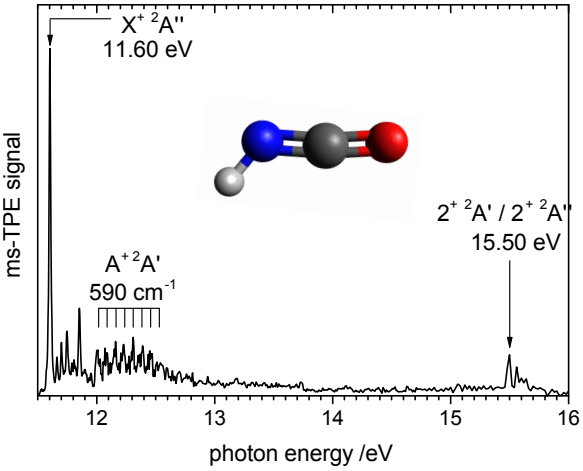


Figure 5.2.: Mass-selected TPE spectrum of HNCO. The first peak at 11.60 eV and the following vibrational structure is assigned to the ionization energy into the $X^+$ $^2A$" ground state. The progression beginning around 12 eV is assigned to the $A^+$ $^2A$' excited state and the structure at 15.50 eV to the second excited state, whose symmetry cannot be unambiguously assigned (see text for details). Figure adapted from ref. [230].

The spectrum features different structures, which can be assigned to different electronic states in the $HNCO^+$ cation. The first peak at 11.60 eV can

be assigned to the ionization energy leading to the $X^+\ ^2A$" cationic ground state of isocyanic acid and agrees with previous PES studies.[225–227] Below 12 eV, four further pronounced, but less intense peaks are observed. Setting in around 12 eV, the spectrum features a distinct progression with a spacing of 590 $cm^{-1}$. This progression can be assigned to the first excited electronic state $HNCO^+\ A^+\ ^2A$'. Another pronounced band followed by a less intense one is visible at 15.50 eV and can be assigned to the next excited electronic state.

#### 5.1.1.1. TPE Spectrum of the $^2$A" $HNCO^+$ ground state

**Rotational ΔK subbands in the 0-0 transition**

A detailed zoom into the most pronounced band in the TPE spectrum of HNCO reveals an additional structure as visible in fig. 5.3. The small peaks and shoulders can be assigned to rotational band structure. A full resolution of rotations in the TPE spectrum cannot be expected, since the chosen step size of 2 meV and the energy resolution of about 3 meV is too big.

HNCO is a planar molecule with $C_s$ symmetry and thus belongs to the group of asymmetric top molecules. Experiments show that all three rotational constants for the neutral molecule are different (A"= 30.645 $cm^{-1}$, B"=0.369 $cm^{-1}$, C"=0.364 $cm^{-1}$).[218] However, it is obvious that B" and C" are nearly identical and almost two orders of magnitude lower than A". The asymmetry parameter $\kappa$ (cf. eq. (2.24)) is -0.9996 and HNCO can therefore be approximated as a near prolate symmetric top molecule. In a $I^r$ basis, the energy of the rotational levels of the neutral ground state can in good approximation be calculated using eq. (2.22).

$$E(J, k_a) = [(B" + C")/2]J(J+1) + [A" - (B" + C")/2]k_a^2 \qquad (5.1)$$

As the first summand in this equation is small compared to the second one

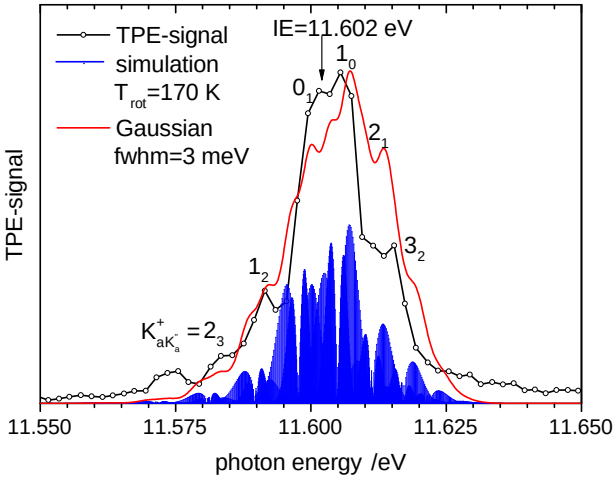


Figure 5.3.: Detailed view of the band assigned to the 0-0 transition for the $X^+\ ^2A$" $HNCO^+$ ground state. A resolution of $\Delta K_a$ subbands responding the photoionization selection rules $\Delta K_a = \pm 1$ is observed. A simulation of the rovibrational intensities for a rotational temperature of 170 K supports this assignment (blue sticks, red line: convolution with Gaussian 3 meV). Hence, the ionization energy can be assigned to 11.602±0.005 eV. The band at 15.572 eV is assigned to a sequence band. Figure adapted from ref. [230].

with B" and C" being significantly lower than A", it becomes obvious that the $K_{\mathrm{a}} = |k_a|$ structure is well separated and therefore $\Delta K_a$-subbands are likely to be resolved in the spectrum.

For simulating the intensities of rovibrational transitions, an orbital ionization model can be employed as discussed in sec. 2.4.3. Fig. 5.4 shows the HOMO of the neutral HNCO ground state computed on B3LYP/6-311G(2d,d,p) level of theory. The HOMO features two nodal planes. One in the molecular plane and one perpendicular to it. In good approximation, it can thus be considered as a single $\mathrm{d_{xz}}$ atomic orbital with the angular momentum components $l" = 2$ and $\lambda" = \pm 1$ and no significant contribution of $l$-mixing is expected to occur.

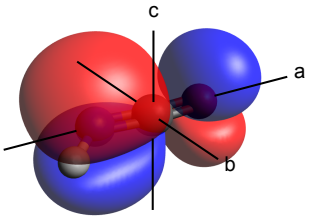


Figure 5.4.: HOMO of the X $^1$A' ground state of HNCO and orientation of the main rotational axis. In a $\mathrm{I^r}$ basis for near prolate asymmetric top molecules, the $a$-axis corresponds to the $z$-axis.

From the orbital out of which the electron is ejected, the photoelectron's angular momentum quantum number $l$ ($l = l" \pm 1 = 1$ or 3) can be derived (cf. eq. (2.30)). The electron is hence emitted into the $p$- or $f$-continuum. For ionization out of the HOMO of the $\mathrm{C_s}$-symmetric molecule HNCO, in first order the photoionization selection rule in eq. (2.28) permits only rotational transitions between states of the same irreducible representation, i.e. $A' \leftrightarrow A'$ and $A'' \leftrightarrow A''$. In asymmetric top molecules of $\mathrm{C_s}$ symmetry, the symmetry of the asymmetric top wavefunctions is $a'$ ($a''$) for even (odd) $K_c$.[231] That is why transitions between the HNCO X $^1$A' and $\mathrm{HNCO^+}$ $^2$A" ground states

are only allowed between rovibronic level with different $K_c''\,K_c^+$ parities. For simulating the rovibronic transitions in the threshold photoelectron spectrum of HNCO, the relative ionization cross sections were computed according to eq. (2.33). Using the approximations discussed above, the only single-center expansion coefficients different from zero are $C^{d_{xz}}_{l''=2\,\lambda''=\pm1}$, which can be taken unity. The asymmetric top functions were expanded in the basis of symmetric top functions. The $3j$ -symbol, which expresses the coupling between the two states, restricts the photoionization selection rules further. For the system discussed here, this means that only transitions meeting the criteria $\Delta N = 0, \pm1, \pm2$ and $\Delta k = \pm1$ are simulated. For a near prolate symmetric top molecule like HNCO, the $\Delta k$ selection rule reduces to $\Delta K_a$. As the HOMO can be approximated as a single atomic orbital and thus a single $l''$ value, the term comprising the radial transition integrals in eq. (2.33) is constant and can thus be taken unity. The rovibronic energy levels for both neutral and cation were computed using the approximation for a near-prolate symmetric top. For the neutral molecule, the experimental rotational constants of Yamada *et al.* were used. Computations on B3LYP/6-311G(2d,d,p) predict a slightly smaller value for $A^+$ in comparison to the neutral molecule, while the two other constants remain more or less unchanged ($B^+$=0.364 $cm^{-1}$ and $C^+$=0.359 $cm^{-1}$). As will be discussed later in this section in more detail, the computed geometry for the cation is not sufficiently accurate, especially in terms of the HNC bonding angle, which has a great effect on the $A^+$ constant. That is why the latter was varied systematically. In agreement with the predicted change of the $A$ constant in the Franck-Condon fit (*vide infra*), a value of $A^+$=27.50 $cm^{-1}$ was chosen. A rotational temperature of 170 K was assumed for the simulation, which might at first glance seem too high for a molecular beam experiment. As in the same beam time attempts were made to pyrolyze HNCO, the source was equipped with a pyrolysis tube, which was not removed for the non-pyrolysis experiments. This leads to non-negligible turbulences of the molecular beam and thus a less efficient cooling of the

sample molecules. The obtained simulation of the rovibronic transitions and a convolution of the simulated spectrum is depicted in fig. 5.3. Transitions following the selection rule $\Delta K_a = \pm 1$ are assigned to the partially resolved band structure of the 0-0 transition. The simulation predicts population of rotational levels in the neutral molecule up to $K_a'' = 3$. Around 15.572 eV, there is another broad band visible, which is not included in the simulation and might also contain contributions from transitions $K_a^+ = 3 \leftarrow K_a" = 4$. However, a higher rotational temperature is not expected under the chosen experimental conditions. Thus, this band is assigned to a transition from a vibrationally excited state in the neutral molecule (*vide infra*). The ionization energy of HNCO can be determined with a high degree of accuracy from the simulation and the assignment of the $\Delta K$ subbands yielding a value of 11.602±0.005 eV. The transition $J_{K_a K_c}$ $0_{00} \leftarrow 0_{00}$ does not fulfill the photoionization selection rules according to eq. 2.28. That is why no line at this precise energy is included in the shown simulation. The computed ionization energy of isocycanic acid is 11.506 eV on CBS-QB3 level and also matches the assigned experimental value reasonably well.

#### Vibrational bands of the $HNCO^+$ $^2A"$ ground state

The first band maximized at 11.605 eV is followed by four distinct bands at 11.66, 11.70, 11.75, and 11.85 eV. In addition, several bands with intensities only slightly above noise level are observed. All these bands can be assigned to transitions into vibrationally excited states of the $HNCO^+$ $^2A"$ state. Fig. 5.5 shows an expanded view of the respective part of the TPE spectrum alongside an assignment and a Franck-Condon fit of the band structure. Note that no coincidence scheme was used for this part of the spectrum because the sample did not contain any contaminations and dissociative photoionization sets in only at higher energies.

The most intense peaks can be assigned to the fundamental modes of the $5(a')^+$ NCO in plane bending mode at 495 $cm^{-1}$, the $4(a')^+$ HNC in plane

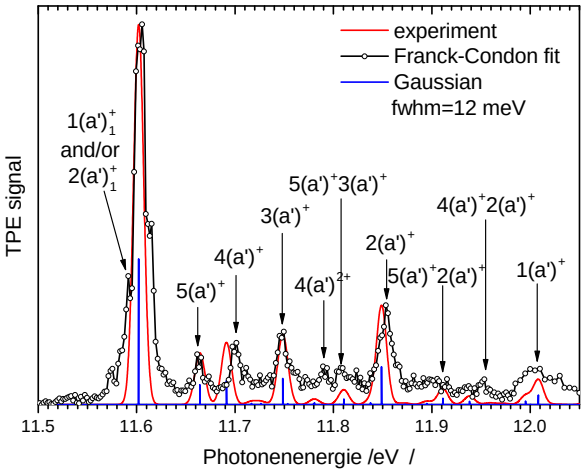


Figure 5.5.: Expanded view of the threshold photoelectron spectrum showing the vibrational bands of the $HNCO^+$ $^2A$" ground state. Note that the step size increases at 12.0 eV as the spectrum is assembled from two overlapping scans. The four pronounced bands are assigned to fundamental vibrations of the cation, while some combination bands are observed in addition. A Franck-Condon fit of $HNCO^+$, based on B3LYP/6-311G(2d,d,p) and the experimental geometry for the neutral state, confirms this assignment. The peak position of the simulated $4(a')^+$ mode shows a relatively large deviation from the experimental TPE spectrum due to a disturbed potential energy surface along the HNC angle coordinate. Another band is visible at 11.57 eV, which is assigned to a sequence band.

bending mode at 790 $cm^{-1}$, the 3(a')$^+$ N=C stretching mode at 1170 $cm^{-1}$, and the 2(a')$^+$ C=O stretching mode at 2030 $cm^{-1}$. The 1(a')$^+$N-H stretching mode is assigned to the broad band at 12.0 eV (3210 $cm^{-1}$). This band is assumed to contain also contribution from the first excited state. Therefore the wavenumber of the N-H stretching mode can be less accurately determined than the other observed modes. Some of the bands even feature double peaks and shoulders similar to the 0-0 transition, which can again be ascribed to rovibronic structure. The vibrational modes of $HNCO^+$ are visualized in fig. 5.6 and the determined wavenumbers show a good agreement with computations on B3LYP/6-311G(2d,d,p) level of theory. However, it is obvious that the computed value for the 4(a')$^+$ mode wavenumber shows an unusually large deviation from the one extracted from the TPE spectrum. This can be ascribed to a significant distortion of the $X^+$ $^2$A" potential energy surface along the HNC angle coordinate. Time-dependent DFT computations (TD-B3LYP/6-311G(2d,d,p)) predict a vertical excitation energy of 12.34 eV for the transition to the first excited electronic state $A^+$ $^2$A', i.e. less than 1 eV above the $X^+$ state. For the $X^+$ state, an electron is removed from the non bonding in plane $\pi_{nb}$ orbital, while for the $A^+$ state, ionization occurs out of the non bonding out of plane $\pi_{nb}$ orbital. For a linear $HNCO^+$ geometry, both states become degenerate, i.e. $X^+$ and $A^+$ can be regarded as the two components of a Renner-Teller degenerate state. The conical intersection between those two states has already been discussed in the literature.[227] As a consequence, methods employing single-determinant wavefunctions fail in describing the potential correctly due to the breakdown of the Born-Oppenheimer approximation. An incorrect potential energy surface leads also to defective wavenumbers for the respective vibrational mode as a high degree of anharmonicity is expected. DFT uses single-determinant wavefunctions and calculates harmonic vibrations, which explains the observed deviation for 4(a')$^+$. In previous PES studies, neither the 4(a')$^+$, nor the 5(a')$^+$ bending mode have been observed.[225–227] As both neutral and cationic isocyanic acid are

planar and transform according to the $C_s$ symmetry group, an excitation of the 1(a")$^+$ NCO out of plane bending mode is neither expected, nor observed.

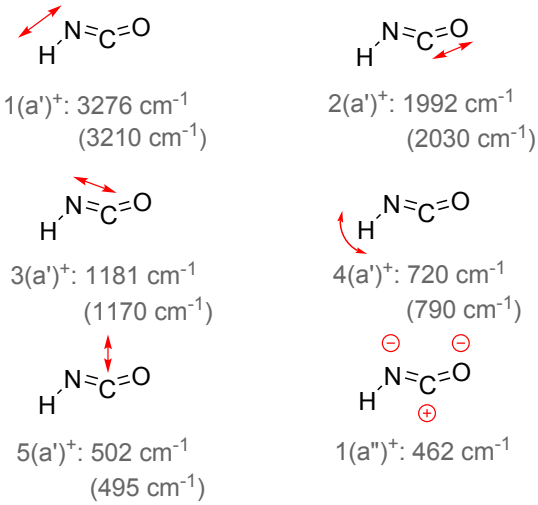


Figure 5.6.: Vibrational modes and scaled wavenumbers on B3LYP/6-311G(2d,d,p) level of theory for $HNCO^+$ $^2$A". Experimental wavenumbers are given in parentheses.

Franck Condon factors were computed to validate the assignment above. The geometry of the neutral ground state has been determined to a high degree of certainty by experimental and high-level computational methods. [218,232] That is why the line intensities were not only simulated, but also fitted to the experimental TPE spectrum by systematically distorting the $HNCO^+$ structure obtained by the B3LYP/6-311G(2d,d,p) computations. In this procedure, the assumption is made that the force constants do not change upon deflecting a certain coordinate. Hence, only the intensities are fitted, but the wavenumbers of the vibrational modes remain constant. The result of the Franck-Condon fit is depicted in fig. 5.5 and table 5.1 compares the geometry parameters of the neutral molecule with the computed geometry of $HNCO^+$ $^2$A" and the fitted

one:

Table 5.1.: Molecular structure of neutral and cationic HNCO. The geometry of HNCO X $^1$A' is known from mircro-wave experiments, while the HNCO$^+$ X$^+$ $^2$A" geometry has been computed on B3LYP/6-311G(2d,d,p) level. In addition, the fitted geometry for the X$^+$ state is listed.

| | **HNCO X $^1$A'** lit.[218] | **HNCO$^+$ X$^+$ $^2$A"** calc. | **HNCO$^+$ X$^+$ $^2$A"** fit |
|---|---|---|---|
| r(NH) | 0.995 Å | 1.033 Å | 1.034 Å |
| r(NC) | 1.214 Å | 1.260 Å | 1.268 Å |
| r(CO) | 1.166 Å | 1.139 Å | 1.141 Å |
| <(HNC) | 123.9 ° | 124.5 ° | 122 ° |
| <(NCO) | 172.6 ° | 170.9 ° | 167 ° |

The fitted geometry reveals that, while the bond lengths seem to be well described on the employed level of theory, the bonding angles have to be deflected to a greater extent to obtain a good agreement with the experimental spectrum. This confirms that the computational method fails to describe the cationic structure accurately and a rather large deviation between experimental and computed wavenumber for the HNC in plane bending mode is the result. In comparison to the neutral molecule, the HNCO$^+$ ground state has smaller bonding angles, which leads to a greater total moment of inertia along the $a$ axis. As a result, the $A^+$ rotational constant is expected to be slightly smaller than the neutral $A$" constant. Since the computation does not reflect the exact geometry, an absolute value cannot be obtained, but the observations in the Franck-Condon fit confirm that the $A^+$ constant of 27.50 cm$^{-1}$ used for the simulation of rovibronic transitions (*vide su*pra) seems a realistic choice. The $B^+$ and $C^+$ constants are less influenced by these coordinates and should therefore be well described by the computations. The intensities of the vibrationally excited bands are reproduced well in the Franck-Condon

fit. Thus, the geometry of the cation, based on experimental evidence, is predicted to a higher degree of certainty compared to quantum chemical computations. The Franck-Condon fit allows in addition to assign some smaller bands in the spectrum, which are barely above noise level, to combination bands (see fig. 5.5 for the assignment). Note that all overtones of the $4(a')^+$ mode and those combination bands comprising a contribution of this mode are red shifted in the simulation in comparison to the experiment due to the computational error of this vibration discussed above.

#### 5.1.1.2. TPE Spectrum of $HNCO^+$ excited states

As already stated above, the vertical excitation energy to the $HNCO^+ A^{+2}A'$ state is less than 1 eV above the ionization energy. Hence, the progression in the TPES setting in around 12 eV is assigned to the first excited state. The band system shown in fig. 5.7 features seven distinct components with a regular spacing of 590 $cm^{-1}$. Another band is covertly visible on each side of the progression. Those are also assigned in fig. 5.7. The spacing matches the expected wavenumber of an HNC-bending mode of the cationic state and also agreees well with the wavenumbers of 565 $cm^{-1}$ [225] and 610 $cm^{-1}$ [226] observed in previous experiments. To validate this assignment, TD-DFT computations were performed to obtain the $A^+$ minimum structure and the vibrational frequencies. However, the computations failed and did not converge to a minimum. Scanning the HNC bonding angle for the cation's ground and first excited state on the (TD-)B3LYP/6-311G(2d,d,p) reveals the reason. As visible in the inset of fig. 5.7, the molecule relaxes to a linear geometry on the $A^+$ potential energy surface. The calculated $A^+$ and $X^+$ surfaces come very close at an HNC angle of 180 ° and therefore computational methods which use single-determinant wavefunctions (like B3LYP) fail. Relaxation to the ground state surface is possible via a conical intersection, which has already been discussed in the literature. [227]

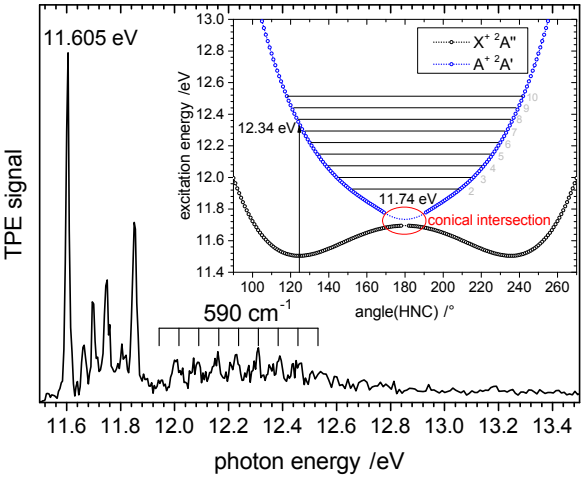


Figure 5.7.: The TPES features a regularly spaced progression (590 $cm^{-1}$) setting in around 12 eV, which can be assigned to the $A^+$ $^2A'$ state. The inset shows relaxed scans of the potential energy surfaces of ground and first excited state along the HNC bonding angle coordinate. The potential curves computed on (TD-)B3LYP/6-311G(2d,d,p) level come very close for a near linear $HNCO^+$ geometry and thus the $A^+$ state can relax to the $X^+$ state via a conical intersection.

For the first excited cationic state, ionization occurs out of the bonding $a'(\pi_b)$ HOMO-1. The HOMO $a''(\pi_{nb})$, out of which is ionized to reach the $X^+$ state, is depicted in fig. 5.4. The HOMO-1 has the same shape, but lies in the molecular plane, i.e. it is oriented perpendicular to the HOMO. When $HNCO^+$ gets linear, the HOMO and HOMO-1 are degenerate. The $X^+$ $^2A$" and $A^+$ $^2A'$ states can thus also be seen as the two Renner-Teller components of a degenerate state. To make a tentative assignment of the observed bands in the TPES, the $A^+$ potential curve was extrapolated to a minimum (11.74 eV) and, assuming a harmonic potential, the vibrational levels' energies of the

590 $cm^{-1}$ mode were determined. Hence, the band at 12.0 eV is assumed to be the second overtone of the HNC bending mode, followed by higher overtones. As no anharmonicity is observed in the progression, the vibrational levels are expected to lie considerably above the conical intersection, which is in agreement with the presented assignment. Nevertheless, an error in the assignment of ±1 vibrational level has to be assumed.

At 15.50 eV, another pronounced peak is observed, which is assigned to the next excited state of $HNCO^+$. Similar to previous computations,[227] TD-B3LYP/6-311++G(d,p) predicts that for ionization out of the in plane $a'(\pi_b)$ HOMO-2 of HNCO only 35 meV less energy is needed compared to ionization out of the out of plane HOMO-3. Therefore, a contribution of the third excited state to the observed bands in the TPES cannot be excluded. Fig. 5.8 shows the mass-selected TPE spectrum alongside Franck-Condon simulations for the $2^+$ $^2$A' and the $2^+$ $^2$A" state.

The excitation energy to the second excited state of $HNCO^+$ can therefore be assigned to 15.50±0.02 eV, as the Franck-Condon simulations show for both considered states a sharp peak for the 0-0 transition. The less intense peak at 15.56 eV (+480 $cm^{-1}$) can be assigned to the HNC in plane bending mode and the NCO in plane bending mode, whose wavenumbers are computed to be 477 (556) $cm^{-1}$ and 582 (478) $cm^{-1}$ for the $2^+$ $^2$A' ($2^+$ $^2$A") state. Above 15.56 eV, the mass-selected TPE signal vanishes because dissociative photoionization to $HCO^+$+N is expected to set in (cf. sec. 5.1.1.3). Thus, the spectral features do not provide evidence for a definitive assignment of the second excited state in $HNCO^+$.

#### 5.1.1.3. Dissociative Photoionization of HNCO

The dissociative photoionization of isocyanic acid was studied, in addition, which sets in about 4 eV above the ionization threshold. The vibrational band at 15.56 eV, above which no further band structure is observed in the mass-

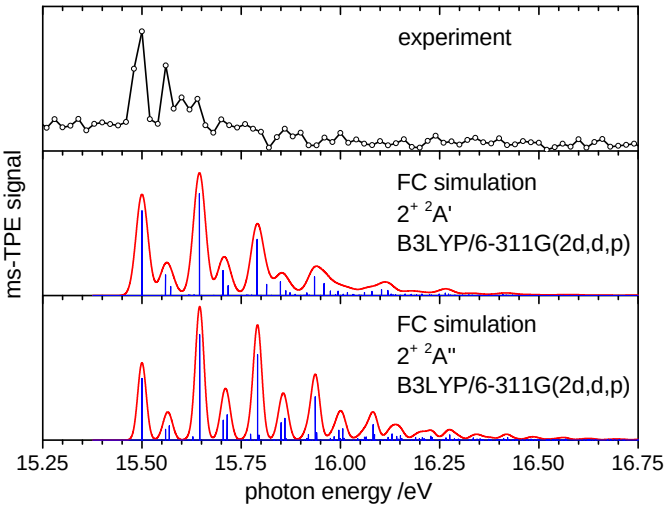


Figure 5.8.: TPES of the second excited state of $HNCO^+$ (upper panel). The second and third excited state are very close in energy and have similar Franck-Condon simulations (lower panels, fwhm=35 meV). Only the first two bands are resolved since DPI to $HCO^+$sets in.

selected TPES of $HNCO^+$ (m/z=43) and the mass-selected TPE signal drops to zero, sets the lower limit for the appearance energy of the first fragment ion of dissociative photoionization AE(HNCO, $HCO^+$)≥15.56 eV. This is in very good agreement with the previously reported value of 15.55±0.03 eV from a PEPICO experiment.[227] Photon energy scans up to 18.0 eV were also conducted in the present study and, next to $HCO^+$ (m/z=29), appearance of the fragment ions $NCO^+$ (m/z=42) and $NH^+$ (m/z=17) was observed.

The usual way to investigate dissociative photoionization is to plot and analyze a breakdown diagram (cf. sec. 2.5.3), which can be fitted using statistical the-

ory and appearance energies are obtained. The first DPI fragmentaion channel observed in previous studies at an appearance energy of 15.55±0.03 eV is HNCO → $HCO^+$+N, resulting in a fragment ion with m/z=29.[227] At 15.6 eV, molecular nitrogen $N_2$ (m/z=28) is ionized, which cannot be completely removed from the experimental chamber, since the residual pressure is still in the $10^{-8}$ mbar range with the molecular beam turned off. Since $N_2$ is not cooled by adiabatic expansion, its peak in the TOF-MS spectrum is thermally broadened. In addition, the ionization origin features a broad distribution and, as a result, the ions are not as efficiently focused by the Wiley-McLaren extraction fields as an ion originating from the molecular beam. This leads to a further broadening of the TOF distribution of nitrogen. As visible in the upper panel of fig. 5.9, where the summed up MS for a scan from 16.0 to 17.5 eV is depicted, complete separation of the m/z=29 ion signal from the thermally broadened m/z=28 peak is not possible since the mass peak m/z=29 is also broad due to the kinetic energy release. Consequently, the mass-selected TPE spectrum of m/z=29 will also have contributions from $N_2$ threshold electrons. Using the DELICIOUS III double imaging spectrometer in the ion momentum focusing mode,[153] circumvents this interference. The molecules in the molecular beam have a high velocity vector in the beam direction and are therefore not detected in the center of the ion delay line anode, but shifted in direction of the molecular beam. The thermal background electrons, by contrast, hit the detector at the center and are vertically blurred. The inset in the lower panel of fig. 5.9 shows the ion image for the photon energy scan discussed here. In this picture, the molecular beam propagates horizontally from left to right, while the synchrotron radiation runs perpendicular to it. Ions from the molecular beam have a horizontal velocity component and therefore hit the detector further to the right than background ions. Projection onto the molecular beam axis yields the velocity distribution of the molecular beam and information on the beam profile is obtained by projecting the image onto the synchrotron radiation axis. By analyzing only

the ion signal of the highlighted spot corresponding to ions from the molecular beam, the contribution of $N_2$ background signal can be excluded, as m/z=28 and m/z=29 can then be easily separated in the TOF-MS as can be seen in fig. 5.9.

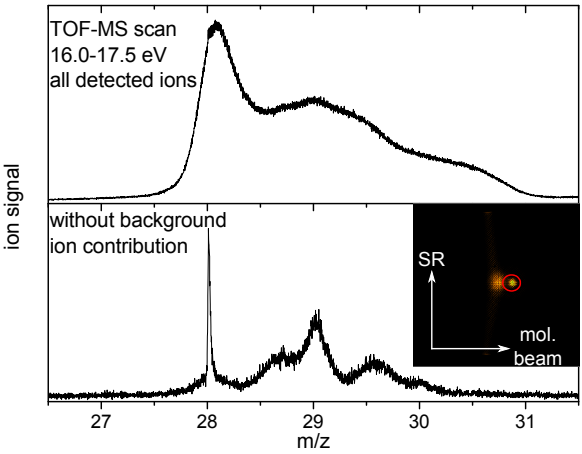


Figure 5.9.: Mass spectra between m/z=26.5 and 31.5 summed up for a scan from 16.0 to 17.5 eV. For the upper pattern, all detected ions were considered, while for the TOF-MS in the lower pattern, contributions of background ions were subtracted by choosing the ion region of interest highlighted in the inset.

In theory, this procedure enables one to analyze mass-selected TPE spectra free of any thermal background signal. In this experiment however, the signal-to-noise ratio in the TPES obtained by the proceeding described above was too low to compile a breakdown diagram for extracting accurate appearance energies. That is why only photion yield curves are depicted in fig. 5.10. Scanning a range of more than 2 eV took several hours, which made it difficult to work under constant experimental conditions. The sample reservoir was cooled to about -40°C in an ethanol/dry ice bath. Adding dry ice to prevent

further heating of the bath sometimes resulted in a rapid temperature decline. As a consequence, unsteadiness in the PIE curves appears. Significant discontinuities have thus been erased manually by shifting the curves to obtain a steady gradient. Smaller steps, e.g. at 16.9 eV are nevertheless still visible in fig. 5.10.

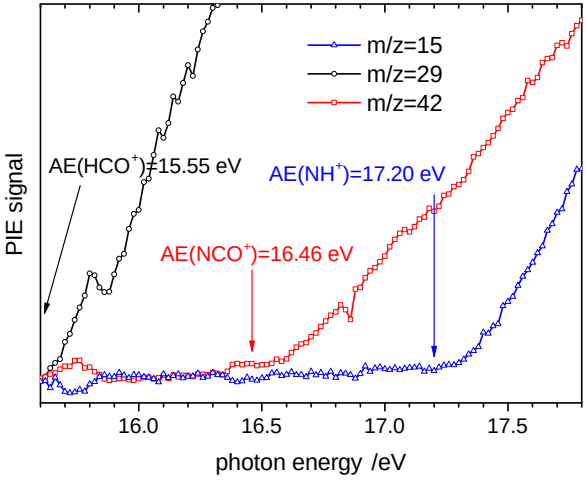


Figure 5.10.: PIE curves for the fragment ions from DPI of HNCO. The onset energies agree well with the literature appearance energies labeled in the graph.[227] As the curves showed unsteadiness due to massive temperature drops caused by unbalanced cooling. Note that, for better visualization, the different curves are not on the same absolute scale.

Below 18 eV, dissociative photoionization to three different fragment ions is observed. The PIE curve of m/z=29 ($NCO^+$) starts to rise just below 15.6 eV, but as already discussed in the beginning of this section, the disappearance of the precursor TPE signal yields a more accurate value for the lower limit of

the appearance energy AE(HNCO, $HCO^+$)≥15.56 eV. A significant rearrangement has to occur for this channel, which means that the timescale of the dissociation is expected to be slow.[227] Even with a breakdown diagram it would have been difficult to obtain a more precise value. At 16.4 eV the ion signal of m/z=42 starts to rise, as DPI to $NCO^+$+H starts to set in, while at 17.2 eV m/z=15 ($NH^+$+CO) rises. Both ion onset energies are in good agreement with the reported appearance energies AE(HNCO,$NCO^+$)=16.46±0.03 eV and AE(HNCO,$NH^+$)=17.20±0.05 eV by Wilsey *et al.*[227]

### 5.1.2. Inner Shell Spectroscopy of HNCO

The goal of the inner shell photoionization experiments on isocyanic acid was to validate findings of experiments conducted by M. Gühr and co-workers at the Linac Coherent Light Source (LCLS) free electron laser. Those experiments fall into line with the investigation of the photoexcited dynamics of the DNA base thymine.[144] Thymine, like the other nucleobases, shows an unexpected high photostability towards UV light in comparison to other organic molecules since it efficiently converts light into other forms of energy (e.g. heat) and therefore protects our genetic code from damage.[233] Ultrafast transitions between different electronic states occuring at so-called conical intersections of the corresponding potential energy surfaces lead to an efficient relaxation of the photoexcited molecule. Such radiationless processes happen on a pico- to femtosecond timescale and result from the coupling of nuclear and electronic motion. Consequently, these processes violate the Born-Oppenheimer approximation, which makes them interesting also from a theoretical point of view. In the experiment mentioned above, thymine molecules in the gas phase were excited by a 266 nm UV pump laser pulse, followed by a time-delayed SXR probe pulse with a photon energy of 565 eV from the LCLS free electron laser.[144] Free electron lasers are the latest generation of synchrotron light sources, which combine the properties of ultra short light pulses and high pulse energies of a laser with the advantage of easy tunability of an electron storage ring. Photon pulses up to the hard x-ray photon energy range are accessible with FELs, which opens up many new fields of research.[234] SXR core-ionizes the molecule regardless of the molecular geometry being highly localized. With the chosen photon energy, ionization occurs out of an oxygen 1s orbital, and the Auger decay can then be analyzed. The signal strength of the analyzed normal Auger signal does therefore not decrease due to reduced Franck-Condon overlap upon vibrational relaxation. Another advantage of Auger spectroscopy for experiments

on SASE based FEL light sources is that the kinetic energy of the Auger electron is not influenced from the spectral jitter of the FEL (see sec. 2.6.2). In the experiment mentioned above, the UV pump excites thymine from the electronic ground state to the $\pi\pi^*$ state. The timescale of the electronic relaxation back to the ground state or to the $n\pi^*$ state was then investigated by time-resolved normal Auger spectroscopy. The majority of the photoexcited $\pi\pi^*$ state thymine molecules was found to populate the $n\pi^*$ state in a 200-fs electronic relaxation.[144] In a follow-up experiment, the UV pump pulse intensity was increased and the normal Auger spectrum was probed with a 570 eV free electron laser pulse as a function of time. As visible in fig. 5.11, the Auger spectrum of thymine, which shows only a very broad band centered around 504 eV and is approximately 10 eV wide due to a very high density of states and lifetime broadening, changes significantly with increasing delay. Three sharp features at 500.5, 497.3, and 496.6 eV evolve starting at a delay of around 400 fs, which indicates dissociation to a smaller oxygen-containing molecule with a lower density of states. The steady state is reached at about 1200 ps and a transient blue shift of the sharp features is observed. Multi-photon processes of the strong UV pump pulse at 266 nm (4.66 eV) are hence assumed to induce dissociative photoionization of thymine. Interaction of ionizing radiation with nucleobases and their building blocks is also of a strong astrophysical interest.[236,237] The principal dissociative photoionization pathway of thymine is reported to be the loss of HNCO leading to the fragment ion $C_4H_5NO^+$ (m/z=83) and was determined to set in at 10.7 eV.[236] It has also been explored by theory.[238] Three 266 nm photons are hence at least necessary to dissociatively ionize thymine, which corresponds to a probe pulse photon energy of 13.98 eV. Different DPI channels are leading to different fragments that are also accessible at this photon energy, which is why the Auger spectra of possible neutral fragments have to be compared to the results of the LCLS experiment. The normal Auger spectra of possible oxygen-containing DPI fragments like CO, $CO_2$ and NO have been measured previously,[163] and

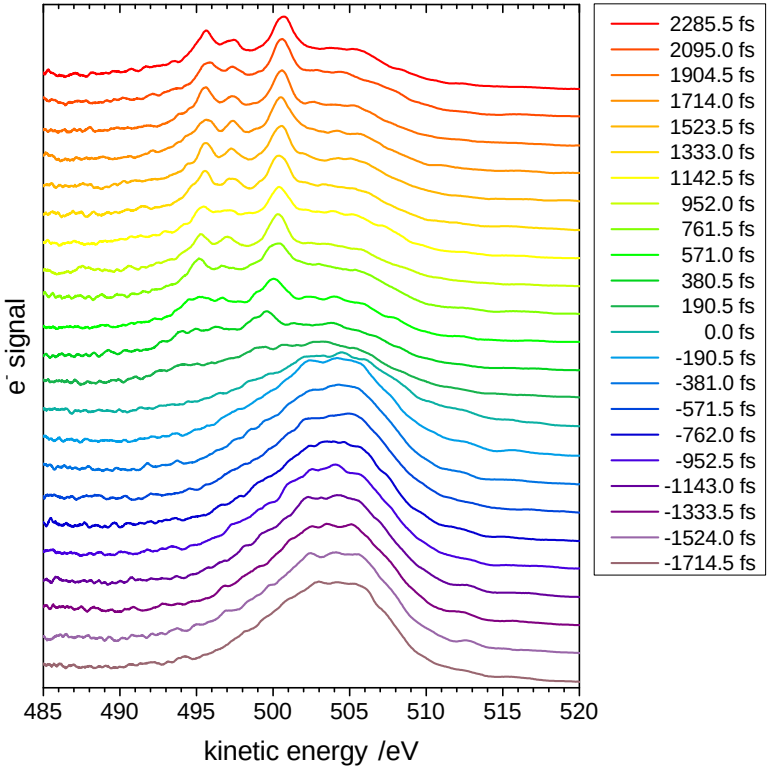


Figure 5.11.: Transient O 1s normal Auger spectra of thymine after 266 nm multiphoton UV pump recorded at the LCLS free electron lasers by M. Gühr and co-workers. Three sharp bands evolve over a timescale of 400 fs to 2 ps. The negative time delays represent the steady state of thymine. Unpublished raw data from ref. [235].

do not present a reasonable match to the recorded normal Auger spectrum at high delay times. By contrast, the normal Auger spectrum of HNCO has not been investigated so far and is therefore sought to validate the hypothesis that dissociative photoionization of thymine to HNCO and a daughter ion of m/z=83 is observed in the transient Auger spectrum. The comparison steady state Auger spectrum can be recorded also at an electron storage ring, in which a less sophisticated setup can be used to obtain a high quality comparison spectrum in a relatively short time. This experiment exploits therefore the advantages of both 'generations' of synchrotron light sources. On closer examination of the transient Auger spectra, a sharpening of the developing bands and a shift to higher kinetic energies is observed for higher delay times. While the former observation can be explained by a gradually decreasing density of states of the neutral fragment as it moves away from the ionic one, the latter one can be ascribed to a lowering of the kinetic energy of the Auger electron as it interacts with the charged dissociation fragment. The electron has to overcome the Coulomb potential of the cation, which is why the kinetic energy is reduced for short distances. The transient shift of the observed bands is therefore a direct measure of the distance between the probed fragment and the second dissociation product as a function of the delay. A definitive assignment of the observed bands in the transient Auger spectrum of thymine to HNCO might additionally provide interesting information on the timescale of the dissociative photoionization process.

Beyond this motivation, isocyanic acid represents a highly interesting species for inner shell photoionization studies. It is a rather small molecule with 16 valence electrons, which enables to apply reliable theoretical methods at an acceptable computational cost. In addition, it is isoelectronic to $CO_2$, an extensively investigated benchmark molecule for Auger and x-ray absorption spectroscopy, but has a reduced symmetry ($C_s$) and contains all the important elements of organic species: carbon, hydrogen, nitrogen, and oxygen. A

clean sample is crucial for high quality spectra, as inner-shell coincidence experiments are very complex due to the dissociative character of most of the probed states. Mass-selectivity, unlike in the VUV photoionization experiment, is therefore not an unambiguous criterion to discriminate against signal from sample contamination. Conventional photoelectron spectra at 100 eV were hence recorded for each of the HNCO batches, which were prepared by treating KNCO with phosphoric acid (see sec. B.1), to check the purity. A typical spectrum, for which two sweeps for electron kinetic energies between 70 and 90 eV in 10 meV steps were added, are shown in fig. 5.12.

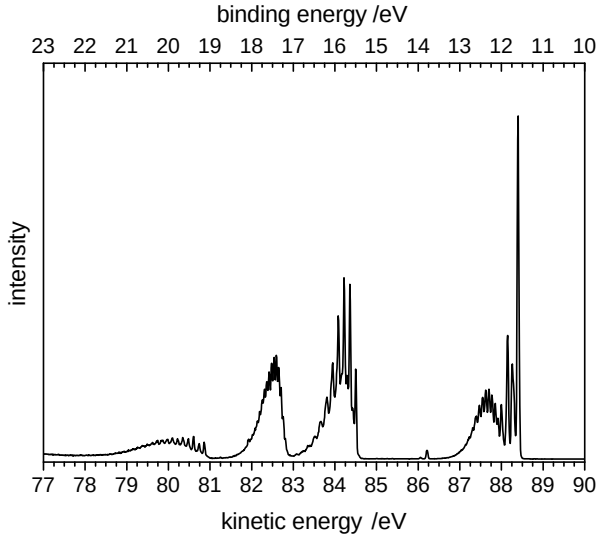


Figure 5.12.: Conventional photoelectron spectrum of HNCO at a photon energy of 100 eV. The peak at a binding energy of 13.79 eV is assigned to an impurity of $CO_2$.

The three lowest excited states of the HNCO cation are observed at the same binding energies as in the TPE spectrum (see sec. 5.1.1). In addition, two pro-

gressions at higher binding energies with a 465 $cm^{-1}$ and 1000 $cm^{-1}$ spacing, respectively, are visible, which are in perfect agreement with previous He(I) PE spectra.[226] The broad band centered at 17.47 eV can be assigned to the cationic state following ionization out of the 7a' orbital, and the progression setting in at 19.13 eV to the state following the 6a' valence orbital ionization. The small peak at a binding energy of 13.79 eV comes from minimal impurities of $CO_2$ from the synthesis. The amount of impurity is estimated to 0.8 % from the integral over the PE signal of the structure assigned to $CO_2$ and the PE signal of the $X^+\ ^2A''$ and $A^+\ ^2A'$ state of $HNCO^+$ (note that the two highest occupied molecular orbitals of HNCO correspond to the degenerate $1\pi_g$ HOMO in $CO_2$), which can be neglected in the following inner shell spectra.

#### 5.1.2.1. Normal Auger Spectra of HNCO

The normal Auger spectrum of isocyanic acid was recorded at the O 1s edge at a photon energy of 570 eV. The kinetic energy of the Auger electrons was scanned between 460 and 520 eV in 50 meV steps and 20 sweeps were added to obtain the normal Auger spectrum shown in fig. 5.13. Comparing the spectrum with the data from the LCLS experiment at long delays, as also depicted in fig. 5.13, shows a good agreement. It was only realized after this comparison that the calibration of the original LCLS data was off by about 4 eV. This is also the case for the previously published time-resolved Auger spectra after single photon excitation of thymine, which were recorded at the same LCLS beamtime.[144] It does, however, not affect the major findings of these experiments, i.e. the timescale of electronic relaxation of thymine after UV excitation. All LCLS spectra shown in this thesis are correctly calibrated. The spacing, shape and relative intensity of the observed bands in the LCLS and the SOLEIL spectra is very similar. It can therefore be concluded that the bands in the O 1s Auger spectrum of thymine after multiphoton UV excitation can indeed be assigned to isocyanic acid from dissociative pho-

toionization. The bands in the LCLS spectrum are a bit broader than in the one recorded at the synchrotron. This might be due to space charge effects, which are often observed in FEL photoemission experiments.[239–241] The high intensity of a free electron laser leads to an immediate release of many electrons, such that an electron cloud forms in front of the sample. The Coulomb interaction between the emitted electrons within this cloud alters the photoemission spectrum and leads to a broadening.

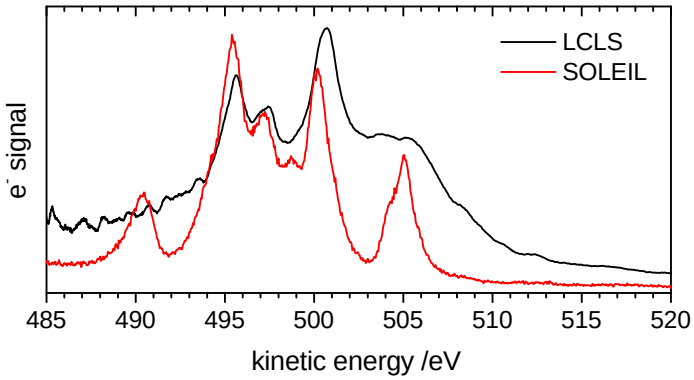


Figure 5.13.: Comparison of the O 1s Auger spectrum of HNCO recorded at SOLEIL (red) with the Auger steady state spectrum of thymine at long delay (2.3 ps) after multiphoton UV excitation from the LCLS experiment (black, cf. fig. 5.11).[235]

In addition to the O 1s Auger spectrum of HNCO, the spectra at the N 1s and C 1s edges were measured because this complete set of data facilitates the interpretation of the observed bands in the spectra. A photon energy of 465 eV was utilized at the nitrogen edge and the Auger electron signal was recorded in 20 sweeps iwith 50 meV steps from 325 to 390 eV. The carbon 1s Auger spectrum was recorded at 350 eV for Auger electron kinetic energies between 220 and 280 eV with the same step size and number of sweeps.

An unambiguous assignment of the observed bands to the final states is not possible without elaborate quantum chemical computations as discussed in sec. 2.6.2. As the energy of the final dicationic state in the Auger process is directly related to the kinetic energy of the emitted Auger electron, the energies of excited dicationic states can be calculated for example with time-dependent DFT without high computational cost. The obtained excitation energies can be related to the band in the Auger spectrum corresponding to the cationic ground state, i.e. the band with the highest kinetic energy, in which there are two electron vacancies in the former HOMO. Following this procedure, a preliminary assignment of the bands in the high kinetic energy part of the spectrum is possible. Doubly excited final dicationic states have to be considered for the lower kinetic energy part of the spectrum, which are not included in standard time-dependent DFT computations. In addition, the assignment can be guided by the well analyzed Auger spectrum of $CO_2$, which is isoelectronic to HNCO. Fig. 5.14 shows the order of the valence orbitals and the three lowest virtual orbitals in HNCO and $CO_2$ computed on the B3LYP/6-311G(d,p) level of theory. Note that the energetic order of the orbitals might change for doubly ionized states. The degeneracy of the $\pi$-orbitals in $CO_2$ is lifted in HNCO due to a reduced, i.e. non-linear, symmetry. The shapes of the molecular orbitals of HNCO and their energetic spacing are very similar to those of $CO_2$. A high similarity of the Auger spectra is therefore expected.

The oxygen 1s and carbon 1s normal Auger spectra of carbon dioxide, which served as calibration standard for the HNCO experiments, are depicted in fig. 5.15. The Auger spectra of $CO_2$ have previously been investigated by Moddeman and co-workers,[163] who divided the spectrum in three parts. The spectral region of the bands labeled in fig. 5.15 from 1 to 7 was assigned to normal Auger processes, in which only weakly bound outer valence orbitals ($1\pi_g$ to $4\sigma_g$) are involved (K-WW). The region comprising bands labeled as

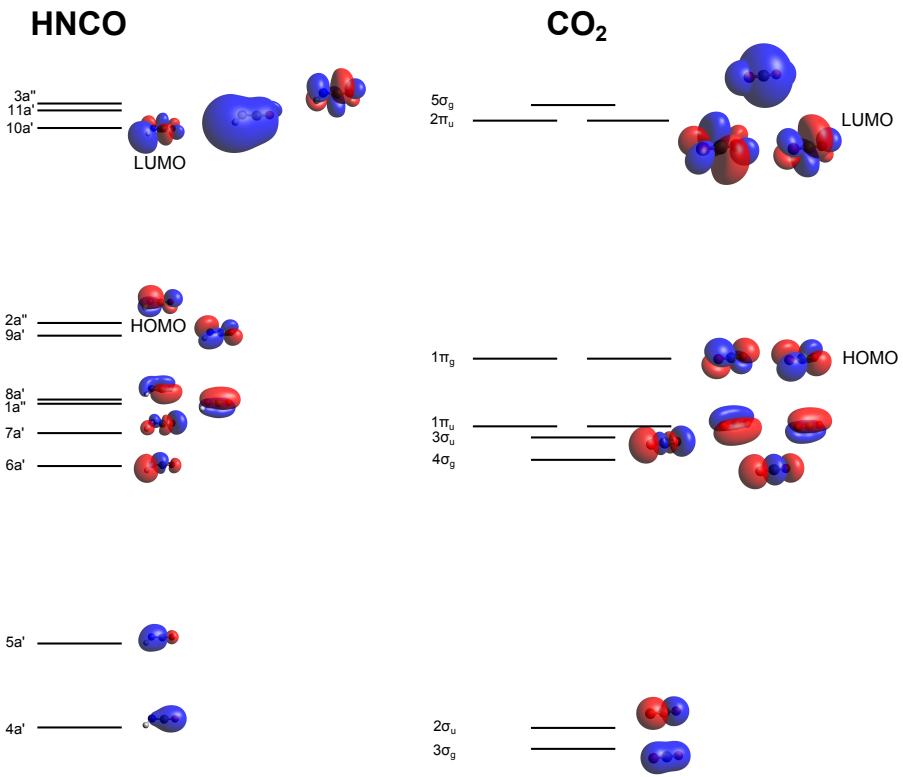


Figure 5.14.: Energetic order of the valence orbitals and three lowest virtual orbitals in HNCO and $CO_2$.

8-12 was correlated to Auger processes with final dicationic states, which have vacancies in one weakly bound outer valence orbital and in one strongly bound inner valence orbital ($2\sigma_u$ and $3\sigma_g$) (K-SW), while processes leading to final states with two inner valence orbital holes are observed at even lower kinetic energies (K-SS). This approximate classification was later validated by assigning the bands to specific Auger processes with the help of accurate quantum chemical computations.[140,242] The peak at 501.9 eV (O 1s) and 258.6 eV results from an Auger process leading to the dicationic ground state of $CO_2$ $1\pi_g^{-2}\,{}^1\Delta_g$, ${}^1\Sigma_g$, while those at lower kinetic energies are related to excited dicationic final states. The absolute peak positions and the assignment to the final dicationic configuration is tabulated in tab. 5.2.

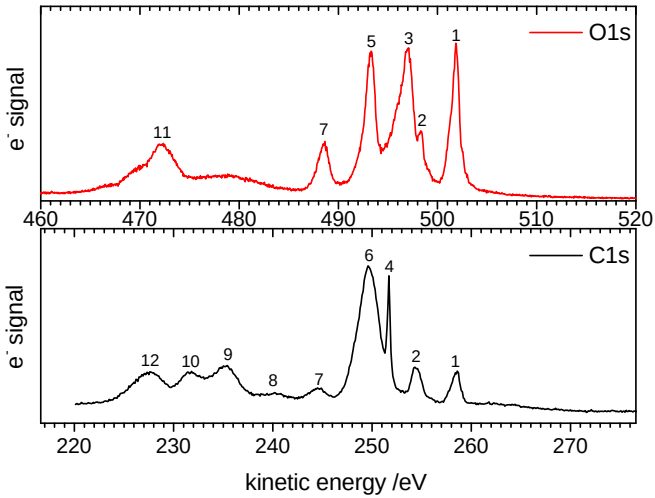


Figure 5.15.: $CO_2$ normal Auger spectrum at the oxygen and carbon edge.

The normal Auger spectra of HNCO at the oxygen, nitrogen and carbon edge are depicted in fig. 5.16. When plotted below each other, it becomes obvious

Table 5.2.: Band positions in the Auger spectra of $CO_2$ and assignment of the final state configuration.[140,242]

| | O 1s | C 1s | Final configuration |
|---|---|---|---|
| 1 | 501.9 eV | 258.6 eV | $1\pi_g^{-2}$ |
| 2 | 498.4 eV | 254.2 eV | $3\sigma_u^1\,1\pi_g^3$ |
| 3 | 497.0 eV | | $4\sigma_g^1\,1\pi_g^3$ |
| 4 | | 251.7 eV | $3\sigma_u^{-2}$ |
| 5 | 493.3 eV | | $1\pi_u^3\,1\pi_g^3$ |
| 6 | | 249.7 eV | $1\pi_u^{-2}$ |
| 7 | 488.6 eV | 244.6 eV | $4\sigma_g^1\,3\sigma_u^1$ |
| 8 | | 240.1 eV | $4\sigma_g^{-2}$ |
| 9 | | 235.2 eV | $2\sigma_u^1\,1\pi_u^3$ |
| 10 | | 231.6 eV | $3\sigma_g^1\,4\sigma_g^1$ |
| 11 | 472.2 | | $2\sigma_u^1\,3\sigma_u^1$ |
| 12 | | 227.5 eV | $1\pi_u^{-2}$ |

that certain bands appear at the same energy relative to the peak at the highest kinetic energy. Those are related to Auger processes leading to the same final dicationic state. The energies of electronically excited doubly ionized states of HNCO were computed on TD-B3LYP/cc-pVDZ level of theory and were taken into consideration for a preliminary assignment of the spectral features. Comparing the oxygen and carbon edge HNCO spectra with the corresponding ones of $CO_2$ reveals further similarities. The HNCO spectra are slightly shifted to higher kinetic energies. The lower electronegativity of nitrogen compared to oxygen increases the electron density of the valence electrons in HNCO on the carbon atom and also on the oxygen atom compared to $CO_2$. The binding energy of the core electrons is consequently lower, which also results in higher kinetic energies for Auger electrons in the C 1s and O 1s spectra. As discussed, the bands at 505.1 eV (O 1s), 371.9 eV (N 1s), and 261.2 eV (C 1s) are assigned to the Auger process leading to the electronic ground state of $HNCO^{++}$, $^1$A' $(2a")^{-2}$. The labeled bands in fig. 5.16 can

be assigned, in analogy to the approach of Moddeman and co-workers,[163] to K-WW Auger processes (1-9) and K-SW processes (10-13). The 4a' and 5a' molecular orbitals of isocyanic acid have a large proportion of 2s character and are therefore more tightly bound than the other outer valence orbitals. Comparing the spectral features with those of $CO_2$ and with computed energies of singly excited dicationic states enables to make a preliminary assignment of the observed bands in the normal Auger spectra of HNCO. The absolute peak positions and the assignment to the configuration of the final state is listed in tab. 5.3. Accurate quantum chemical computations are necessary to validate and replenish this assignment and can then be used to simulate the Auger spectra.

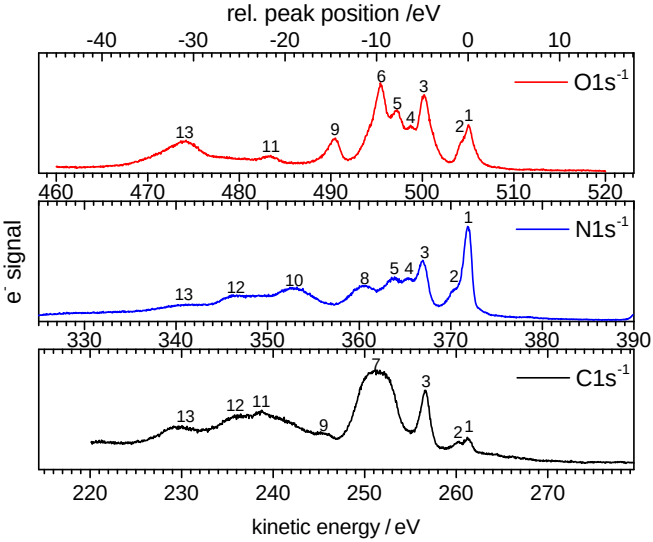


Figure 5.16.: Normal Auger spectra of HNCO at the oxygen, nitrogen, and carbon edge.

Table 5.3.: Band positions in the O 1s, N 1s, and C 1s normal Auger spectra of HNCO. A preliminary assignment is given for some bands based on relative energies computed on TD-B3LYP/cc-pVDZ level of theory and comparison with the spectrum of $CO_2$.

| | O 1s | N 1s | C 1s | calc. | final configuration | corresponding $CO_2$ band |
|---|---|---|---|---|---|---|
| 1 | 505.1 eV | 371.9 eV | 261.2 eV | 0.00 eV | $(2a")^{-2}$ | 1 |
| 2 | 504.2 eV | 370.4 eV | 260.3 eV | -0.42 eV | $(9a')^1(2a")^1$ | 1 |
| 3 | 500.1 eV | 366.9 eV | 256.6 eV | -5.60 eV | $(7a')^1(2a")^1$ | 2 |
| 4 | 498.7 eV | 365.5 eV | | -7.88 eV | $(6a')^1(2a")^1$ | 3 |
| 5 | 497.2 eV | 363.8 eV | | | $(1a")^1(2a")^1$ | 5 |
| 6 | 495.4 eV | | | -11.47 eV | $(8a')^1(2a")^1$ | 5 |
| 7 | | | 251.3 eV | | $(8a')^1(1a")^1$, $(8a')^{-2}$, $(2a")^{-2}$ | 6 |
| 8 | | 360.5 eV | | | | |
| 9 | 490.3 eV | | 245.5 eV | | $(6a')^1(7a')^1$ | 7 |
| 10 | | 352.9 eV | | | | |
| 11 | 483.3 eV | | 238.8 eV | -22.64 eV | $(4a')^1(2a")^1$ | |
| 12 | | 346.4 eV | 236.0 eV | | | |
| 13 | 474.0 eV | 340.7 eV | 229.5 eV | | $(4a')^1(5a')^1$ | 11 |

### 5.1.2.2. NEXAFS Spectra of HNCO

The NEXAFS spectra of isocyanic acid near the oxygen, nitrogen, and carbon edge shown in fig. 5.17 were recorded by scanning the photon energy in steps of 20 meV and recording the ion yield. A photon energy between 532 and 541 eV was scanned for excitation of an oxygen core electron, while the energy regions 399-408 eV and 287-297 eV were scanned for the nitrogen and carbon edge, respectively. All three spectra show two broad bands separated by approximated 1.5 eV in the low energy region. A third band in between those two is visible in the nitrogen NEXAFS spectrum. While no further structure is visible near the oxygen K-edge, the nitrogen and carbon spectra feature further bands at higher photon energies.

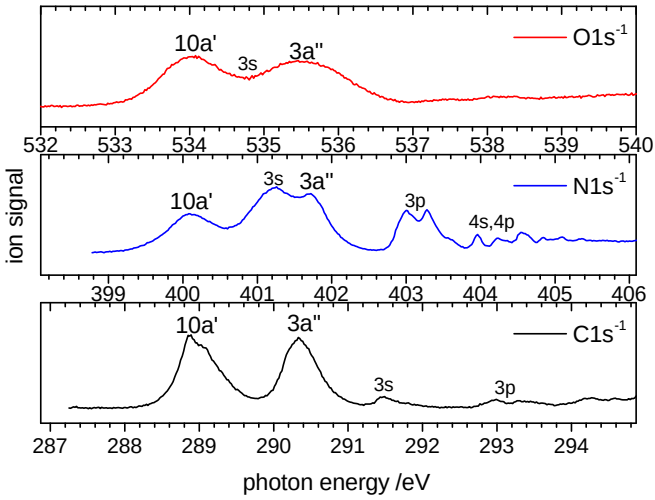


Figure 5.17.: NEXAFS spectra of HNCO near the oxygen, nitrogen, and carbon edge.

As the computation of core-excited states is computationally challenging, a comparison with the corresponding carbon dioxide spectra is again applied for a preliminary assignment. The K-shell absorption spectra of $CO_2$ have been investigated by energy loss spectroscopy [243] and NEXAFS. [164] Fig. 5.18 shows the two corresponding spectra, which were recorded for calibration, and the assignment of the observed bands. A strong and broad absorption line assigned to the transition of the respective core electron to the $2\pi_u^*$ virtual orbital is observed in both $CO_2$ spectra. As the core excited state of $CO_2$ has a bent geometry, excitation of the OCO-bending mode, which is not resolved, leads to a significant broadening of the band. An asymmetry is observed due to a higher ion signal intensity on the high energy side of the $\pi^*$ band in the O 1s $^{-1}$ spectrum, which features a broad shoulder. This is explained by a superposition with the lowest energy 3s-Rydberg transition, which is observed at a higher photon energy relative to the $\pi^*$ band in the carbon spectrum. For oxygen, this transition to a $\sigma_g$ orbital is dipole allowed because there are two oxygen K-shell orbitals in $CO_2$. One has $\sigma_g$ symmetry and the other one $\sigma_u$. [243] The transition is, by contrast, dipole forbidden for excitation of a carbon K-shell electron. Excitation of the antisymmetric stretching and bending mode of the $\pi^*$ dipole allowed state, which is only 2 eV lower in energy, lends intensity to the carbon 3s Rydberg state by vibronic coupling, which is why the 3s-Rydberg state is observed nevertheless in the C 1s NEXAFS spectrum. Vibrational structure is resolved for the carbon Rydberg states, which has been assigned in previous studies to the symmetric and antisymmetric stretching mode in the respective state. [244,245]

A corresponding assignment is possible for the bands in the HNCO NEXAFS spectra as shown in fig. 5.17. The degeneracy of the LUMO orbital is lifted in HNCO in comparison to carbon dioxide. This explains the occurrence of two broad bands in the low energy part of each of the spectra separated by about 1.5 eV. These are assigned to transitions from the K-shell orbitals

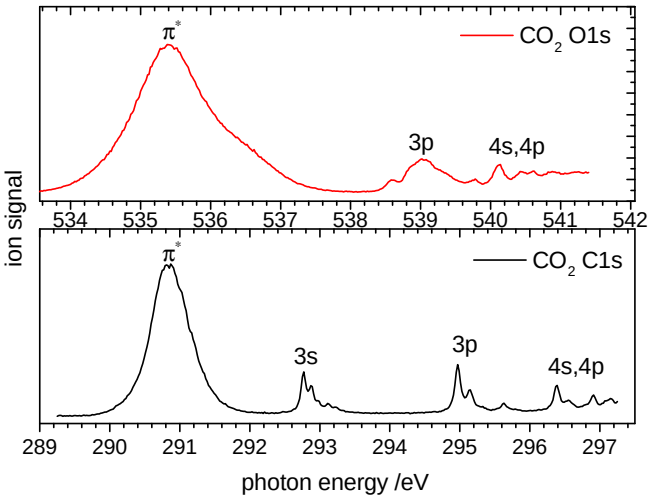


Figure 5.18.: O $1s^{-1}$ and C $1s^{-1}$ NEXAFS spectra of carbon dioxide. The bands are assigned according to the literature.[164,243]

to the 10a' and 3a" virtual orbitals, respectively. The energy of Rydberg orbitals is the lower, the higher the nuclear charge of the element. This explains the high background between the 10a' and 3a" bands in the oxygen spectrum and the additional band in the nitrogen spectrum at 401.2 eV, as the carbon 3s Rydberg state lies energetically between the core-excited 10a' and 3a" states. The band assigned to the carbon 3s Rydberg state lies at a higher photon energy, well separated from the 3a" band. Excitations to the respective 3p Rydberg orbital (nitrogen, carbon) and the 4s,4p ones (nitrogen) are also observed. The NEXAFS excitation energies along with a preliminary assignment is summarized in tab. 5.17.

NEXAFS spectra are the basis for resonant Auger experiments (see sec. 2.6.2), which are an efficient tool to resolve molecular dynamics site-specifically.[144]

Table 5.4.: Peak positions and possible assignments of the bands in the NEXAFS spectra of HNCO.

| O $1s^{-1}$ | N $1s^{-1}$ | C $1s^{-1}$ | possible assignment |
|---|---|---|---|
| 534.0 eV | 400.1 eV | 288.9 eV | $(10a')^1$ |
| 535.5 eV | 401.7 eV | 290.3 eV | $(3a'')^1$ |
| 534.8 eV | 401.2 eV | 291.5 eV | 3s Rydberg |
| – | 403.0 eV | 293.0 eV | 3p Rydberg |
| – | 403.9 eV | – | 4s,4p Rydberg |

In addition, it has been shown that soft x-ray absorption spectroscopy can also be applied to investigate concentrations of combustion products in flames on-line. [67]

### 5.1.3. Summary HNCO

Photoionization of isocyanic acid HNCO was investigated both for valence shell orbitals as well as for inner shell orbitals. HNCO was synthesized by treating the potassium salt either with stearic acid and heating it under vacuo or with phosphoric acid. A threshold photoelectron spectrum was recorded utilizing synchrotron radiation at SOLEIL. Due to the high spectral resolution, $\Delta K_a = \pm 1$ transitions are visible in the TPES and the rotational structure of the $HNCO^+$ $X^+$ $^2A''\leftarrow$HNCO X $^1A'$ band belonging to the respective vibrational ground states was analyzed in the framework of the orbital ionization model. This made it possible to determine an accurate value for the ionization energy of HNCO IE=11.602±0.005 eV. Vibrational structure of the $HNCO^+$ $X^+$ $^2A''$ ground state was observed, including the HNC- and NCO- in plane bending modes not visible in previous spectra. A good approximation of the cation's geometry was obtained by a Franck-Condon fit. The determined geometry differs slightly from DFT computations in the HNC and NCO bonding angles since the $X^+$ potential is perturbed due to a conical intersection

with the first excited state at a linear geometry for $HNCO^+$. For the first excited $A^+$ $^2A'$ state, a progression with a 590 $cm^{-1}$ spacing was observed and assigned to overtones of the HNC-bending mode. Excitation to the $A^+$ state coincides with a large geometry change, which leads to small Franck-Condon factors for small vibrational quantum numbers. Hence, a definitive assignment of the adiabatic excitation energy and the quantum numbers of the observed bands is not possible. The transition energy into the second excited state of $HNCO^+$was found to be 15.50±0.03 eV. A lower limit for the appearance energy of $AE_{0K}(HCO^+)\geq$15.56 eV was determined. Further parallel DPI channels to $NCO^+$ and $NH^+$ were also observed and the appearance energies reported in the literature could be confirmed.

The normal Auger and NEXAFS spectra at the oxygen, carbon, and nitrogen edge were successfully recorded in a second series of experiments with soft X-ray radiation. The oxygen K-shell Auger spectrum helped to assign the time resolved UV pump/SXR probe spectra of thymine in a combined FEL/synchrotron study. They confirmed that the nucleobase thymine undergoes dissociative photoionization to an m/z=83 fragment and neutral HNCO after 266 nm multiphoton ionization on a timescale of approximately 400 fs. A preliminary assignment of the bands observed in the oxygen, nitrogen, and carbon edge Auger spectra was conducted based on time dependent density functional theory and comparison with the Auger spectrum of $CO_2$. An expected high similarity of the spectra of HNCO and $CO_2$ was observed, as both molecules are isoelectronic. In addition, the near edge x-ray absorption fine structure of HNCO was analyzed and a preliminary assignment was given here, too. More sophisticated quantum chemical computations will help validating and replenishing the assignment.

## 5.2. Carbonyl Amidogen NCO

As can be seen in fig. 5.1 the carbonyl amidogen radical NCO plays also a central role in the RAPRENO$_x$ process being a dissociation product of isocyanic acid. Therefore, it is a very important reactive intermediate in combustion chemistry. In addition, NCO is assumed to contribute to the formation of HNCO in the interstellar space.[246] The NCO radical has been subject to several spectroscopic studies.[247–253] Several were focused on the photodissociation of the radical.[249,251,252] Another important goal in previous investigations was to study the Renner-Teller effect of NCO,[253] which was also extensively exploited from the theoretical point of view.[254–256] The photoionization of carbonyl amidogen was investigated by Dyke *et al.*[257] employing He(I) photoelectron spectroscopy. In this experiment, NCO was generated by H abstraction from HNCO with fluorine atoms. As the experiment was not conducted mass-selectively, the obtained photoelectron spectrum contained also the signal of the precursor HNCO, residual gases like $O_2$, $CO_2$ , CO, $N_2$ and of other reaction products like HF and F. As the ionization onset of NCO overlaps with the PES signal of HNCO, a subtraction scheme was employed to analyze the spectrum. Seven photoelectron bands resulting from ionization out of the $2\pi$, $7\sigma$ and $6\sigma$ molecular orbitals were assigned, while the ionization energy was determined to be $11.76\pm0.01$ eV. A vibrational progression consisting of six components spaced by $1000\pm30\,\mathrm{cm}^{-1}$ was reported for the $NCO^+\ {}^3\Sigma^-$ ground state despite the strong interference of the HNCO signal. Vibrations for higher electronic states were also rudely resolved. To overcome the issues with signal overlap, Ruscic *et al.* employed photoionization mass spectrometry, which yielded the same ionization energy.[229]

### 5.2.1. NCO Radical Generation

The carbonyl amidogen radical was generated by flash pyrolysis of chlorine isocyanate and photoionized with synchrotron radiation at the Swiss Light Source. The precursor was freshly synthesized according to the literature [258] (sec. B.2) and diluted in 2.0 bar of Ar while the sample container was cooled to -40°C. Passing the pyrolysis tube, which was heated to 950°C, the chlorine-carbon bond was cleaved and the NCO radical (m/z=42) was obtained, while the precursor (m/z=79/81) has almost disappeared. As the mass spectra at 12.5 eV depicted in fig. 5.19 shows, several side products from secondary reaction channels are formed upon pyrolysis, while the sample contains impurities with m/z=43 and m/z=70/72/74.

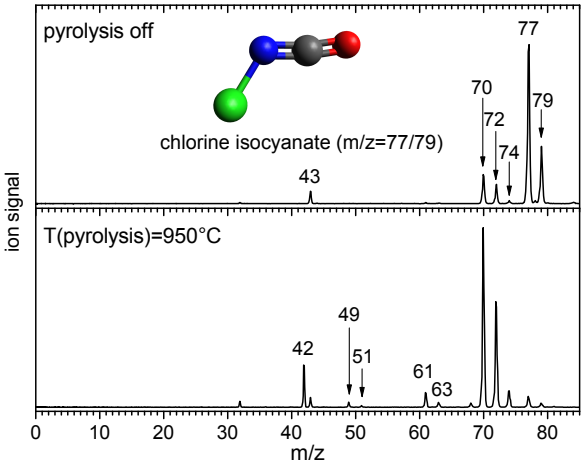


Figure 5.19.: Mass spectra of chlorine isocyanate at 12.5 eV with the pyrolysis turned off and a pyrolysis temperature of 950°C. Carbonyl amidogen (m/z=42) is generated in the pyrolysis of chlorine isocyanate (m/z=79/81), while several side products are observed, too.

The dominant peaks in the mass spectrum are m/z=70/72/74, which show the typical 10 : 6.4 : 1 isotope pattern for $^{35}Cl_2$ : $^{35}Cl^{37}Cl$ : $^{37}Cl_2$. A typical 3 : 1 chlorine pattern is observed for m/z=49/51 and m/z=61/63, while for m/z=43 and m/z=68 only a single peak is present in the spectrum. As there are not many alternatives for such low masses, the assignment of these peaks to isocyanic acid (HNCO, m/z=43), nitrogen monochloride (NCl, m/z=49/51), cyanogen chloride (Cl-CN, m/z=61/63), cyanogen isocyanate ($C_2N_2O$, m/z=68), and $Cl_2$ (m/z=70/72/74) seems plausible. To confirm this theory, the mass-selected TPES for these mass peaks shown in fig. 5.20 were also analyzed. The energy scan region was however chosen to cover the spectrum of the NCO radical (11.5-12.6 eV). That is why the scan does not include all ionization onsets of these side products.

The ionization energy of $Cl_2$ was determined in a high-resolution PFI-ZEKE experiment to be 11.4875 eV [259] and thus matches the recorded ms-TPES for m/z=70/72/74, in which the high energy part of the peak for the 0-0 transition is visible. The observed progression with a spacing of 80 meV agrees also well with the literature and can be assigned to the first six overtones of the vibration in the $Cl_2^+$ ground state. For m/z=68, the ionization threshold seems to be below the start of the energy scan, too, as the TPE signal drops at 11.5 eV. For cyanogen isocyanate NC-NCO, an adiabatic ionization energy of 11.49 eV was reported from a He(I) PES study. [260] A vibrational band at 11.75 eV assigned to the asymmetric stretch in NCO and a broad band around 12 eV are additionally reported, which is, despite the low signal/noise ratio, also found in the corresponding spectrum in fig. 5.20. Therefore, this assignment seems plausible. The ms-TPES of m/z=61/63 shows four pronounced peaks and can be assigned to cyanogen chloride, for which an IE of 12.34 eV has been determined employing conventional PES. [261] While the peak at 12.29 eV is a hot or sequence band, the four peaks at 11.33, 11.37, 11.44, and 11.48 eV can be assigned to the $0_0^0$ and $3_0^1$ transitions of the two spin-orbit components of

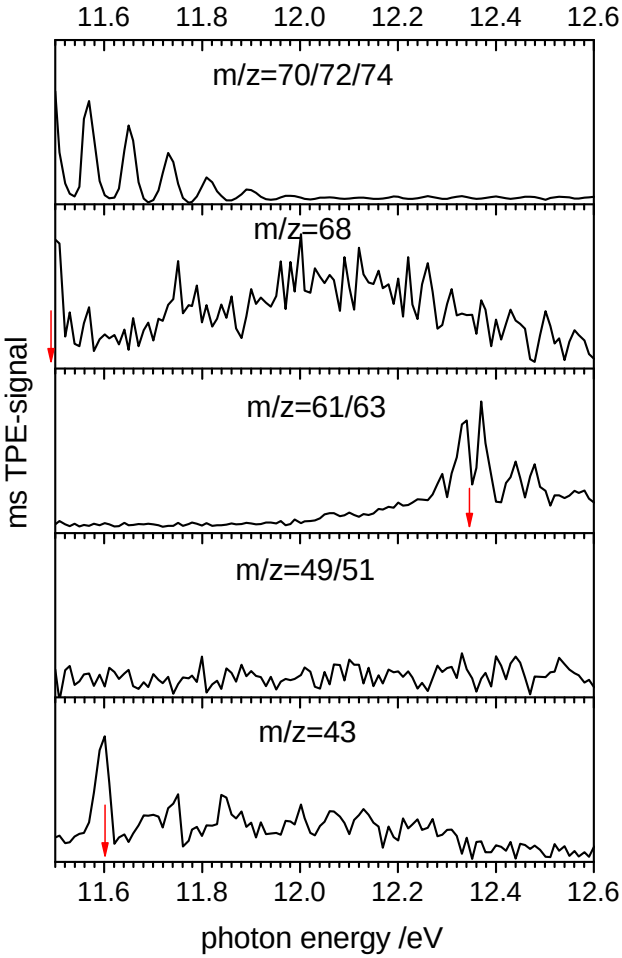


Figure 5.20.: Ms-TPE spectra for the side products $Cl_2$, $N_2C_2O$, Cl-NC, NCl, and HNCO of the Cl-NCO pyrolysis from 11.5 to 12. eV. The red arrows indicate the literature values for the ionization energy. Details are given in the text.

the cationic ground state in Cl-CN.[262] No TPE signal above noise level is obtained for m/z=49/51. As the isotope pattern in the MS-TOF unambiguously indicates that the molecule contains one chlorine atom, it seems likely that it is nitrogen monochloride. In the literature, an ionization energy of 9.82 eV is reported,[263] i.e. well below the scanned energy region. As the first excited state of N-Cl is computed to be at 14.38 eV[263] and no vibrational excitation is expected more than 1.5 eV above the IE for such a small molecule, it seems logical that no TPE signal is observed. The last side product in the pyrolysis of Cl-NCO with an ionization energy below 12.6 eV is isocyanic acid. The TPE spectrum has already been extensively discussed in the previous chapter and the observed ionization energy matches the reported 11.602±0.005 eV. All these side products must be generated in secondary reactions. While the formation of $Cl_2$ can be easily explained by the reaction of two Cl radicals, which are expected to be formed next to NCO, other bonds in the precursor than the C-Cl bond have to be cleaved. An important pathway seems to be the precursor's decomposition to NC, as there are two side products observed, which might originate from bimolecular reactions of NC with Cl or NCO. The cyano radical has however not been observed by itself, as it ionizes only above 14.2 eV.[264] It is also thinkable that Cl-CN is formed after oxygen cleavage off the precursor and subsequent isomerization. Nevertheless, Cl-NCO is a potent precursor for the generation of the carbonyl amidogen radical utilizing flash pyrolysis because it shows, besides $Cl_2$, the most intense peak in the mass-spectrum.

### 5.2.2. TPE Spectrum of NCO

The TPE spectrum of carbonyl amidogen was recorded from 11.5 to 12.6 eV employing a step size of 10 meV. The 150 $mm^{-1}$ grating at the SLS VUV beam line and a threshold photoelectron resolution of 5 meV was used yielding a total photon energy resolution of 9.5 meV. Every data point was averaged for

nine minutes to increase the signal/noise ratio. Fig. 5.21 shows the obtained mass-selected threshold photoelectron spectrum, which can be divided in two parts: The peak progression beginning at 11.76 eV and the band system originating at 12.93 eV.

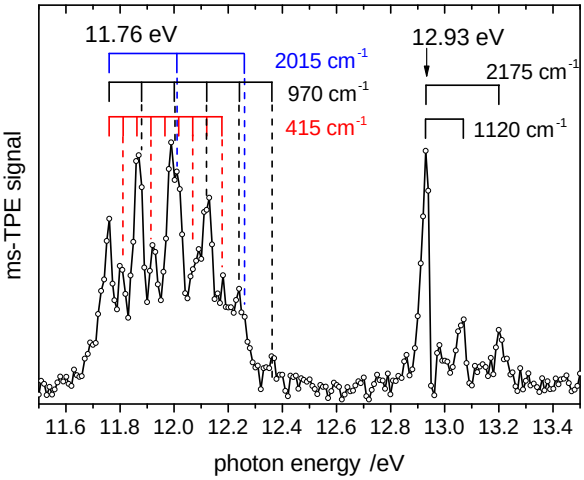


Figure 5.21.: Ms-TPE spectrum of carbonyl amidogen. The spectrum features two band systems originating at 11.76 eV and 12.93 eV, which are assigned to the $NCO^+$ ground state $X^+\ ^3\Sigma^-$ and first excited state $a^+\ ^1\Delta$.

The ionization energy was determined to be 11.76 eV in a previous PES experiment [257], which agrees well with the computed value of 11.78 eV employing the CBS-QB3 composite method. The first peak maximum in fig. 5.21 can thus be assigned to the ionization energy for the cationic ground state. The highest molecular orbital in NCO $X\ ^2\Pi$ is a doubly degenerate non-bonding $\pi$-orbital with three electrons. Hence, ionization out of this orbital can lead to

three different electronic states in the ion: the totally symmetric $^1\Sigma^+$ state, $^1\Delta$, and the triplet state $^3\Sigma^-$. The latter is energetically the lowest one. The TPES for this electronic ground states features an extensive vibrational structure. The intense peaks at 11.76, 11.87, 11.99, 12.13, 12.24, and 12.36 are separated by about $1000\,\mathrm{cm}^{-1}$(125 meV). The peaks are relatively broad and in some of them shoulders are visible. Hence it is possible to assign these bands to two independent progressions with a spacing of $2015\,\mathrm{cm}^{-1}$ and $970\,\mathrm{cm}^{-1}$, which can be assigned to the stretching modes (*vide infra*). Fermi resonances might occur since the two progressions are divided by a factor of roughly two, but the spectral resolution is too low to observe the expected splitting. The less intense peaks at 11.80, 11.92, 12.08, and 12.28 eV can be assigned to yet another underlying progression with a $415\,\mathrm{cm}^{-1}$ spacing, which has its origin in the 11.76 eV peak, too. For further analysis of the peak structure in the TPES belonging to the $NCO^+$ ground state, computations on CBS-QB3 level of theory were performed. Both the neutral molecule ($X\ ^2\Pi$) and the cation ($X^+\ ^3\Sigma^-$) are predicted to be linear with a $C_{\infty v}$ symmetry. For the two stretching modes in the cation, $1(\sigma^+)^+$ and $2(\sigma^+)^+$, unscaled wavenumbers of $1996\,\mathrm{cm}^{-1}$ and $949\,\mathrm{cm}^{-1}$ are predicted, while for the degenerate bending mode $1(\pi)^+$ a value of $399\,\mathrm{cm}^{-1}$ is obtained. As both states are linear, only an excitation of the NC- and CO-stretching modes is expected upon ionization. The Franck-Condon simulation in fig. 5.23 shows that transitions into excited states of the stretching modes explain well the intense progressions with experimental wavenumbers of $2015\,\mathrm{cm}^{-1}$ and $970\,\mathrm{cm}^{-1}$. As the molecule is linear, the simulation program ezSpectrum [172] was used and hot and sequence bands calculated for a temperaure of 950°C were included. However, neither the intensities are correctly predicted, nor is the $415\,\mathrm{cm}^{-1}$ progression included in the simulation. The latter matches well the NCO bending mode in the cation. As discussed above, the bonding angle remains constant upon ionization and hence an excitation of the bending mode is not expected. They do therefore not appear in the FC simulation. An alternative explanation for

this progression might be autoionization resonances of a superexcited state with bent geometry. This has for example been observed in the TPES of $CO_2$,[265–267] a molecule similar to NCO. For some of those peaks in the TPE spectrum belonging to the 415 $cm^{-1}$ progression, the PIE curve (fig. 5.22) shows small steps and peaks, which supports the theory that autoionizing states contribute to the spectrum.

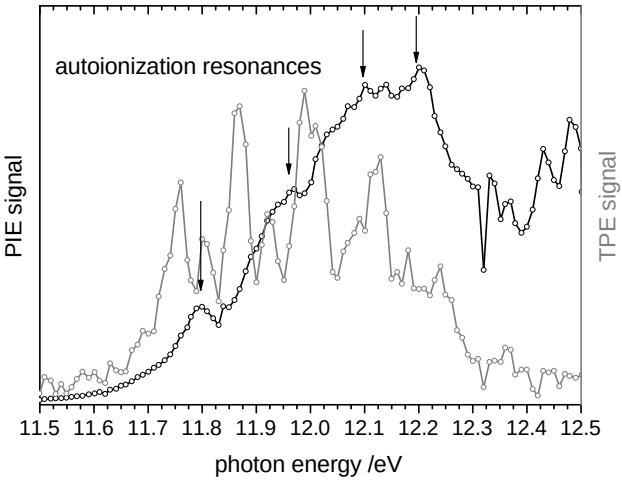


Figure 5.22.: Small steps and peaks are visible in the PIE curve of NCO which coincide with some peaks in the TPES (grey) and can thus be assigned to autionization resonances.

At 12.93 eV, a second band system is visible featuring an intense peak followed by two smaller peaks at 13.07 and 13.20 eV. This structure and the transition energy of 12.93 eV can be assigned to the first excited state of $NCO^+$ $^1\Delta$. Two distinct vibrational bands at 1120 $cm^{-1}$ (+140 meV) and 2175 $cm^{-1}$ (+270 meV) are observed matching the CO- and CN stretching modes. CBS-

QB3 computations predict a slightly higher ionization energy of 13.27 eV, but the stretching modes wavenumbers agree reasonably well with 1105 $cm^{-1}$ and 1951 $cm^{-1}$. Again, a linear geometry for the $^1\Delta$ state is predicted, i.e. the degenerate bending mode is neither expected, nor observed. The Franck-Condon simulation depicted in fig. 5.23 shows a very good agreement of experimental and computed spectrum.

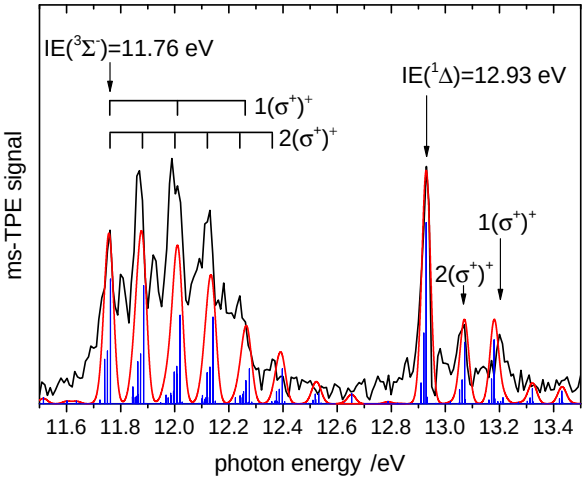


Figure 5.23.: Franck-Condon simulation for the $X^+\ ^3\Sigma^-$ and $a^+\ ^1\Delta$ state of $NCO^+$ including hot and sequence bands (blue sticks, red line: convolution with gaussian fwhm=35 meV). The respective ionization energies are 11.76±0.02 and 12.93±0.02 eV. The simulation is based on unscaled B3LYP/6-311G(2d,d,p) computations. Figure adapted from ref. [230].

The second excited state $^1\Sigma^+$, which also originates from ionization out of the $2\pi$ orbital, is expected at 13.56 eV. [257] However, it could not be recorded since beamtime at a synchrotron facility is limited. For ionization out of a

non-bonding orbital, like the $2\pi$ orbitals in NCO X $^2\Pi$, one would expect a sharp peak for the 0-0 transitions and only very weak to no vibrational structure because bond lengths and angles should only minimally or not at all change upon ionization. Furthermore, due to the spin-orbit degeneracy, an intensity ratio of 3 : 2 : 1 should be observed for the electronic states $^3\Sigma^-$ : $^1\Delta$ : $^3\Sigma^+$ like in the TPES of isoelectronic $N_3$.[268] The recorded spectrum disagrees with the prediction of peak intensities for the $NCO^+$ ground state, while for the $^1\Delta$ state the expectation that the 0-0 transition is the most intense peak is met. In addition, the intensity ratio for the ground state to the first excited state is rather 3 : 1 than 3 : 2. B3LYP/6-311G(2d,d,f) computations yield a significant increase of the N=C bond by 10 pm, while the C=O decreases by 5 pm when comparing neutral and cation in the respective ground state. Therefore it has to be assumed that the electron is not solely ionized from a non-bonding orbital and that the description of the $X^+$ $^3\Sigma^-$ state requires a mulitreference approach. A single-determinant wavefunction as used in DFT is not appropriate for computing this behavior correctly. As more reliable multireference computations are challenging and great experience in theory is needed, no attempt was made to improve the computations. The disagreements of the Franck-Condon simulation with the experimental spectrum can be ascribed to the observation described above. In addition, it cannot be excluded that the peaks assigned to autoionization resonances may also originate in part from the multireference character of the cationic ground state.

### 5.2.3. Summary NCO

The carbonyl amidogen radical NCO was generated by flash pyrolysis of chlorine isocyanate (Cl-NCO). Cleavage of the precursor does not exclusively occur on the Cl-C bond at 950°C as several side products were observed, which must originate from secondary reactions of other fragments generated

in pyrolysis. Employing the iPEPICO scheme, it was possible to obtain an undisturbed TPES of NCO and the ionization energy was determined to be IE($^3\Sigma^-$)=11.76±0.02 eV. Excitation of the stretching modes in $NCO^+$ are observed and wavenumbers of 2015 $cm^{-1}$ and 970 $cm^{-1}$ were determined. In addition, a progression with a 415 $cm^{-1}$ spacing is visible and was assigned to autoionization resonances of a superexcited state with bent geometry. The transition energy to the $a^+\ ^1\Delta$ state was determined to be 12.93±0.02 eV and the $2(\sigma^+)^+$ and $1(\sigma^+)^+$ modes were observed at 1120 $cm^{-1}$ and 2175 $cm^{-1}$, respectively.

## 5.3. Pyrrolyl $C_4H_4N$

As discussed in the introduction, nitrogen in biological materials, like coal and tar, is found in a high percentage (50-80 %) in pyrrolic structures.[2] The pyrrolyl radical $C_4H_4N$ can thus be seen as a model system for nitrogen-containing structures in fuels, from which conclusions can be transferred to more complex heterocyclic molecules of biological relevance. It is assumed to be involved in the combustion of pyrrole[27,28] and pyridine.[269] In the latter, hydrogen abstraction and addition of oxygen leads to the pyridoxy radical, which decomposes further to pyrrolyl. Pyrrolyl is isoelectronic to the furan radical cation and, more important, cyclopentadienyl. Quantum chemistry shows that pyrrolyl has a $C_{2v}$-symmetric, non-aromatic electronic ground state with five $\pi$-electrons.[270] Thus, the electronic ground state of pyrrolyl has the irreducible representation $^2A_2$ and the nitrogen lone pair is located in a $\sigma$-orbital. The three highest occupied molecular orbitals of pyrrolyl are illustrated in fig. 5.24. The generation of pyrrolyl from N-H-bond breakage in pyrrole can therefore not easily proceed on the pyrrole $^1A_1$ ground state, as this would result in the $^2A_1$ excited electronic state of pyrrolyl, but must proceed via an excited electronic state. Another possibility is that a rearrangement of pyrrole to pyrrolenine precedes the H-atom cleavage.[26,270] That is why the generation of isolated pyrrolyl radicals has been challenging so far. The first indirect prove of pyrrolyl by radical-radical reaction products was reported in

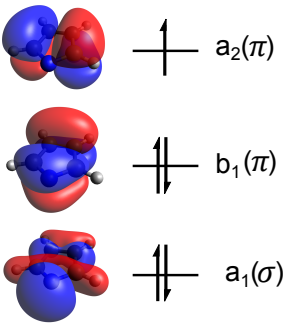


Figure 5.24.: The three highest molecular orbitals of the X $^2A_2$ ground state of pyrrolyl.

1983, when 1-phenylpyrrole was cleaved by flash photolysis.[271] The photostability of pyrrole, for which a major photodissociation channel is pyrrolyl + H, has been investigated quite extensively.[272–275] Two different pathways have been found for the formation of pyrrolyl after UV photo-excitation of pyrrole. Direct dissociation on an excited state potential energy surface of pyrrolyl leads to fast H atom products. It can be concluded from the vibrational structure in the translational energy release of the observed H atoms that pyrrolyl is generated in the $^2A_2$ ground state.[275] Slow H atom products are also observed and assigned to a unimolecular decay of highly internally excited ground state pyrrole after internal conversion from an initially excited state.[272] The enthalpy of formation for pyrrolyl was derived to be $259\pm8\,\mathrm{kJ\,mol^{-1}}$[272] and $301.9\pm0.5\,\mathrm{kJ\,mol^{-1}}$,[275] respectively, from the measured bond dissociation energy in pyrrole and the enthalpies of formation at 0 K of pyrrole and atomic hydrogen. Ab initio computations predict the room temperature heat of formation to be $\Delta_f H^0_{298K}=296\pm2\,\mathrm{kJ\,mol^{-1}}$.[270] The pyrrolyl electronic ground state was investigated employing photodetachment PES.[276] Here, the pyrrolide anion was prepared by deprotonation of pyrrole. Ionization leads to the pyrrolyl radical in the $^2A_2$ ground state. The electron affinity was determined to be $EA=2.145\pm0.010\,\mathrm{eV}$. Employing theory, the photodetachment spectrum and the vibrational structure of pyrrolyl's electronic ground state could be reproduced in a Franck-Condon simulation.[277,278] No vibrational structure was observed for the $1^2B_1$ first excited state in the experimental spectrum, but a conical intersection to the ground state is presumed and discussed in detail in the theoretical works.[277,278] So far, beyond the rather elaborate photolysis of pyrrole, no efficient pathways to generate pyrrolyl have been discovered and therefore spectroscopic data on the pyrrolyl radical are scarce. TPES is a suitable method to check the efficiency of radical generation, verify the isomeric form of the composition $C_4H_4N$, determine the ionization energy and characterize the vibrational structure in the cation.

### 5.3.1. Precursor Selection and Mass Spectra

No reports on the generation of pyrrolyl by pyrolysis exist to the best of our knowledge. The direct generation of pyrrolyl by pyrolysis of N-aminopyrrole ($C_4H_4N\text{-}NH_2$) was not successful (see section A.4). The hydrocarbon analogue radical, cyclopentadienyl, was observed as a fragment in the pyrolysis of anisole (methoxybenzene).[279–281] In a two-step decomposition reaction methyl and CO are subsequently cleaved off. As cylopentadienyl and pyrrolyl are isoelectronic, the nitrogen analogue, methoxypyridine, was considered for the generation of pyrrolyl. There are three isomers which differ by the position of the substituted methoxy group: 2-, 3-, and 4-methoxypyridine. 2-methoxypyridine has the lowest boiling point at 142°C and is therefore also expected to have the highest vapor pressure, which is advantageous for gas phase experiments. However, experiments have shown that flash pyrolysis of this isomer at 600°C leads to an equilibrium between 2-methoxypyridine and N-methylpyridone as depicted in fig. 5.25.[282] Hence, 3-methoxypyridine was chosen from the remaining isomers because its boiling point (180°C) is slightly lower than 4-methoxypyridine's one (190°C).

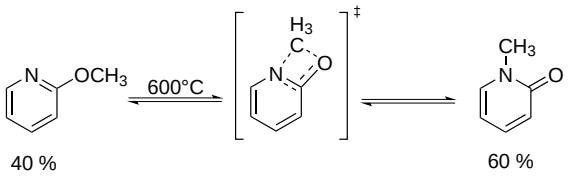


Figure 5.25.: Rearrangement of 2-methoxypyridine to N-methylpyridone as observed by Lister *et al.* at a pyrolysis temperature of 600°C.[282]

The vapor pressure of 3-methoxypyridine turned out to be high enough to place the sample container outside the vacuum apparatus. As it was on the other hand too low to be measured on an absolute scale, the concentration of the precursor in the molecular beam, which was diluted in 1.9 bar of argon,

cannot be determined. It is therefore only estimated to be below 2 %. Fig. 5.26 shows mass spectra of 3-methoxypyridine for different pyrolysis temperatures and a photon energy of 10.0 eV. Below 500°C, only the precursor is visible at m/z=109. At 500°C pyrolytically induced fragmentation sets in and signals at m/z=94, 66, and 15 are observed, which agrees with the expected pyrolysis pathway. First methyl (m/z=15) is cleaved from the precursor leading to 3-oxypyridine (m/z=94), which subsequently loses CO (m/z=28) resulting in the pyrrolyl radical (m/z=66). A peak corresponding to CO is not observed in this mass spectrum since the corresponding ionization energy is above 10.0 eV. Increasing the temperature to 600°C shifts the ratio of the precursor peak and the pyrrolyl peak in favor of the latter one. At higher temperatures, the 3-methoxypyridine peak completely vanishes, but also the pyrrolyl signal diminishes as further fragmentation reactions (m/z=54, 40, 39) and dimerization (m/z=132) are expected. To verify the suspected generation of the pyrrolyl radical, to determine its ionization energy, and to investigate the other species formed upon pyrolysis, mass-selected threshold photoelectron spectra were recorded at a pyrolysis temperature of 565°C (*vide infra*). This temperature was chosen to maximize the pyrrolyl signal intensity.

### 5.3.2. TPE Spectrum of Pyrrolyl

The mass-selected TPE spectrum corresponding to the observed m/z=66 peak was recorded under the experimental conditions described above. Fig. 5.27 shows the obtained spectrum, for which a photon energy step size of 5 meV and an acquisition time of 3 min per data point was used. Although the signal/noise ratio is only moderate, a sharp peak at 9.11 eV can be unambiguously observed. Further broad bands are visible at 9.21, 9.31 eV and 9.43 eV and a second sharp peak can be determined at 9.48 eV, which is also followed by a smaller peak at 9.53 eV and a broad band starting to rise at 9.58 eV. At lower photon energies, small features at 8.84 and 8.87 eV are visible.

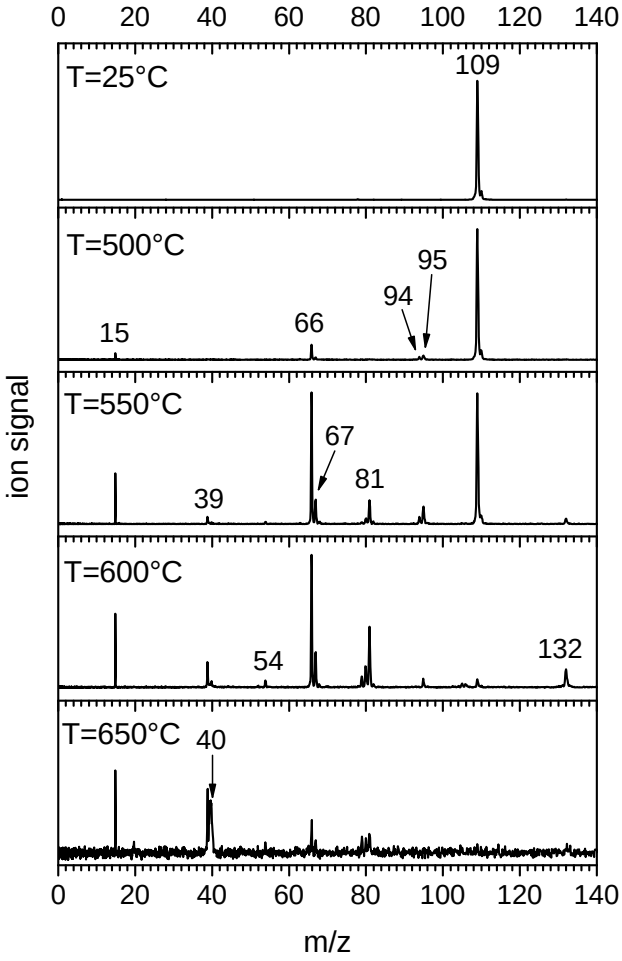


Figure 5.26.: Mass spectra of the precursor 3-methoxypyridine for different pyrolysis temperatures at a photon energy of 10.0 eV.

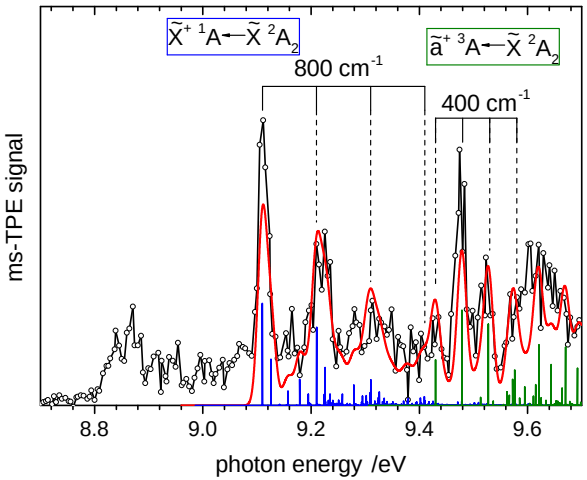


Figure 5.27.: Mass-selected TPE spectrum of m/z=66 and Franck-Condon simulation for the pyrrolyl radical (blue sticks: singlet ground state; green sticks: triplet first excited state; red line: Gaussian convolution fwhm=20 meV). The ionization energies for the two lowest cationic states were assigned to IE(X $^1$A)=9.11±0.02 eV and IE(a$^+$ $^3$A)=9.43±0.05 eV.

Computations on the CBS-QB3 level of theory predict an ionization energy of 9.17 eV for the X$^+$ $^1$A singlet ground state and an excitation energy 9.43 eV for the transition to the a$^+$ $^3$A first triplet state in the pyrrolyl cation. These values are in reasonable agreement with the observed prominent features in the spectrum. As both singlet and triplet cation are distorted non-planar molecules of $C_1$ symmetry with the nitrogen atom lying outside the $C_4$ plane, while the neutral ground state of pyrrolyl has $C_{2v}$ symmetry, excitation of the corresponding vibrational modes are expected to be resolved in the TPE spectrum. These would explain the ob-

served progressions with spacings of 800 and 400 $cm^{-1}$, respectively. To verify the assignment of the spectrum to the pyrrolyl radical, a Franck-Condon simulation was performed. Setting the IE of pyrrolyl to 9.11 eV and the excitation energy to the triplet ion to 9.43 eV results in a very good match of the experimental spectrum and the simulation, as visible in fig. 5.27. An error of 10 meV was added to the error of the photon energy resolution to consider the Stark shift and the ionization energy of the pyrrolyl radical is hence determined to be 9.11±0.02 eV. A larger error bar has to be assumed for the triplet energy, as shifting the simulation by 50 meV to an onset at 9.48 eV results also in a reasonable, though inferior match with the experiment. Hence, the excitation energy of the first triplet cation in pyrrolyl is assigned to be 9.43±0.05 eV. The simulated bands enable to assign the observed 800 $cm^{-1}$progression to the C-C stretching mode (B3LYP/6-311G(2d,d,p), unscaled: 808 $cm^{-1}$), which is visualized in fig. 5.28. Several other stretching modes of the ring backbone are computed to be active, mostly in combination bands, and explain the relatively high background level between the resolved progression bands. The 400 $cm^{-1}$ progression belonging to the triplet can be assigned to an out-of-plane ring deformation mode, in which the nitrogen atom moves out of the molecular plane. The latter mode was computed at 393 $cm^{-1}$. Further ring deformation and breathing modes are also computed to contribute to the observed TPE spectrum.

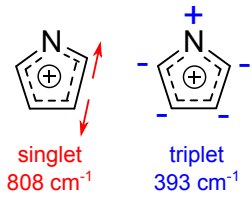


Figure 5.28.: Excited vibrational modes in the pyrrolyl TPE spectrum.

Contrary to the TPE spectrum of the isoelectronic cyclopentadienyl radical,[283,284] the electronic ground state of the pyrrolyl cation is a singlet and not a triplet state. The neutral X $^2E"_1$ ground state of cyclopentadienyl

has a $D_{5h}$ symmetry. The HOMO is a degenerate $\pi$-orbital of $e_1$" symmetry with three electrons. Ionization of the $5\pi$-radical thus leads to a cation with four $\pi$ electrons. Three electronic states are possible for this electron configuration: $^1A_1^{'}$, $^3A_2^{'}$, and $^1E_2^{'}$. As the cation with $D_{5h}$ symmetry is a Hückel antiaromatic molecule and therefore very unstable, the $^1E_2^{'}$ state is stabilized by a Jahn-Teller distortion. The bond lengths of the stabilized cation are no longer equal and the cation has an allylic character.[284] As the Jahn-Teller stabilization is lower than the electron-electron repulsion in the singlet state, the triplet cation is energetically favored in cyclopentadienyl. The nitrogen atom in pyrrolyl leads to a reduced symmetry ($C_{2v}$) and there exist hence no degenerate orbitals. The large nitrogen 2p orbital character of the $b_1$ orbital leads to a stabilization with respect to the $a_2$ orbital (see fig. 5.24).[276] Ionization of the pyrrolyl ground state therefore leads exclusively to a singlet cationic state. The equilibrium geometry of the ground state cation is also slightly distorted to avoid the antiaromatic character. The four $\pi$-electrons are therefore not fully delocalized over the complete ring system.

The Franck-Condon simulation for pyrrolyl does not explain the observed structure between 8.8 and 9.0 eV. Hot and sequence bands are expected to occur, but the energy difference to the 0-0 ionization transition is too large for this explanation. Hence, the contribution of one or several other isomers has to be considered. Quantum chemistry yielded sixteen further structures of the composition $C_4H_4N$, for which both neutral molecule and cation are stable. While all neutral isomers differ by less than 3.4 eV, only three isomers were found to have the same absolute energy as pyrrolyl, within the accurancy of the employed CBS-QB3 level: (E)-1-cyanoallyl, (Z)-1-cyanoallyl, and 2-cyanoallyl. While for the formation of 2-cyanoallyl, a CN- or $CH_2$ shift has to occur, only an H-atom-migration is necessary for each of the 1-cyanoallyl isomers. The Franck-Condon simulation of 2-cyanoallyl yields no convincing match with the experimental spectrum, although the ionization energy for

the singlet ground state (8.94 eV) was computed to be in the expected region. Fig. 5.29 shows the Franck-Condon simulations for (E)- and (Z)-1-cyanoallyl. The respective ionization energies were set to 8.84 eV (computed: 8.92 eV) and 8.87 eV (computed: 8.96 eV) for the (E)- and (Z)-isomer. Like this, the observed double peak structure can be explained. All considered $C_4H_4N$ isomers and their computed ionization energy are tabulated in the appendix D.

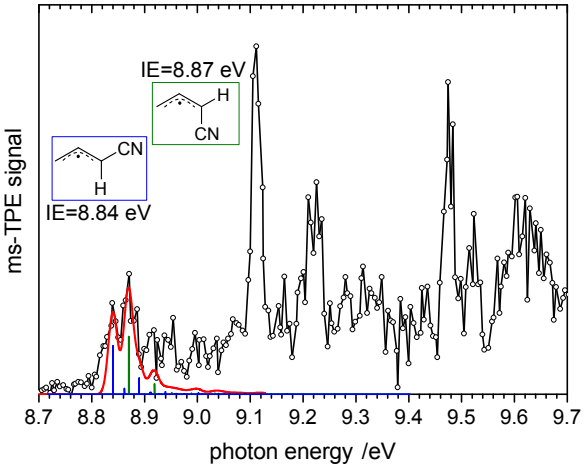


Figure 5.29.: Franck-Condon simulation for (E)- (blue sticks) and (Z)-cyanoallyl (green sticks), which are equally stable $C_4H_4N$ isomers as pyrrolyl (red line: Gaussian convolution fwhm=20 meV).

### 5.3.3. Pyrolysis Mechanism of 3-Methoxypyridine

Next to the m/z=66 signal observed in the mass spectra (cf. fig. 5.26), the peaks at m/z=15, 39, 40, 54, 67, and 81 could be identified as methyl,[50,120] propargyl,[51] cyanomethyl,[285] methylenecyclopropane,[286] pyrrole,[287] and N-methylpyrrole[288] from their respective threshold photoelectron spectra,

which have already been discussed extensively in the literature. The signal/noise ration in the TPE spectra of m/z=94 and 95 was very low. Hence, it can only be speculated that these belong to 3-oxypyridine (94), which is the corresponding side product upon methyl loss, and 3-hydroxypyridine (95), presumably formed by a bimolecular reaction of the former radical with hydrogen. The pyrolysis of 3-methoxypyridine obviously proceeds via a similar pathway as anisole, for which a subsequent loss of methyl and CO is reported.[279–281] According to CBS-QB3 computations, an energy of 272 kJ mol$^{-1}$ is needed for the methyl cleavage and the formation of 3-oxypyridine. The pathway for the CO loss, which proceeds via several intermediates and associated transtion states, is outlined in fig. 5.30. As in the decomposition of phenoxy, the first intermediate is a bicyclic structure, which is favored over an open chain presumably because of the delocalisation of the unpaired electron.[289] Two possibilities exist for the following opening of the three-membered ring since the presence of the nitrogen leads to an asymmetry in contrast to phenoxy, the first intermediate in the decomposition of anisole to cyclopentadienyl. Although the structure in which pyrrolyl is substituted in 2-position is 11.7 kJ mol$^{-1}$ more stable than the isomer substituted in 3-position, the transition state leading to the latter is lower in energy (201.4 kJ mol$^{-1}$ vs. 209.2 kJ mol$^{-1}$). Both intermediates lead however to the same products: pyrrolyl and CO. The CO loss reaction from 3-oxypyridine is endergonic by 62.6 kJ mol$^{-1}$. Compared to the formation of cyclopentadienyl from anisole,[289] slightly less energy is thus necessary for the generation of pyrrolyl, which is in agreement with the findings that pyrrolyl is already observed at relatively moderate pyrolysis temperatures. The first barrier in the pyrolysis mechanism of the precursor 3-methoxypyridine, i.e. the methyl loss leading to the oxy-radical, was computed to be 272.6 kJ mol$^{-1}$. This step's activation energy is therefore higher than for the subsequent pyrrolyl formation. Re-thermalization is hence likely to occur in the pyrolysis tube, which leads to prompt rearrangement of 3-oxypyridine in the sweet-spot of the reactor.[146] Consequently, it is highly

unlikely to observe the 3-pyridoxy radical which is in good agreement with our experimental findings and also observed similarly for phenoxy radicals formed from anisole.[290,291]

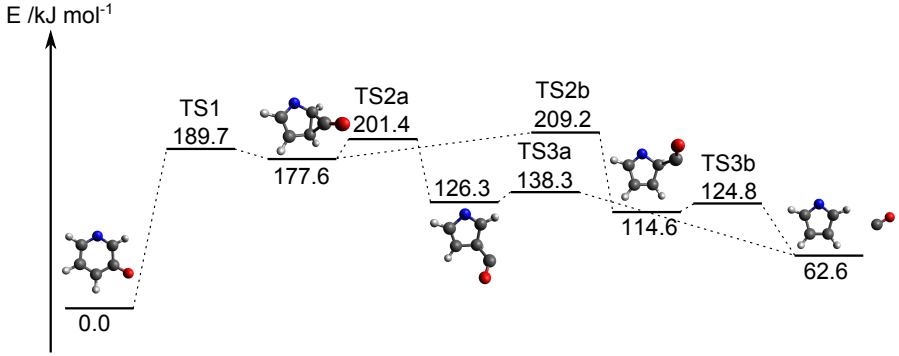


Figure 5.30.: Computed reaction pathway (CBS-QB3) from 3-pyridoxy to the pyrrolyl radical and CO. The rate is determined by the barriers to the transition states TS2a and TS2b.

As visible from fig. 5.26, the pyrrolyl radical seems to decompose only slightly above the temperature required for its first observation. At 10 eV, propargyl $C_3H_3$ and cyanomethyl $C_2H_2N$ (m/z=39 and 40) are identified from their TPE spectra, which are possible decomposition products. To check for the corresponding side products HCN (m/z=27) and $C_2H_2$ (m/z=26), mass spectra were recorded at higher photon energies because HCN ionizes only at 13.61 eV[292] and acetylene at 11.40 eV.[293] The right-hand spectrum of fig. 5.31 shows the mass spectrum at 12.0 eV, in which a peak at m/z=26 is clearly visible and can thus be assigned to acetylene. The cyano radical CN, which would also correspond to m/z=26, can be excluded, as its ionization energy is above 14 eV. The mass spectrum at a photon energy of 14.0 eV showed a very low signal/noise ratio since it is dominated by residual gases in the vacuum chamber and contains thus many false coincidences. Nevertheless

a small peak at m/z=27 was visible, verifying the formation of HCN.

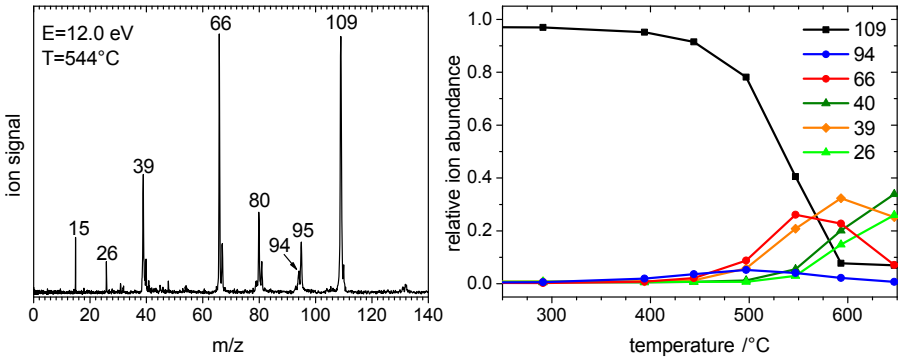


Figure 5.31.: Mass spectrum at a pyrolysis temperature of 544°C (left) and pyrolysis breakdown plot (right) of 3-methoxypyridine both at a photon energy of 12.0 eV.

On the left of fig. 5.31 the relative ion signals are plotted as a function of the pyrolysis temperature in a breakdown diagram for a photon energy of 12.0 eV. It illustrates that the methyl loss leading to m/z=94 is the primary step in the decomposition of 3-methoxypyridine being the first pyrolysis product mass observed. With the appearance of m/z=66 between 450 and 500°C, the 3-pyridoxy signal disappears again. The breakdown diagram is in agreement with the hypothesis that propargyl, cyanomethyl, and HCN originate from the further decomposition of pyrrolyl. The latter two rise simultaneously, which supports the assumptions that both have the same origin. The conclusions from the temperature dependent mass spectra on the pyrolysis mechanism of 3-methoxypyridine are summarized as a scheme in fig. 5.32.

The observed decomposition scheme of pyrrolyl is equivalent to the pyrolysis of cyclopentadienyl, which decomposes to acetylene and the propargyl radical.[280,281,291] The presence of a nitrogen atom in pyrrolyl leads to two decomposition pathway to HCN+propargyl or $C_2H_2$+cyanomethyl. Fig. 5.33

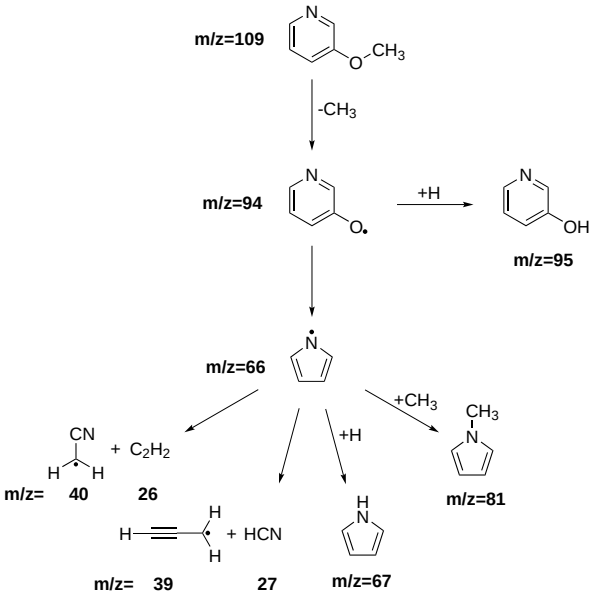


Figure 5.32.: Possible pyrolysis mechanism of 3-methoxypyridine, which explains the observations in the mass spectra.

shows the mechanisms leading to these products computed on CBS-QB3 level of theory. Both pathways are initiated by a [1,5] sigmatropic H-shift leading to cyclic $\sigma$-radical intermediates. Ring opening and C-N or C-C bond fission, respectively, yield the products, which are almost equally stable. The HCN+propargyl pathway, though, is associated with higher activation barriers and a less favored open chain intermediate. The positive mesomeric effect of the nitrogen atom next to the radical center increases the electron density at the radical center and therefore leads to a destabilization. The activation barriers for both decomposition pathways are about $120\,\mathrm{kJ\,mol^{-1}}$ and $50\,\mathrm{kJ\,mol^{-1}}$ lower than for the decomposition of $C_5H_5$ to acetylene and propargyl.[279,291,294] These computations show which effects influence the ca-

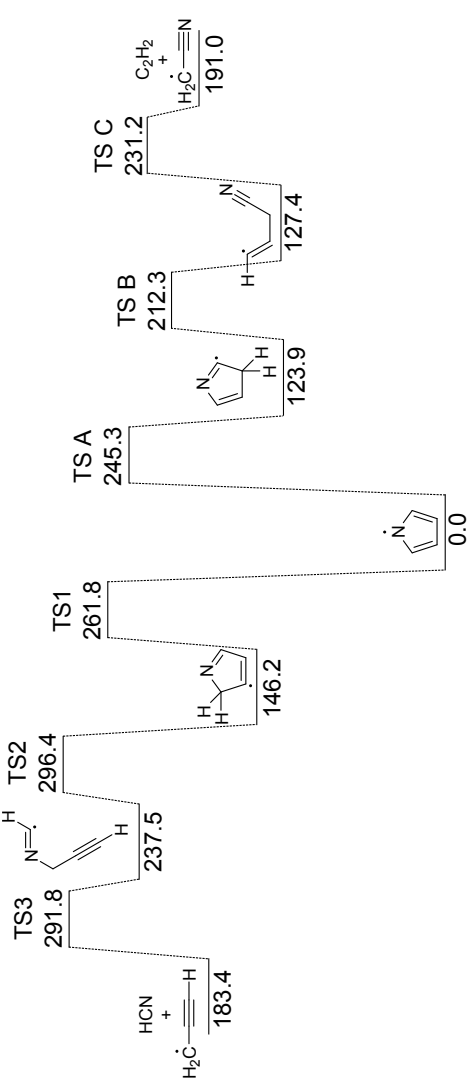


Figure 5.33.: Mechanism for the decomposition of the pyrrolyl radical upon pyrolysis computed on CBS-QB3 level of theory.

pability of a precursor to be converted successfully to a radical. Note that the activation barriers for the decomposition pathways are lower than the energy which has to be initially deposited into the precursor to cleave the methyl group. Although fast re-thermalization in the reactor is assumed, which leads to further decomposition of the first intermediates (*vide supra*), there are two reasons why the pyrrolyl radical is observed nevertheless. First, the tight transition states in the decomposition mechanism of the pyrrolyl radical increase the radical's lifetime at the same internal energy in comparison to the first intermediate, 3-pyridoxy, for which the potential wells in the pyrolysis mechanisms are shallower. Second, the internal energy of 3-pyridoxy divides between the pyrrolyl radical and the side products methyl and carbon monoxide. The internal energy of the pyrrolyl radical is lower than for the precursor at the same temperature. This shows that there is only a very narrow temperature range, for which the pyrrolyl radical can be successfully produced from 3-methoxypyridine. Precursors for which the activation barrier for the radical generation is only slightly higher would lead to an immediate decomposition of the radical due to re-thermalization and an observation of the radical would consequently be impossible.

### 5.3.4. DPI of 3-Methoxypyridine and Enthalpy of Formation of Pyrrolyl

Investigating the photoionization of the precursor used in pyrolysis experiments is crucial to check if the recorded TPE spectrum contains signal from dissociative photoionization processes. In addition, as discussed in sec. 2.5.1, thermochemical properties can be derived from these experiments via thermochemical cycles under certain circumstances. A conventional photoelectron spectrum of 3-methoxypyridine was recorded previously yielding a vertical ionization energy of 8.98 eV.[295] Fig. 5.34 shows the threshold photoelectron spectrum of 3-methoxypyridine recorded in 10 meV steps for the photon en-

ergy. For all precursor measurements, the sample was effusively introduced into the main chamber of the vacuum apparatus.

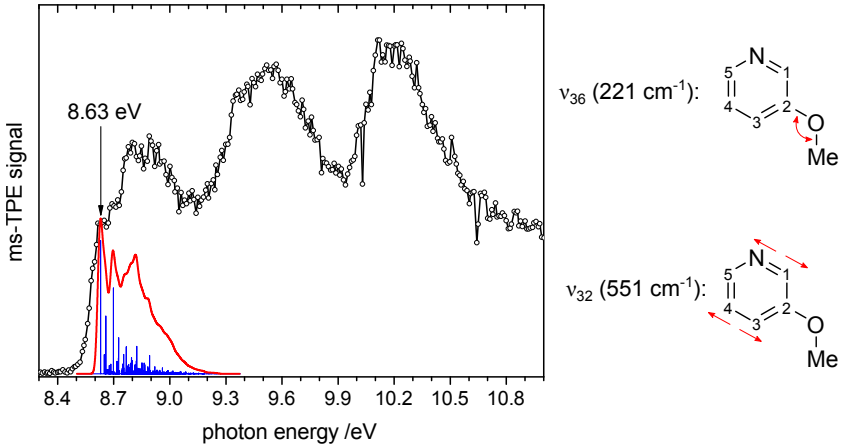


Figure 5.34.: Threshold photoelectron spectrum of 3-methoxypyridine. The ionization energy is assigned to 8.63±0.02 eV and the Franck-Condon simulation (blue sticks; red line: convolution with Gaussian fwhm=30 meV) reproduces the onset and the position of the observed steps in the TPE signal. The vibrational modes with the highest Franck-Condon activity are depicted on the right. The broad bands centered around 9.5 and 10.2 eV arise from transitions to excited states in the cation.

A sharp onset is observed at 8.5 eV in the TPE spectrum of 3-methoxypyridine and a first step in the TPE curve is visible at 8.63 eV. The spectrum features a second step at 8.70 eV (+565 $cm^{-1}$) and three broad bands are visible centered around 8.9, 9.5, and 10.2 eV. Computations on CBS-QB3 level of theory yield an ionization energy of 8.64 eV. A Franck-Condon simulation for transitions between the neutral and cationic ground state, which is also included in fig. 5.34, predicts a sharp peak for the 0-0 transition. The adiabatic ionization energy of 3-methoxypyridine is therefore assigned to be IE=8.63±0.02 eV.

The spectrum is significantly red shifted by 350 meV in comparison to the previously reported one.[295] The step in the TPE spectrum at 8.70 eV can be assigned to the fundamental band of the $\nu_{32}$ ring deformation in the cation computed at 551 $cm^{-1}$ (B3LYP/6-311G(2d,d,p)). According to the DFT optimized geometries, the C1-C2, C2-C3, C4-C5, and C5-N bonding distances (see fig. 5.34 for atom numbering) are elongated by between 0.5 and 4.8 pm, while the N-C1 and C3-C4 bonds are shortened by 1.6 pm and 2.5 pm, respectively, upon ionization. This explains the Franck-Condon activity of the associated ring deformation mode. In additon, the C2-O-C(methyl) bonding angle widens by 4.5° upon ionization, which is why large Franck-Condon factors are computed for transitions to excited states of the $\nu_{36}$ COC-bending mode. TD-B3LYP/6-311G(d,p) computations predict four electronically excited states of the cation within 3 eV of the ground state (+0.55, +1.51, +2.98, +3.08 eV). The broad bands at 8.9, 9.5 and 10.2 eV can hence be assigned to these excited states.

At higher photon energies, the precursor dissociatively ionizes as illustrated in fig. 5.35. The parent ion has completely vanished at 12.75 eV and four daughter ions at m/z=108, 94, 79, and 66 are visible. A small peak at m/z=39 is visible at 14.00 eV, which grows at even higher photon energies.

As discussed in the methods section, the appearance energies of the daughter ions can be determined by modeling the breakdown diagram, in which the relative abundances of the parent and daughter TPE signals are plotted against the photon energy. As the mass resolution of the iPEPICO spectrometer is not high enough to disentagle the m/z=108 daughter ion peak from the m/z=109 parent ion peak, the change of the parent peak's center of gravity $\mu$ was used to determine the branching ratio between parent and the 1 amu lighter daughter.[296] The center of gravity of the parent peak was identified by considering the time of flight region comprising both the m/z=108 and 109 signal. The resulting centers of gravity were then plotted versus the photon

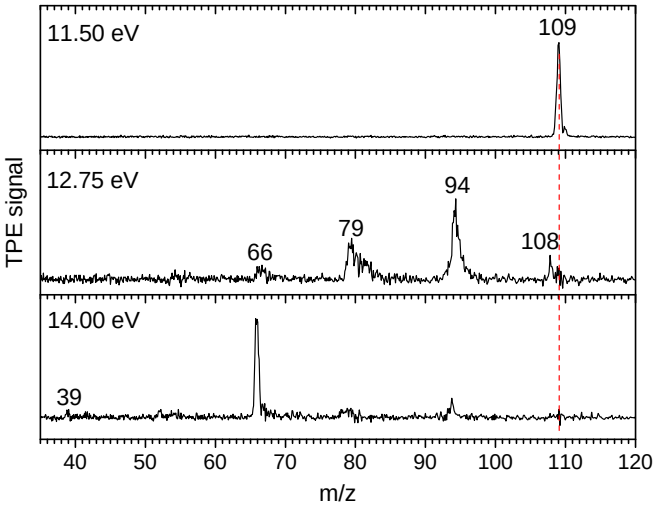


Figure 5.35.: TPE mass spectra of 3-methoxypyridine at 11.50, 12.75, and 14.00 eV. The disappearance of the precursor and simultaneous appearance of new mass peaks indicates dissociative photoionization.

energy as shown in fig. 5.36, in which a fit of the experimental data with a sigmoidal function (OriginPro: 'Boltzmann' fitting function) is also shown.

The branching ratio $a$ between the parent and daughter ion peak with the arrival times $t_1$ and $t_2$ can then be obtained from the center of gravity using the following equation:

$$\mu = at_1 + (1 - a)t_2 \tag{5.2}$$

Following this procedure, the complete breakdown diagram for the dissociative photoionization of 3-methoxypyridine between 11.5 and 16.0 eV is obtained as depicted in fig. 5.37.

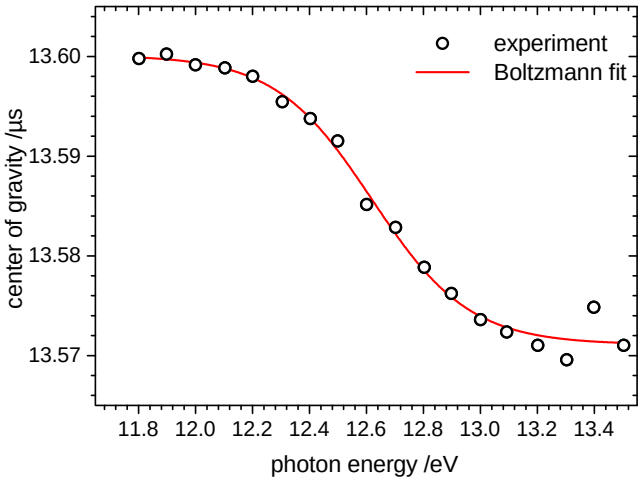


Figure 5.36.: Center of gravity of the parent ion peak as a function of the photon energy. The time of flight decreases with the photon energy because of dissociative photoionization. The red line shows a fit with a sigmoidal function.

The parent cation 3-methoxypyridinium (m/z=109) signal starts to decrease at a photon energy of about 11.7 eV. Simultaneously, three new mass channels appear in the breakdown diagram. The channel of m/z=108 correponds to the hydrogen loss, which has already been discussed above. In addition, m/z=94, which matches a loss of $CH_3$, and m/z=79, which has to go along with a 30 amu neutral fragment, i.e. $CH_2O$, appear. At around 12.5 eV the former three mass channels start to disappear again and the rise of m/z=66, which corresponds to the mass of the pyrrolylium cation, is observed. As the slopes of the abundance curves in the breakdown diagram are rather shallow, this channel is assumed to be also a competing parallel pathway of the dis-

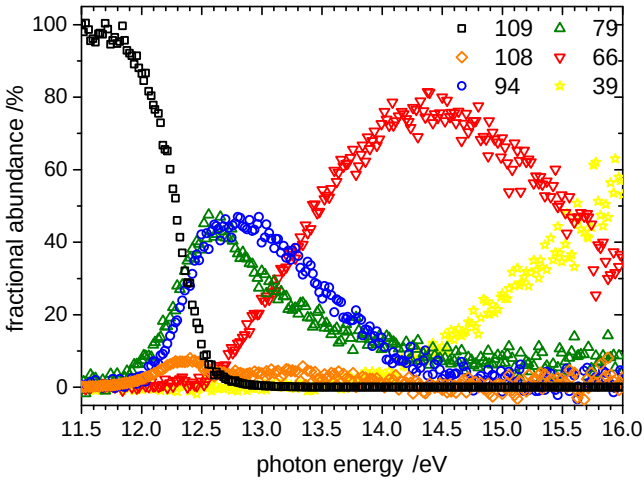


Figure 5.37.: Breakdown diagram for the DPI of 3-methoxypyridine.

sociation channels to the other three daughter ions and not a sequential one. The m/z=66 recedes again at around 14.5 eV and a new channel corresponding to m/z=39 opens up. The latter channel is most probably a sequential dissociation from the m/z=66 daughter ion and therefore corresponds to the loss of a 27 amu neutral fragment, i.e. HCN, leading to $C_3H_3^+$.

The respective dissociation channels and pathways were computed on CBS-QB3 level of theory, as vibrational frequencies and rotational constants of the dissociating ions, transition states and products are necessary to fit the breakdown diagram employing statistical rate theory (see sec. 2.5.2). Only the first four parallel dissociation channels, i.e. m/z=108, 94, 79, and 66, were considered because this work's focus was on the m/z=66 ion, as it promised further information on the pyrrolyl radical. Fig. 5.38 shows the computed dissociation pathways for these channels and the associated energies. The pathways for the

formation of the daughter ions m/z=108 and m/z=94 can be described by simple dissociation steps, which are not associated with reverse barriers. Hydrogen loss on the methyl group is favored over a loss of one of the ring hydrogen atoms and the appearance energy for m/z=108 is computed to be $AE_{calc}$(3-methoxypyridine; 3-methylene-pyridoxy$^+$)=11.43 eV. The CBS-QB3 value for the methyl loss is $AE_{calc}$(3-methoxypyridine; 3-pyridoxy$^+$)=11.73 eV. As the m/z=79 channel corresponds to a loss of formaldehyde, $H_2CO$ (30 amu), and therefore leads to the pyridine cation, a hydrogen transfer from the methyl group to the ring carbon in *meta* position has to occur. This H atom migration is associated with a transition state, which, according to the computations, directly leads to the m/z=79 daughter ion. The appearance energy of the m/z=79 daughter is therefore defined by this transition state and is computed to be $AE_{calc}$(3-methoxypyridine; pyridine$^+$)=11.73 eV. For a parallel dissociation channel leading to m/z=66 corresponding to a loss of a $C_2H_3O$ (43 amu), i.e. $COCH_3$ or CO+$CH_3$, a rearrangement of the dissociating ion to a five-membered ring system has to take place first. The computations predict a structure in which the carbon atom in 2-position of the five-membered ring is substituted as depicted in fig. 5.38 to be thermodynamically favored. This structure lies 10.95 eV above the neutral 3-methoxypyridine. The transition state for the formation of this intermediate ion is computed to lie at 11.77 eV and cleavage of $COCH_3$ leads to the pyrrolylium cation (m/z=66). Although the computations find a minimum structure for a $COCH_3$ neutral fragment, the corresponding appearance energy of 14.67 eV is significantly higher than the observed onset in the breakdown diagram in fig. 5.37. A relaxed scan on B3LYP/6-31G(d) level of theory of the O-$CH_3$ coordinate reveals that the potential energy well is very shallow in $COCH_3$ and the activation barrier leading to the dissociation to CO and $CH_3$ is only 26 meV (2.5 kJ mol$^{-1}$), which is beyond the accuracy for DFT computations. Dissociation to the m/z=66 daughter ion is therefore assumed to lead to the formation of two neutral fragments: carbon monoxide and the methyl radical. This dissociation proceeds along a

barrierless reaction coordinate and the appearance energy for pyrrolylium is computed to be $AE_{calc}$(3-methoxypyridine; pyrrolyl$^+$)=12.65 eV.

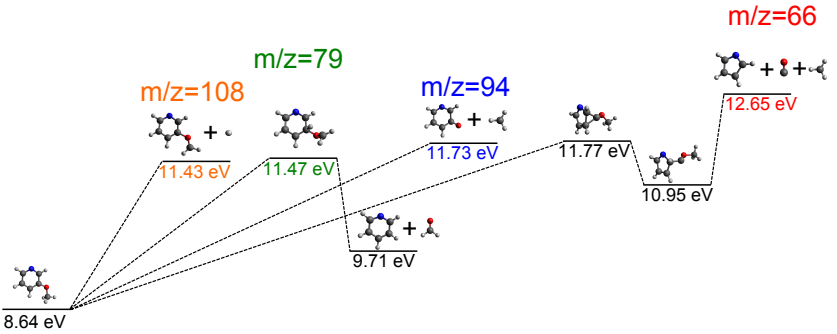


Figure 5.38.: Dissociative photoionization channels of 3-methoxypyridine computed on CBS-QB3 level of theory.

As visible in fig. 5.35 the daughter ion peaks in the TPE mass spectra are broad and asymmetric. Hence, a simultaneous fit of the breakdown diagram and the time of flight distributions is necessary, as the dissociation rates are slow. As RRKM is known to underestimate appearance energies for pathways with slow rate constants and therefore large kinetic shifts,[297] SSACM was hence used for the channels leading to m/z=108, 94, and 66. RRKM theory was employed for the dissociation pathway leading to m/z=79 because this pathway is associated with a large reverse barrier of 760 meV (73 kJ mol$^{-1}$), i.e. a tightly bound transition state, which is why SSACM is not applicable. The isomerization in the pathway leading to m/z=66 was neglected in the model as the isomerization transition state lies significantly below the dissociation threshold.

The fit of the experimental breakdown curve and time of flight distributions is shown in fig. 5.39 and 5.40, respectively. Both show a very good agreement of theory and experiment. The slight deviations in the m/z=108 breakdown curve owes presumably the empirical derivation of the TPE signal and the

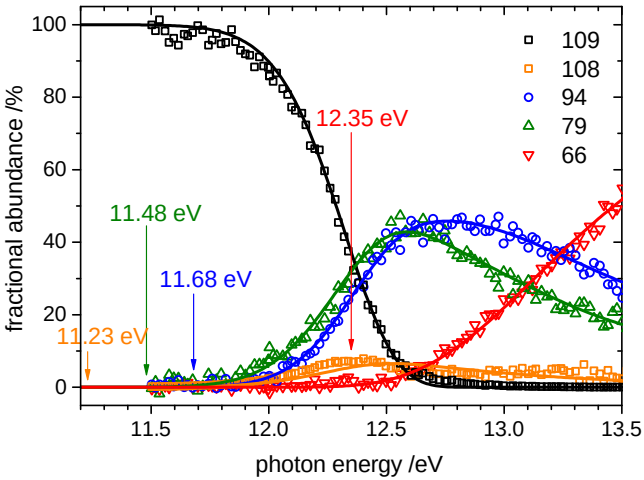


Figure 5.39.: Experimental (symbols) and fitted (lines) breakdown diagram of 3-methoxypyridine.

overall small fractional abundance of this channel in the breakdown diagram and TOF spectra, which makes modeling more difficult. The fitted appearance energies are summarized in tab. 5.5 and compare well with the values computed on CBS-QB3 level of theory. The accuracy of the fitted appearance energy was determined by varying one barrier height and fitting all other parameters. The highest and lowest barrier, for which an acceptable fit was still obtained, represent the limits of the appearance energies' error bars. An acceptable fit was defined in this case as a fit, for which the goodness of the fit value of the MinimalPEPICO program is lower than 115 % of the goodness of the fit value, which is obtained when all barriers are fitted simultaneously.

Dissociative photoionization of the precursor 3-methoxypyridine does not contribute to the recorded TPE spectrum of the pyrrolyl radical since the ap-

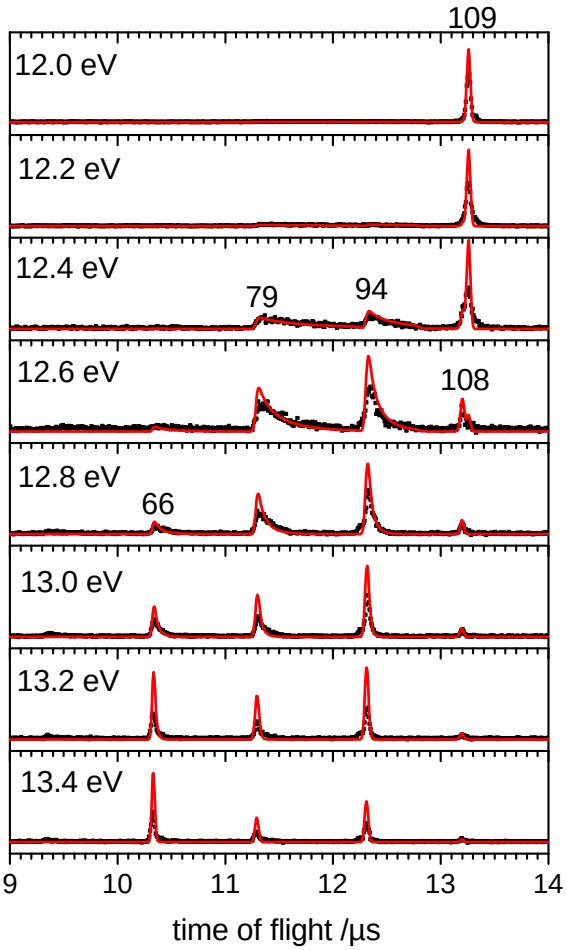


Figure 5.40.: Experimental (black squares) and fitted (red lines) time of flight distributions of 3-methoxypyridine.

Table 5.5.: Fitted and computed (CBS-QB3) appearance energies for the dissociative photoionization of 3-methoxypyridine.

| m/z (daughter ion) | $AE_{fit}$ | $AE_{calc}$ | $\Delta E$ |
|---|---|---|---|
| 108 | 11.23±0.25 eV | 11.39 eV | -0.16 eV |
| 94 | 11.68±0.05 eV | 11.73 eV | -0.05 eV |
| 79 | 11.48±0.02 eV | 11.47 eV | +0.01 eV |
| 66 | 12.35±0.03 eV | 12.65 eV | -0.30 eV |

pearance energy for pyrrolyl cation is $AE_{0K}$(3-methoxypyridine; pyrrolyl$^+$)= 12.35±0.03 eV and therefore well above the recorded spectral range. The computations illustrated in fig. 5.38 show that dissociative photoionization to the pyrrolyl cation is not associated with a reverse barrier. Derivation of thermochemical properties via a thermochemical cycle as depicted in fig. 5.41 is therefore possible.

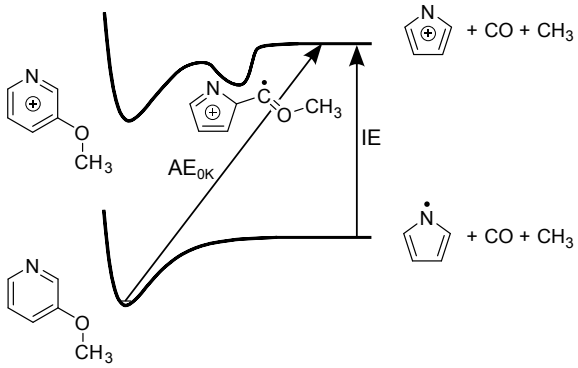


Figure 5.41.: Thermochemical cycle for the formation of pyrrolyl from 3-methoxypyridine.

As the ionization energy of the pyrrolyl radical and the appearance energy of the pyrrolyl cation from the precursor are known, the enthalpy of formation of the pyrrolyl radical $\Delta_f H^0_{0K}(C_4H_4N)$ can be derived provided that the heats of formation for the precursor $\Delta_f H^0_{0K}(C_6H_7NO)$ and the neutral fragments ($\Delta_f H^0_{0K}(CH_3)$ and $\Delta_f H^0_{0K}(CO)$) are also known.

$$\begin{aligned}\Delta_f H^0_{0K}(C_4H_4N) &= \Delta_f H^0_{0K}(C_6H_7NO) + AE_{0K}(C_4H_4N^+) \\ &\quad -\Delta_f H^0_{0K}(CH_3) - \Delta_f H^0_{0K}(CO) - IE(C_4H_4N)\end{aligned} \tag{5.3}$$

While for methyl and carbon monoxide experimental values for the enthalpy of formation at 0 K are tabulated (149.03±0.10 and -113.81±0.17 kJ mol$^{-1}$, respectively),[298] the enthalpy of formation for the precursor 3-methoxypyridine was only estimated from a transfer of the mean value for methoxy substitution for methoxybenzene, 3-methoxybenzoic acid and *trans*-3-methoxycinnamic acid to a substitution of pyridine in *meta* position.[299] The obtained value for the molar enthalpy of formation of 3-methoxypyridine at room temperature is $\Delta_f H^0_{298K}(C_6H_7NO)$=-10.8±5.1 kJ mol$^{-1}$. The enthalpy of formation can be converted to 0 K when considering the enthalpy corrections for the molecule $[H_{298K} - H_{0K}]_{molecule}$ and for the constituent elements $[H_{298K} - H_{0K}]_{elements}$.[298]

$$\Delta_f H^0_{0K} = \Delta_f H^0_{298K} - [H_{298K} - H_{0K}]_{molecule} + [H_{298K} - H_{0K}]_{elements} \tag{5.4}$$

Experimental values were used for the enthalpy correction of the constituent elements,[300] while for the enthalpy correction for the precursor the translational, rotational and vibrational contributions for a nonlinear polyatomic molecule were considered:[298]

$$H_{298K} - H_{0K} \simeq \frac{5}{2}k_B T + \frac{3}{2}k_B T + \sum_{vib} \frac{h\nu}{\exp(h\nu/k_B T) - 1} \tag{5.5}$$

Here $k_B$ is the Boltzmann constant, $T$ the temperature, i.e. 298 K, $h$ is the Planck constant and $\nu$ are the vibrational frequency of the 39 normal modes of 3-methoxypyridine computed at the B3LYP/6-311G(2d,d,p) level of theory. Following this procedure, a 0 K enthalpy of formation of $\Delta_f H^0_{0K}(C_6H_7NO)$= 23.75 kJ mol$^{-1}$ was obtained and an error margin of ±10.00 kJ mol$^{-1}$ was assumed. Inserting this value, the experimental appearance energy of the pyrrolyl cation $AE_{0K}(C_4H_4N^+)$=12.35±0.03 eV= 1191.6±2.9 kJ mol$^{-1}$ and the ionization energy $IE(C_4H_4N)$=9.11±0.02 eV=879.0±1.9 kJ mol$^{-1}$ determined from the TPE spectrum in eq. (5.3) yields an enthalpy of formation for pyrrolyl radical of $\Delta_f H^0_{0K}(C_4H_4N)$ =+301.1±15.1 kJ mol$^{-1}$. This value is in perfect agreement with the enthalpy of formation determined previously by Ashfold and co-workers (301.9±0.5 kJ mol$^{-1}$)[275] and proves that iPEPICO is a suitable tool to determine thermochemical properties of elusive species.

### 5.3.5. Summary Pyrrolyl

3-Methoxypyridine was found to be a suitable precursor for the pyrolytic generation of the pyrrolyl radical $C_4H_4N$ in its electronic ground state. Pyrrolyl has a non-aromatic, $C_{2v}$-symmetric ground state with five $\pi$-electrons with the irreducible representation $^2A_2$, which is isoelectronic to cyclopentadienyl $C_5H_5$. The nitrogen lone pair is a $\sigma$-orbital, which lies in the ring plane. Pyrolysis of 3-methoxypyridine leads to 3-oxypyridine in the first step, which further decomposes to the pyrrolyl radical and carbon monoxide. The TPE spectrum of the pyrrolyl radical was recorded and the ionization energy was assigned to IE=9.11±0.02 eV. An 800 cm$^{-1}$ vibrational progression was observed for the singlet cation ground state and assigned to a ring deformation mode. In addition, the excitation energy to the $a^+\ ^3A_2$ triplet state was determined to be 9.43±0.05 eV. The TPE spectrum features a progression, in which the components are spaced by 400 cm$^{-1}$, for the triplet cation. The pyrolysis of 3-methoxypyridine at 550°C does not exclusively lead to the cyclic

$C_4H_4N$ isomer, which is why further features are visible in the mass-selected TPE spectrum for m/z=66. This structure could be assigned to (E)- and (Z)-1-cyanoallyl, which are computed to be equally stable as the pyrrolyl radical. Ionization energies of IE((E)-1-cyanoallyl)=8.84±0.02 eV and IE((Z)-1-cyanoallyl)=8.87±0.02 eV were determined. It was furthermore observed that two fragmentation channels of the pyrrolyl radical exist leading either to cyanomethyl+acetylene or propargyl+HCN. A computational study of the decomposition mechanism of the precursor and of the radical was conducted. In addition, the photoionization of the precursor molecule 3-methoxypyridine was studied. The ionization energy of 3-methoxypyridine was assigned to be 8.63±0.02 eV from the TPE spectrum. Dissociative photoionization to five daughter ions (m/z=108, 94, 79, 66, and 39) was observed up to a photon energy of 16.0 eV and the appearance energies of the first four daughter ions, which constitute competing parallel dissociation channels were determined employing statistical rate theory. As the dissociation to the pyrrolyl cation m/z=66 does not include a reverse barrier, the enthalpy of formation for the pyrrolyl radical at 0 K could be derived via a thermochemical cycle and a value of $\Delta_f H^0_{0K}(C_4H_4N)$=+301.1±15.1 kJ mol$^{-1}$ was obtained.

## 5.4. Pyrolysis of 3-Bromopyridine

Second after pyrrolic functionalities, 20-40 % of the nitrogen in coal is found to be bound in pyridinic structures.[2] The pyrolysis of pyridine, which can thus be seen as a model system for these functionalities, has been thoroughly investigated.[29–31] The primary step in the pyrolysis of pyridine is found to be a hydrogen abstraction leading to one of the three pyridyl radical isomers. As the unpaired electron in these radicals is located in a $\sigma$-orbital, they are very reactive and therefore have short lifetimes. They have been isolated in matrices, in which ESR[301] and IR[302] spectroscopy was conducted. Recently, though in low yields, 2-pyridyl was also successfully produced in the gas phase by photolysis experiments on 2-chloropyridine and 2-bromopyridine conducted by Zhang and co-workers.[303] Because of their high reactivity, pyridyl radicals fragment further. Experiments[29,31] and computations[304] showed that a further H abstraction leads to a molecule of the composition $C_5H_3N$, which is assumed to be the open-chain cyanovinylacetylene. This molecule was observed in the photodissociation of 2-pyridyl, which had been generated by photolysis of 2-chloropyridine.[303] Photoion yield curves of cyanovinylacetylene have already been recorded yielding an IE of 9.33±0.05 eV, which is reported to be in exact agreement with B3LYP/6-31G(d) computations.[29,31] The microwave spectrum of cyanovinylacetylene was also measured in previous studies, as carbon chains with cyano groups have been identified as astronomically relevant molecules.[305] In the following, the pyrolysis of 3-bromopyridine, which is assumed to be a precursor for the 3-pyridyl radical and its further fragmentation products, is discussed. Although the vapor pressure of 3-bromopyridine is very low, the precursor was installed outside the vacuum chamber, but heated to 50°C. 3-bromopyridine was then seeded in only 1.0 bar of argon. The lower background pressure reduces the upper limit for the beam velocity prior to the expansion and therefore leads to relatively long residence times of the precursor and the generated products in the heated zone. Milder conditions

usually suited better for radical generation by flash pyrolysis resulted in very low signal/noise ratio, which did not enable a reliable data analysis.

### 5.4.1. Hydrocarbon Pyrolysis Products

Halogenated molecules have proven to be very efficient precursors for generation of hydrocarbon radicals upon pyrolysis (e.g. ref.[49,51,306,307]). While a very high pyrolysis temperature is necessary for cleaving the carbon-halogen bond in chlorinated precursors, iodides have the disadvantage that elemental iodine will be produced as a side product, which has a low ionization energy and a high photoionization cross section, and therefore often leads to a large number of false coincidences in the PEPICO experiment. Thus, 3-bromopyridine was assumed to be the most promising precursor to investigate the 3-pyridyl radical and its subsequent decomposition. An ionization energy of 9.75 eV was determined for 3-bromopyridine by electron-impact ionization.[308] Fig. 5.42 shows the room temperature TPE spectrum recorded at the SLS storage ring. The first peak maximum is observed at 9.34 eV and can be assigned to the ionization energy. The previously reported value is therefore revised. This is in reasonable agreement with CBS-QB3 computations, in which a value of 9.43 eV is obtained. A Franck-Condon simulation of the photoelectron spectrum is also depicted in fig. 5.42, which reproduces well the peak structure in the experimental spectrum. The observed bands can be assigned to excitations of ring deformation modes in the cation, as the computations predict that the ring structure changes significantly upon ionization: While the neutral molecule is planar (point group $C_s$), the cation features dihedral angles of about 5°. A deviation of simulation and experiment is noticed at higher photon energies. Here, a number of overtones and combination bands are expected. As the simulation computes only a finite number of transitions, the simulation does not reproduce the experimental spectrum correctly at high photon energies.

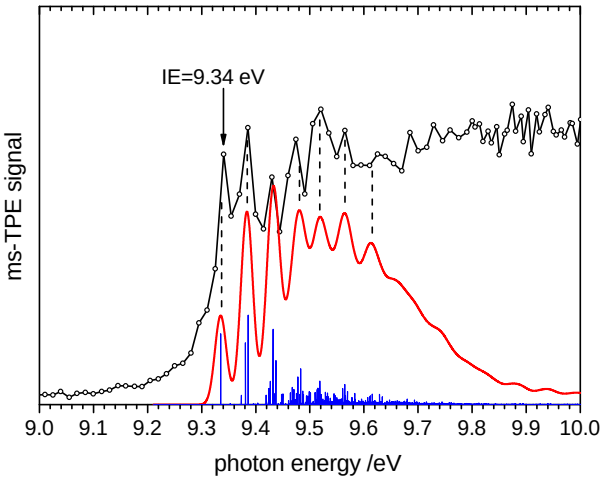


Figure 5.42.: Threshold photoelectron spectrum and Franck-Condon simulation (blue sticks, red lines: Gaussian 25 meV) of 3-bromopyridine. The ionization energy can be determined 9.34±0.02 eV. Figure reprinted from ref. [309], Copyright (2015), with permission from Elsevier.

Cleavage of the C-Br bond in 3-bromopyridine requires a high pyrolysis temperature. Fig. 5.43 shows that even at a pyrolysis power of 65 W, which corresponds to a temperature of approximately 1000°C, the precursor is still prominently visible in the mass spectrum. In addition, a number of peaks in the lower m/z region occur.

The 3-pyridyl radical has the m/z ratio 78. A small peak for this value is observed in the mass spectrum and will be discussed later (sec. 5.4.2). In the following, the mass-selected TPE spectra of the other peaks, depicted in fig. 5.44, are discussed first.

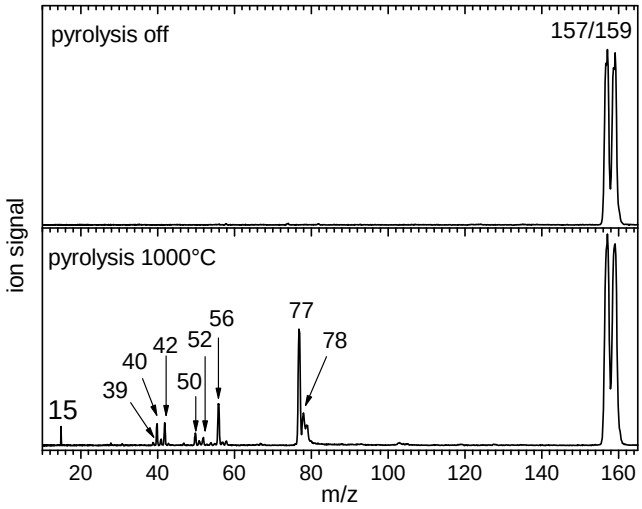


Figure 5.43.: Mass spectra at 10.5 eV with pyrolysis turned off (upper panel) and an estimated pyrolysis temperature of 1000°C (pyrolysis power: 65 W). Figure reprinted from ref. [309], Copyright (2015), with permission from Elsevier.

The mass-selected TPE spectrum of m/z=15 is a perfect match with the methyl spectrum since the intense peak at 9.84 eV coincides with the reported ionization energy of $CH_3$. [50,120] As the precursor does not contain a methyl group, it is assumed that $CH_3$ is produced by a subsequent decomposition of another primary pyrolysis product. At 8.70 eV, a distinct peak is observed in the ms-TPE spectrum of m/z=39, which can therefore be assigned to the propargyl spectrum. [51] The mass peak m/z=40 does not originate from a single $C_3H_4$ isomer. The mass-selected TPE features a progression setting in around 9.7 eV, which can be assigned to the excitation of the torsional mode in allene. [126] The sharp peak at 10.37 eV corresponds, however, to the ion-

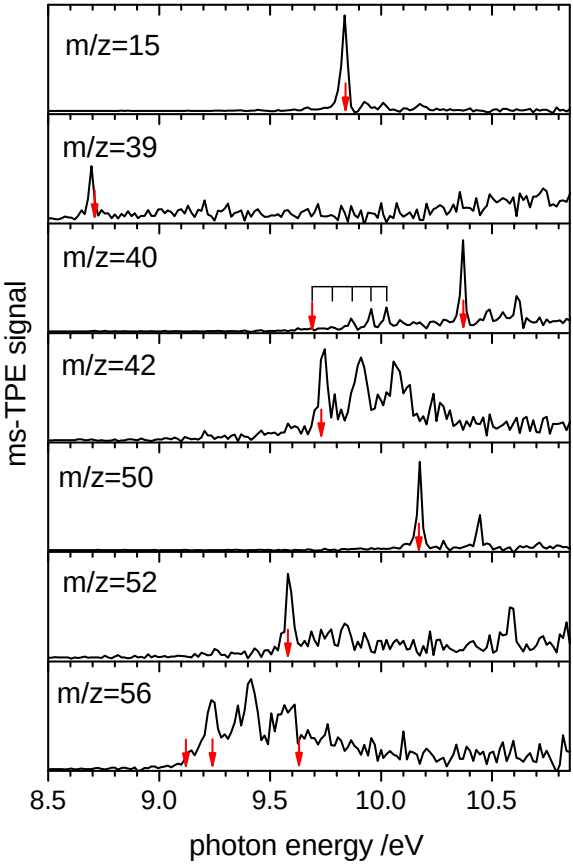


Figure 5.44.: Mass-selected TPE spectra of 3-bromopyridine's pyrolysis products. With the help of these spectra, the peaks in the mass spectrum can be assigned to methyl (15), propargyl (39), allene and propyne (40), propene (42), 1,3-butadiyne (50), vinylacetylene (52), and the three isomers of butene (56).

ization energy of propyne,[310] for which also vibrational structure is resolved in the spectrum. The m/z=42 TPE spectrum identifies the corresponding mass peak as propene $C_3H_6$ since the spectrum features a peak at 9.74 eV, which is, as well as the observed C=C progression, in very good agreement with high resolution ZEKE-PFI studies.[311] Another pyrolysis product is diacetylene (m/z=50), for which an ionization energy of 10.17 eV is determined and the excitation of the symmetric C≡C triple bond stretching mode with a wavenumber of 2200 $cm^{-1}$ is observed as reported in the literature.[312,313] Pyrolysis of 3-bromopyridine leads in addition to the formation of vinylacetylene as proves the ms-TPE spectrum for m/z=52. A peak at 9.59 eV is observed, which corresponds to the reported ionization energy of vinylacetylene.[313] The most intense peak in the mass spectrum shown in fig. 5.43 is m/z=56. The sharp ionization onset at 9.25 eV and the observed progression of the C=C stretching mode at about 1400 $cm^{-1}$ are in good agreement with previous spectra of isobutene, in which an ionization energy of 9.24 eV was reported.[314] However, small contributions of the other two $C_4H_8$ isomers 1-butene and 2-butene with ionization energies of 9.63 and 9.12 eV cannot be excluded.[313]

The mass spectrum in fig. 5.43 features in addition peaks at m/z=77 and 78, which can be assigned to ions of the composition $C_5H_3N$ and $C_5H_4N$, respectively. As both peaks belong to structures comprising a nitrogen atom and the threshold photoelectron spectra of those molecules have not yet been studied, the corresponding TPE spectra will be discussed in more detail in the next section.

### 5.4.2. TPE Spectrum of Cyanovinylacetylene

Pyrolysis of 3-bromopyridine results in a mass peak at m/z=77, which must therefore correspond to a molecule of the composition $C_5H_3N$. Its generation can be explained by the elimination of HBr from the precursor or, more likely, by the initial cleavage of a bromine atom leading to the 3-pyridyl radical, from

which then a hydrogen atom is eliminated. Possible mechanisms for the latter pathway for the formation of four different isomers which fulfill the postulated sum formula are depicted in fig. 5.45. Note that no H-atom migration is necessary for these mechanisms. Direct cleavage of hydrogen from 3-pyridyl can lead to 2,3-didehydropyridine (A) or 3,4-didehydropyridine (B). By contrast, an initial ring scission step might also be possible, which is followed by the hydrogen elimination. This leads to cyanovinylacetylene (C) or N-2-propynylidene-ethynamine (D). Liu *et al.* computed the decomposition of the 3-pyridyl radical on QCISD(T)/cc-pVDZ level of theory and found cyanovinylacetylene to be the thermodynamically favored product with an activation barrier of 295 kJ mol$^{-1}$.[304] The activation barrier for the dissociation to the didehydropyridines A and B is reported to be 66 and 44 kJ mol$^{-1}$ higher, while for channel D 173 kJ mol$^{-1}$ more energy is needed.

The mass-selected TPE spectrum of m/z=77 was used to identifiy the isomer, which is generated upon pyrolysis of 3-bromopyridine. The spectrum was recorded with a step size of 15 meV, an acquisition time of four minutes per data point and a pyrolysis power of 65 W. As no thermocouple was used to measure the pyrolysis temperature, it can only be estimated to have been about 1000°C based on previous experiments. The upper panel of fig. 5.46 shows the obtained spectrum. A very distinct peak with a maximum at 10.04 eV is visible, followed by several less intense bands at 10.20, 10.30, 10.55, 11.08, and 11.17 eV. The ionization energy of the observed species can thus be assigned to 10.04±0.02 eV. For the $C_5H_3N$ isomers proposed in fig. 5.45, only for cyanovinylacetylene an ionization energy has been reported previously.[29,31] The value of 9.33 eV was however obtained only from a flame PIMS experiment, which is much less accurate than threshold photoelectron spectroscopy. Therefore quantum chemistry was employed to compare the computed ionization energies of the different isomers with the experimentally determined value.

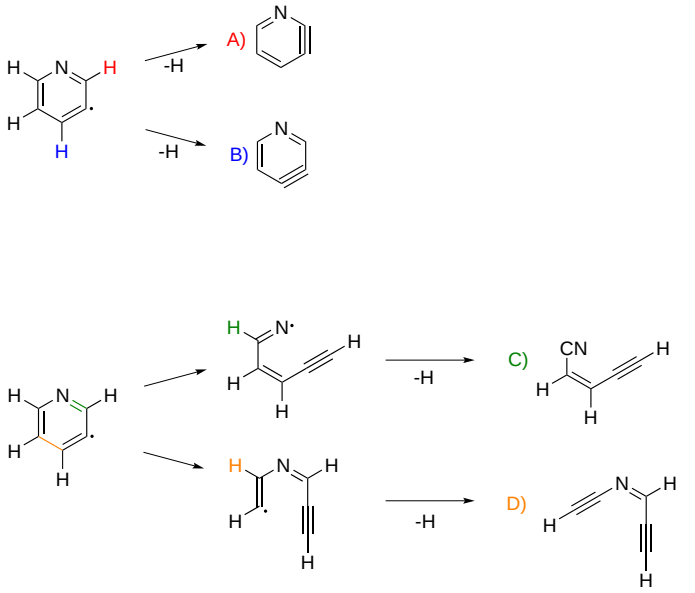


Figure 5.45.: Possible mechanisms for the formation of $C_5H_3N$ isomers from the 3-pyridyl radical. Isomers A) and B) can be formed by direct H-elimination, while the mechanisms of C) and D) involve a ring scission and a subsequent H-elimination step. For the latter two structures only the *cis* stereoisomer is shown. The eliminated hydrogen atoms or cleaved bonds are accentuated by color.

As can be seen in table 5.6, the computed IEs of the two cyanovinylacetylene stereoisomers are in good agreement with the observed onset at 10.04 eV. On an absolute energy scale, the *trans* isomer is 23 meV (2.2 kJ mol$^{-1}$) more stable than the *cis* one (CBS-QB3 computations). Nevertheless, Franck-Condon simulations for both stereoisomers were performed and compared with the experimental spectrum, as depicted in the lower two panels of fig. 5.46. The simulation of *trans*-cyanovinylacetylene matches the experimental spectrum slightly better. Although it is the thermodynamically favored stereoisomer

Table 5.6.: Computed ionization energies for selected $C_5H_3N$ isomers.

| | IE (CBS-QB3) |
|---|---|
| 2,3-didehydropyridine (A) | 9.17 eV |
| 3,4-didehydropyridine (B) | 9.81 eV |
| *cis*-cyanovinylacetylene (C) | 9.99 eV |
| *trans*-cyanovinylacetylene (C) | 10.00 eV |
| *cis*-N-2-propynylidene-ethynamine (D) | 8.98 eV |
| *trans*-N-2-propynylidene-ethynamine (D) | 8.96 eV |

and the deviation between experimental and computed ionization energy is smaller, the peak in the mass spectrum at m/z=77 observed in the pyrolysis of 3-bromopyridine cannot unambiguously assigned to *trans*-cyanovinylacetylene only. A contribution of the *cis* stereoisomer cannot be excluded due to the small energy gap and high structural similarity.

By comparing the computed vibrational modes for the cation and the predicted intensities in the Franck-Condon simulation with the observed bands in the ms-TPE spectrum, an assignment of the vibrational bands can be made, though, as the geometry changes of the *cis* and *trans* stereoisomers are very similar. The band observed at 10.20 eV (+1250 $cm^{-1}$) can be assigned to the C3=C4 stretching mode, for which a wavenumbers of 1222 $cm^{-1}$(*trans*) and 1182 $cm^{-1}$(*cis*) was computed (see fig. 5.47 for atom numbering). The band contains in addition the contribution of a second vibrational mode, the asymmetric C2-C3=C4 stretching mode (*trans:* 1477 $cm^{-1}$, *cis*: 1437 $cm^{-1}$). The distinct band at 10.30 eV can be assigned to the C1≡C2-C3 asymmetric stretching mode computed at 2055 $cm^{-1}$ (*trans*) and 2054 $cm^{-1}$ (*cis*), for which the second overtone is also covertly visible at 10.55 eV. The Franck-Condon simulation also predicts an excitation of the C5≡N stretching mode at 2142 $cm^{-1}$ (*trans*) and 2151 $cm^{-1}$ (*cis*), respectively, which also contributes to the band at 10.30 eV. The excitations of the vibrational modes can also be

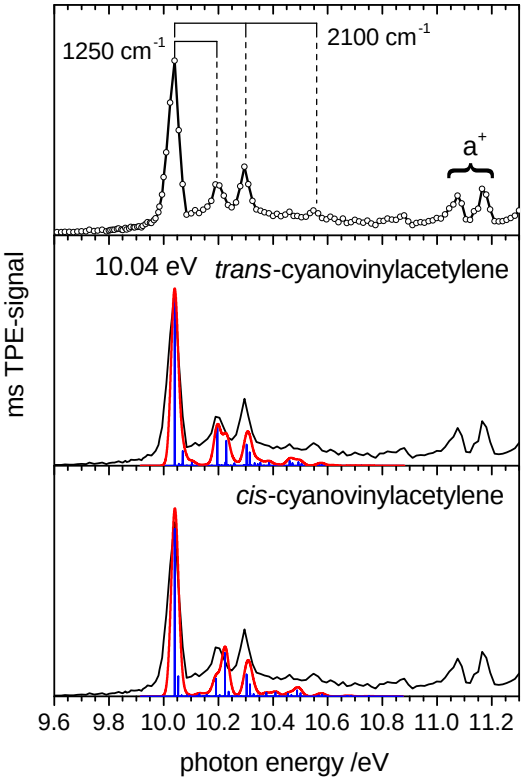


Figure 5.46.: Mass-selected TPE spectrum of cyanovinylacetylene (m/z=77, upper panel). The two lower panels show Franck-Condon simulations (blue sticks, red lines: Gaussian fwhm=30 meV) for the *trans* and *cis* isomer. Both stereoisomers show a high structural similarity and can therefore not be distinguished in the TPE spectrum. The IE for both isomers was determined to be 10.04±0.02 eV. The bands labeled with $a^+$ are assigned to the first electronically excited states of the *cis* and *trans* stereoisomer, respectively. Figure adapted from ref. [309].

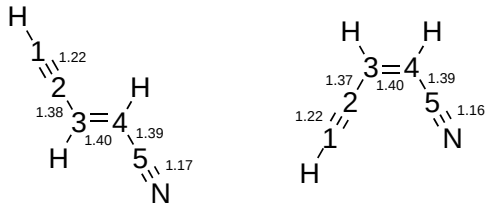


Figure 5.47.: Structures of the *trans*- and the *cis*- cyanovinylacetylene cations. Bond lengths are given in Å.

concluded from the change of geometry upon ionization, which is nearly identical for the two stereoisomers. The formal single bonds C2-C3 and C4-C5 are shortened by 3.9 pm and 2.8 pm, respectively, while the formal C3-C4 double bond is elongated by 5.0 pm upon ionization. As illustrated in fig. 5.47, the formal single and double bonds in the cation C2-C3, C3-C4, and C4-C5 can hardly be distinguished by the bond length. Hence, a greater degree of π-electron delocalization in the cation is concluded. The C1≡C2 and C5≡N triple bonds are also predicted to get slightly elongated upon ionization by 1.9 and 1.0 pm, respectively. All vibrational wavenumbers and bond lengths were computed on B3LYP/6-311G(2d,d,p) level of theory, which were also the basis for the Franck-Condon simulation. Two further distinct peaks are visible in the TPE spectrum at 11.08 eV and 11.17 eV, labeled $a^+$ in fig. 5.46. Energies of 11.00 (*cis*) and 11.09 eV (*trans*) are predicted for the first excited states of the two stereoisomers by TD-B3LYP/6-311G(d,p) computations. The computed difference in the transition energies of ΔE=90 meV compares well with the separation of these two peaks. Only the 0-0 transitions from the neutral to these cationic states are predicted to have high Franck-Condon factors, which makes an assignment of these peak to a vibrational progression of only one isomer unlikely. The contribution of other isomers seems also not plausible because the computed ionization energies for the isomers (A), (B), and

(D) (see fig. 5.45 and tab. 5.6) do not match. Consequently the peaks at 11.08 and 11.17 eV are assigned to the first excited states of cationic *cis*- and *trans*-cyanovinylacetylene, which is also consistent with the presence of both isomers in the experiment.

### 5.4.3. 3-Pyridyl

Cleavage of the bromine-carbon bond in 3-bromopyridine leads to 3-pyridyl, a σ-radical, which usually are highly reactive. For that reason, the lifetime of such radicals is expected to be short leading either to secondary reactions, like H-abstraction from another molecule, H-elimination, or to fragmentation of the molecule. Pyrolysis of 3-bromopyridine leads to a signal at m/z=78 in the mass spectrum (cf. fig. 5.43), which is expected for the 3-pyridyl radical. A mass-selected TPE spectrum was therefore recorded using the same parameters as for cyanovinylacetylene (sec. 5.4.2), which is depicted in fig. 5.48. A gentle rise of the electron signal can be observed in the spectrum setting in at 9.5 eV. At 10.04 eV, a distinct peak is visible. It is conspicuous that a peak at exactly the same energy is observed for cyanovinylacetylene (m/z=77). In addition, small peaks at 10.20 and 10.30 eV are visible, which are also present in the TPE spectrum of cyanovinylacetylene. Comparing the absolute TPE signal at the photon energy of 10.04 eV recorded for m/z=77 and m/z=78, which was done in the same scan, the m/z=78 signal is only about 10 % of the m/z=77 one. The $^{13}$C signal of cyanovinylacetylene should be 5.4 % and therefore contributes significantly to the m/z=78 TPE spectrum. The inset of fig. 5.48 shows the ms-TPE spectrum of m/z=78 after subtraction of the $^{13}$C signal of $C_5H_3N$. Here, the spectrum exhibits only a broad rise and shows no distinct features. CBS-QB3 computations predict an ionization energy of 8.09 eV, which is significantly below the detected TPE onset observed in the spectrum. Another possible explanation for the observation of a m/z=78 signal is dissociative photoionization of the precursor, which is not completely

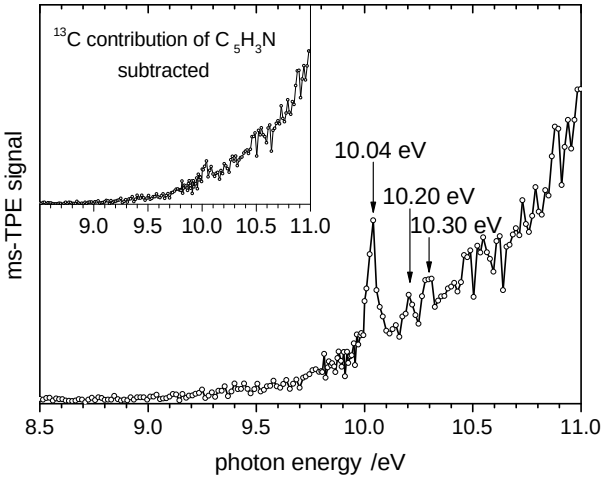


Figure 5.48.: Mass-selected TPE spectrum of the peak with m/z=78 observed in the pyrolysis of 3-bromopyridine. The peaks observed at 10.04, 10.20, and 10.30 eV can be attributed to the $^{13}$C signal of cyanovinylacetylene, which is generated in much greater abundance under the chosen experimental conditions. The inset shows the ms-TPE spectrum after subtraction of the $^{13}$C contribution. Due to the unstructured and slow rise of the TPE signal, it is concluded that m/z=78 is only generated by dissociative photoionization. The thermal energy from the pyrolysis leads to DPI at lower photon energies.

converted by pyrolysis as visible in fig. 5.43.

The plot on the left of fig. 5.49 shows the breakdown diagram of 3-bromopyridine recorded from 10.0 to 13.0 eV at room temperature with an energy step size of 50 meV. Each data point was averaged for 60 s. The precursor (m/z=157/159) indeed undergoes dissociative photoionization to m/z=78 corresponding to the formation of the 3-pyridyl cation and a bromine atom. The time-of-flight distributions on the right of fig. 5.49 indicate that the dissociation rate is slow on the timescale of the experiment, as the daughter ion peak at 11.4 µs is broad and asymmetric for lower photon energies. A relaxed scan of the reaction coordinate revealed that the dissociation does not have a reverse barrier and the appearance energy for the bromine loss was computed to be 11.96 eV on CBS-QB3 level of theory. RRKM theory was employed to simultaneously fit the breakdown diagram and the TOF distributions. As the dissociation is barrierless, a loose transition state with a C-Br bonding distance fixed at 5.00 Å was optimized and the obtained frequencies and rotational constants were used to calculate the transition state's rovibronic sum of states. The fit, also shown in fig. 5.49, reproduces well the experimental breakdown diagram and TOF distributions. An appearance energy of 11.71±0.05 eV was thus determined for the formation of 3-pyridylium from 3-bromopyridine.

The obtained appearance energy lies well above the observed signal onset in the ms-TPE spectrum of m/z=78. However, the appearance energy is related to a temperature of 0 K. As discussed in sec. 2.5.3, temperature leads to a red shift of the breakdown curves. In the experiment, a pyrolysis temperature of about 1000°C was applied. This means that the breakdown diagram in fig. 5.49, which was recorded at room temperature, will be significantly shifted to lower photon energies under the used pyrolysis conditions. Fig. 5.50 shows the calculated internal energy distributions for the parent ion at 25°C and at 1000°C. The difference between appearance energy and ionization energy of the parent is the ion internal energy necessary for the dissociation; in this

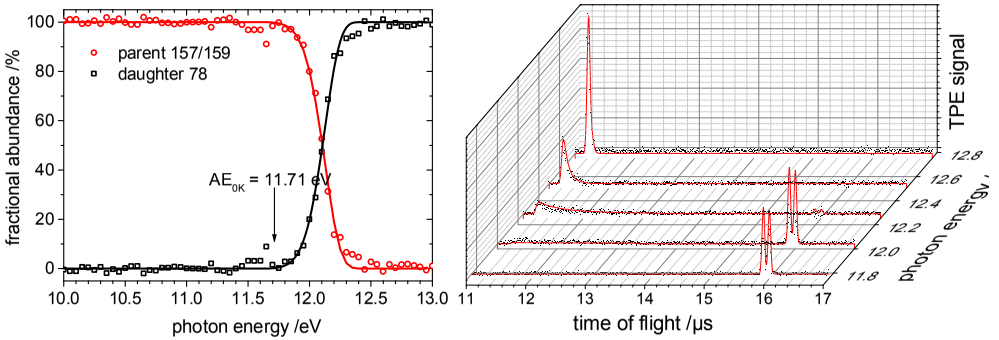


Figure 5.49.: Breakdown diagram (symbols: experimental data, lines: fit) and TOF distributions for the dissociative photoionization of 3-bromopyridine. An appearance energy of 11.90±0.05 eV for the fragmentation to 3-pyridylium and atomic bromine is derived. Figure reprinted from ref.[309], Copyright (2015), with permission from Elsevier.

case 2.56 eV. The distribution in fig. 5.50 illustrates that the observed onset for dissociative photoionization should be well below 10 eV at a temperature of 1000°C. Therefore the explanation that the TPE signal of the m/z=78 channel comes predominantly from dissociative photoionization seems valid.

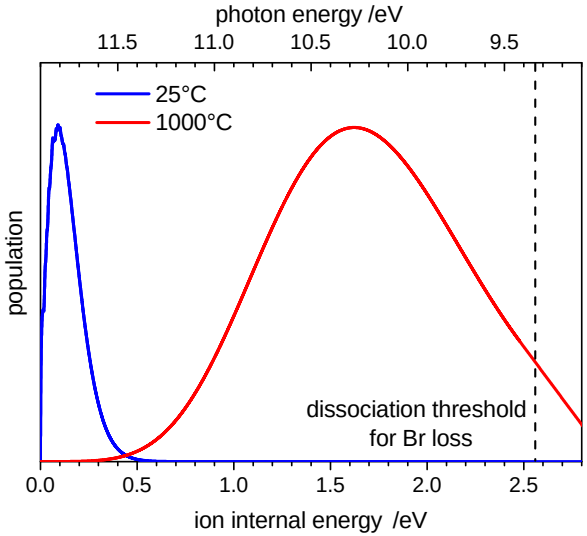


Figure 5.50.: Internal energy distributions of the 3-bromopyridine cation at 25°C and 1000°C. The upper axis defines the photon energy which is necessary to prepare parent ions with enough internal energy to dissociatively ionize. The dashed vertical line indicates the disociation threshold.

### 5.4.4. Summary Pyrolysis of 3-Bromopyridine

The pyrolysis of 3-bromopyridine, for which an ionization energy of 9.34 eV was determined, was investigated using TPEPICO. Very high temperatures are necessary to induce partial fragmentation of the precursor, which even at 1000°C is still clearly visible in the mass spectrum. Several, already well investigated hydrocarbons are generated under pyrolytic conditions. The initial step in the pyrolysis of 3-bromopyridine is assumed to be the cleavage of the C-Br bond leading to the 3-pyridyl radical. This radical was however not detected due to its very high reactivity and instability. A major channel for the decomposition of 3-pyridyl was found to be the ring opening and simultaneous hydrogen loss leading to cyanovinylacetylene. The *trans*- as well as the *cis*-isomer are assumed to contribute to the TPE spectrum. Information on this closed-shell $C_5H_3N$ species have been scarce to date. The ionization energy for this nitrogen-containing intermediate was determined to be 10.04±0.02 eV and the vibrational structure of the two stereoisomeric cations, whose structural change upon ionization is nearly identical, were analyzed in the TPE spectrum. Bands that can most likely be assigned to electronically excited states of *cis*- and *trans*-cyanovinylacetylene cations were observed at 11.08±0.02 eV and at 11.17±0.02 eV, in addition. A signal for m/z=78 corresponding to the pyridyl cation was observed in the mass-spectrum, but could be ascribed to be produced from thermalized dissociative photoionization of the precursor.

## 5.5. 3-Picolyl

A model compound for substituted heteroaromatic radicals is the picolyl radical $C_6H_6N$, which is isoelectronic to benzyl $C_7H_7$, a very important combustion intermediate. That is why the pyrolysis of picoline, in which the initial decomposition step leads to the formation of picolyl has been investigated previously.[315–317] There are three isomers for picolyl, as the ring can be substituted in ortho-, meta-, or para-position to the nitrogen atom. All isomers are found to be more or less equally stable,[318,319] although fluorescence excitation spectra could only be obtained for 3-picolyl.[320] It remains unclear, whether the different electronic nature of 3-picolyl in contrast to 2- and 4-picolyl can be explained by the lack of a resonance structure in which the radical center is localized on the nitrogen atom.[320] In 1963, Palmer *et al.* determined the ionization energies for 2-, 3-, and 4-picolyl to be IE=8.17±0.10, 7.92±0.10, and 8.40±0.15 eV, respectively, employing electron impact ionization.[321] The ionization energy for 3-picolyl was later revised using photoionization mass spectrometry yielding a value of 7.62±0.03 eV.[320] In the following, an improved value for the ionization energy of 3-picolyl obtained by threshold photoelectron spectroscopy is reported.

### 5.5.1. Radical Generation of 3-Picolyl

3-Picolylamine has been found to generate efficiently the 3-picolyl radical under pyrolytic conditions as illustrated in fig. 5.51.[321] Due to the low vapor pressure of 3-picolylamine, for the experiments at the SLS, the liquid precursor was applied on glass wool, which was positioned inside the experimental chamber, directly in front of the nozzle. Gentle heating of the nozzle to 30°C was sufficient to transfer the precursor into the gas phase. At a pyrolysis temperature of 600°C, fragmentation of 3-picolylamine is observed. Fig. 5.52 shows mass spectra for this pyrolysis temperature, but two different backing

pressures of the carrier gas. It is obvious that this pressure is crucial for the generation of 3-picolyl. For a high dilution, i.e. a high backing pressure, which was in the depicted example 2.4 bar of Ar, the radical generation is very efficient, as m/z=92 is the most intense signal in the mass spectrum at 9.5 eV. Lowering the backing pressure (0.7 bar in the lower panel of fig. 5.52) increases the concentration of the precursor in the molecular beam and the residence time in the heated zone of the pyrolysis tube. This favors bimolecular reactions and further fragmentation of the radical. This is proven by the corresponding mass spectrum, in which the radical peak at m/z=92 decreases significantly at the expense of m/z=91 (hydrogen loss), 93 (hydrogen addition), and 90 ($H_2$ loss). The increased residence time in the pyrolysis region also leads to a complete conversion of the precursor (m/z=108) and the occurrence of several new masses at m/z=39 (presumably propargyl), 64 ($C_2H_4$ loss of 3-picolyl), 65, and 66 ($C_2H_2$ loss of 3-picolyl). For recording the TPE spectrum of 3-picolyl, a high dilution of the precursor was chosen.

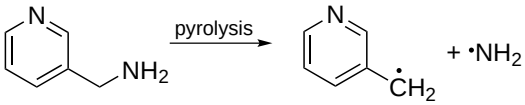


Figure 5.51.: Pyrolysis of 3-picolylamine to the 3-picolyl radical and amidogen.

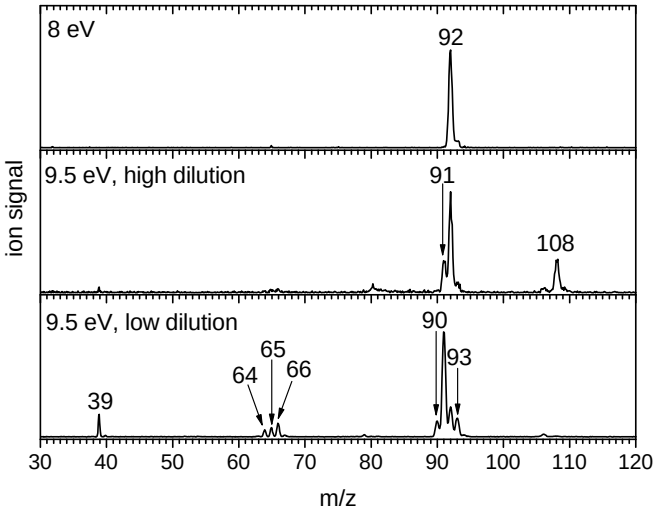


Figure 5.52.: Mass spectra of 3-picolylamine at a pyrolysis temperature of 600˚C. The experimental conditions in the upper two panels were optimized for the efficient generation of the 3-picolyl radical, while the lower panel shows mass spectra for a lower dilution of the precursor in the molecular beam.

### 5.5.2. TPE Spectrum of 3-Picolyl

The mass spectrum at 8 eV in fig. 5.52 shows that no pyrolysis products other than the desired radical are ionized at this photon energy. As a consequence, the TPE spectrum for 3-picolyl at the ionization onset could be recorded without using the coincidence scheme for mass-selectivity. The result is shown in fig. 5.53. The spectrum was recorded in steps of 5 meV and an acquisition time of 4 min per data point.

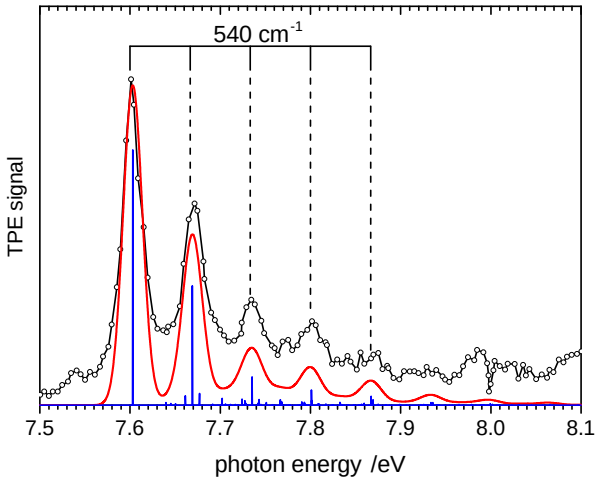


Figure 5.53.: TPE spectrum and Franck-Condon simulation (blue sticks, red lines: convolution with gaussian fwhm=25 meV) of 3-picolyl. The spectrum yields an ionization energy of 7.600±0.015 eV.

A sharp peak is observed at 7.60 eV followed by four components of a progression with a spacing of 67 meV (540 $cm^{-1}$). By comparison with the computed ionization energy for 3-picolyl of 7.64 eV (CBS-QB3), the first band

(fwhm=25 meV) can be assigned to the ionization energy yielding an experimental value of 7.600±0.015 eV. With the help of a Franck-Condon simulation, the vibrational structure in the TPE spectrum of 3-picolyl was analyzed on the basis of B3LYP/6-311G(2d,d,p) computations.The simulation also depicted in fig. 5.53 shows a convincing agreement with the experiment. The pronounced progression can thus be assigned to the excitation of the 21(a')$^+$ ring breathing mode, which is visualized in fig. 5.54. The Franck-Condon simulation also predicts the contribution of further ring deformation modes, though with significantly less intensity. Overall, according to the computations, the geometry of 3-picolyl changes only slightly upon ionization with the bond lengths in the ring being elongated or shortened by less than 2 pm. This explains the well resolved structure in the TPE spectrum of the 3-picolyl radical.

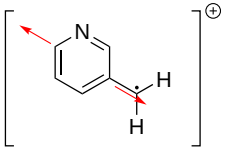


Figure 5.54.: Distortion vectors of the 21(a')$^+$ vibrational mode in 3-picolylium.

### 5.5.3. Summary 3-Picolyl

3-Picolyl was generated by pyrolysis of 3-picolylamine and the ionization energy was determined to be 7.600±0.015 eV from the TPE spectrum in good agreement with computations. A well defined progression was observed in the spectrum and assigned to a ring breathing mode of the cation. The mass spectra at different experimental conditions showed that the radical shows a similar behavior as its hydrocarbon analog, benzyl, under more rude pyrolysis conditions. Benzyl loses a hydrogen atom and undergoes a rearrangement to fulvenallene, which can lose a further hydrogen atom yielding fulvenallenyl. The equivalent masses for 3-picolyl were observed in this experiment. Recording the corresponding TPE spectra might therefore be interesting.

# 6. Photoionization and Pyrolysis of 1,4-Di-tert-Butyl-1,4-Azaborinine

As already outlined in the introduction of this thesis, boron-containing organic compounds are sought for a number of applications in synthesis and especially in the field of functional materials. A common access to boron-containing organic molecules is the replacement of C=C groups with isoelectronic B=N groups. The most famous example for this BN isosterism is borazine, cyclo-$N_3B_3H_6$, known as "inorganic benzene", which was first prepared by Stock and Pohland in 1926.[322] Replacing only one C=C moiety by a B=N group leads to the family of azaborinines, cyclo-$C_4H_6NB$. There are three isomers: 1,2-, 1,3-, and 1,4-azaborinines as depicted in fig. 6.1. 1,2-azaborinine was computed to be the most stable one of those isomers and 1,3-azaborinine the least stable one.[323] The energetic order arises from the strong charge separation in the $\pi$ system for the 1,3-azaborinine, which leads to a high cyclic $\pi$-electron delocalization. Consequently, it is the most aromatic one, whereas 1,4-azaborinines are the least aromatic compounds of this family because the electrons are delocalized one-directionally from N to B.[324] Dewar and coworkers succeeded in the first synthesis of a monocyclic azaborinine[325] and the parent 1,2-dihydro-1,2-azaborinine was first isolated in 2009 by Liu and coworkers.[326] Current research is mostly focused on 1,2-azaborinines because

of the easier access.[327–329] Only few examples for successful syntheses of 1,4-azaborinines, all of which were benzo-fused polycyles, have been reported until recently.[330,331] Braunschweig *et al.* succeeded in the first synthesis of a monocyclic 1,4-azaborinine, 1,4-di-*tert*-butyl-1,4-azaborinine (chemical structure in fig. 6.2).[332] A one-step synthesis employing a rhodium-catalyzed tandem [2+2]/[2+4] cycloaddition process of the educts 1,2-di-*tert*-butyl-iminoborane and acetylene with a high yield was developed.

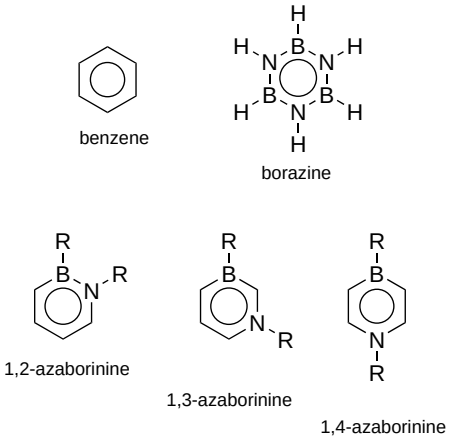


Figure 6.1.: Chemical structures of benzene, borazine, and the three different azaborinine isomers.

Photoionization, especially TPES, yields interesting insight into the electronic structure of the molecule because the spectra contain information on the valence orbital out of which an electron was removed. So far, only selected BN containing heterocycles have been investigated utilizing conventional PES.[333–335] Dissociative photoionization of such molecules has never been investigated. One reason for that is that large sample quantities are required for photoionization experiments, which is challenging when complex synthesis is necessary. In the following, photoionization and dissociative pho-

toionization of 1,4-di-*tert*-butyl-1,4-azaborinine is discussed, which gives insight into electronic properties of the neutral molecule and yields information on the structure and bonding in the cation. In addition, pyrolysis was applied to initiate thermal fragmentation of the azaborinine to gain access to elusive BN-containing molecules which are not yet accessible by conventional synthesis. Another goal was to study retro-hydroboration reactions, which are presumed to occur under thermolytic conditions.[336,337]

Note that in the following mass peaks are always assigned to the $^{11}$B isotopomer, which is about four times more abundant than the $^{10}$B isotopomer.

## 6.1. Photoionization of 1,4-Di-tert-Butyl-1,4-Azaborinine

Photoionization of 1,4-di-*tert*-butyl-1,4-azaborinine was investigated using the iPEPICO setup at the X04DB VUV beamline at the SLS. The solid sample was brought directly into the ionization chamber via the effusive inlet system. No heating was required since the sample has a high vapor pressure at room temperature. For the threshold photoelectron spectrum, the energy range from 7.5 to 16.0 eV was scanned in 10 meV steps. Each data point was averaged for 60 s. The acquisition time for the TOF distributions used in the fitting procedure for analyzing dissociative photoionization was 12 min.

### 6.1.1. TPE Spectrum of 1,4-Di-tert-Butyl-1,4-Azaborinine

Fig. 6.2 shows the TPE spectrum of the azaborinine from 7.5 to 12.5 eV. The spectrum features three distinct peaks at 7.95, 8.08 and 8.18 eV and drops again reaching a minimum at 8.5 eV. Above 8.5 eV, a step-wise, but almost constant rise in the TPE signal with three local maxima is observed.

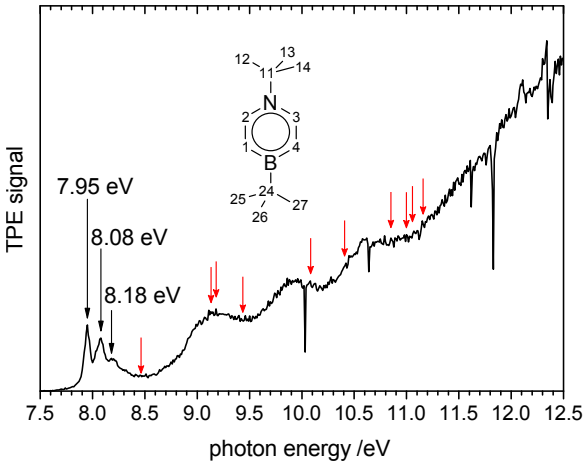


Figure 6.2.: TPE spectrum and chemical structure of 1,4-di-*tert*-butyl-1,4-azaborinine. Three distinct peaks are observed and several steps at higher energies indicate higher electronic states. The computed excitation energies (TD-B3LYP/TZVP for the first ten excited states are indicated by red arrows.

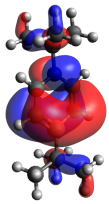

Figure 6.3.: HOMO of the azaborinine.

The first peak maximum at 7.95 eV can be assigned to the ionization energy of 1,4-di-*tert*-butyl-1,4-azaborinine, which is in very good agreement with the value predicted in CBS-QB3 computations, IE(CBS-QB3)=7.92 eV. The TPE signal already starts to rise at 7.6 eV. As the experiment was conducted at room temperature and the sample was flowing effusively into the ionization chamber (i.e. no adiabatic cooling in a molecular beam), excited vibrational states in the neutral are assumed to be populated and therefore contribute to the TPE signal below the ionization energy as hot or sequence

bands. B3LYP/6-311G(2d,d,p) computations reveal that the HOMO is localized mostly at the ring skeleton and has a non-bonding $\pi$-character as illustrated in 6.3. The parts of the HOMO localized at the substituents is smaller and has a bonding character. Consequently, a relatively sharp ionization onset is expected since the bonding properties should not change significantly and only few vibrational modes should be excited in the cation. As will be shown later in this section, the peaks at 8.08 and 8.18 eV can be explained by vibrational structure of the cationic ground state. This contradicts our original assignment of these peaks to low lying excited electronic states.[338] Vertical excitation energies were computed for higher excited states in the cation. Ten states are found to contribute to the TPE spectrum according to the computations. As highlighted by the red arrows in fig. 6.2, most of the computed energies match well with the observed trend in the TPE spectrum, which shows several steps with small maxima. As visible, the broad bands are often congested by the contribution of several neighboring ionic states. A Franck-Condon simulation was performed to analyze the observed vibrational structure in the cationic ground state and to validate the assignment of the ionization energy. While reviewing the simulation published earlier,[338] which only yielded a good agreement for the first band centered around 7.95 eV, but not for the two prominent bands at 8.08 and 8.18 eV, it was noticed that this simulation predicts primarily modes to be active that can be described as rotations of the *tert*-butyl or methyl groups. The experiment was conducted at room temperature. Hence, the *tert*-butyl groups in the azaborinine rotate freely, since the associated barrier is computed to be less than 10 meV ($1\,\mathrm{kJ\,mol^{-1}}$). Rotation of the methyl groups are assumed to have even lower barriers. Inclusion of these modes leads to a defective simulation, as a high excitation of those vibrations is predicted due to the different geometries in the neutral molecule and cation, which are assumed as static. For that reason the Franck-Condon simulation was redone while excluding fourteen low-energy vibrational modes that correspond to rotations of the *tert*-butyl and methyl

groups in the azaborinine. Fig. 6.4 shows the result of the simulation based on B3LYP/TZVP computations.

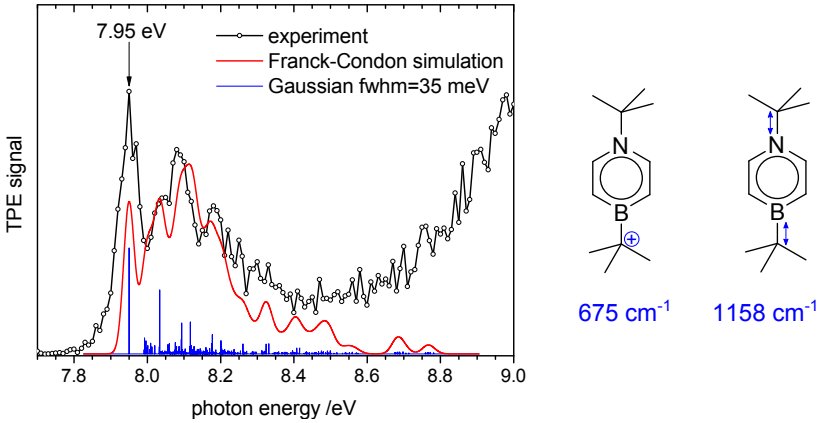


Figure 6.4.: The band structure in the TPE spectrum of 1,4-di-*tert*-butyl-1,4-azaborinine is well reproduced in a Franck-Condon simulation. Low-energy vibrational modes, which describe rotations of the methyl and *tert*-butyl groups, are not included in the simulation since unhindered rotation for these groups is assumed at the experimental temperature of 298 K. The two vibrational modes belonging to the intense bands in the spectrum are depicted on the right. An ionization energy of 7.95±0.02 eV is obtained from the simulation.

The obtained simulation shows a much better agreement with the experimental TPE spectrum than the one published previously and enables a more detailed assignment of the observed bands in the TPE spectrum. The computations on B3LYP/TZVP level of theory predict a rather large change in geometry. A table comparing neutral and cation geometry is included in the appendix F. The most obvious change is the loss of planarity. The dihedral angle (B-C1-C2-N) increases from 0 to 7.3° (see 6.2 for atom numbering). Simultaneously, the *tert*-butyl group connected to the boron atom moves out of

the plane and the corresponding dihedral angle (H-C1-B-C24) in the cation is 14.6°. In addition, the bond length N-C11 is elongated by 2.8 pm, while the B-C24 bond is shortened by 1.7 pm. In the Franck-Condon simulation, the progression of the C1-B-C24 out of plane bending mode at 675 $cm^{-1}$ is computed to have a large intensity, while the N-C11 and B-C24 stretching mode at 1158 $cm^{-1}$ features also an intense contribution to the simulation. In addition, numerous ring deformation modes are computed to be excited, but with a lower intensity, thus responsible for the background in the spectrum. Setting the ionization energy 7.95 eV yields the best agreement of experimental TPE spectrum and FC simulation. However, the 0-0 transition is significantly underestimated and the band is too narrow after convolution of the stick spectrum with a fwhm=35 meV Gaussian function. This might be a consequence of the omission of the low energy torsional modes in the Franck-Condon simulation. Excitation of those and other low energy modes in the neutral molecule are presumably responsible for the rather shallow TPE signal onset because hot and sequence bands should also contribute to the spectrum recorded at room temperature. Nevertheless, the assignment of the ionization energy to 7.95 eV is in good agreement with the CBS-QB3 computations and the Franck-Condon simulation yields a convincing reproduction of the experimental TPE spectrum.

### 6.1.2. DPI of 1,4-Di-tert-Butyl-1,4-Azaborinine

Mass spectra for different photon energies were recorded to investigate dissociative photoionization of 1,4-di-*tert*-butyl-1,4-azaborinine. As can be seen on the left of fig. 6.5, only the parent peak at m/z=191 is observed at 9.0 eV. No sample contamination by side products of the synthesis is visible. The boron isotope pattern cannot be resolved for the parent peak due to thermal broadening and because the spectrometer's resolution is too low in this time-of-flight region, i.e. a rather broad signal is obtained. At 12.0 eV, dissociative

photoionization is observed to set in since the signal at m/z=191 diminishes and new peaks at m/z=176 and m/z=135 appear. Further fragment ions, m/z=120, 79, and 57, are visible at a photon energy of 15.0 eV.

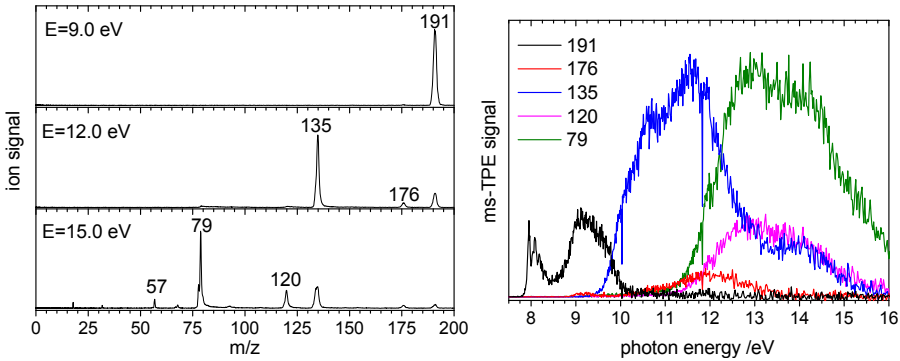


Figure 6.5.: TOF mass spectra (left) of 1,4-di-*tert*-butyl-1,4-azaborinine (mz=191) for different photon energies indicate dissociative photoionization to m/z=176, 135, 120, 79, and 57. The mass-selected TPE spectra corresponding to the respective ion peaks (right) show the appearance onsets. The ms-TPE signal of m/z=57 is below noise level and is thus not included in the spectrum.

The mass-selected TPE signals depicted on the right in fig. 6.5 show the respective electron signals' dependencies. As the TPE signal of m/z=57 is below noise level and is thus determined to be only a minor channel, it is not included in the analysis. The parent signal m/z=191 starts to drop at around 9.4 eV and a signal increase in the mass channels m/z=176 and 135 is observed. This can be interpreted as the onset of two parallel dissociation pathways of the parent ion. Around 12.0 eV, the TPE signal of m/z=135 decreases and a rise of the channels m/z=120 and m/z=79 is observed. The latter two channels are thus assumed to be sequential dissociation pathways of the daughter ion m/z=135 that open simultaneously. The TPE signal of m/z=135 does not drop to zero again, but reaches a plateau around 13 eV. This is an indication

that an isomer or another DPI channel might contribute to the spectrum, as will be discussed below. To analyze the dissociative photoionization of 1,4-di-*tert*-butyl-1,4-azaborinine in detail, the fractional abundance of the ms-TPE signal of the parent and daughter ions is plotted against the photon energy in a breakdown diagram as depicted in fig. 6.6.

The breakdown diagram shows the relative mass-selected TPE signal contributions and signal dependencies of the observed mass channels and confirms the conclusions drawn from the ms-TPE spectra. Modeling of the dissociation mechanisms is necessary to determine accurate appearance energies for the various daughter ions. Precise information on the dissociation mechanism, which might contain rearrangements and reverse barriers, is necessary as discussed in sec. 2.5.3 Quantum chemistry was employed to scan the various dissociation coordinates on B3LYP/TZVP level of theory and relative energies to the neutral parent molecule were computed for intermediates, transition states and product ions with the CBS-QB3 composite method. The first daughter ion at m/z=176 corresponds to a loss of 15 amu, i.e. methyl radical. Obviously, methyl can either be cleaved off the boron-bound *tert*-butyl group or the nitrogen-bound one. The product originating from the former cleavage is found to be 60 meV lower in energy than the one from the latter mechanism. As both dissociations are computed to proceed barrier-less, it is concluded that, for the observed m/z=176 daughter ion, the methyl group is lost on the boron-bound *tert*-butyl group. However, this channel is neglected in the subsequent analysis, since the corresponding fractional abundance never exceeds 7 %. Parallel to this channel, m/z=135 rises rapidly at 9.4 eV, which corresponds to a loss of 56 amu, isobutene. Again, the neutral fragment can originate from either of the two *tert*-butyl substituents. The N-H product ion is computed to be 490 meV (48 kJ mol$^{-1}$) more stable than the B-H product ion. However, a hydrogen-atom migration has to occur, which implies a complex dissociation mechanism involving transition states and intermediates.

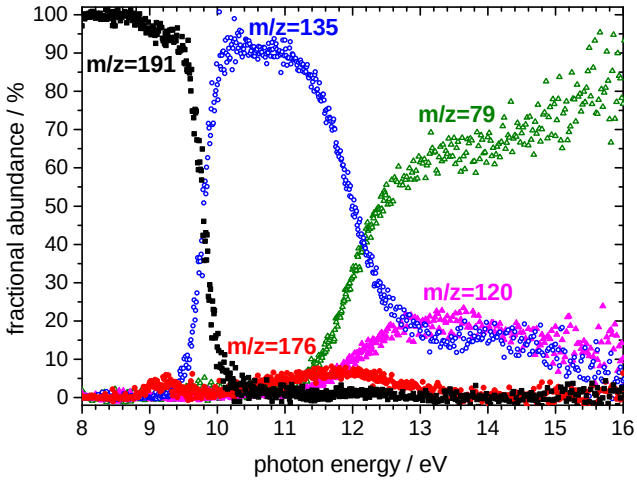


Figure 6.6.: Breakdown diagram of 1,4-di-*tert*-butyl-1,4-azaborinine (m/z=191). At 9.4 eV DPI of the parent ion sets in via the two parallel dissociation channels m/z=176 (methyl loss) and 135 (loss of isobutene). Around 11.0 eV the dominating m/z=135 channel dissociates further, as the two sequential channels m/z=120 (methyl loss) and m/z=79 (loss of isobutene) open simultaneously. The channel leading to m/z=176 is neglected in the subsequent analysis due to its weak intensity. Figure reprinted from ref.[338]. 

The transition state for the H-shift leading to the B-H product is found to be 720 meV (70 kJ mol$^{-1}$) more stable than the one leading to the N-H product. Hence, the B-H product is formed and the mechanism shown in fig. 6.7 is assumed to describe the observed dissociative photoionization step correctly: A loosely-bound $\pi$ complex is formed via a four-membered transition state at 8.50 eV. From this intermediate state at 8.40 eV, a barrier-less dissociation of isobutene leading to the B-H isomer 1-*tert*-butyl-4*H*-1,4-azaborinylium occurs. The associated appearance energy is computed to be 9.32 eV. The mechanism leading to the daughter ion m/z=135 can be described as a retro-hydroboration in the cation. In the neutral molecule, hydroborations involving an isobutene moiety are found to proceed via very similar mechanisms.[339] The finding that the isobutene is lost first on the boron side is contradictory to recent results from Braunschweig *et al.* who observed isobutene elimination from a N*t*Bu group of a neutral 1,2-azaborinine under thermolytic conditions, rather than from a B*t*Bu group.[327] In the 1,2-isomer, steric effects of the two adjacent *t*Bu group are likely to influence the outcome of isobutene elimination. However, electronic differences between the two isomers and the fact that dissociation processes might be different for the neutral molecule and cation are assumed to also play a role.

As discussed above, the TPE signal of m/z=135 drops again and two dissociation channels open simultaneously. M/z=120 corresponds to a methyl loss and competes with the m/z=79 channel, in which a second equivalent of isobutene is lost. Computations reveal a third parallel channel for this consecutive dissociation leading to m/z=134 by losing a hydrogen atom. Due to thermal broadening of the peaks in the TOF-MS, the low spectrometer resolution and the overlap with the $^{10}$B isotope of the m/z=135 daughter ion, this channel could not be analyzed. The corresponding appearance energy was computed to be 11.49 eV. This is a consistent explanation why the m/z=135 signal does not drop to zero, but reaches a plateau at 13 eV. The mechanisms of the other

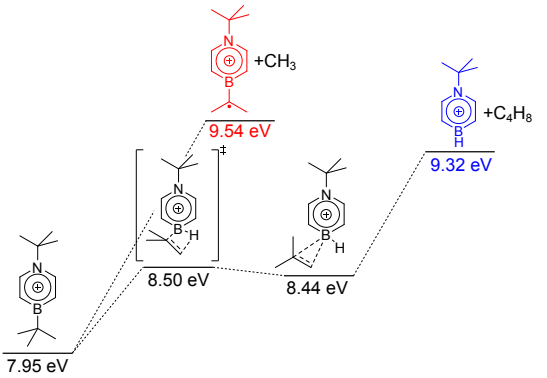


Figure 6.7.: Computed mechanism and relative energies to the neutral parent molecule on CBS-QB3 level for the two first parallel dissociation pathways m/z=176 (red) and m/z=135 (blue). While the methyl loss proceeds via a direct dissociation pathway, the loss of isobutene is associated with a two-step mechanism with a loosely bound $\pi$-complex intermediate state. It can thus be described as a retro-hydroboration in the cation.

two parallel channels revealed similar results like for the dissociation of the parent ion as illustrated in fig. 6.8. A scan along the reaction coordinate leading to 1-$C_3H_6$-4*H*-1,4-azaborinine (m/z=120) reveals a small reverse barrier of 4 kJ mol$^{-1}$ for this dissociation step. CBS-QB3, by contrast, computes the structure corresponding to the found transition state with a lower energy than the product ion. As the impact on the accuracy of fitted appearance energies of such a low reverse barrier is assumed to be small, the reverse barrier for this pathway was disregarded in the subsequent analysis. The first step in the dissociation to the 1,4-dihydro-1,4azaborinylium cation m/z=79 is again an H-shift initiated by a four-membered transition state at 11.10 eV. A loosely bound $\pi$ complex intermediate is found at 10.16, which dissociates to the daughter ion along a coordinate without reverse barrier. The computed appearance energies are 10.92 eV for m/z=120 and 11.10 eV for m/z=79. The

appearance energy of the latter channel is determined by the energy of the involved transition state, which is 460 meV higher in energy than the products. An energy of 10.64 eV is computed for those.

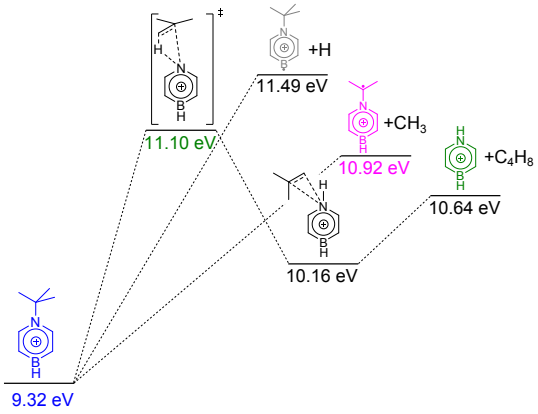


Figure 6.8.: Parallel photoionization pathways and relative CBS-QB3 energies for the fragmentation of the first daughter ion, 1-*tert*-butylazaborinylium (blue). The mechanisms leading to m/z=134 (grey) and m/z=120 (magenta) are computed to proceed barrierless. For the loss of isobutene (green), a rearrangement mechanism via a four-membered transition state similar to the first dissociation step is necessary. As the transition state at 11.10 eV lies energetically above the dissociation products, the appearance energy of the m/z=79 channel is defined by the energy of this transition state.

The findings in the computational study of the azaborinine's dissociative photoionization were used as input for simultaneously modeling the breakdown curves and time of flight distributions as described in sec. 2.5.3. All three daughter ion peaks show a distinct asymmetry in the recorded spectra (see fig. 6.10), which indicates slow dissociation of metastable parent ions. These spectra were hence also fitted to obtain information on the dissociation rates.

Slow dissociation rates lead to kinetic shifts of the signal onsets to higher photon energies. The thermal shift, which has an opposing effect on the signal onsets, was also considered by using a temperature of 298 K for the model, since the experiment had been conducted at room temperature. As the dissociation mechanism involves rearrangements and transition states, the RAC-RRKM theory approach was chosen for modeling the experimental data (cf. sec. 2.5.2). For those dissociation pathways, in which no 'real' transition state was found, the vibrational frequencies and rotational constants of a loose transition state were used. Loose transition states were computed by freezing the respective length of the bond that is cleaved to 4.5 Å and optimizing the other geometric parameters. As the channel leading to m/z=134 is congested with the m/z=135 signal, but could not be included in the analysis, the breakdown diagram was only modeled between 8.0 and 12.5 eV (fig. 6.9).

Both breakdown diagram and TOF distributions show a very good agreement of experiment and model as can be seen in fig. 6.9 and 6.10. Hence, it was possible to determine the appearance energies for the first three daughter ions of 1,4-di-*tert*-butyl-1,4-azaborinine on a high level of accuracy. The obtained values agree well with the CBS-QB3 computations as presented in tab. 6.1.

The dissociative photoionization of 1,4-di-*tert*-butyl-1,4-azaborinine comprises a complex mechanism with rearrangements and transition states with reverse barriers. Hence, it was not possible to derive any bond dissociation energies in the cation to obtain quantitative information on the bonding in the investigated molecule. Nevertheless, the experiment proved that a retro-hydroboration reaction leading to the elimination of isobutene is also a favorable dissociation reaction in the cation.

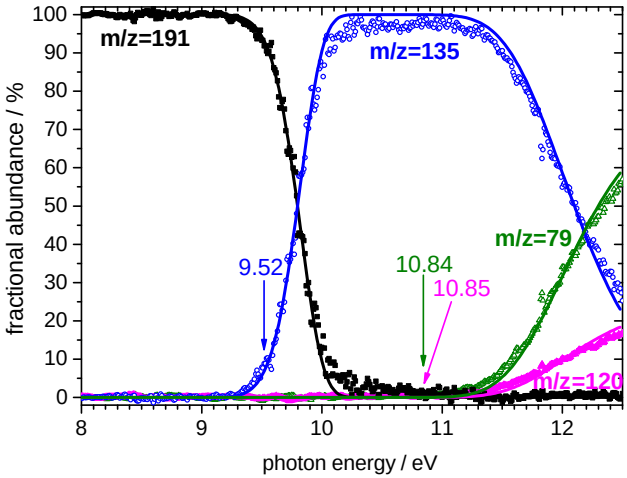


Figure 6.9.: Experimental (symbols) and fitted (lines) breakdown curves for 1,4-di-*tert*-butyl-1,4-azaborinine. The appearance energies of the respective channels are indicated by the arrows. Figure reprinted from ref.[338]. © 2014 Wiley-VCH Verlag GmbH&Co. KGaA, Weinheim.

Table 6.1.: Comparison of the appearance energies for the first three daughter ions of 1,4-di-*tert*-butyl-1,4-azaborinine for fit and CBS-QB3 computations.

| m/z | $AE_{0K}$ (fit) /eV | $AE_{0K}$ (CBS-QB3) /eV |
|---|---|---|
| 135 | 9.52 | 9.32 |
| 120 | 10.85 | 10.92 |
| 79 | 10.84 | 11.10 |

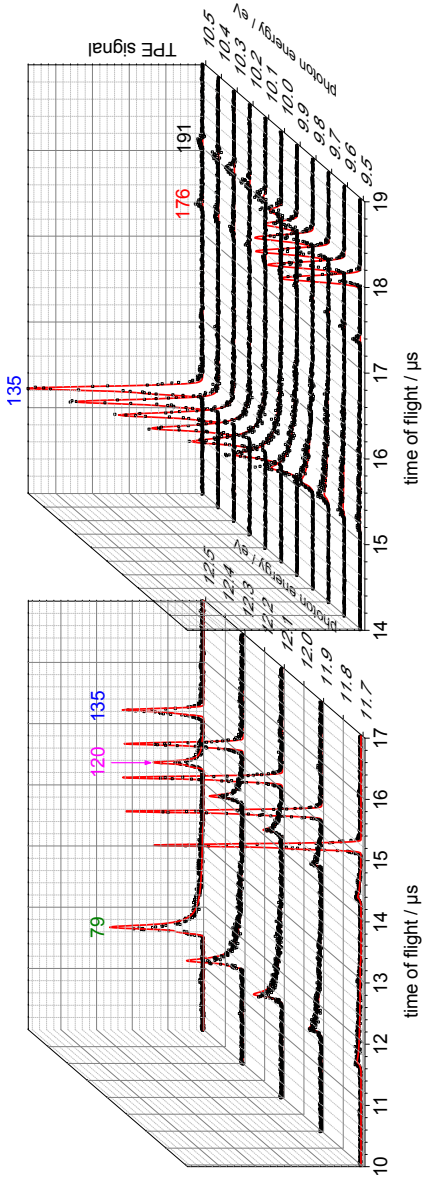


Figure 6.10.: Experimental (squares) and fitted (red lines) TOF distributions for the dissociative photoionization of 1,4-di-*tert*-butyl-1,4-azaborinine. The figure on the right depicts the first isobutene loss for photon energies from 9.5 to 10.5 eV, while on the left the TOF distributions for the sequential dissociation of the first daughter ion is fitted for photon energies from 11.7 to 12.5 eV. Figure adapted from ref. [338].

## 6.2. Pyrolysis of 1,4-Di-tert-Butyl-1,4-Azaborinine

In a second experiment, the pyrolysis of 1,4-di-*tert*-butyl-1,4-azaborinine was investigated. The solid sample was placed for this study inside the experimental chamber using the source described in sec. 3.1 and gently heated to 60°C. The sample vapor was seeded in 0.1 bar of argon, expanded in the vacuum and pyrolyzed in an electrically heated SiC tube. Fig. 6.11 shows TOF mass spectra at 9 eV for different pyrolysis conditions. As no thermocouple was connected to the reactor, the actual pyrolysis temperatures can only be estimated from similar experimental setups. 10 W are assumed to correspond to about 300°C and 30 W to about 700°C. Mass peaks from the preceding experiment (9-Fluorenone, m/z=180 and pyrolysis products) are still visible and marked with an asterisk. These do however not perturb the following analysis, since the iPEPICO experiment offers mass-selectivity.

At 9 eV and the pyrolysis turned off, the parent peak at m/z=191 is the only one visible in the mass spectrum, while under low pyrolysis temperatures a pronounced peak at m/z=135 corresponding to a loss of isobutene is observed. At an estimated pyrolysis temperature of 700°C, the precursor peak has completely disappeared and a number of mass peaks appear between 39 and 120 amu.

The mass-selected TPE spectrum of the ion signal m/z=135 shows a structureless slow onset and is hence assigned to the 1-*tert*-butyl-4*H*-azaborinylium cation as a DPI fragment ion. The appearance energy at 0 K was determined to be 9.52 eV in the previous section. At a photon energy of 9 eV, as was employed for recording the mass spectra, an ion internal energy of 0.52 eV is necessary to induce dissociation. Pyrolysis at about 300°C leads to an increased thermal energy in the dissociating parent ion and thus a thermal shift of the observed onset energy to lower photon energies. Fig. 6.12 shows the computed thermal energy distribution for the azaborinine parent cation derived from the rovibronic density of states at room temperature and at 300°C.

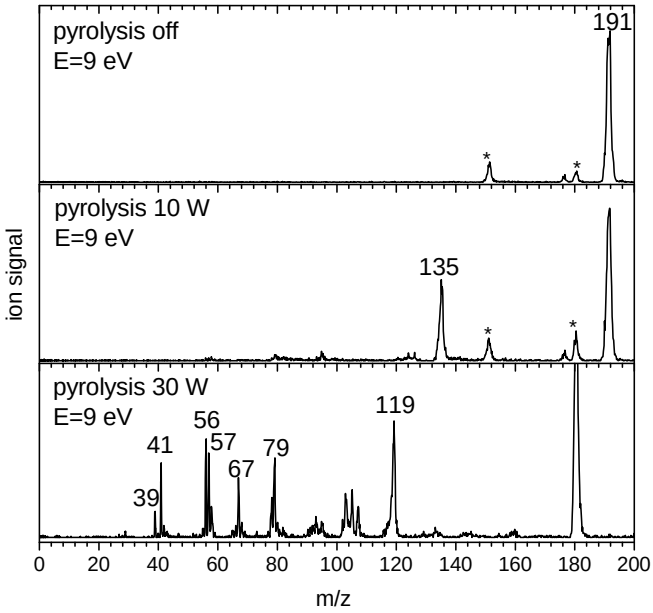


Figure 6.11.: Time-of-flight mass spectra of 1,4-di-*tert*-butyl-1,4-azaborinine for different pyrolysis conditions at 9 eV. 10 W pyrolysis power corresponds to about 300°C and shifts the DPI onset for the daughter ion m/z=135 below 9 eV. When harsher pyrolysis conditions are applied (lower pannel, ≈700°C) the precursor is completely converted into a number of different fragments. Peaks marked with an asterisk are due to contamination from a previous experiment. Figure adapted from ref. [338].

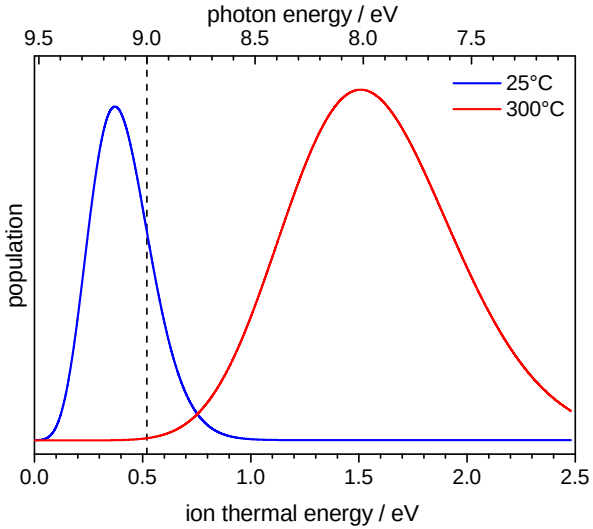


Figure 6.12.: Thermal energy distributions of the parent ion m/z=191 for room temperature and 300°C. For the photon energy used in fig. 6.11 (dashed line, 9.0 eV) an internal energy of 0.52 eV is necessary for dissociative ionization. At room temperature, only few ions have a sufficient thermal energy to dissociate, while at 300°C the majority of the parent ions will undergo dissociative photoionization. Note that the energy distributions are not normalized for better exemplification. Figure adapted from ref. [338].

As the population maximum for the room temperature ion lies at an internal energy of 0.35 eV and the distribution is relatively narrow, only few molecules are dissociatively ionized at a photon energy of 9.00 eV. Increasing the temperature to 300°C results in a shift of the energy distribution to a maximum at 1.60 eV ion thermal energy coinciding with a significant broadening. Thus, most of the prepared parent ions possess enough internal energy to dissociate and the daughter ion m/z=135 is observed even 0.52 eV below the 0 K appearance energy. If m/z=135 were a pyrolysis product, at least a small m/z=56 signal, corresponding to isobutene, the second pyrolysis product, should be visible in the mass spectrum at 10 W pyrolysis power. Even though the IE of isobutene is 9.24 eV,[314] thermal isobutene molecules (T≈300°C) should contribute to an ion signal high enough to be observed in the mass spectrum. As this is not not the case, it is concluded that m/z=135 is formed predominantly from dissociative photoionization, in which isobutene is cleaved off as a neutral fragment. At a pyrolysis temperature of around 700°C, peaks at m/z=39, 41, 56, and 57 showing no typical boron isotope pattern are observed. These can thus be assigned to hydrocarbons of the composition $C_3H_3$, $C_3H_5$, $C_4H_8$, and $C_4H_9$. Mass-selected threshold photoelectron spectra were recorded for these species to identify the respective isomer (fig. 6.13).

The ms-TPE spectrum for m/z=39 shows a distinct peak at 8.70 eV, which is in good agreement with the ionization energy of propargyl IE=8.71±0.02 eV.[51] Even the observed vibrational bands covertly visible in the recorded spectrum agree well with the literature TPES. For m/z=41, the TPE spectrum features a pronounced peak at 8.14 eV followed by two less intense bands forming a progression with a spacing of 50 meV. The observed species can thus be assigned to the allyl radical, for which an ionization energy of 9.13±0.01 eV and an excitation of the CCC bending mode at 52 meV was reported in a previous TPES experiment.[340] The TPE spectrum for m/z=56 has a very high signal/noise ratio. It can thus easily be assigned to isobutene, as the

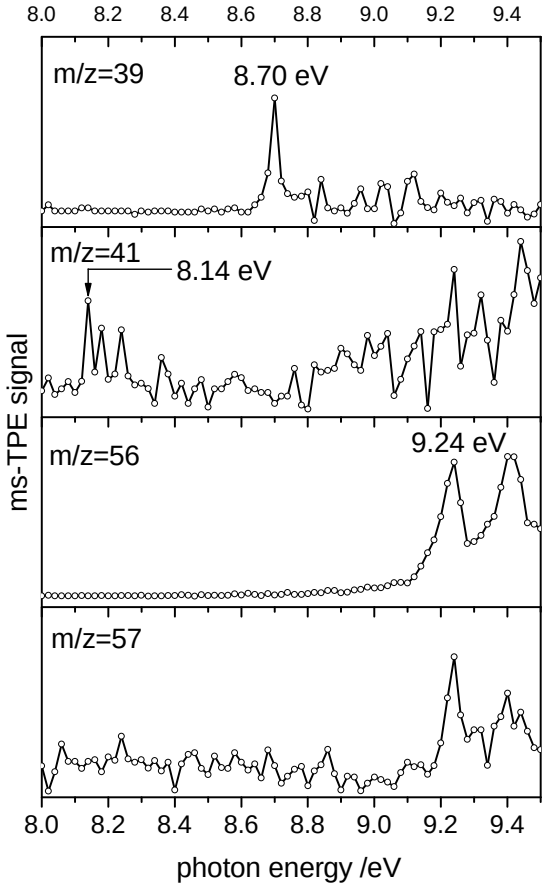


Figure 6.13.: Mass-selected TPE spectra of the hydrocarbon pyrolysis products propargyl (m/z=39), allyl (m/z=41), isobutene (m/z=56), and *tert*-butyl (m/z=57). For *tert*-butyl, the photon energy of the scanned energy range excites the radical in a Franck-Condon gap. That is why only the $^{13}$C signal of isobutene appears in the ms-TPES of m/z=56.

observed first peak maximum at 9.24 eV is in good agreement with the literature (IE=9.239 eV).[314] A C-C stretch vibrational band at +1350 $cm^{-1}$ is also observed. The signal/noise ratio is far lower for the TPE of m/z=57. The peaks at 9.24 eV and 9.40 eV coincide with the m/z=56 spectrum and are hence assigned to the $^{13}C$ signal of isobutene. However, the peak ratio m/z=56:57 in the mass spectrum in fig. 6.11 shows that another isomer must contribute to the signal. *Tert*-butyl is reported to have an ionization onset of 6.70 eV,[341] well below the scanned photon energy range. In the conventional PE spectrum no excited state was observed between 8.0 and 9.5 eV. It is thus assumed that the mass peak can be assigned also to the *tert*-butyl radical because a TPE signal is neither expected, nor observed in the experiment. Occurrence of these four hydrocarbons can be explained by formation of *tert*-butyl being the first bond cleavage step in the pyrolysis mechanism. Further loss of hydrogen leads to isobutene, from which subsequently allyl is formed by $CH_3$ cleavage. The ionization energy of $CH_3$ is higher than 9.0 eV, which explains why m/z=15 is not present in the shown mass spectra. Allyl can undergo an $H_2$ loss finally leading to the propargyl radical.

In the mass spectrum of fig. 6.11 recorded at a pyrolysis power of 30 W, three double peaks divided by 1 amu feature a distinct $^{10}B/^{11}B$ isotope pattern: m/z=67, 79, and 119 (for the $^{11}B$ isotopomers). This indicates the presence of exactly one boron atom. Hence the peaks can be assigned to species of the composition $C_3H_6BN$, $C_4H_6BN$, and $C_7H_{10}BN$ respectively.

Mass-selected TPE spectra at 700°C pyrolysis temperature were recorded in a photon energy range from 7.0 to 9.2 eV with a 20 meV step size to identify the species generated upon pyrolysis. Due to the low signal rate, several scans were added up resulting in a total acquisition time of 16 min per data point. Fig. 6.14 shows the mass-selected TPE spectrum for m/z=119.

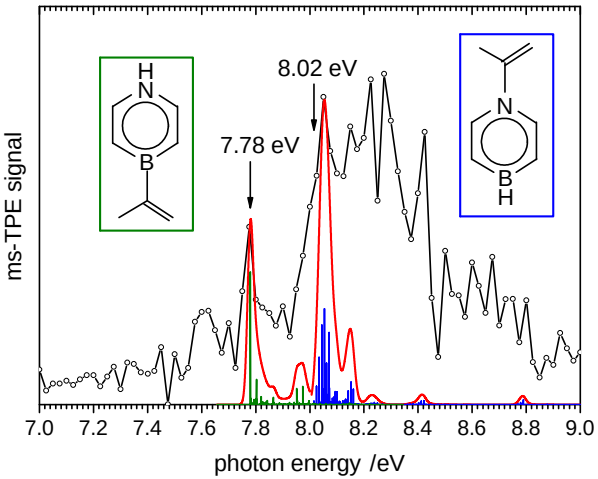


Figure 6.14.: Mass-selected TPE spectrum and FC simulation (sticks; red line, convolution with Gaussian fwhm=40 meV) of 1-(1-methylethenyl)-4*H*-1,4-azaborinine (green) and 4-(1-methylethenyl)-1*H*-1,4-azaborinine (blue), for which the TPES and the IEs of 7.78±0.05 and 8.02±0.05 eV, respectively, were tentatively assigned.

Compared to the precursor, fragment(s) with m/z=72 have to be cleaved upon pyrolysis for the formation of a boron-containing species with m/z=119. This can be explained by a simultaneous or consecutive loss of isobutene (m/z=56) and methane (m/z=16). As there are two *tert*-butyl groups present in the molecule, two isomers exist: 4-(1-methylethenyl)-1*H*-1,4-azaborinine and 1-(1-methylethenyl)-4*H*-azaborinine, in which the hydrocarbon substituent is connected either to the N atom or to the B atom. CBS-QB3 computations predicted ionization energies of 8.17 eV for the NH isomer and 8.26 eV for the BH isomer. A Franck-Condon simulation for both isomers is provided

in fig. 6.14. Both ionization energies and simulated spectra do not yield a convincing agreement between experiment and computation. Therefore, the assignment is only tentative since it is based mainly on chemical intuition. Other isomers were considered, but did not yield a more convincing agreement.

The signal peak m/z=79 corresponds to the loss of two isobutene equivalents. The ion was also observed to be formed by dissociative photoionization from the precursor molecule (*vide supra*). Loss of isobutene under thermal conditions was previously observed for a similar species [336] and seems thus a logical explanation. The mass-selected TPE spectrum for m/z=79 is depicted in fig. 6.15.

The spectrum features five distinct peaks at 8.40, 8.50, 8.66, 8.80 and 8.90 eV. No pronounced onset can be identified and assigned to the ionization energy. Again, CBS-QB3 computations were performed and an ionization energy of 8.79 eV was obtained for 1,4-dihydro-1,4-azaborinine. Using this value for the 0-0 transition in a Franck-Condon simulation yields a good match with the high energy part of the spectrum. Thus, another isomer is assumed to contribute to the spectrum. As reported in the literature, [323] computations revealed that 1,2-dihydro-1,2-azaborinine is significantly more stable than the 1,4-isomer by $93\,\mathrm{kJ\,mol^{-1}}$. Since the pyrolysis temperature was relatively high and the exposure time in the reactor comparably long, a rearrangement to the thermodynamically more stable isomer is assumed to be a likely reaction. A contribution of the 1,3-isomer seems however unlikely, as it lies $32\,\mathrm{kJ\,mol^{-1}}$ higher in energy than the 1,4-isomer. The computed ionization energy of the 1,2-isomer is 8.51 eV and a vertical value of 8.6 eV was reported in a conventional PES study. [335] Using an ionization energy of 8.27 eV for 1,2-dihydro-1,2-azaborinine in the Franck-Condon simulation reveals a convincing agreement of computed and experimental spectrum. For both isomers, computations predict an excitation of ring-deformation modes, which are responsible for the observed peak structure.

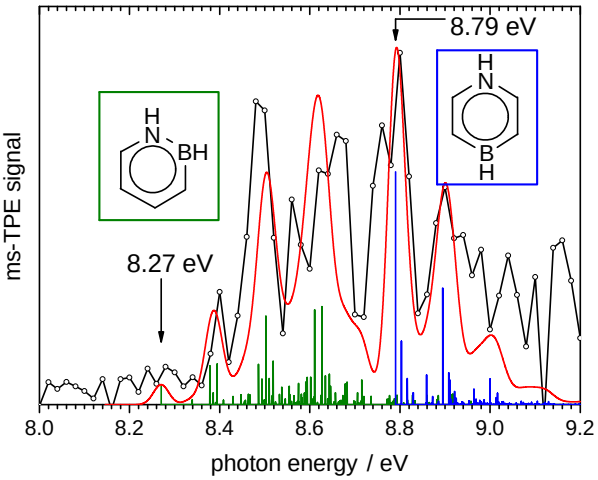


Figure 6.15.: Mass-selected TPE spectrum and FC simulation (red line, convolution with Gaussian fwhm=40 meV) of 1,2-dihydro-1,2-azaborinine (green sticks) and 1,4-dihydro-1,4-azaborinine (blue sticks). Ionization energies of 8.27±0.05 eV for the thermodynamically favored 1,2-azaborinine and 8.79±0.05 eV for the 1,4-isostere were determined. Figure adapted from ref. [338].

Another hint that rearrangement processes take place under the chosen experimental conditions is the observation of the mass peak m/z=67 corresponding to $C_3H_6BN$. A straightforward pyrolysis mechanism for 1,4-di-*tert*-butyl-1,4-azaborinine, which corresponds to elimination of fragments of the mass 124 amu, does not exist. The mass-selected TPE spectrum features a pronounced peak at 8.22 eV and a very distinct vibrational structure (see fig. 6.16). A valid assignment of the ms-TPES to one or more isomers should therefore be possible. That is why absolute and ionization energies were computed for isomers of the composition $C_3H_6BN$. Fig. 6.17 depicts the structures

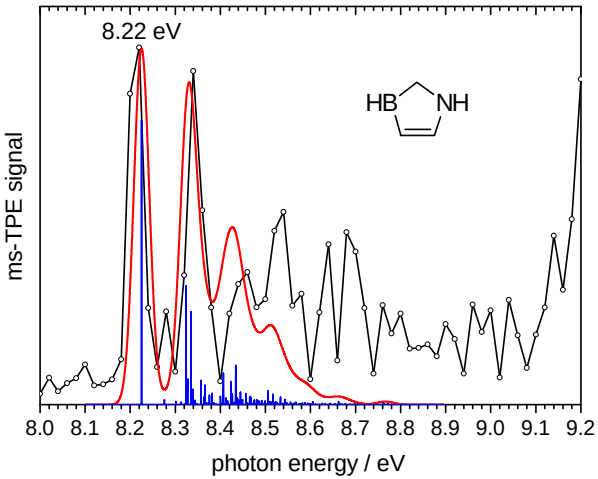


Figure 6.16.: Mass-selected TPE spectrum and FC simulation (blue sticks; red line, convolution with Gaussian fwhm=40 meV) of 1,2-dihydro-1,3-azaborole. The IE was determined to be 8.22±0.02 eV. The signal increase at 9.1 eV is caused probably by the contribution of a different isomer.

of ten $C_3H_6BN$ species for which both a stable neutral and cationic structure were obtained. The thermodynamically most stable isomers are the structures C and D. While the computed B3LYP/TZVP ionization energy for C is well outside the assumed error margin for DFT computations, D did not yield a matching Franck-Condon simulation. The only isomer for which a good agreement both for the ionization energy and the FC simulation is obtained is, although 35 meV (3.4 kJ $mol^{-1}$) higher in energy, structure A, 1,2-dihydro-1,3-azaborole. On the CBS-QB3 level, an ionization energy of 8.22 eV was derived, which is exactly the first peak maximum in the recorded spectrum.

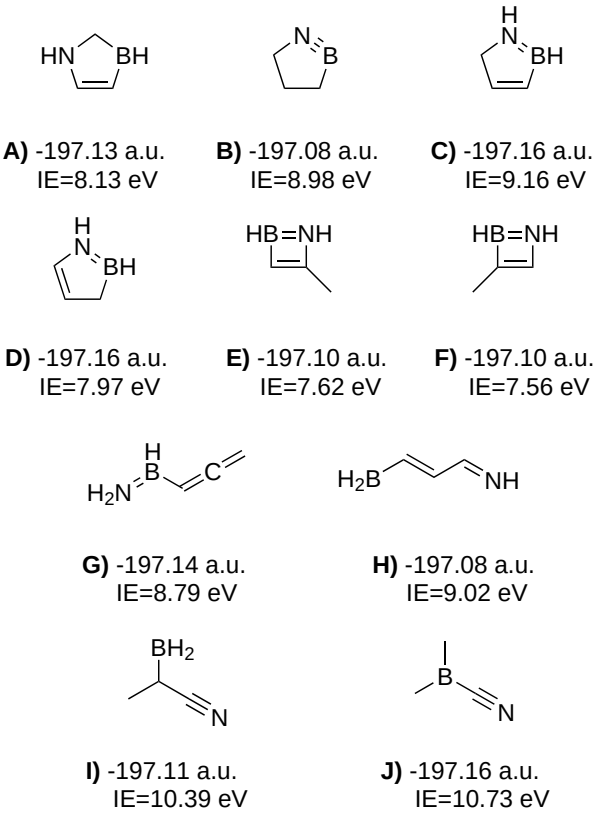


Figure 6.17.: Chemical structures for isomers of the composition $C_3H_6BN$ (m/z=67) and computed (B3LYP/TZVP) ionization energies. Other isomers were also considered, but only for the shown species both a stable neutral molecule and cation were obtained. Figure adapted from ref.[338].

Fig. 6.16 shows the Franck-Condon simulation for 1,2-dihydro-1,3-azaborole. The agreement with the experimental spectrum, which features only a rather low signal/noise ratio, is good. The observed vibrational band at 8.34 eV can be ascribed to two in plane ring-deformation modes. Further overtones and combination bands are congested in the background. At the edge of the recorded photon energy range, an increase of the TPE signal is observed. This can be explained either by an excited state in the cation or, more likely, by another isomer, e.g. the thermodynamically favored 1,5-dihydro-1,2-azaborole (structure C in fig. 6.17). The latter isomer's IE was computed to be 9.66 eV on CBS-QB3 level.

## 6.3. Summary 1,4-Di-tert-Butyl-1,4-Azaborinine

Photoionization and pyrolysis of 1,4-di-*tert*-butyl-1,4-azaborinine, for which a synthetic route has only been found recently,[332] was investigated in an iPEPICO experiment. The TPE spectrum yielded an ionization energy of 7.95±0.02 eV and vibrational structure in the ground state was analyzed in a Franck-Condon simulation. Several excited states of the cation arising from ionization of lower valence shell molecular orbitals are also visible in the spectrum. Dissociative photoionization of the parent molecule sets in above 9.2 eV. The first major dissociation channel is the loss of isobutene leading to m/z=135. A parallel elimination of methyl is observed, but neglected as the branching ratio in the breakdown ratio is clearly in favor of the former channel. Quantum chemical computations revealed that the BH product is preferentially formed in this dissociation step. The mechanism was found to be a retro-hydroboration in the cation involving a four-membered transition state for the H atom migration and a loosely-bound $\pi$ complex as an intermediate. This first dissociation step is followed by two competing sequential channels: loss of methyl leading to m/z=120 and elimination of a second

isobutene equivalent leading to m/z=79. The latter dissociation pathway was found to be very similar to the retro-hydroboration step. Modeling of the reaction rates with statistical theory yielded appearance energies of 9.52±0.05, 10.85±0.05, and 10.84±0.05 eV (m/z=135, 120, and 79, respectively). Although the involvement of reverse barriers and H atom migrations prevents from determining bond-dissociation energies in the cation, the experiment yields interesting insight into the bonding in monocyclic 1,4-azaborinines. Instead of elimination of *tert*-butyl by bond cleavage of the heteroatom-carbon bond, H atom migration and loss of the thermodynamically more stable leaving group isobutene is the favored pathway. The experiment thus supports the assumption, which also holds in the cation, that the retro-hydroboration reaction leading to the cleavage of B-C bonds with isobutene as a leaving group is a favored dissociation reaction.

In a second experiment, the molecule was pyrolyzed in a chemical reactor and the reaction products were identified. The precursor is completely converted to its pyrolysis products at a temperature of around 700°C. Formation of several hydrocarbons is observed and could be assigned to *tert*-butyl, isobutene, allyl radical, and propargyl radical by the corresponding mass-selected TPE spectrum. Three peaks at m/z=119, 79, and 67 show a distinct isotope pattern, thus indicating a boron-containing species. The recorded mass-selected TPE spectra for these mass channels featured, although rather long acquisition times per data point were used, only a low signal/noise ratio, which made an assignment challenging. M/z=119 was tentatively assigned to the two isomers 4-(1-methylethenyl)-1*H*-1,4-azaborinine and 1-(1-methylethenyl)-4*H*-azaborinine and IEs of 7.78±0.05 and 8.02±0.05 eV were determined. 1,4-dihydro-1,4-azaborinine and 1,2-dihydro-1,2-azaborinine, both m/z=79, were observed to ionize at 8.79±0.05 and 8.27±0.05 eV, respectively. Numerous isomers were considered for m/z=67. 1,2-dihydro-1,3-azaborole was found to yield the best match when comparing the experimental TPES with the Franck-

Condon simulation. Hence, the ionization energy for this five-membered ring was found to be 8.22±0.02 eV. The experimental conditions for the pyrolysis study enabled several fragmentation and rearrangement reactions to take place. The experimental data provide no insight into the associated mechanisms. However, it proves that the yet unobserved species 1,4-dihydro-1,4 azaborinine and 1,2-dihydro-1,3-azaborole are stable in the isolated gas phase.

# 7. Conclusion

The photoionization of nitrogen-containing molecules is addressed in this thesis. The work is primarily centered on nitrogen-containing intermediates relevant in combustion processes, in which they lead to the formation of nitrogen oxides, a major environmental concern. Comparably little experimental information on those intermediates is found in the literature so far because these species are difficult to generate and isolate. Especially open-shell intermediates, like radicals, have very short lifetimes. Photoionization experiments with VUV synchrotron radiation were performed to determine ionization energies of those nitrogen-containing transient species and analyze the corresponding cations' vibrational structure by threshold photoelectron spectroscopy. Beyond, the absolute photoionization cross section of cyclopropenylidene was determined, inner shell spectroscopy was employed to characterize Auger decay processes in isocyanic acid and the dissociative photoionization and pyrolysis of 1,4-di-*tert*-butyl-1,4-azaborinine was investigated.

The nitrogen-containing intermediates were either freshly prepared and stored under cryogenic temperatures during the experiment (HNCO) or generated *in situ* by vacuum flash pyrolysis of suitable precursor molecules. While most of the precursors are commercially available, organic synthesis was also employed to specifically design a molecule that is cleanly converted to a specific intermediate under thermal treatment. The weakest bond in a molecule is cleaved first upon pyrolysis, which then leads to the generation of a radical or carbene. A molecular beam of the highly diluted sample molecules in a

carrier gas guarantees a sufficiently long lifetime for spectroscopic characterization. The iPEPICO (imaging photoelectron photoion coincidence) setups of the VUV beamlines at the Swiss Light Source and Synchrotron SOLEIL were utilized to record mass-selected threshold photoelectron spectra after photoionization with monochromatic synchrotron radiation. This technique enables to correlate electrons and ions from the same ionization event. Signal from unpyrolyzed precursor molecules or side products in the pyrolysis does hence not affect the recorded spectra. TPE spectra reveal the ionization energy and often contain vibrational structure of the cationic species. Computed ionization energies and Franck-Condon simulations of the TPE spectra help interpret the experimental data. An unambiguous identification of a certain compound from these data is in most cases possible, which is why photoionization mass spectrometry and PEPICO is applied to detect the molecular composition of flames on-line. In addition, iPEPICO is a powerful tool to unravel dissociative photoionization processes. This is important to exclude that a daughter ion from DPI contributes to a radical TPE signal, as the weakest bond in the neutral molecule is usually also the weakest one in the cation. In addition, appearance energies of daughter ions often grant access to bond dissociation energies in the precursor cation and standard enthalpies of formation. In some cases, conclusions on the neutral species can then be drawn via thermochemical cycles.

## Highlighted Results

- The absolute photoionization cross section of $c$-$C_3H_2$, cyclopropenylidene, was determined ranging from the carbene's ionization energy of 9.17 eV to 9.80 eV. The cross section at 9.5 eV, for example was determined to be 4.456±1.717 Mb. It was shown that mass discrimination effects are negligible small for the continuous molecular beam in pyrolysis experiments.
- Rotational $\Delta K$ subbands and the yet unobserved bending modes were resolved in the TPE spectrum of isocyanic acid, HNCO, for the ground state. The ionization energy could thus be accurately determined to be 11.602±0.005 eV.
- The O 1s Auger spectrum of isolated HNCO confirmed that HNCO is generated in the dissociative photoionization as a neutral fragment at 14 eV from thymine on a timescale of about 400 fs. Bands in the O 1s, N 1s, and C 1s normal Auger and NEXAFS spectra of HNCO, which is isoelectronic to $CO_2$, were preliminarily assigned.
- The NCO radical was generated from chlorine isocyanate and a clean TPE spectrum was recorded, which confirmed the previously reported ionization energy of 11.76 eV. A yet unobserved progression in the TPE spectrum was assigned to the NCO bending mode, which gains intensity through autoionization.
- Pyrrolyl, $C_4H_4N$, was successfully generated from 3-methoxypyridine and the ionization energy was determined to be 9.11±0.02 eV from the TPE spectrum. The appearance energy of the pyrrolyl cation from the precursor was determined to be 12.35±0.03 eV, which enabled to derive the standard enthalpy of formation of the pyrrolyl radical via a thermochemical cycle: $\Delta_f H_{0K}$=301.1±15.1 kJ mol$^{-1}$
- Cyanovinylacetylene was observed as a pyrolysis product of 3-bromopyridine and an ionization energy of 10.04±0.02 eV was obtained.

- The ionization energy of the 3-picolyl radical, generated from pyrolysis of 3-picolylamine, was determined to be 7.600±0.015 eV from the TPE spectrum.
- A retro-hydroboration in the cation was identified in the DPI mechanism of 1,4-di-*tert*-butyl-1,4-azaborinine (IE=7.95±0.02 eV), and the appearance energies of this channel and two consecutive fragmentation channels were determined.
- Two yet unobserved boron-containing heterocycles, 1,4-dihydro-1,4-azaborinine (IE=8.79±0.05 eV) and the five-membered ring 1,2-dihydro-1,3-azaborole (IE=8.22±0.02 eV), were identified as pyrolysis products of the substituted azaborinine.

# 8. Zusammenfassung

Die vorliegende Arbeit beschäftigt sich mit der Photoionisation von stickstoffhaltigen Molekülen. Im Mittelpunkt stehen dabei vor allem stickstoffhaltige Intermediate, die in Verbrennungsprozessen zur Bildung von umweltschädlichen Stickoxiden führen. In der Literatur wird bislang vergleichsweise wenig über Experimente an diesen Intermediaten berichtet, da es schwierig ist diese herzustellen und zu isolieren. Vor allem offenschaligen reaktive Moleküle, wie beispielsweise Radikale, haben sehr kurze Lebensdauern. Mit Hilfe von Photoionisationsexperimente mit VUV Synchrotronstrahlung wurden anhand von Schwellenphotoelektronenspektren Ionisierungsenergie von solchen stickstoffhaltigen transienten Verbindungen bestimmt und die Schwingungsstruktur der jeweiligen Kationen analysiert. Außerdem wurde der absolute Photoionisationsquerschnitt von Cyclopropenyliden bestimmt, mittels Innerschalenspektroskopie wurden Augerprozesse der Isocyansäure untersucht und die dissoziative Photoionisation und Pyrolyse von 1,4-di-*tert*-butyl-1,4-Azaborinin wurde analysiert.

Die stickstoffhaltigen Intermediate wurden entweder unmittelbar vor dem Experiment hergestellt und während des Experiments bei sehr niedrigen Temperaturen gehalten (HNCO) oder *in situ* durch Pyrolyse eines geeigneten Vorläufermoleküls erzeugt. Während die meisten verwendeten Vorläufer kommerziell erhältlich sind, wurden auch spezielle Verbindungen synthetisiert, die unter Pyrolysebedingungen möglichst ohne Nebenprodukte zu einem bestimmten Intermediat konvertiert werden können. In der Pyrolyse wird in den

meisten Fällen die schwächste Bindung des Vorläufers zuerst gebrochen, was dann zur Bildung eines Radikals oder Carbens führt. Die Lebenszeit dieser Intermediate in einem Molekularstrahl der hochverdünnten Probe in einem Trägergas ist ausreichend lang für eine spektroskopische Charakterisierung. Nach der Photoionisation mit monochromatischer Synchrotronstrahlung wurden massenselektive Schwellenphotoelektronenspektren an den iPEPICO (imaging photoelectron photoion coincidence) Setups der VUV Beamlines an der Swiss Light Source und dem Synchrotron SOLEIL aufgenommen. Mit Hilfe dieser Technik können Elektronen und Ionen des selben Ionisationsereignisses zugeordnet werden. Damit können Störsignale des unpyrolyisierten Vorläufermoleküls und von Nebenprodukten der Pyrolyse eliminiert werden. Schwellenphotoelektronenspektren liefern die Ionisierungsenergie und in den meisten Fällen kann auch die Schwingungsstruktur des Kations aufgelöst werden. Ionisierungsenergien aus quantenchemischen Rechnungen und Franck-Condon Simulationen der Schwellenphotoelektronenspektren stützen die Interpretation der experimentellen Daten. In den meisten Fällen kann aus diesen Datensätzen eine bestimmte Verbindung eindeutig identifiziert werden. Darum wird Photoionisations-Massenspektrometrie und PEPICO auch dafür angewendet die molekulare Zusammensetzung von Flammen on-line zu analysieren. Außerdem eignet sich iPEPICO hervorragend dafür dissoziative Photoionisationsprozesse (DPI) zu untersuchen. Dies ist unter anderem auch wichtig um auszuschließen, dass ein Tochterion aus der DPI des Vorläufers zum Schwellenphotoelektronensignal des Radikals beiträgt, da die schwächste Bindung des neutralen Moleküls normalerweise auch die schwächste Bindung des Kations ist. Die Auftrittsenergien der Tochterionen liefern außerdem in vielen Fällen Bindungsdissoziationsenergien des Kations und Standardbildungsenthalpien. Idealerweise können über thermochemische Kreisprozesse somit auch Rückschlüsse auf die neutrale Verbindung gezogen werden.

## Wichtige Erkenntnisse

- Der absolute Photoionisationsquerschnitt von $c$-$C_3H_2$, Cyclopropenyliden, wurde im Bereich zwischen der Ionisierungsenergie des Carbens von 9.17 eV und 9.80 eV bestimmt. Bei einer Photonenenergie von 9.5 eV wurde ein Photoionisationsquerschnitt von 4.453±1.717 Mb erhalten. Es wurde gezeigt, dass Massendiskriminierungseffekte im kontinuierlichen Molekularstrahl für Pyrolyseexperimente vernachlässigbar sind.
- Rotations $\Delta K$ Teilbanden und die bislang nicht beobachteten Biegeschwingungen wurden im Schwellenphotoelektronenspektrum von Isocyansäure, HNCO, aufgelöst. Die Ionisierungsenergie konnte somit sehr genau auf 11.602±0.005 eV bestimmt werden.
- Das O 1s Augerspektrum von reiner HNCO bestätigte, dass HNCO als Neutralfragment in der dissoziativen Photoionisation von Thymin bei 14 eV auf einer Zeitskala von etwa 400 fs entsteht. Eine vorläufige Zuordnung der Banden der O 1s, N 1s und C 1s nichtresonanten Auger und NEXAFS Spektren von HCNO, das isoelektronisch zu $CO_2$ ist, wurde außerdem gezeigt.
- Das NCO Radikal wurde pyrolytisch aus Chlor-Isocyanat erzeugt und es konnte ein Schwellenphotoelektronenspektrum frei von Störsignalen aufgenommen werde. Dadurch wurde die Ionisierungsenergie von 11.76 eV aus früheren Experimenten bestätigt. Eine bislang unbeobachtete Progression im Schwellenphotoelektronspektrum wurde der NCO Biegeschwingung zugeordnet, die durch Autoionisationsprozesse Intensität gewinnt.
- Pyrrolyl, $C_4H_4N$, konnte erfolgreich aus 3-Methoxypyridin generiert werden und die Ionisierungsenergie wurde zu 9.11±0.02 eV bestimmt. Die Auftrittsenergie des Pyrrolylkations aus DPI des Vorläufermoleküls beträgt 12.35±0.03 eV. Damit konnte über einen thermochemischen Kreisprozess die Standardbildungsenthalpie des Pyrrolyl Radikals berechnet

werden: $\Delta_f H_{0K}$ =301.1±15.1 kJ mol$^{-1}$

- Cyanovinylacetylen wurde als Pyrolyseprodukt von 3-Brompyridin identifiziert und die Ionisierungsenergie wurde zu 10.04±0.02 eV bestimmt.
- Eine Ionisierungsenergie von 7.600±0.015 eV konnte für das 3-Picolyl Radikal, das durch Pyrolyse von 3-Picolylamin erzeugt wurde, ermittelt werden.
- In der DPI von 1,4-di-*tert*-butyl-1,4-Azaborinin (IE=7.95±0.02 eV) wurde eine Retrohydroborierung im Kation beobachtet und die dazugehörige Auftrittsenergie neben den zweier weiterer sequentieller Fragmentierungskanälen bestimmt.
- Zwei bislang unbeobachtete borhaltige Heterozyklen, 1,4-dihydro-1,4-Azaborinin (IE=8.79±0.05 eV) und der Fünfring 1,2-dihydro-1,3-Azaborol (IE=8.22±0.02 eV), wurden als Pyrolyseprodukte des substituierten Azaborinins identifiziert.

# A. Further Projects

## A.1. Ionization Energy of Phenylpropargyl radicals

Propargyl $C_3H_3$ is a very important intermediate in combustion processes, as self-reaction of two such radicals leads to benzene.[342] Subsequent hydrogen elimination and reaction with a third $C_3H_3$ moiety followed by another hydrogen elimination leads to hydrocarbons of the composition $C_9H_7$, which were identified in the pyrolysis of toluene.[343] There are three isomers of this composition, which are all resonantly stabilized radicals: indenyl, 1-phenylpropargyl (1PPR), and 3-phenylpropargyl (3PPR). Reilly *et al.* produced 1PPR from discharges of a mixture of hydrocarbons and identified it in the laser-induced fluorescence spectrum.[344] IR/UV double resonance spectroscopy showed that both 1PPR and 3PPR dimerize efficiently and selectively to *para*-terphenyl ($C_{18}H_{14}$) and 1-phenylethynyl-naphthalene ($C_{18}H_{12}$).[58] This observation underlines the importance of PPR radicals in PAH formation. Using the respective brominated precursors, the three isomers could be generated by flash pyrolysis and the ionization energies were determined in photoionization experiments at the SLS.[345] However, an accurate ionization energy was obtained only for indenyl from the TPE spectrum (IE=7.53±0.02 eV). For 1PPR, the ionization energy was determined to be 7.4±0.1 eV from the PIE curve only and for 3PPR, the TPE spectrum exhibited a rather low signal/noise ratio. Hence, the ionization energy for 3PPR was only tentatively assigned to IE=7.20±0.05 eV. As the photon flux at the SLS

has been improved since, mostly due to the newly installed 150 lines $mm^{-1}$ grating providing a significantly higher photon flux, the ionization energies of 1PPR and 3PPR were reinvestigated. Both radicals were again generated by flash pyrolysis of the brominated precursors, which were synthesized according to the literature.[346–348]

**1PPR:** The ionization energy for 1PPR was previously determined to be 7.4±0.1 eV from a photoion yield spectrum.[345] The 150 $mm^{-1}$ monochromator grating at the X04DB beamline increased the photon flux by a factor of ten compared to the previous experiment with the 600 $mm^{-1}$ grating. Hence, it was possible to record a threshold photoelectron spectrum of 1PPR. The radical was generated by pyrolysis of 3-phenyl-3-bromopropyne at a temperature of about 700°C. As benzyl radicals are also formed under these pyrolysis conditions, the TPE spectrum was recorded mass-selectively with a step size of 5 meV and an acquisition time of 8 min per data point. The spectrum depicted in fig. A.1 shows a shallow rise of electron signal at 7.15 eV which can be explained by the occurrence of hot and sequence bands due to vibrational excitation of the neutral molecules. A distinct peak with the maximum at 7.24 eV is observed, followed by further intense peaks at 7.28 and 7.36 eV. The first peak maximum at 7.24 eV is assigned to the ionization energy of 1PPR. Due to the broad nature of this band an error margin of ±0.02 eV is assumed. This is in good agreement with computations on CBS-QB3 level of theory, which predict an IE of 7.30 eV. The revised value lies below the one reported previously from a simple photoion yield spectrum,[345] but is close to the upper limit of the range between 5.1 and 7.3 eV predicted by Reilly *et al.* from a multiphoton ionization experiment.[344] A Franck-Condon analysis based on B3LYP/6-311G(2d,d,p) geometries and vibrational frequencies revealed that the C1-C2-C3 bending mode computed at 432 $cm^{-1}$ (54 meV) is excited upon ionization. The peak at 7.28 eV can thus be assigned to this vibrational mode. The peak at 7.36 eV can be explained by the excitation of a combination band

of the C4-C1-C2 in plane bending mode with a ring deformation mode computed at 990 $cm^{-1}$ (122 meV) and 1005 $cm^{-1}$(125 meV). The atom numbering and the Franck-Condon simulation, which yields a reasonable match with the experimental data, are also depicted in fig. A.1. Although the signal/noise ratio is not overly high in the obtained ms-TPE spectrum, the determined improved ionization energy was recently confirmed by T. W. Schmidt and coworkers.[349] In their experiment a two-color scheme was employed to record a PIE curve and an even more accurate ionization energy of 7.232±0.001 eV was reported. This new value sits well within the above stated error bars.

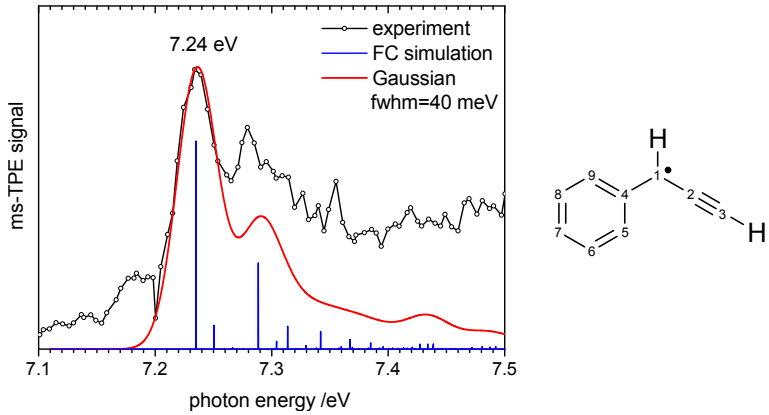


Figure A.1.: Mass-selected TPE spectrum, Franck-Condon simulation and chemical structure of 1-phenyl-propargyl. The ionization energy is determined to be 7.24±0.02 eV. Figure reprinted from ref.[350]. © 2014 Wiley-VCH Verlag GmbH&Co. KGaA, Weinheim.

**3PPR:** 3PPR was generated by pyrolysis of 1-phenyl-3-bromo-propyne at 700°C. Fig. A.2 shows the TPE spectrum. Each data point was averaged for 9 min and the step size was again 5 meV. Note that this time all electrons were considered in the TPE spectrum, as no further mass peaks besides m/z=115 were observed in the investigated photon energy range and the vapor pressure

of the 3PPR precursor is higher than for the 1PPR one. This allowed utilizing the 600 $mm^{-1}$ grating offering a higher photon resolution. The spectrum features a sharp rise resulting in a peak maximized at 7.25 eV, which is followed by two further distinct peaks at 7.30 and 7.35 eV forming a progression with a spacing of 425 $cm^{-1}$. Some smaller bands are visible in the spectrum at higher photon energies. A value of 7.28 eV is obtained for the ionization energy from CBS-QB3 computations, which also predict only a moderate change of geometry upon ionization. The ionization energy of 3PPR is therefore assigned to 7.25±0.01 eV from the TPE spectrum. This ionization energy lies within the error margin of the 7.20±0.05 eV reported in the previous experiment. The Franck-Condon simulation (B3LYP/6-311G(2d,d,p)) also depicted in fig. A.2 is in very good agreement with the experimental spectrum. The observed 425 $cm^{-1}$ progression can be assigned to a symmetric ring deformation mode with a computed wavenumber of 417 $cm^{-1}$.

Although the TPE spectra of 1PPR and 3PPR are quite similar both in terms of adiabatic ionization energy and observed vibrational progression, an isomerization between the two isomers in the pyrolysis region can be excluded. On one hand, an IR/UV double resonance spectrum confirmed that the two radicals are cleanly generated by pyrolysis of the respective bromide precursor.[351] On the other hand, a closer look at the TPE spectra reveals some distinct differences. The signal/noise ratio is better in the 3PPR spectrum, although the monochromator grating providing a lower photon flux was utilized. In addition, the bands in the 1PPR spectrum are significantly broader than in the 3PPR spectrum. Partly, this is of course due to the lower photon energy resolution of the 150 $mm^{-1}$ grating. Excitation of an out-of-plane vibration in 1PPR as predicted by computations plays also a non-negligible role in the broadening of the observed bands. The experiment has proven that the quality of the data obtained at the SLS X04DB beamline has significantly improved, as the ionization energies of 1PPR and 3PPR could be determined

to a higher degree of accuracy in comparison to the experiments performed in 2009.

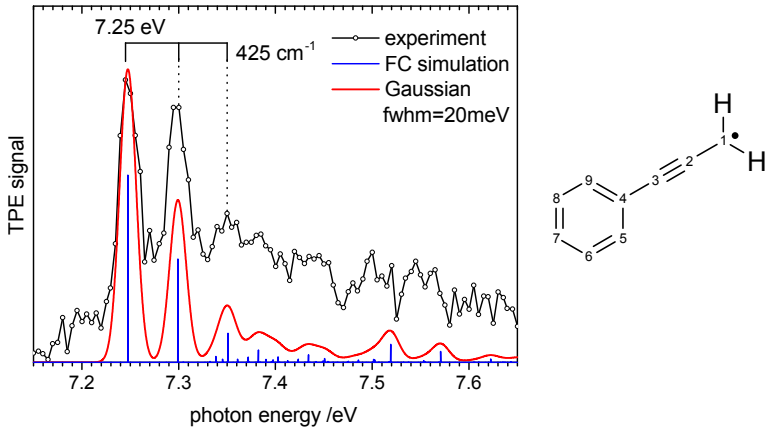


Figure A.2.: TPE spectrum, Franck-Condon simulation and chemical structure of 3-phenyl-propargyl. The first peak maximum at 7.25±0.01 eV is assigned to the ionization energy. Figure reprinted from ref. [350]. © 2014 Wiley-VCH Verlag GmbH&Co. KGaA, Weinheim.

## A.2. Dissociative Photoionization of Cyclopropenylidene

Cyclopropenylidene is not only an important combustion intermediate (see chapter 4), but has also been detected in interstellar clouds.[185,187,188] High energy electromagnetic radiation, e.g. from Lyman-Alpha-Emitters (121.6 nm, 10.2 eV), can ionize most organic molecules molecules, which is one reason why ion-molecule reactions are of great importance in the interstellar space.[9,352] Analysis of the dissociative photoionization of $C_3H_2$ yields insight into the thermochemical properties of both the parent and the daughter cations. The cleavage of a hydrogen atom upon dissociative photoionization was identified as the lowest lying DPI channel for cyclopropenylidene in previous experiments performed in our group.[348] In these studies, 3-chlorocyclopropene was utilized as a pecursor for the pyrolytic generation of the cyclic $C_3H_2$ carbene (m/z=38). HCl (m/z=36/38, IE=12.745 eV[353]) is the secondary pyrolysis product. As DPI of the carbene only sets in above the IE of HCl, the TPE signal of the parent molecule contains a contribution of the $H^{37}Cl$ isotope. This was considered by subtracting the $H^{35}Cl$ TPE signal from the m/z=38 signal employing a weighting factor reflecting the natural isotope ratio of chlorine. However, the TPE signal of $H^{35}Cl$ seemed also to contribute to the m/z=37 TPE signal corresponding to the $C_3H^+$ daughter ion. An empirical factor was used in this case to correct the $C_3H^+$ TPE signal. The breakdown diagram was then plotted, but the parent signal fraction did not decrease to 0 at high photon energies. It was consequently assumed that the $H^{37}Cl$ contribution was not subtracted correctly. The breakdown diagram was fitted nevertheless assuming a fast dissociation process of the cation and the appearance energy was determined to be $AE_{0K}$=13.6 eV. However, a temperature of 2000 K had to be utilized for obtaining a good agreement of fit and experimental data. This temperature is unrealistically high for the pyrolysis power

of 40 W, which was found to be the optimum for a nearly complete conversion of 3-chlorocyclopropene, even when neglecting any cooling effects in the molecular beam. As a selective mono-chlorination could not be achieved in the synthesis of 3-chloro-cyclopropene, chloro-cyclopropenylidene was identified as a second pyrolysis product of the precursor sample. The chloro-carbene also dissociatively ionizes to $C_3H^+$ and the appearance energy for the deuterated analogue was determined to be $AE_{0K}$(*c*-$C_3DCl$; $C_3D^+$)=13.3 eV.[348] It seems therefore likely that $C_3H^+$ was generated from two different parent molecules in this experiment, which makes a detailed analysis of the DPI of cyclopropenylidene impossible. This problem can be overcome by using a different pyrolysis precursor. As discussed in chapter 4, cyclopropenylidene can be efficiently generated from a quadricyclane precursor yielding the desired carbene and benzene.[183,184] A sample of this precursor of high purity ensured that DPI channels different from the cyclopropenylidene can be excluded. The breakdown diagram in the photon energy range between 12.6 and 14.1 eV was then recorded at the Swiss Light Source. Fig. A.3 shows the breakdown diagram and the TOF distributions of ions detected in coincidence with threshold electrons. The data were accumulated from four individual scans employing a 50 meV step size and a total acquisition time of 8.5 min per data point. As for the photoionization cross section, the pyrolysis temperature was set to T=470°C during the experiment.

Although the signal/noise ratio is relatively low, as Franck-Condon factors are very small for the employed photon energy range, it is apparent that the $C_3H_2^+$ parent ion signal starts to decrease at 12.9 eV. The slope of the breakdown curves is shallow and the parent fraction reaches zero around 13.7 eV. The ion TOF distributions in coincidence with threshold electrons shows a symmetric peak shape for the m/z=37 daughter ion indicating a fast dissociation process. The energy of the parent ion's disappearance should therefore correspond the $AE_{0K}$. Quantum chemical computations were performed to identify the DPI

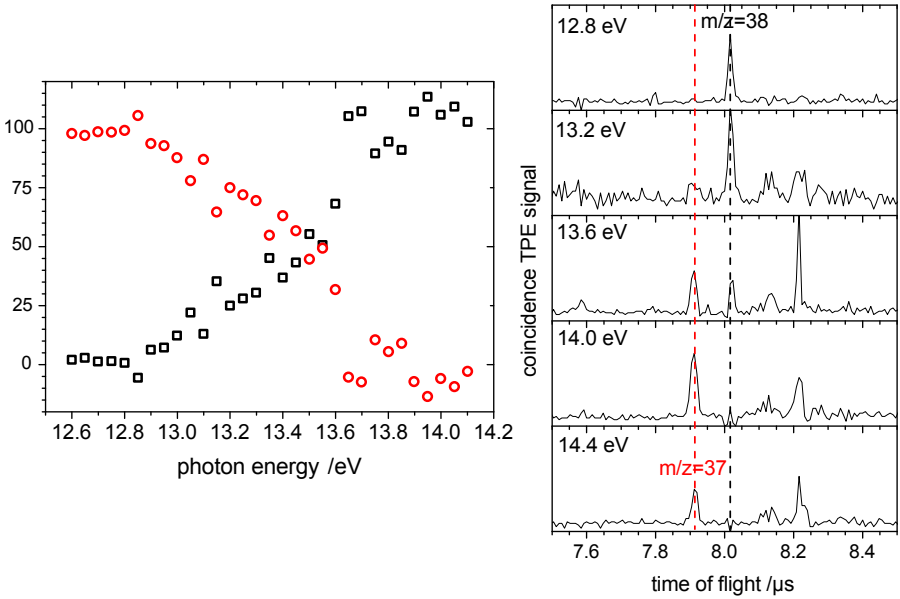


Figure A.3.: Experimental breakdown diagram and TOF distributions for the DPI of cyclopropenylidene.

mechanism and energetics of cyclopropenylidene. In agreement with previous computations,[348,352] cyclic $C_3H^+$ was found not to be a minimum on the potential energy surface, but a transition state leading to linear $C_3H^+$. The activation barrier for dissociative photoionization of cyclopropenylidene on this direct hydrogen loss pathway was computed to be 14.29 eV on CBS-QB3 level of theory. This is in clear disagreement with the observation in the experimental breakdown diagram because the appearance energy of $C_3H^+$ should be several hundreds of meV lower based on the experimental data. Hence, a rearrangement of the parent ion has to be considered. There exist two further stable $C_3H_2^+$ isomers: $HCCCH^+$ and $H_2CCC^+$. $HCCCH^+$ lies only 0.25 eV (24 kJ mol$^{-1}$) higher in energy than the cyclopropenylidene cation. Wong and

Radom report an activation barrier of 1.75 eV for the rearrangement of cyclic $C_3H_2^+$ based on MP2/6-31G(d) computations.[352] However, these computations could not be reproduced and calculations on different levels of theory failed to locate a transition state structure. Hence, it remains unclear if rearrangement to the linear propargylene cation precedes the hydrogen loss of $C_3H_2^+$ and if so, how high the activation barrier for such a rearrangement is. The hydrogen loss of linear $HCCCH^+$ was computed to precede on a pathway without a reverse barrier and, assuming the rearrangement transition state lying below the products, the appearance energy for the $HCCCH^+$ ion from cyclopropenylidene is consequently computed to be $AE_{0K}$($c$-$C_3H_2$; $l$-$C_3H^+$)=13.60 eV on the CBS-QB3 level. Alternatively, a rearrangement to $H_2CCC^+$ is possible, for which an activation barrier of 3.29 eV was obtained. $H_2CCC^+$ lies 1.96 eV higher in energy than the cyclopropenylidene cation. Hydrogen loss of $H_2CCC^+$ again leads to linear $C_3H^+$ and hydrogen preceding on a barrierless pathway. The appearance energy for this DPI channel therefore does not differ from the channel involving the rearrangement to the propargylene cation and both pathways seem to match the experimental data. The modeled mechanisms for the DPI of cyclopropenylidene to $C_3H^+$ and atomic hydrogen is illustrated in fig. A.4.

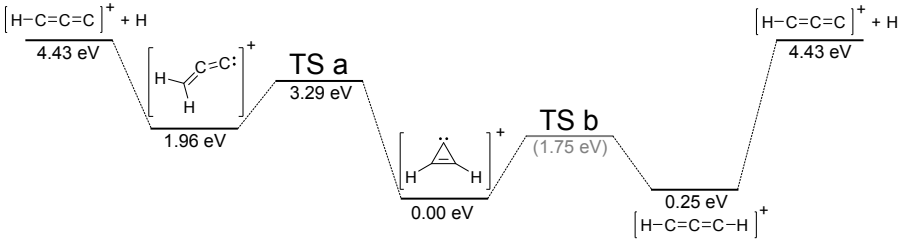


Figure A.4.: DPI mechanism of cyclopropenylidene computed on CBS-QB3 level of theory.

Based on these computations, attempts to fit the breakdown diagram were made employing the simplified statistical adiabatic channel model (SSACM, see sec. 2.5.3) because the dissociation has no reverse barrier. Fig. A.5 shows fits assuming a rovibrational temperature of 470°C, the temperature of the pyrolysis tube during the experiments, and of 930°C. An appearance energy of 13.67 eV (470°C) and 13.93 eV (930°C) is obtained from the respecitve fits. It does not make any observable difference in the fitted curves and appearance energies, whether $HCCCH^+$ or $H_2CCC^+$ are defined as dissociating ions.

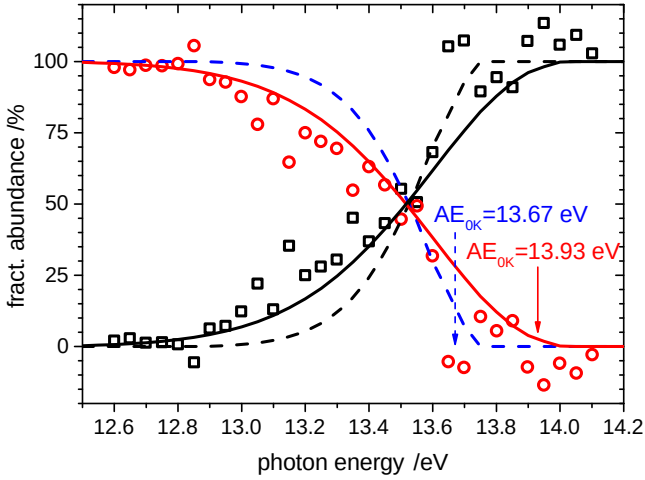


Figure A.5.: Modeled breakdown diagram for the DPI of cyclopropenylidene assuming temperatures of 470°C (dashed lines, daughter blue) and 930°C (solid lines, daughter red).

It is obvious that the 470°C fit does not agree well with the experimental breakdown curve as the slope of the modeled curves are much steeper than the experimental ones. The fit at 930°C, by contrast, matches well the ex-

periment, but is an unrealistically high choice of temperature. As discussed above, the TOF distributions unambiguously indicate fast dissociation rates. The fractional abundance of the parent ion only depends on the rovibronic density of states of the dissociating ion and the temperature as demonstrated in eq. (2.43) and (2.44). There are two possibilities why a good fit is only obtained utilizing an unrealistically high temperature. Either the rovibronic density of state of the dissociating ion is not calculated correctly, or the internal energy distribution of the ion does not follow a Boltzmann distribution as assumed in the calculation.

The DOS of neutral cyclopropenylidene was calculated from the harmonic frequencies and rotational constants for the fit and was then transposed onto the ionic manifold. Here, the approximation is made that the photoionization probability is uniform for all rovibronic states, which works in general the better, the larger the molecule.[134] As $C_3H_2$ is rather small, this assumption might be incorrect with photoionization selection rules coming into play. The isomerization of the cation prior to dissociation was also not considered for the fit. If the barrier for the isomerization is near the dissociation limit, the isomerization has to be considered explicitly.[129] The observed rate constant $k_{obs}$ for such cases can be approximated in the RRKM approach as:

$$k_{obs} = \frac{N^{\ddagger}_{iso}}{h\rho(E)}\left(\frac{N^{\ddagger}_{diss}}{N^{\ddagger}_{iso} + N^{\ddagger}_{diss}}\right) \tag{A.1}$$

Here, $N^{\ddagger}_{iso}$ and $N^{\ddagger}_{diss}$ are the sum of states for the transition states leading to isomerization and dissociation, respectively. At the dissociation limit, there is only one open channel leading to dissociation, i.e. $N^{\ddagger}_{diss} = 1 \ll N^{\ddagger}_{iso}$. Consequently, the dissociation is the rate limiting step and eq. (A.1) simplifies

for photon energies near the dissociation limit:

$$k_{obs} = \frac{N^{\ddagger}_{diss}}{h\rho(E)} \tag{A.2}$$

At photon energies well above the dissociation limit, the sum of states of the dissociation transition state increases more rapidly than the sum of states of the isomerization's one, as the former is a loose transition state.[129] The rate for passing the activation barrier associated with the isomerization then limits the observed rate constant.

$$k_{obs} = \frac{N^{\ddagger}_{iso}}{h\rho(E)} \tag{A.3}$$

However, since the TOF distributions indicate a fast dissociation rate for the DPI of cyclopropenylidene, the barrier for isomerization of $C_3H_2^+$ should be significantly lower than the dissociation limit. Hence, although no transition state structure could be located for the isomerization to linear $C_3H_2^+$, the isomerization is assumed to play only a minor role and does therefore not explain the deviation of the fit from the experiment at 470 °C. The computed appearance energy of the $C_3H^+$ ion lies 4.18 eV and 2.47 eV above the energy of the dissociating ions $HCCCH^+$ and $H_2CCC^+$, respectively. The approximation that the neutral's DOS can be simply transposed on the cationic manifold therefore seems to be valid since the DOS of states at the dissociation limit will be high enough that there will not be significant differences between the various ionic structures. An aspect that is not considered in the DOS utilized for the shown fit of the breakdown diagram is the anharmonicity of the vibrational modes. As a relatively high internal energy is necessary for the $C_3H_2^+$ cations to dissociate, higher quantum numbers of high-energy modes might be significantly populated, but are omitted in the DOS calculation as a harmonic approximation is employed. It was for example observed in the

photodissociation of propargyl that anharmonicity has to be taken into account to obtain a good agreement with the experimental dissociation rates of small molecules.[354] For the photodissociation of propargyl, an additional scaling factor for the vibrational wavenumbers of propargyl derived from the heat capacity of small hydrocarbons of 0.71 was employed to account for anharmonicity. An adaption of this procedure was attempted for the fit of the breakdown curves of cyclopropenylidene, but yielded no improved match for realistic scaling factors. Consequently, anharmonicity is most likely not the only component which is compensated by assuming a temperature of 930°C to obtain a reasonable fit of the experimental data. Previous studies of dissociative photoionization processes at room temperature have shown that the population of the ionic states is well reproduced by assuming a Boltzmann distribution of this temperature within an error bar of ±30-40 K.[84,338,355,356] Unpublished data on the dissociative photoionization of methane in a molecular beam heated in a pyrolysis tube show also a good match of fit and experiment for internal energy distributions calculated by the Boltzmann formula at the respective reactor temperature. The Franck-Condon simulation of the $C_3H_2$ TPE spectrum shown in fig. (4.5) indicates that there is no vibrational cooling in the molecular beam and the temperature of cyclopropenylidene should therefore equal 470°C. However, the literature does not provide reports on dissociative photoionization of thermalized parent ions at 470°C or even higher temperatures, so it hasn't been tested yet if Boltzmann distributions can really be assumed for these significantly thermalized ions. It could be speculated that high-energy (e.g. CH stretching) modes, which are not Franck-Condon active and therefore not reproduced in the FC simulation, are excited upon pyrolysis and therefore lead to a significant broadening of the breakdown diagram. However, sequence bands representing transitions from vibrationally excited states to the cationic vibrational ground state should have been observed in the TPE spectrum depicted in fig. 4.5.

The dissociative photoionization of cyclopropenylidene can be studied when using the quadricyclane precursor since neither parent ion signal, nor daughter ion signal are perturbed by contributions originating from side-products of the pyrolysis. The TOF distributions revealed a fast dissociation process for the loss of an hydrogen atom and the appearance energy for $C_3H_2^+$ can therefore be assigned to the photon energy at which the parent ion signal dissappears, i.e. in the range between 13.7 eV and 13.9 eV. Computations reveal that isomerization of the cyclopropenylidene cation to *l*-$C_3H_2^+$ or $H_2CCC^+$ takes place prior to the dissociation step. Both isomers lead to the linear $C_3H^+$ isomer and no reverse barriers are associated with the mechanistic pathways. The computed $AE_{0K}$=13.60 eV compares well with the experimental data. A good fit of the breakdown curve was however only obtained assuming an unrealistically high temperature of 930°C. The assumption of a too high temperature was also necessary for the modeling of the data of the chloro-cyclopropenylidene precursor. Although several potential sources of errors, which might compensate the high temperature, have been identified, a concluding explanation and model of the breakdown diagram is still missing.

## A.3. Pyrolysis of 3,3'-Azopyridine

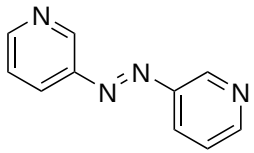

Figure A.6.: Chemical structure of 3,3'-azopyridine.

Azobenzene efficiently produces phenyl, a reactive $\sigma$-radical, upon pyrolysis.[357] 3,3'-azopyridine (fig. A.6) was hence considered as a precursor for the 3-pyridyl radical, which is isoelectronic to phenyl. The synthesis of the precursor is described in sec. B.3. The sample was placed inside the vacuum chamber and gently heated to 65°C. As can be seen in fig. A.7, a strong signal for the precursor at m/z=184 is observed. The peaks at m/z=68 and m/z=86 can presumably be ascribed to sample contamination, but cannot be assigned to certain compounds. Increasing the pyrolysis power to 10 W reveals new peaks in the mass spectrum at m/z= 78 and 106. As observed for the precursor 3-bromopyridine, the TPE spectrum of the m/z=78 signal corresponding to the pyridylium ion does not feature any structure and seems to be generated by DPI of the precursor, only. M/z=106 is also a DPI fragment ion (-pyridyl) of the precursor. Thermal decomposition of the precursor seems to occur at 20 W pyrolysis power since the precursor and m/z=106 daughter ion signal are significantly less intense. Additional peaks at m/z=54 and 79 are observed, which are assigned to butadiene and pyridine. The observation of pyridine is an indication that 3-pyridyl is initially released upon pyrolysis of 3,3'-azopyridine, but abstracts an H-atom from a reaction partner in bimolecular reaction in the pyrolysis tube. Interestingly, W. Sander and co-workers published the successful matrix isolation of the three isomeric pyridyl radicals, which were generated by pyrolysis of the respective azopyridine precursors, only a few weeks after these experiments had been conducted.[302]

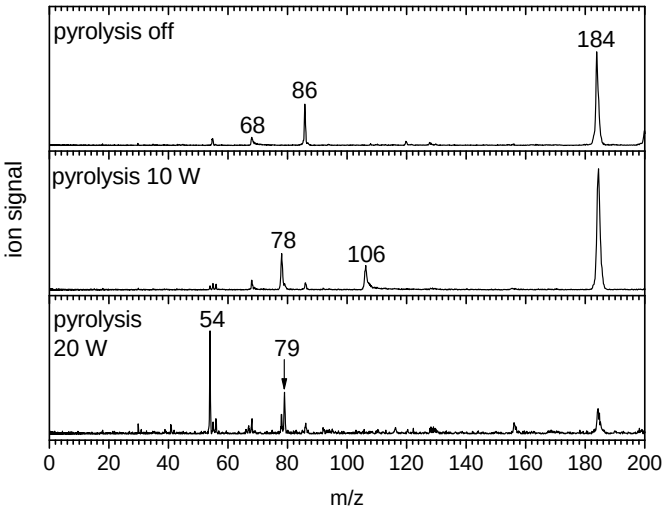


Figure A.7.: Mass spectra of 3,3'-azopyridine for different pyrolysis powers at 9.5 eV.

## A.4. Pyrolysis of N-Aminopyrrole

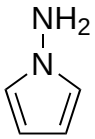


Figure A.8.: Chemical structure of N-amino-pyrrole.

As discussed in sec. 5.3, cleavage of the N-X bond of a N-substituted pyrrole derivative will initially not generate the pyrrolyl radical in its $^2A_2$ ground state, but in the $^2A_1$ excited state, for which the unpaired electron is located in the nitrogen $\sigma$-orbital. It will therefore be interesting to learn if this excited state can be directly probed by TPES. It is also thinkable that the excited state relaxes to the ground state, e.g. via a conical intersection. Furthermore, isomerization to a more stable structure might occur. N-aminopyrrole was chosen as a precursor (see fig. A.8) because the N-N bond is the molecule's most labile bond and hence expected to be cleaved first. N-aminopyrrole is a liquid with a high vapor pressure, which is easily accessible by organic synthesis (sec. B.4). In addition, the second pyrolysis fragment $NH_2$ is also an interesting nitrogen centered radical. Fig. A.9 shows the mass spectrum of N-aminopyrrole at a photon energy of 9.5 eV and a reactor temperature of 700°C. An intense precursor signal (m/z=82) is still visible, but decomposition has already set in as peaks at m/z=66 and m/z=67 are observed. The inset in fig. A.9 shows the lower part of a mass spectrum at 12.0 eV for the same experimental conditions. The signal at m/z=16 corresponds to the amidogen radical $NH_2$. However, most of the generated radical seems to immediately form $NH_3$ (m/z=17) in a bimolecular reaction. As the $NH_2/NH_3$ ratio is lower compared to $NH_2$ precursors investigated previously,[358] the chemistry of the $NH_2$ channel was not pursued any further.

The most intense peak besides the precursor signal in the mass spectrum is observed at m/z=67. This signal could be assigned to pyrrole from the mass-selected TPE spectrum. Obviously, pyrrolyl generated in an electron-

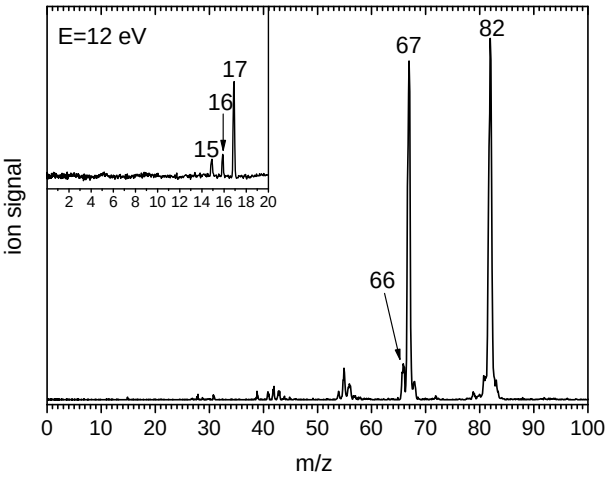


Figure A.9.: Mass spectrum of N-aminopyrrole at 9.5 eV and a pyrolysis temperature of 700°C. The inset shows the lower part of the mass spectrum at 12.0 eV.

ically excited state abstracts a hydrogen atom in a bimolecular reaction in the chemical reactor and forms pyrrole. However, a small signal for m/z=66 corresponding to a $C_4H_4N$ species is visible in the mass spectrum. Fig. A.10 shows the corresponding ms-TPE spectrum, which suffers from a low signal/noise ratio, though. A peak at 8.87 eV above noise level is nevertheless observed. Comparing the spectrum with the ms-TPES recorded for $C_4H_4N$ in the 3-methoxypyridine experiment (fig. 5.27 and 5.29), an assignment of the observed m/z=66 to cyanoallyl seems possible. Due to the large step size of 15 meV in the shown spectrum, the double peak originating from the (E)- and (Z)-isomer cannot be resolved. Considering, that the cyanoallyl stereoisomers are computed to be thermodynamically equally stable as the pyrrolyl radical,

it seems likely that the electronic relaxation of the cyclic species coincides with a structural change. It might therefore be worthwhile to re-investigate the TPE spectrum in the energy range between 8.7 and 9.0 eV, although this will be a time-consuming experiment due to the low signal intensity.

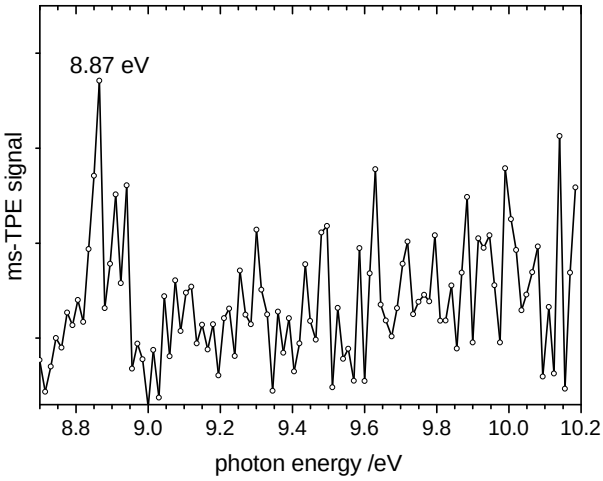


Figure A.10.: Mass-selected TPE spectrum of m/z=66 in the pyrolysis of N-aminopyrrole.

## A.5. Pyrolysis of Di-tert-Butyl-Iminoborane

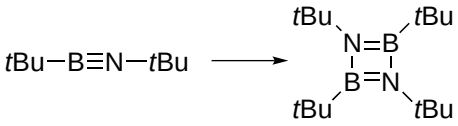


Figure A.11.: Dimerization of di-*tert*-butyl-iminoborane.

Iminoborane, HBNH, is the simplest BN counterpart of an organic molecule, isoelectronic to acetylene $C_2H_2$. So far, only few spectroscopic data on the isolated species exist,[359–363] although it is assumed to be an important building block of borazine. Guided by the observation that two equivalents of isobutene are cleaved in the pyrolysis of 1,4-di-*tert*-butyl-1,4-azaborinine, di-*tert*-butyl-iminoborane was considered a promising precursor for the *in situ* generation of iminoborane. The synthesis of di-*tert*-butyl-iminoborane[364] was carried out in the group of Prof. Dr. Holger Braunschweig (Institute of Inorganic Chemistry, University of Würzburg). The liquid sample can be stored at -20°C for several days and evaporates at 10°C in vacuo. It has therefore a sufficiently high vapor pressure for gas phase experiments in a molecular beam. Di-*tert*-butyl-iminoborane has a relatively high metastability since only 50 % are reported to have dimerized to 1,2,3,4-diazaboretidine after three days at 50°C, as illustrated in fig. A.11.

Fig. A.12 shows room temperature mass spectra at 9, 10, and 12 eV of the sample. The parent cation (m/z=139) seems to be quite unstable and dissociatively ionizes to a daughter ion with m/z=124 just at its ionization limit. M/z=124 corresponds to a loss of methyl upon DPI. At 12 eV, a second DPI fragment is visible at m/z=82 corresponding to a loss of a *tert*-butyl group. The peaks at 108/110, 93/95, and 73 are assigned to $Me_3SiCl$, which is used in the synthesis, and its DPI fragment ions $Me_2SiCl^+$ and $Me_3Si^+$.[365] A detailed analysis of the DPI would be challenging due to the unstable parent ion and was therefore omitted.

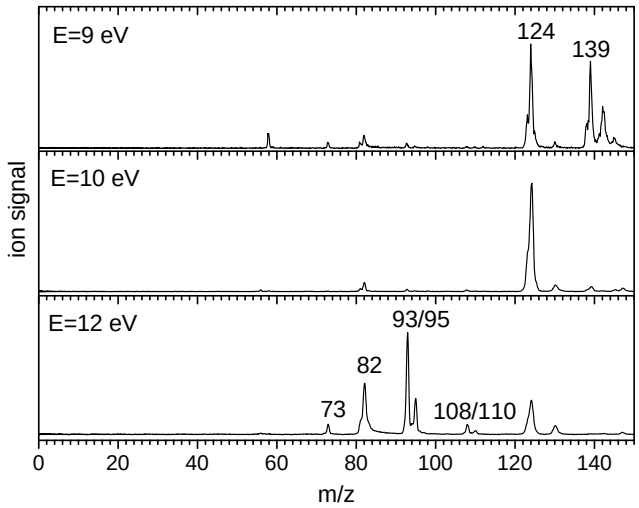


Figure A.12.: Mass spectra of di-*tert*-butyl-iminoborane for different photon energies.

Expecting the observation of HBNH as a decomposition product of di-*tert*-butyl-iminoborane, pyrolysis experiments were performed. Fig. A.13 shows mass spectra at a photon energy of 10.0 eV for different reactor temperatures. At a heating power of 20 W, new peaks at m/z=40, 42, and 56 are observed, which are assigned to propyne, propene, and isobutene originating from the *tert*-butyl substituents. Signals for m/z=15 and 26 corresponding to methyl and acetylene are observed at a pyrolysis power of 55 W, which is on the upper operational limit for scans lasting several hours. In addition, two small signals featuring the typical boron isotope pattern are observed at m/z=93 and m/z=107. Neutral fragments of 32 amu, presumably two methane moieties, have to be cleaved for the generation of m/z=107. M/z=93 corresponds a loss of neutral fragments of 46 amu, e.g. two methyl groups and one methane

fragment. Attempts to record threshold photoelectron spectra to identify the structure of these pyrolysis products were made, but yielded no result. It is remarkable that, although isobutene is generated upon pyrolysis, no mass peak corresponding to one of the *tert*-butyl-iminoborane isomers or even to iminoborane is observed.

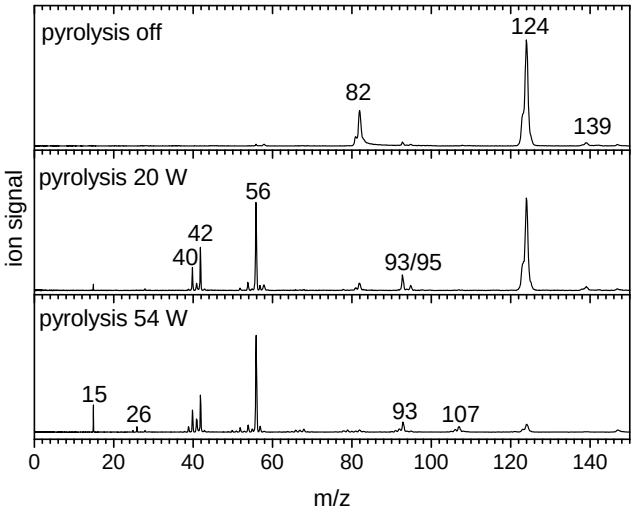


Figure A.13.: Mass spectra of di-*tert*-butyl-iminoborane at 10.0 eV for different pyrolysis conditions.

# B. Synthesis

All chemicals were bought at *Chemikalienausgabe der Fakultät für Chemie und Pharmazie (University of Würzburg), Sigma-Aldrich,* and *abcr* and used without further purification unless stated otherwise. NMR spectra were recorded on a *Bruker Avance II HD 400* spectrometer at the *Institute of Organic Chemistry (University of Würzburg)* and gas phase IR spectra on a *Bruker IFS120HR* FT-IR spectrometer.

## B.1. Isocyanic Acid

Different synthetic routes for isocyanic acid have been described in the literature.[222,366–368] While for the valence-shell photoionization experiments HNCO was prepared following the procedure of Drozdoski *et al.* ,[222] isocyanic acid was synthesized according to the description of Ashby and Werner for the inner-shell photoionization experiments,[367] as the yield in the latter route turned out to be significantly higher. HNCO polymerizes to cyanuric acid above 0°C and must therefore be constantly cooled. The purity of the sample was checked by comparing gas phase IR spectra to the literature.[217,219]

### HNCO Synthesis with Stearic Acid

35.07 g (123.3 mmol) of stearic acid were combined with 5.00 g (61.6 mmol) of vacuum-dessicated potassium cyanate and the mixture was heated in vacuo (<8 mbar) to 92°C while stirring. The evolving gas was collected in a trap cooled to -196°C with liquid nitrogen. After 3 h, gas formation ceased and further impurities were removed from the raw product by a trap-to-trap distillation from -40°C to -100°C (ethanol/liquid nitrogen mixtures) under dynamic vacuum conditions. The product, which contained traces of $CO_2$, was collected in the sample container. The maximum yield, which was determined after HNCO had polymerized to cyanuric acid, was 43 mg (1.0 mmol; 1.6 %).

*IR (gas phase):* $\tilde{\nu}$ /$cm^{-1}$: 556 ($\delta$(NCO) in plane), 696 ($\delta$(NCO) out of plane), 787 ($\delta$(HNC) in plane), 1311($\nu$(N=C=O) sym.), 2267 ($\nu$(N=C=O) asym.), 3562 ($\nu$(CH))

### HNCO Synthesis with Phosphoric Acid

10 mL of a saturated aqueous solution of potassium cyanate (7.5 g; 92.5 mmol) were added to 10 mL of phosphoric acid (85 %) in small portions via a syringe in vacuo (<10 mbar) over 20 min. The temperature of the flask was kept constant by cooling in a water bath. The evolving gas was collected in a trap cooled to -196°C with liquid nitrogen. Impurities were then removed by a trap-to-trap distillation from -30°C to -80°C (ethanol/liquid nitrogen mixtures) under dynamic vacuum conditions. The reaction was finished when the gas evolution in the first cooling trap stopped after about 60 min. The contamination by $CO_2$ was determined to be less than 1 % from a 100 keV photoelectron spectrum. The maximum yield, which was determined after HNCO had polymerized to cyanuric acid, was 2.2 g (51.1 mmol; 55.3 %).

*IR (gas phase):* $\tilde{\nu}$ /$cm^{-1}$: 557 ($\delta$(NCO) in plane), 697 ($\nu$(NCO) out of plane), 787 ($\delta$(HNC) in plane), 1324($\nu$(N=C=O) sym.), 2269 ($\nu$(N=C=O) asym.),

3560 ($\nu$(CH))

## B.2. Chlorine Isocyanate

Chlorine isocyanate was synthesized following the route first described by Nachbaur *et al.*[258,369] 20.0 g (86.1 mmol) of trichloroisocyanuric acid were placed in a Schlenk flask equipped with a thermometer and heated in a heating mantle (level II) in vacuo (1 mbar) for 90 min. A gas evolved at a temperature of 110°C and a yellow liquid was collected in a trap cooled to -196°C with liquid nitrogen. The raw product was further purified in a trap-to-trap distillation between -40°C (ethanol/liquid nitrogen) and -120°C (pentane/liquid nitrogen) under dynamic vacuum conditions. A yellow liquid was obtained with an estimated yield of 1.5 g (19.4 mmol; 22%), which contained still some contamination of $Cl_2$ and HNCO as observed in the IR (lit.[370]) and TPE spectra.

*IR (gas phase)*: $\tilde{\nu}$ /cm$^{-1}$: 557 ($\delta$(NCO) in plane), 614 ($\nu$(C-Cl)), 706 ($\delta$(NCO) in plane), 1299($\nu$(N=C=O) sym.), 2219 ($\nu$(N=C=O) asym.)

## B.3. 3,3'-Azopyridine

The synthesis of 3,3'-azopyridine was conducted according to Brown and Granneman.[371] 2.5 g (26.6 mmol) 3-aminopyridine dissolved in 50 mL of water were added dropwise to 150 mL (231.5 mmol) of an aqueous NaOCl solution (10 %) over a period of 90 min. The reaction mixture was extracted with ether. The solid was filtrated and also extracted with ether. After drying the organic phase over $MgSO_4$, the solvent was evaporated. 1.0 g (5.4 mmol; 20.3 %) of 3,3'-azopyridine, a red solid, were obtained. When following the route suggested as described by Thies *et al.*[372], in which the NaOCl solution is added to 3-aminopyridine, no product could be isolated.

$^1$*H-NMR (400 MHz, $CDCl_3$):* $\delta$=9.23 (dd, 2H), 8.74 (dd, 2H), 8.17 (ddd, 2H), 7.47 (ddd, 2H) ppm

## B.4. N-Aminopyrrole

*N*-Aminopyrrole was synthesized following the instruction described by Dey and Lightner.[373] Phthalimide (1) was converted into the product in three steps, as depicted in fig. B.1.

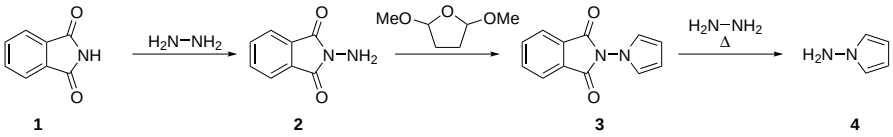


Figure B.1.: Synthesis of *N*-aminopyrrole.

***N*-Aminophthaltimide (2).** 5.3 mL (5.2 g, 104 mmol) of hydrazine-monohydrate were added dropwise to an ice-cold suspension of 14.7 g (100 mmol) phthalimide (1) in 100 mL of dry ethanol. The mixture was stirred for 2 h at 5°C, before 200 mL of ice-water were added. The solid was filtrated, washed with water and dried in air. 10.2 g (63 mmol; 63 %) of the white, crystalline solid (2) were obtained.

$^1$*H-NMR (400 MHz, $CDCl_3$):* $\delta$=4.17 (brs, 2H), 7.72 (dd, 2H), 7.84 (dd, 2H)

***N*-Phthalimidopyrrole (3).** 7.5 g (46.2 mmol) of (2) and 7.5 mL (7.3 g, 55.5 mmol) of 2,5-dimethoxytetrahydrofuran were dissolved in 75 mL of dioxane and heated at reflux for 30 min. After addition of 7.5 mL 5N HCl the solution darkened. The mixture was cooled, filtrated and the precipitate was washed with a dioxane/water mixture (1:3). 5.74 g (27.0 mmol, 58 %) of (3) were isolated.

$^1$*H-NMR (400 MHz, $CDCl_3$):* $\delta$=6.25 (dd, 2H), 6.64 (dd, 2H), 7.76 (dd, 2H), 7.89 (dd,2H) ppm

***N*-Aminopyrrole (4).** 2.2 mL (2.2 g, 43 mmol) of hydrazine-monohydrate were added to a solution of 5 g (23 mmol) *N*-Phthalimidopyrrole (3) in 65 mL of methanol and heated at reflux for 60 min. After cooling, 1.5 mL acetic acid were added and the mixture was heated at reflux for further 15 min. After filtration, the precipitate was washed with methanol and the solvent of the combined organic solutions was evaporated yielding a yellow oil. After addition of ca. 80 mL of aqueous sodium hydroxide (40 %), the organic product was extracted with diethylether (3x50 mL). The ether was then evaporated and 1.31 g (16 mmol, 68 %) of a yellow liquid were obtained. The product (4) can be stored at -25°C for several weeks.
$^1$*H-NMR (400 MHz, CDCl$_3$):* $\delta$=4.86 (brs, 2H), 6.04 (dd,2H), 6.70 (dd,2H) ppm

# C. Absolute Photoionization Cross Section of Cyclopropenylidene

Table C.1.: Absolute photoionization cross section of cyclopropenylidene.

| $h\nu$ /eV | $\sigma_i$ /Mb |
|---|---|
| 8.80 | 0.029 |
| 8.81 | 0.038 |
| 8.82 | 0.026 |
| 8.83 | 0.039 |
| 8.84 | 0.040 |
| 8.85 | 0.031 |
| 8.86 | 0.041 |
| 8.87 | 0.076 |
| 8.88 | 0.030 |
| 8.89 | 0.037 |
| 8.90 | 0.039 |
| 8.91 | 0.052 |
| 8.92 | 0.037 |
| 8.93 | 0.067 |
| 8.94 | 0.056 |

| $h\nu$ /eV | $\sigma_i$ /Mb |
|---|---|
| 9.13 | 0.282 |
| 9.14 | 0.260 |
| 9.15 | 0.352 |
| 9.16 | 0.616 |
| 9.17 | 0.811 |
| 9.18 | 0.813 |
| 9.19 | 0.927 |
| 9.20 | 0.906 |
| 9.21 | 0.962 |
| 9.22 | 0.967 |
| 9.23 | 1.079 |
| 9.24 | 1.034 |
| 9.25 | 1.081 |
| 9.26 | 1.129 |
| 9.27 | 1.065 |

| $h\nu$ /eV | $\sigma_i$ /Mb |
|---|---|
| 9.46 | 3.791 |
| 9.47 | 3.828 |
| 9.48 | 4.052 |
| 9.49 | 4.363 |
| 9.50 | 4.453 |
| 9.51 | 4.694 |
| 9.52 | 5.047 |
| 9.53 | 4.999 |
| 9.54 | 5.117 |
| 9.55 | 5.152 |
| 9.56 | 5.380 |
| 9.57 | 5.427 |
| 9.58 | 5.710 |
| 9.59 | 6.166 |
| 9.60 | 5.971 |

| | |
|---|---|
| 8.95 | 0.056 |
| 8.96 | 0.081 |
| 8.97 | 0.132 |
| 8.98 | 0.087 |
| 8.99 | 0.068 |
| 9.01 | 0.112 |
| 9.01 | 0.127 |
| 9.02 | 0.141 |
| 9.03 | 0.129 |
| 9.04 | 0.166 |
| 9.05 | 0.161 |
| 9.06 | 0.169 |
| 9.07 | 0.200 |
| 9.08 | 0.218 |
| 9.09 | 0.245 |
| 9.10 | 0.234 |
| 9.11 | 0.258 |
| 9.12 | 0.251 |

| | |
|---|---|
| 9.28 | 1.186 |
| 9.29 | 1.354 |
| 9.30 | 1.760 |
| 9.31 | 1.782 |
| 9.32 | 2.031 |
| 9.33 | 2.192 |
| 9.34 | 2.329 |
| 9.35 | 2.251 |
| 9.36 | 2.456 |
| 9.37 | 2.768 |
| 9.38 | 2.810 |
| 9.39 | 2.914 |
| 9.40 | 2.844 |
| 9.41 | 2.971 |
| 9.42 | 3.187 |
| 9.43 | 3.208 |
| 9.44 | 3.375 |
| 9.45 | 3.536 |

| | |
|---|---|
| 9.61 | 6.575 |
| 9.62 | 6.589 |
| 9.63 | 6.619 |
| 9.64 | 6.890 |
| 9.65 | 6.970 |
| 9.66 | 7.210 |
| 9.67 | 7.455 |
| 9.68 | 7.652 |
| 9.69 | 7.711 |
| 9.70 | 8.045 |
| 9.71 | 8.068 |
| 9.72 | 8.132 |
| 9.73 | 8.743 |
| 9.74 | 8.506 |
| 9.75 | 9.083 |
| 9.76 | 9.009 |
| 9.77 | 9.056 |

# D. Computed IEs of $C_4H_4N$ isomers

Absolute energies and ionization energies of 16 isomers of the composition $C_4H_4N$ were computed on CBS-QB3 level of theory for comparison with the recorded ms-TPE spectrum of m/z=66 in the pyrolysis of 3-methoxypyridine. The chemical structures and energies are depicted in fig. D.1.

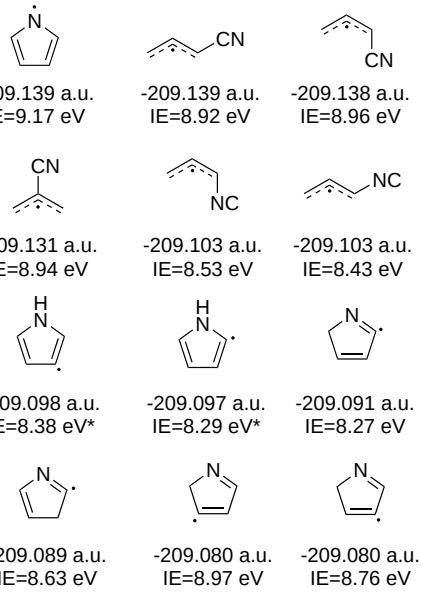

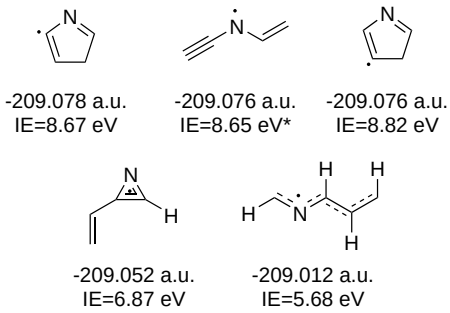


Figure D.1.: Absolute and ionization energies of $C_4H_4N$ isomers computed on the CBS-QB3 level. IE's marked with an asterisk indicate triplet cationic ground states.

# E. SPES Data Treatment for SLS

### A) Saving (mass-selected) electron images from raw data

Mass-selected electron images can be saved for each photon energy utilizing a script for the i2PEPICO_Analysis_2.0 software of the Swiss Light Source VUV beamline, for which an example is depicted in fig. E.1:

```
1  Resolu := 0.01
2  TMin := 12.413
3  TMax := 12.625
4  Offset := 10.00
5
6  AddCoincCrit[AddEvent[Im1,0,0,ROIAll,TOFStart,Im1],AddEvent[Ch6,TMin,TMax,nil,TOFStop,nil]]
7  AddCoincCrit[AddEvent[Im1,0,0,ROIAll,TOFStart,Im1],AddEvent[Ch6,{TMin+Offset},{TMax+Offset},nil,TOFStop,nil]]
8  AddCoincCrit[AddEvent[Im1,0,0,ROIAll,TOFStart,Im1],AddEvent[Ch6,TMin,TMax,nil,TOFStop,nil]]
9  AddCoincCrit[AddEvent[Im1,0,0,ROIAll,TOFStart,Im1],AddEvent[Ch6,0,50,nil,TOFStop,nil]]
10
11 CycleFiles[CurrInFolder, scan_021.A_*]
12
13 Load[CurrInFolder,CycFile, 0, 50, Resolu]
14 FillLoadedParams
15 PrintEPICSFixedStr[Concat[LoadedParam[Start,E],"\ eV"]]
16
17 PlotImage[Im1Res[3],Im2]
18 Multiply[Im1Res[2],-1]
19 Add[Im1Res[1],Im1Res[2]]
20 PlotImage[Im1Res[1],Im1]
21
22 PlotTOF[TOFRes[1]]
23
24 SaveIm[Im1Res[4],ROIAll,false,CurrInFile,im]
25
26 Next
```

Figure E.1.: Screenshot of the script for extracting electron images from SLS ras data with the i2PEPICO_Analysis_2.0 software.

line 1: resolution of the TOF spectrum in µs

line 2: lower TOF limit for selected mass peak

line 3: upper TOF limit for selected mass peak

line 4: offset for false coincidence area

line 6/8: coincidence criterion for selected mass peak

line 7: coincidence criterion for false coincidences

line 9: coincidence criterion for non-mass-selected electron image

line 18/19: subtract false coincidence image (this is a workaround as the program is only able to execute the operations addition and multiplication)

line 24: save the electron image corresponding to the fourth coincidence criterion (here: no mass-selection)

Details on the syntax can be found in the manual of the i2PEPICO_Analysis_2.0 software.

**B) Abel Transformation and Radial Integration**

The electron image can be reconstructed employing the pBASEX algorithm, which is implemented in the LabView program Analyse-7.8a_2014 developed by Lionel Poisson. Screenshots of the software panels (fig. E.2 and E.3) and explanations are given in the following.

By selecting 'Run Imaging Analysis' the program is started. First, the path of the experimental images saved in ASCII mode has to be selected under 'path data' and 'path parameter'. It is advantageous to load an image directly at the ionization threshold since in the next step the center of the image has to be selected. A new window opens after clicking on 'Symmetry' in the 'Image Modification' sub-panel, in which the image center is defined by the cursor position. After confirming the image center, the transformation algorithm 'pBASEX' is selected in the 'Image Transformation' sub-panel. By clicking on the 'calculate' button, a new window opens, in which the basis parameters 'High Res - High Prec' and the root of the basis functions, which have to be stored on the working hard disk, and the desired basis ('P0-HRHP-I') are selected.

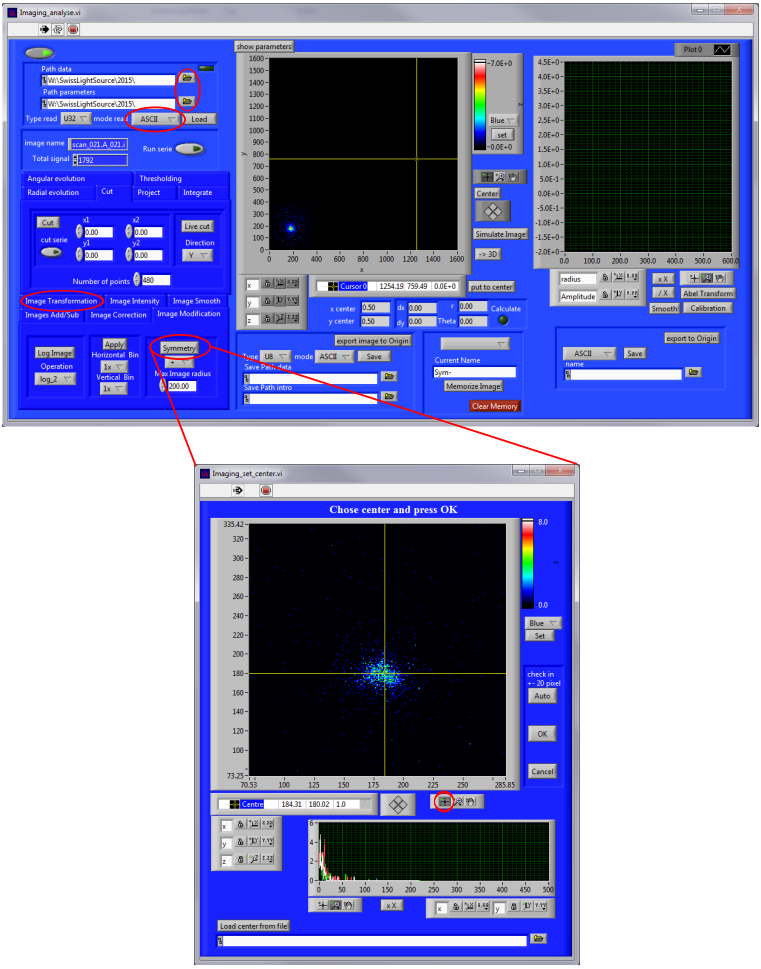


Figure E.2.: Screenshot of the main panel of the Analyse-7.8a_2014 program for image processing.

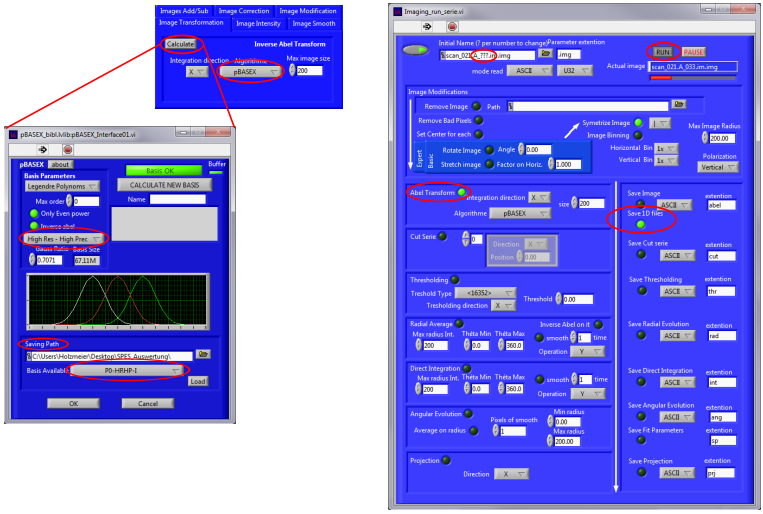

Figure E.3.: Screenshot of selected sub-panels of the Analyse-7.8a_2014 program for image processing.

The running number of the selected image has to be replaced by '?' in the Imaging_run_serie.vi window. After selecting 'Abel Transform' and 'Save 1D files' the program can be started and one-dimensional plots of the electrons' velocity distribution are saved for each photon energy.

### C) Construction of the 2D Photoionization matrix and SPES

The two-dimensional photoionization matrix can be constructed utilizing the Labview .vi 'SPES_SLS.vi'. A screenshot is given in fig. E.4. Besides the 1D plots, the respective corresponding photon energies and an energy calibration is needed to transform the distributions from the velocity space to the energy space. Calibration can be performed on the Ar autoionization resonances between the $^2P_{3/2}$ and $^2P_{1/2}$ ionization limits, which are observed as bright spots on the $^2P_{3/2}$ line in the two-dimensional photoionization matrix. The program executes then the matrix transformation and projection over the

photon energy axis up to a certain electron energy limit finally yields the SPES spectrum.

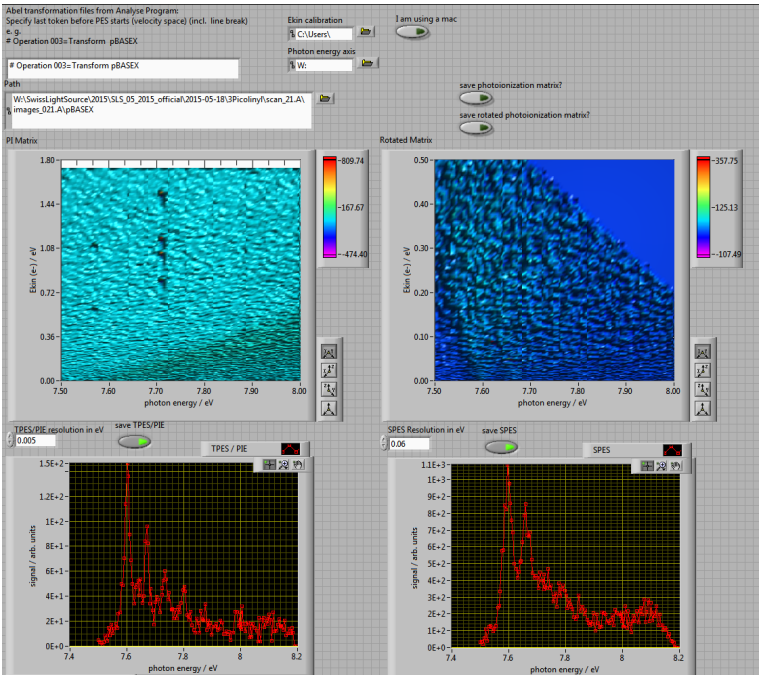


Figure E.4.: Screenshot of the SPES_SLS.vi panel for constructing photoionization matrices and plotting SPES spectra.

The performance of the here presented analysis scheme for data recorded at the SLS is compared to the 'traditional' TPES treatment utilizing the circle/ring scheme for the example of the 3-picolyl radical in fig. E.5. It is obvious that, contrary to the expectations, no increased signal/noise ratio could be obtained in SPES. A small peak broadening is observed for SPES in comparison to 'traditional' TPES and the resolution of vibrational bands is even worse for SPES. TPES from the photoionization matrix shows, how-

ever, lower fwhm and the vibrational bands especially the second and third overtone are more pronounced. The unexpected under-performance of SPES with SLS data, which is contrary to the well reasoned findings at the DESIRS beamline, might be due to the fact that the imaging detector at X04DB beamline has so far only been used and optimized for the traditional analysis scheme. Here, only electrons with very low kinetic energies are considered, for which focusing in VMI is significantly more efficient than for particles with higher energies. Because of the quadratic dependency of the electrons' kinetic energy from the velocity, the error is also squared for the kinetic energy, which leads to a significant broadening in the photoionization matrix. The result for SPES might therefore be increased by optimizing the VMI settings for a high resolution up to a kinetic energy of at least 100 meV. In addition, the Abel transformation seems to work less efficiently than in the DESIRS data treatment because the overall count rates are relatively low. Increasing the basis set might lead to an improvement.

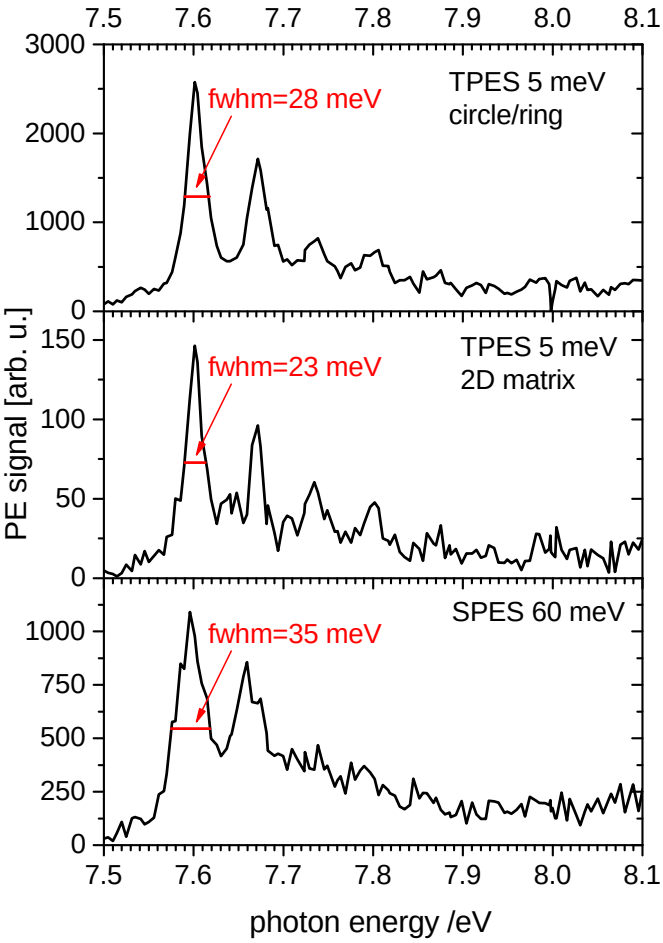


Figure E.5.: Comparison of 'traditional' TPES (upper panel) data treatment and TPES and SPES obtained from a 2D photoionization matrix for 3-picolyl recorded at the SLS.

# F. Geometry of 1,4-Di-tert-butyl-1,4-azaborinine

The computed structures for 1,4-di-*tert*-butyl-1,4-azaborinine and the corresponding cation are included in the supporting information of the paper published in 2014.[338] However, the structure published for the neutral molecule does not correspond to the absolute minimum of the potential energy surface. A rotamer in which the two *tert*-butyl groups are positioned in a staggered conformation is found to be 1.2 meV (0.12 kJ mol$^{-1}$) more stable than the eclipsed conformer, which also is a minimum on the energy surface. As the energy difference is very low and the *tert*-butyl groups are assumed to rotate freely under the experimental conditions, the effects on the interpretation of the experimental data is negligible. Nevertheless, for reasons of completeness, the revised structural data are listed in the following table F.1. For atom numbering see fig. 6.2. Bond lengths (R) are given in Å; bonding angles and dihedral angles are given in °.

Table F.1.: Computed geometries for neutral and cationic 1,4-di-*tert*-butyl-1,4-azaborinine.

| | neutral | cation |
|---|---|---|
| R(1,2) | 1.365 | 1.374 |
| R(1,5) | 1.086 | 1.083 |

| | neutral | cation |
|---|---|---|
| R(13,18) | 1.090 | 1.089 |
| R(13,19) | 1.092 | 1.090 |

| R(1,B) | 1.521 | 1.538 |
|---|---|---|
| R(2,6) | 1.078 | 1.077 |
| R(2,N) | 1.371 | 1.363 |
| R(3,4) | 1.360 | 1.364 |
| R(3,7) | 1.081 | 1.078 |
| R(3,N) | 1.375 | 1.377 |
| R(4,8) | 1.086 | 1.083 |
| R(4,B) | 1.526 | 1.539 |
| R(B,24) | 1.607 | 1.591 |
| R(N,11) | 1.511 | 1.539 |
| R(11,12) | 1.534 | 1.530 |
| R(11,13) | 1.539 | 1.538 |
| R(11,14) | 1.539 | 1.538 |
| R(12,15) | 1.091 | 1.091 |
| R(12,16) | 1.091 | 1.091 |
| R(12,17) | 1.090 | 1.089 |
| A(2,1,5) | 114.7 | 115.7 |
| A(2,1,B) | 121.0 | 118.9 |
| A(5,1,B) | 124.3 | 125.2 |
| A(1,2,6) | 121.4 | 121.6 |
| A(1,2,N) | 123.6 | 122.9 |
| A(6,2,N) | 115.0 | 115.5 |
| A(4,3,7) | 121.8 | 122.0 |
| A(4,3,N) | 123.8 | 123.3 |
| A(7,3,N) | 114.4 | 114.7 |
| A(3,4,8) | 114.8 | 115.9 |
| A(3,4,B) | 120.8 | 118.7 |
| A(8,4,B) | 124.4 | 125.2 |
| A(1,B,4) | 111.7 | 113.0 |

| R(13,20) | 1.091 | 1.091 |
|---|---|---|
| R(14,21) | 1.092 | 1.090 |
| R(14,22) | 1.090 | 1.089 |
| R(14,23) | 1.091 | 1.091 |
| R(24,25) | 1.545 | 1.527 |
| R(24,26) | 1.539 | 1.527 |
| R(24,27) | 1.545 | 1.587 |
| R(25,28) | 1.093 | 1.091 |
| R(25,29) | 1.094 | 1.092 |
| R(25,30) | 1.096 | 1.094 |
| R(26,31) | 1.094 | 1.091 |
| R(26,32) | 1.096 | 1.094 |
| R(26,33) | 1.094 | 1.092 |
| R(27,34) | 1.096 | 1.097 |
| R(27,35) | 1.094 | 1.091 |
| R(27,36) | 1.093 | 1.090 |
| A(18,13,19) | 107.7 | 107.4 |
| A(18,13,20) | 108.1 | 108.7 |
| A(19,13,20) | 108.4 | 108.1 |
| A(11,14,21) | 109.8 | 108.6 |
| A(11,14,22) | 112.3 | 113.0 |
| A(11,14,23) | 110.6 | 111.1 |
| A(21,14,22) | 107.7 | 107.3 |
| A(21,14,23) | 108.4 | 108.0 |
| A(22,14,23) | 108.1 | 108.7 |
| A(B,24,25) | 109.4 | 116.1 |
| A(B,24,26) | 112.7 | 116.3 |
| A(B,24,27) | 109.4 | 91.5 |
| A(25,24,26) | 108.4 | 110.9 |

| | | | | | |
|---|---|---|---|---|---|
| A(1,B,24) | 125.4 | 123.3 | A(25,24,27) | 108.5 | 110.2 |
| A(4,B,24) | 122.9 | 123.5 | A(26,24,27) | 108.4 | 110.1 |
| A(2,N,3) | 119.0 | 121.3 | A(24,25,28) | 111.8 | 112.8 |
| A(2,N,11) | 122.7 | 121.4 | A(24,25,29) | 111.5 | 111.0 |
| A(3,N,11) | 118.2 | 117.3 | A(24,25,30) | 110.8 | 110.2 |
| A(N,11,12) | 111.7 | 111.3 | A(28,25,29) | 107.5 | 108.1 |
| A(N,11,13) | 108.9 | 107.4 | A(28,25,30) | 107.6 | 107.5 |
| A(N,11,14) | 108.9 | 107.9 | A(29,25,30) | 107.5 | 107.1 |
| A(12,11,13) | 108.2 | 109.2 | A(24,26,31) | 111.6 | 112.8 |
| A(12,11,14) | 108.2 | 109.3 | A(24,26,32) | 111.0 | 110.2 |
| A(13,11,14) | 111.0 | 111.8 | A(24,26,33) | 111.6 | 111.0 |
| A(11,12,15) | 112.4 | 112.8 | A(31,26,32) | 107.4 | 107.5 |
| A(11,12,16) | 112.4 | 112.7 | A(31,26,33) | 107.6 | 108.1 |
| A(11,12,17) | 107.9 | 107.5 | A(32,26,33) | 107.4 | 107.1 |
| A(15,12,16) | 109.0 | 109.6 | A(24,27,34) | 110.8 | 104.4 |
| A(15,12,17) | 107.5 | 106.9 | A(24,27,35) | 111.5 | 113.8 |
| A(16,12,17) | 107.5 | 107.0 | A(24,27,36) | 111.8 | 113.7 |
| A(11,13,18) | 112.3 | 112.8 | A(34,27,35) | 107.5 | 107.4 |
| A(11,13,19) | 109.8 | 108.6 | A(34,27,36) | 107.6 | 107.5 |
| A(11,13,20) | 110.5 | 111.2 | A(35,27,36) | 107.5 | 109.6 |
| D(5,1,2,6) | 0.0 | 0.7 | D(N,11,13,18) | 61.6 | 63.1 |
| D(5,1,2,N) | -180.0 | -177.5 | D(N,11,13,19) | -178.6 | -177.9 |
| D(B,1,2,6) | 180.0 | -174.5 | D(N,11,13,20) | -59.1 | -59.2 |
| D(B,1,2,N) | 0.0 | 7.3 | D(12,11,13,18) | -176.8 | -176.1 |
| D(2,1,B,4) | 0.0 | -15.1 | D(12,11,13,19) | -57.0 | -57.1 |
| D(2,1,B,24) | 180.0 | 159.4 | D(12,11,13,20) | 62.5 | 61.6 |
| D(5,1,B,4) | 180.0 | 170.1 | D(14,11,13,18) | -58.2 | -55.0 |
| D(5,1,B,24) | 0.0 | -15.4 | D(14,11,13,19) | 61.6 | 63.9 |
| D(1,2,N,3) | 0.0 | 2.1 | D(14,11,13,20) | -178.9 | -177.4 |
| D(1,2,N,11) | -180.0 | -180.0 | D(N,11,14,21) | 178.6 | 177.5 |

| | | |
|---|---|---|
| D(6,2,N,3) | -180.0 | -176.2 |
| D(6,2,N,11) | 0.0 | 1.7 |
| D(7,3,4,8) | 0.0 | -0.3 |
| D(7,3,4,B) | 180.0 | 174.3 |
| D(N,3,4,8) | 180.0 | 178.3 |
| D(N,3,4,B) | 0.0 | -7.1 |
| D(4,3,N,2) | 0.0 | -2.2 |
| D(4,3,N,11) | 180.0 | 179.8 |
| D(7,3,N,2) | -180.0 | 176.5 |
| D(7,3,N,11) | 0.0 | -1.5 |
| D(3,4,B,1) | 0.0 | 15.0 |
| D(3,4,B,24) | -180.0 | -159.4 |
| D(8,4,B,1) | 180.0 | -170.9 |
| D(8,4,B,24) | 0.0 | 14.6 |
| D(1,B,24,25) | -120.7 | -153.7 |
| D(1,B,24,26) | 0.0 | -20.5 |
| D(1,B,24,27) | 120.7 | 92.9 |
| D(4,B,24,25) | 59.3 | 20.2 |
| D(4,B,24,26) | -180.0 | 153.4 |
| D(4,B,24,27) | -59.3 | -93.2 |
| D(2,N,11,12) | 0.0 | 2.0 |
| D(2,N,11,13) | 119.4 | 121.5 |
| D(2,N,11,14) | -119.5 | -117.8 |
| D(3,N,11,12) | 180.0 | 180.0 |
| D(3,N,11,13) | -60.6 | -60.5 |
| D(3,N,11,14) | 60.5 | 60.2 |
| D(N,11,12,15) | -61.7 | -63.7 |
| D(N,11,12,16) | 61.7 | 61.1 |
| D(N,11,12,17) | -180.0 | 178.7 |
| D(N,11,14,22) | -61.7 | -63.6 |
| D(N,11,14,23) | 59.1 | 58.8 |
| D(12,11,14,21) | 57.0 | 56.4 |
| D(12,11,14,22) | 176.7 | 175.3 |
| D(12,11,14,23) | -62.5 | -62.3 |
| D(13,11,14,21) | -61.6 | -64.6 |
| D(13,11,14,22) | 58.1 | 54.2 |
| D(13,11,14,23) | 178.9 | 176.7 |
| D(B,24,25,28) | -58.7 | -49.0 |
| D(B,24,25,29) | 61.7 | 72.4 |
| D(B,24,25,30) | -178.6 | -169.1 |
| D(26,24,25,28) | 178.1 | 175.4 |
| D(26,24,25,29) | -61.6 | -63.2 |
| D(26,24,25,30) | 58.1 | 55.3 |
| D(27,24,25,28) | 60.5 | 53.2 |
| D(27,24,25,29) | -179.1 | 174.7 |
| D(27,24,25,30) | -59.4 | -66.9 |
| D(B,24,26,31) | 60.2 | 49.0 |
| D(B,24,26,32) | -180.0 | 169.1 |
| D(B,24,26,33) | -60.2 | -72.4 |
| D(25,24,26,31) | -178.6 | -175.4 |
| D(25,24,26,32) | -58.8 | -55.4 |
| D(25,24,26,33) | 61.0 | 63.1 |
| D(27,24,26,31) | -61.0 | -53.3 |
| D(27,24,26,32) | 58.8 | 66.8 |
| D(27,24,26,33) | 178.6 | -174.7 |
| D(B,24,27,34) | 178.6 | -179.8 |
| D(B,24,27,35) | -61.7 | -63.1 |
| D(B,24,27,36) | 58.7 | 63.4 |

| | | |
|---|---|---|
| D(13,11,12,15) | 178.5 | 177.9 |
| D(13,11,12,16) | -58.1 | -57.3 |
| D(13,11,12,17) | 60.2 | 60.3 |
| D(14,11,12,15) | 58.2 | 55.3 |
| D(14,11,12,16) | -178.5 | -179.9 |
| D(14,11,12,17) | -60.2 | -62.2 |

| | | |
|---|---|---|
| D(25,24,27,34) | 59.4 | 61.6 |
| D(25,24,27,35) | 179.1 | 178.3 |
| D(25,24,27,36) | -60.5 | -55.3 |
| D(26,24,27,34) | -58.1 | -61.1 |
| D(26,24,27,35) | 61.6 | 55.7 |
| D(26,24,27,36) | -178.1 | -177.9 |

# List of Figures

# List of Tables

# Bibliography


[1] EPA Notice of Violation to Volkswagen, September 18, 2015. http://www3.epa.gov/otaq/cert/documents/vw-nov-caa-09-18-15.pdf (accessed October 28, 2015).

[2] P. Glarborg, A. D. Jensen, J. E. Johnsson, *Prog. Energy Combust.*, 2003, **29**, 89–113.

[3] Regulation (EC) No 715/2007 of the European Parliament and of the Council of 20 June 2007 on type approval of motor vehicles with respect to emissions from light passenger and commercial vehicles (Euro 5 and Euro 6) and on access to vehicle repair and maintenance information (OJ L171, 29.6.2007, p.13).

[4] L. Yang, V. Franco, A. Campestrini, J. German, P. Mock, NOx control technologies for Euro 6 diesel passenger cars. ICCT, (September 3, 2015). http://theicct.org/nox-control-technologies-euro-6-diesel-passenger-cars (accessed October 28, 2015).

[5] J. M. Simmie, *Prog. Energy Combust.*, 2003, **29**, 599–634.

[6] W. C. Gardiner, *Gas-phase combustion chemistry*, Springer, New York, 1, 2000.

[7] IUPAC. Compendium of Chemical Terminology, 2nd ed. (the Gold Book). Compiled by A. D. McNaught and A. Wilkinson. Blackwell Scientific Publications, Oxford (1997). XML on-line corrected version: http://goldbook.iupac.org (2006) created by M. Nic, J. Jirat, B. Kosata; updates compiled by A. Jenkins. ISBN 0-9678550-9-8.

[8] K. Kohse-Hoinghaus, B. Atakan, A. Lamprecht, G. Gonzalez Alatorre, M. Kamphus, T. Kasper, N.-N. Liu, *Phys. Chem. Chem. Phys.*, 2002, **4**, 2056–2062.

[9] C. Alcaraz, D. Schröder, I. Fischer in *Encyclopedia of Radicals in Chemistry, Biology and Materials*, ed. C. Chatgilialoglu, A. Studer; John Wiley & Sons, Chichester, 2012; pp. 477–502.

[10] H. Richter, J. B. Howard, *Prog. Energy Combust.*, 2000, **26**, 565–608.

[11] Z. A. Mansurov, *Combust. Explos. Shock Waves*, 2005, **41**, 727–744.

[12] K. Kohse-Höinghaus, P. Oßwald, T. A. Cool, T. Kasper, N. Hansen, F. Qi, C. K. Westbrook, P. R. Westmoreland, *Angew. Chem. Int. Ed.*, 2010, **49**, 3572–3597.

[13] Based on IEA data from 2014 Key World Energy STATISTICS © OECD/IEA 2014, IEA Publishing; modified by Fabian Holzmeier. License: https://www.iea.org/t&c/termsandconditions/.

[14] J. N. Galloway, G. E. Likens, *Atmos. Environ.*, 1981, **15**, 1081–1085.

[15] A. N. Hayhurst, A. D. Lawrence, *Prog. Energy Combust.*, 1992, **18**, 529–552.

[16] M. A. Wójtowicz, J. R. Pels, J. A. Moulijn, *Fuel Process. Technol.*, 1993, **34**, 1–71.

[17] K. D. Bartle, D. L. Perry, S. Wallace, *Fuel Process. Technol.*, 1987, **15**, 351–361.

[18] S. Wallace, K. D. Bartle, D. L. Perry, *Fuel*, 1989, **68**, 1450–1455.

[19] P. Burchill, L. S. Welch, *Fuel*, 1989, **68**, 100–104.

[20] P. F. Nelson, A. N. Buckley, M. D. Kelly, *Symp. (Int.) Combust.*, 1992, **24**, 1259–1267.

[21] S. M. Kirtley, O. C. Mullins, J. van Elp, S. P. Cramer, *Fuel*, 1993, **72**, 133–135.

[22] S. R. Kelemen, M. L. Gorbaty, P. J. Kwiatek, *Energy Fuels*, 1994, **8**, 896–906.

[23] J. Leppälahti, T. Koljonen, *Fuel Process. Technol.*, 1995, **43**, 1–45.

[24] F.-J. Tian, J. Yu, L. J. McKenzie, J.-I. Hayashi, C.-Z. Li, *Energy Fuels*, 2007, **21**, 517–521.

[25] J. A. Miller, C. T. Bowman, *Prog. Energy Combust.*, 1989, **15**, 287–338.

[26] J. C. Mackie, M. B. Colket, P. F. Nelson, M. Esler, *Int. J. Chem. Kinet.*, 1991, **23**, 733–760.

[27] Z. Tian, Y. Li, T. Zhang, A. Zhu, Z. Cui, F. Qi, *Combust. Flame*, 2007, **151**, 347–365.

[28] X. Hong, L. Zhang, T. Zhang, F. Qi, *J. Phys. Chem. A*, 2009, **113**, 5397–5405.

[29] Z. Tian, Y. Li, T. Zhang, A. Zhu, F. Qi, *J. Phys. Chem. A*, 2008, **112**, 13549–13555.

[30] N. R. Hore, D. K. Russell, *J. Chem. Soc., Perkin Trans. 2*, 1998, **2**, 269–276.

[31] X. Hong, T.-c. Zhang, L.-d. Zhang, F. Qi, *Chin. J. Chem. Phys.*, 2009, **22**, 204.

[32] S. T. Perry, T. H. Fletcher, M. S. Solum, R. J. Pugmire, *Energy Fuels*, 2000, **14**, 1094–1102.

[33] P. Glarborg, M. U. Alzueta, K. Dam-Johansen, J. A. Miller, *Combust. Flame*, 1998, **115**, 1–27.

[34] C. A. Taatjes, D. L. Osborn, T. A. Cool, K. Nakajima, *Chem. Phys. Lett.*, 2004, **394**, 19–24.

[35] C. A. Taatjes, N. Hansen, D. L. Osborn, K. Kohse-Höinghaus, T. A. Cool, P. R. Westmoreland, *Phys. Chem. Chem. Phys.*, 2008, **10**, 20–34.

[36] T. Koopmans, *Physica*, 1934, **1**, 104–113.

[37] P. Oßwald, P. Hemberger, T. Bierkandt, E. Akyildiz, M. Köhler, A. Bodi, T. Gerber, T. Kasper, *Rev. Sci. Instrum.*, 2014, **85**, 025101.

[38] J. Krüger, G. A. Garcia, D. Felsmann, K. Moshammer, A. Lackner, A. Brockhinke, L. Nahon, K. Kohse-Hoinghaus, *Phys. Chem. Chem. Phys.*, 2014, **16**, 22791–22804.

[39] D. Felsmann, K. Moshammer, J. Krüger, A. Lackner, A. Brockhinke, T. Kasper, T. Bierkandt, E. Akyildiz, N. Hansen, A. Lucassen, P. Oßwald, M. Köhler, G. A. Garcia, L. Nahon, P. Hemberger, A. Bodi, T. Gerber, K. Kohse-Höinghaus, *Proc. Combust. Inst.*, 2015, **35**, 779–786.

[40] A. T. Droege, P. C. Engelking, *Chem. Phys. Lett.*, 1983, **96**, 316–318.

[41] S. T. Gibson, J. P. Greene, J. Berkowitz, *J. Chem. Phys.*, 1985, **83**, 4319–4328.

[42] J. Baker, M. Barnes, M. C. R. Cockett, J. M. Dyke, A. M. Ellis, M. Feher, E. P. F. Lee, A. Morris, H. Zamanpour, *J. Electron Spectrosc. Relat. Phenom.*, 1990, **51**, 487–511.

[43] G. A. Garcia, X. Tang, J.-F. Gil, L. Nahon, M. Ward, S. Batut, C. Fittschen, C. A. Taatjes, D. L. Osborn, J.-C. Loison, *J. Chem. Phys.*, 2015, **142**, 164201.

[44] S. Willitsch, J. M. Dyke, F. Merkt, *Helv. Chim. Acta*, 2003, **86**, 1152–1166.

[45] D. Bulgin, J. Dyke, F. Goodfellow, N. Jonathan, E. Lee, A. Morris, *J. Electron Spectrosc. Relat. Phenom.*, 1977, **12**, 67–76.

[46] D. W. Kohn, H. Clauberg, P. Chen, *Rev. Sci. Instrum.*, 1992, **63**, 4003–4005.

[47] I. Fischer, T. Schüßler, H.-J. Deyerl, M. Elhanine, C. Alcaraz, *Int. J. Mass. Spectrom.*, 2007, **261**, 227–233.

[48] B. Noller, P. Hemberger, I. Fischer, C. Alcaraz, G. A. Garcia, H. Soldi-Lose, *Phys. Chem. Chem. Phys.*, 2009, **11**, 5384.

[49] P. Hemberger, M. Steinbauer, M. Schneider, I. Fischer, M. Johnson, A. Bodi, T. Gerber, *J. Phys. Chem. A*, 2009, **114**, 4698–4703.

[50] B. K. Cunha de Miranda, C. Alcaraz, M. Elhanine, B. Noller, P. Hemberger, I. Fischer, G. A. Garcia, H. Soldi-Lose, B. Gans, L. A. Vieira Mendes, S. Boyé-Péronne, S. Douin, J. Zabka, P. Botschwina, *J. Phys. Chem. A*, 2010, **114**, 4818–4830.

[51] P. Hemberger, M. Lang, B. Noller, I. Fischer, C. Alcaraz, B. K. Cunha de Miranda, G. A. Garcia, H. Soldi-Lose, *J. Phys. Chem. A*, 2011, **115**, 2225–2230.

[52] M. Steinbauer, P. Hemberger, I. Fischer, A. Bodi, *ChemPhysChem*, 2011, **12**, 1795–1797.

[53] M. Steinbauer, M. Lang, I. Fischer, B. K. Cunha de Miranda, C. Romanzin, C. Alcaraz, *Phys. Chem. Chem. Phys.*, 2011, **13**, 17956–17959.

[54] I. Fischer, *Int. J. Mass. Spectrom.*, 2002, **216**, 131–153.

[55] T. A. Cool, J. Wang, K. Nakajima, C. A. Taatjes, A. Mcllroy, *Int. J. Mass. Spectrom.*, 2005, **247**, 18–27.

[56] N. Hansen, S. J. Klippenstein, C. A. Taatjes, J. A. Miller, J. Wang, T. A. Cool, B. Yang, R. Yang, L. Wei, C. Huang, F. Qi, M. E. Law, P. R. Westmoreland, *J. Phys. Chem. A*, 2006, **110**, 3670–3678.

[57] N. Hansen, T. Kasper, S. J. Klippenstein, P. R. Westmoreland, M. E. Law, C. A. Taatjes, K. Kohse-Hoinghaus, J. Wang, T. A. Cool, *J. Phys. Chem. A*, 2007, **111**, 4081–4092.

[58] K. H. Fischer, J. Herterich, I. Fischer, S. Jaeqx, A. M. Rijs, *J. Phys. Chem. A*, 2012, **116**, 8515–8522.

[59] M. Lang, F. Holzmeier, I. Fischer, P. Hemberger, *J. Phys. Chem. A*, 2013, **117**, 5260–5268.

[60] T. S. Kasper, P. Oßwald, M. Kamphus, K. Kohse-Höinghaus, *Combust. Flame*, 2007, **150**, 220–231.

[61] Y. Li, L. Wei, Z. Tian, B. Yang, J. Wang, T. Zhang, F. Qi, *Combust. Flame*, 2008, **152**, 336–359.

[62] O. Herbinet, W. J. Pitz, C. K. Westbrook, *Combust. Flame*, 2010, **157**, 893–908.

[63] O. Welz, J. D. Savee, D. L. Osborn, S. S. Vasu, C. J. Percival, D. E. Shallcross, C. A. Taatjes, *Science*, 2012, **335**, 204–207.

[64] P. Ehrenfreund, S. B. Charnley, *Annu. Rev. Astro. Astrophys.*, 2000, **38**, 427–483.

[65] V. Vuitton, R. V. Yelle, V. G. Anicich, *Astrophys. J.*, 2006, **647**, L175.

[66] C. Miron, P. Morin in *Handbook of High-resolution Spectroscopy*, ed. M. Quack, F. Merkt; John Wiley & Sons, Ltd, 2011; pp. 1655–1689.

[67] J. Frank, A. Shavorskiy, H. Bluhm, B. Coriton, E. Huang, D. Osborn, *Appl. Phys. B: Lasers Opt.*, 2014, **117**, 493–499.

[68] C. D. Entwistle, T. B. Marder, *Angew. Chem. Int. Ed.*, 2002, **41**, 2927–2931.

[69] W.-L. Jia, D. Song, S. Wang, *J. Org. Chem.*, 2002, **68**, 701–705.

[70] C. D. Entwistle, T. B. Marder, *Chem. Mater.*, 2004, **16**, 4574–4585.

[71] W.-L. Jia, D.-R. Bai, T. McCormick, Q.-D. Liu, M. Motala, R.-Y. Wang, C. Seward, Y. Tao, S. Wang, *Chem. Eur. J.*, 2004, **10**, 994–1006.

[72] W. L. Jia, M. J. Moran, Y.-Y. Yuan, Z. H. Lu, S. Wang, *J. Mater. Chem.*, 2005, **15**, 3326–3333.

[73] N. Matsumi, Y. Chujo, *Polym. J.*, 2008, **40**, 77–89.

[74] A. Wakamiya, K. Mori, T. Araki, S. Yamaguchi, *J. Am. Chem. Soc.*, 2009, **131**, 10850–10851.

[75] Z. M. Hudson, S. Wang, *Dalt. Trans.*, 2011, **40**, 7805–7816.

[76] A. Iida, S. Yamaguchi, *J. Am. Chem. Soc.*, 2011, **133**, 6952–6955.

[77] S. Saito, K. Matsuo, S. Yamaguchi, *J. Am. Chem. Soc.*, 2012, **134**, 9130–9133.

[78] Z. Zhou, A. Wakamiya, T. Kushida, S. Yamaguchi, *J. Am. Chem. Soc.*, 2012, **134**, 4529–4532.

[79] C. Dou, S. Saito, S. Yamaguchi, *J. Am. Chem. Soc.*, 2013, **135**, 9346–9349.

[80] A. Lorbach, A. Hubner, M. Wagner, *Dalt. Trans.*, 2012, **41**, 6048–6063.

[81] G. Imamura, C. W. Chang, Y. Nabae, M. Kakimoto, S. Miyata, K. Saiki, *J. Phys. Chem. C*, 2012, **116**, 16305–16310.

[82] C. Dou, S. Saito, K. Matsuo, I. Hisaki, S. Yamaguchi, *Angew. Chem. Int. Ed.*, 2012, **51**, 12206–12210.

[83] C. Hoffend, F. Schödel, M. Bolte, H.-W. Lerner, M. Wagner, *Chem. Eur. J.*, 2012, **18**, 15394–15405.

[84] K. H. Fischer, M. Schneider, I. Fischer, B. Pfaffinger, H. Braunschweig, B. Sztáray, A. Bodi, *Chem. Eur. J.*, 2012, **18**, 4533–4540.

[85] W. Demtröder, *Laserspektroskopie: Grundlagen und Techniken*, Springer, Berlin [u.a.], 5., erw. und neubearb. Aufl., 2007.

[86] J. Falta, T. Möller, *Forschung mit Synchrotronstrahlung: Eine Einführung in die Grundlagen und Anwendungen*, Studium, Vieweg + Teubner, Wiesbaden, 1. Aufl., 2010.

[87] J. C. Maxwell, *Phil. Trans. R. Soc. London*, 1865, **155**, 459–512.

[88] D. Iwanenko, I. Pomeranchuk, *Phys. Rev.*, 1944, **65**, 343.

[89] F. R. Elder, A. M. Gurewitsch, R. V. Langmuir, H. C. Pollock, *Phys. Rev.*, 1947, **71**, 829–830.

[90] K. Codling, *Rep. Prog. Phys.*, 1973, **36**, 541.

[91] S. Sasaki, K. Kakuno, T. Takada, T. Shimada, K.-i. Yanagida, Y. Miyahara, *Nucl. Instrum. Methods Phys. Res., Sect. A*, 1993, **331**, 763–767.

[92] E. Illenberger, J. Momigny, *Gaseous molecular ions: An introduction to elementary processes induced by ionization*, Steinkopff Verlag and Springer-Verlag, Darmstadt and New York, 1992.

[93] T. A. Carlson, *Annu. Rev. Phys. Chem.*, 1975, **26**, 211–234.

[94] V. Čermák, *J. Electron Spectrosc. Relat. Phenom.*, 1976, **9**, 419–439.

[95] D. M. P. Holland, J. B. West, A. C. Parr, D. L. Ederer, R. Stockbauer, R. D. Buff, J. L. Dehmer, *J. Chem. Phys.*, 1983, **78**, 124–130.

[96] D. Villarejo, R. R. Herm, M. G. Inghram, *J. Chem. Phys.*, 1967, **46**, 4995–4996.

[97] W. B. Peatman, T. B. Borne, E. W. Schlag, *Chem. Phys. Lett.*, 1969, **3**, 492–497.

[98] T. Baer, W. B. Peatman, E. W. Schlag, *Chem. Phys. Lett.*, 1969, **4**, 243–247.

[99] R. Spohr, P. M. Guyon, W. A. Chupka, J. Berkowitz, *Rev. Sci. Instrum.*, 1971, **42**, 1872–1879.

[100] T. Baer, P.-M. Guyon, I. Nenner, A. Tabché-Fouhaillé, R. Botter, L. F. A. Ferreira, T. R. Govers, *J. Chem. Phys.*, 1979, **70**, 1585–1592.

[101] W. C. Wiley, I. H. McLaren, *Rev. Sci. Instrum.*, 1955, **26**, 1150.

[102] K. Muller-Dethlefs, E. W. Schlag, *Annu. Rev. Phys. Chem.*, 1991, **42**, 109–136.

[103] E. R. Grant, M. G. White, *Nature*, 1991, **354**, 249–250.

[104] A. T. J. B. Eppink, D. H. Parker, *Rev. Sci. Instrum.*, 1997, **68**, 3477–3484.

[105] T. Baer, Y. Li, *Int. J. Mass. Spectrom.*, 2002, **219**, 381–389.

[106] B. Sztáray, T. Baer, *Rev. Sci. Instrum.*, 2003, **74**, 3763–3768.

[107] A. Bodi, M. Johnson, T. Gerber, Z. Gengeliczki, B. Sztáray, T. Baer, *Rev. Sci. Instrum.*, 2009, **80**, 034101.

[108] G. A. Garcia, L. Nahon, I. Powis, *Rev. Sci. Instrum.*, 2004, **75**, 4989–4996.

[109] J. C. Poully, J. P. Schermann, N. Nieuwjaer, F. Lecomte, G. Gregoire, C. Desfrancois, G. A. Garcia, L. Nahon, D. Nandi, L. Poisson, M. Hochlaf, *Phys. Chem. Chem. Phys.*, 2010, **12**, 3566–3572.

[110] M. Briant, L. Poisson, M. Hochlaf, P. de Pujo, M.-A. Gaveau, B. Soep, *Phys. Rev. Lett.*, 2012, **109**, 193401.

[111] S. Leach, G. A. Garcia, A. Mahjoub, Y. Bénilan, N. Fray, M.-C. Gazeau, F. Gaie-Levrel, N. Champion, M. Schwell, *J. Chem. Phys.*, 2014, **140**, 174305.

[112] J. M. Hollas, *Moderne Methoden in der Spektroskopie: Mit 72 Tabellen*, Vieweg-Lehrbuch physikalische Chemie, Vieweg, Braunschweig and Wiesbaden, 1995.

[113] R. Signorell, F. Merkt, *Mol. Phys.*, 1997, **92**, 793–804.

[114] P. R. Bunker, P. Jensen, *Molecular symmetry and spectroscopy*, NRC Research Press, Ottawa, 2nd ed., 1998.

[115] R. N. Zare, *Angular momentum: Understanding spatial aspects in chemistry and physics*, Wiley, New York, 1988.

[116] A. D. Buckingham, B. J. Orr, J. M. Sichel, *Philos. Trans. R. Soc. London, Ser. A*, 1970, **268**, 147–157.

[117] M. S. Child, *Theory of molecular Rydberg states*, Cambridge molecular science, Cambridge University Press, Cambridge, UK and New York, 2011.

[118] E. R. Cohen, T. Cvitas, J. F. Frey, B. Holmström, K. Kuchitsu, R. Marquardt, I. Mills, F. Pavese, M. Quack, J. Stohner, H. L. Strauss, M. Takami, A. J. Thor, *Quantities, Units, and Symbols in Physical Chemistry*, RSC Pub., Cambridge, UK, 3rd ed., 2007.

[119] J. Xie, R. N. Zare, *J. Chem. Phys.*, 1990, **93**, 3033–3038.

[120] A. M. Schulenburg, C. Alcaraz, G. Grassi, F. Merkt, *J. Chem. Phys.*, 2006, **125**, 104310.

[121] S. Willitsch, F. Merkt, *Int. J. Mass. Spectrom.*, 2005, **245**, 14–25.

[122] A. M. Schulenburg, *Investigation of organic cations by high-resolution photoelectron spectroscopy* PhD thesis, ETH, Zürich, 2009.

[123] S. Willitsch, J. M. Dyke, F. Merkt, *Mol. Phys.*, 2004, **102**, 1543–1553.

[124] S. Willitsch, C. Jungen, F. Merkt, *J. Chem. Phys.*, 2006, **124**.

[125] A. M. Schulenburg, M. Meisinger, P. P. Radi, F. Merkt, *J. Mol. Spectrosc.*, 2008, **250**, 44–50.

[126] A. M. Schulenburg, F. Merkt, *J. Chem. Phys.*, 2009, **130**, 034308.

[127] K. Vasilatou, J. M. Michaud, D. Baykusheva, G. Grassi, F. Merkt, *J. Chem. Phys.*, 2014, **141**, 064317.

[128] B. Brehm, E. von Puttkamer, *Z. Naturforsch., A: Phys. Sci.*, 1967, **22**, 8–10.

[129] T. Baer, W. L. Hase, *Unimolecular reaction dynamics: Theory and experiments*, Oxford University Press, New York, 1996.

[130] A. Bodi, B. Sztaray, T. Baer, M. Johnson, T. Gerber, *Rev. Sci. Instrum.*, 2007, **78**, 084102.

[131] R. A. Marcus, *J. Chem. Phys.*, 1952, **20**, 359–364.

[132] T. Beyer, D. F. Swinehart, *Commun. ACM*, 1973, **16**, 379.

[133] S. E. Stein, B. S. Rabinovitch, *J. Chem. Phys.*, 1973, **58**, 2438–2445.

[134] B. Sztáray, A. Bodi, T. Baer, *J. Mass. Spectrom.*, 2010, **45**, 1233–1245.

[135] M. Quack, J. Troe, *Ber. Bunsenges. Phys. Chem.*, 1974, **78**, 240–252.

[136] J. Troe, V. G. Ushakov, A. A. Viggiano, *J. Phys. Chem. A*, 2006, **110**, 1491–1499.

[137] B. Sztáray, T. Baer, *J. Phys. Chem. A*, 2002, **106**, 8046–8053.

[138] T. Baer, B. Sztaray, J. P. Kercher, A. F. Lago, A. Bödi, C. Skull, D. Palathinkal, *Phys. Chem. Chem. Phys.*, 2005, **7**, 1507–1513.

[139] J. Stöhr, *NEXAFS spectroscopy*, 25 of *Springer series in surface sciences*, Springer, Berlin and New York, 1st ed. corr. print, 1996.

[140] H. Ågren, *J. Chem. Phys.*, 1981, **75**, 1267–1283.

[141] L. S. Cederbaum, *Theoret. Chim. Acta*, 1973, **31**, 239–260.

[142] F. Tarantelli, A. Sgamellotti, L. S. Cederbaum, *J. Electron Spectrosc. Relat. Phenom.*, 1994, **68**, 297–312.

[143] D. Minelli, F. Tarantelli, A. Sgamellotti, L. S. Cederbaum, *J. Electron Spectrosc. Relat. Phenom.*, 1995, **74**, 1–14.

[144] B. K. McFarland, J. P. Farrell, S. Miyabe, F. Tarantelli, A. Aguilar, N. Berrah, C. Bostedt, J. D. Bozek, P. H. Bucksbaum, J. C. Catagna, R. N. Coffee, J. P. Cryan, L. Fang, R. Feifel, K. J. Gaffney, J. M. Glownia, T. J. Martinez, M. Mucke, B. Murphy, A. Natan, T. Osipov, V. S. Petrović, S. Schorb, T. Schultz, L. S. Spector, M. Swiggers, I. Tenney, S. Wang, J. L. White, W. White, M. Gühr, *Nat. Commun.*, 2014, **5**.

[145] P. Emma, K. Bane, M. Cornacchia, Z. Huang, H. Schlarb, G. Stupakov, D. Walz, *Phys. Rev. Lett.*, 2004, **92**, 074801.

[146] Q. Guan, K. N. Urness, T. K. Ormond, D. E. David, G. B. Ellison, J. W. Daily, *Int. Rev. Phys. Chem.*, 2014, **33**, 447–487.

[147] O. Marcouille, P. Brunelle, O. Chubar, F. Marteau, M. Massal, L. Nahon, K. Tavakloi, J. Veteran, J.-M. Filhol, *AIP Conf. Proc.*, 2007, **879**, 311–314.

[148] L. Nahon, N. de Oliveira, G. A. Garcia, J.-F. Gil, B. Pilette, O. Marcouillé, B. Lagarde, F. Polack, *J. Synchrotron Radiat.*, 2012, **19**, 508–520.

[149] N. de Oliveira, D. Joyeux, D. Phalippou, J. C. Rodier, F. Polack, M. Vervloet, L. Nahon, *Rev. Sci. Instrum.*, 2009, **80**, 043101.

[150] M. Richard-Viard, A. Delboulbé, M. Vervloet, *Chem. Phys.*, 1996, **209**, 159–167.

[151] G. A. Garcia, L. Nahon, C. J. Harding, E. A. Mikajlo, I. Powis, *Rev. Sci. Instrum.*, 2005, **76**, 053302.

[152] G. A. Garcia, H. Soldi-Lose, L. Nahon, *Rev. Sci. Instrum.*, 2009, **80**, 023102.

[153] G. A. Garcia, B. K. Cunha de Miranda, M. Tia, S. Daly, L. Nahon, *Rev. Sci. Instrum.*, 2013, **84**, 053112.

[154] D. Céolin, G. Chaplier, M. Lemonnier, G. A. Garcia, C. Miron, L. Nahon, M. Simon, N. Leclercq, P. Morin, *Rev. Sci. Instrum.*, 2005, **76**, 043302.

[155] M. Johnson, A. Bodi, L. Schulz, T. Gerber, *Nucl. Instrum. Methods Phys. Res., Sect. A*, 2009, **610**, 597–603.

[156] M. Lang, *Valence Shell Photoionization of Soot Precursors with Synchrotron Radiation* PhD thesis, Julius-Maximilians Universität Würzburg, Würzburg, 2015.

[157] A. Bodi, P. Hemberger, T. Gerber, B. Sztáray, *Rev. Sci. Instrum.*, 2012, **83**, 083105.

[158] W. A. Chupka, *J. Chem. Phys.*, 1993, **98**, 4520–4530.

[159] A. Bodi, N. S. Shuman, T. Baer, *Phys. Chem. Chem. Phys.*, 2009, **11**, 11013–11021.

[160] J. Söderström, A. Lindblad, A. N. Grum-Grzhimailo, O. Travnikova, C. Nicolas, S. Svensson, C. Miron, *New J. Phys.*, 2011, **13**, 073014.

[161] C. Miron, PLEIADES beamline at Synchrotron SOLEIL (2012). http://www.synchrotron-soleil.fr/Recherche/LignesLumiere/PLEIADES (accessed September 18, 2015).

[162] P. Baltzer, L. Karlsson, M. Lundqvist, B. Wannberg, *Rev. Sci. Instrum.*, 1993, **64**, 2179–2189.

[163] W. E. Moddeman, T. A. Carlson, M. O. Krause, B. P. Pullen, W. E. Bull, G. K. Schweitzer, *J. Chem. Phys.*, 1971, **55**, 2317–2336.

[164] T. K. Sham, B. X. Yang, J. Kirz, J. S. Tse, *Phys. Rev. A: At., Mol., Opt. Phys.*, 1989, **40**, 652–669.

[165] R. N. S. Sodhi, C. E. Brion, *J. Electron Spectrosc. Relat. Phenom.*, 1984, **34**, 363–372.

[166] C. T. Chen, Y. Ma, F. Sette, *Phys. Rev. A: At., Mol., Opt. Phys.*, 1989, **40**, 6737–6740.

[167] Gausian 09, Revision 0.1, M. J. Frisch, G. W. Trucks, H. B. Schlegel, G. E. Scuseria, M. A. Robb, J. R. Cheeseman, G. Scalmani, V. Barone, B. Mennucci, G. A. Petersson, H. Nakatsuji, M. Caricato, X. Li, H. P. Hratchian, A. F. Izmaylov, J. Bloino, G. Zheng, J. L. Sonnenberg, M. Hada, M. Ehara, K. Toyota, R. Fukuda, J. Hasegawa, M. Ishida, T. Nakajima, Y. Honda, O. Kitao, H. Nakai, T. Vreven, J. A. Montgomery, J. E. Peralta, F. Ogliaro, M. Bearpark, J. J. Heyd, E. Brothers, K. N. Kudin, V. N. Staroverov, R. Kobayashi, J. Normand, K. Raghavachari, A. Rendell, J. C. Burant, S. S. Iyengar, J. Tomasi, M. Cossi, N. Rega, J. M. Millam, M. Klene, J. E. Knox, J. B. Cross, V. Bakken, C. Adamo, J. Jaramillo, R. Gomperts, R. E. Stratmann, O. Yazyev, A. J. Austin, R. Cammi, C. Pomelli, J. W. Ochterski, R. L. Martin, K. Morokuma, V. G. Zakrzewski, G. A. Voth, P. Salvador, J. J. Dannenberg, S. Dapprich, A. D. Daniels, Farkas, J. B. Foresman, J. V. Ortiz, J. Cioslowski, D. J. Fox, Gaussian, Inc, Wallingford CT, 2009, 2009, 2009.

[168] J. A. Montgomery Jr., M. J. Frisch, J. W. Ochterski, G. A. Petersson, *J. Chem. Phys.*, 1999, **110**, 2822–2827.

[169] J. A. Montgomery Jr., M. J. Frisch, J. W. Ochterski, G. A. Petersson, *J. Chem. Phys.*, 2000, **112**, 6532–6542.

[170] NIST Computational Chemistry Comparison and Benchmark Database, NIST Standard Refernce Database Number 101, Release 17b, September 2015, Editor: Russell D. Johnson III., http://cccbdb.nist.gov.

[171] D. Spangenberg, P. Imhof, K. Kleinermanns, *Phys. Chem. Chem. Phys.*, 2003, **5**, 2505–2514.

[172] V. A. Mozhayskiy, A. I. Krylov, ezSpectrum, http://iopenshell.usc.edu/downloads.

[173] J. Wang, B. Yang, T. A. Cool, N. Hansen, T. Kasper, *Int. J. Mass. Spectrom.*, 2008, **269**, 210–220.

[174] Z. Zhou, M. Xie, Z. Wang, F. Qi, *Rapid Commun. Mass Spectrom.*, 2009, **23**, 3994–4002.

[175] N. E. Sveum, S. J. Goncher, D. M. Neumark, *Phys. Chem. Chem. Phys.*, 2006, **8**, 592–598.

[176] B. Gans, L. A. V. Mendes, S. Boyé-Péronne, S. Douin, G. Garcia, H. Soldi-Lose, B. K. Cunha de Miranda, C. Alcaraz, N. Carrasco, P. Pernot, D. Gauyacq, *J. Phys. Chem. A*, 2010, **114**, 3237–3246.

[177] B. Gans, G. A. Garcia, S. Boyé-Péronne, J.-C. Loison, S. Douin, F. Gaie-Levrel, D. Gauyacq, *J. Phys. Chem. A*, 2011, **115**, 5387–5396.

[178] J. D. Savee, S. Soorkia, O. Welz, T. M. Selby, C. A. Taatjes, D. L. Osborn, *J. Chem. Phys.*, 2012, **136**, 134307.

[179] J. D. Savee, J. F. Lockyear, S. Borkar, A. J. Eskola, O. Welz, C. A. Taatjes, D. L. Osborn, *J. Chem. Phys.*, 2013, **139**, 056101.

[180] H. Xu, S. T. Pratt, *J. Phys. Chem. A*, 2013, **117**, 9331–9342.

[181] T. N. Olney, G. Cooper, C. E. Brion, *Chem. Phys.*, 1998, **232**, 211–237.

[182] T. A. Carlson, P. Gerard, M. O. Krause, G. von Wald, J. W. Taylor, F. A. Grimm, *J. Chem. Phys.*, 1986, **84**, 4755–4759.

[183] H. P. Reisenauer, G. Maier, A. Riemann, R. W. Hoffmann, *Angew. Chem. Int. Ed.*, 1984, **23**, 641.

[184] M. S. Schuurman, J. Giegerich, K. Pachner, D. Lang, B. Kiendl, R. J. MacDonell, A. Krueger, I. Fischer, *Chem. Eur. J.*, 2015, pp. 14486–14495.

[185] V. Lavallo, Y. Canac, B. Donnadieu, W. W. Schoeller, G. Bertrand, *Science*, 2006, **312**, 722–724.

[186] H. E. Matthews, W. M. Irvine, *Astrophys. J. Suppl. Ser.*, 1985, **298**, L61–L65.

[187] D. Gerlich, S. Horning, *Chem. Rev.*, 1992, **92**, 1509–1539.

[188] S. D. Prodnuk, S. Grocert, V. M. Bierbaum, C. H. DePuy, *Org. Mass Spectrom.*, 1992, **27**, 416–422.

[189] C. A. Taatjes, S. J. Klippenstein, N. Hansen, J. A. Miller, T. A. Cool, J. Wang, M. E. Law, P. R. Westmoreland, *Phys. Chem. Chem. Phys.*, 2005, **7**, 806–813.

[190] H. Clauberg, D. W. Minsek, P. Chen, *J. Am. Chem. Soc.*, 1992, **114**, 99–107.

[191] P. Hemberger, B. Noller, M. Steinbauer, I. Fischer, C. Alcaraz, B. K. Cunha de Miranda, G. A. Garcia, H. Soldi-Lose, *J. Phys. Chem. A*, 2010, **114**, 11269–11276.

[192] P. Hemberger, B. Noller, M. Steinbauer, K. Fischer, I. Fischer, *J. Phys. Chem. Lett.*, 2010, **1**, 228–231.

[193] P. Hemberger, J. Kohler, I. Fischer, G. Piani, L. Poisson, J.-M. Mestdagh, *Phys. Chem. Chem. Phys.*, 2012, **14**, 6173–6178.

[194] R.-G. Wang, M. A. Dillon, D. Spence, *J. Chem. Phys.*, 1984, **80**, 63–69.

[195] W. M. A. Niessen, *Liquid chromatography–mass spectrometry*, 97 of *Chromatographic science series*, CRC/Taylor & Francis, Boca Raton, 3rd ed., 2006.

[196] J. D. Bittner, *A Molecular Beam Mass Spectrometer Study of Fuel-Rich and Sooting Benzene-Oxygen Flames* PhD thesis, Massachusetts Institute of Technology, Cambridge, 1981.

[197] K. Watanabe, F. M. Matsunaga, H. Sakai, *Appl. Opt.*, 1967, **6**, 391–396.

[198] J. C. Person, P. P. Nicole, *J. Chem. Phys.*, 1970, **53**, 1767–1774.

[199] E. E. Rennie, C. A. F. Johnson, J. E. Parker, D. M. P. Holland, D. A. Shaw, M. A. Hayes, *Chem. Phys.*, 1998, **229**, 107–123.

[200] J. C. Person, P. P. Nicole, *J. Chem. Phys.*, 1971, **55**, 3390–3397.

[201] L. A. Chewter, M. Sander, K. Müller-Dethlefs, E. W. Schlag, *J. Chem. Phys.*, 1987, **86**, 4737–4744.

[202] R. A. Perry, D. L. Siebers, *Nature*, 1986, **324**, 657–658.

[203] R. K. Lyon, J. A. Cole, *Combust. Flame*, 1990, **82**, 435–443.

[204] J. A. Miller, C. T. Bowman, *Int. J. Chem. Kinet.*, 1991, **23**, 289–313.

[205] P. Glarborg, P. G. Kristensen, S. H. Jensen, K. Dam-Johansen, *Combust. Flame*, 1994, **98**, 241–258.

[206] W. P. Trautwein, AdBlue as a reducing agent for the decrease of NOx emissions from diesel engines of commercial vehicles, Deutsche Wissenschaftliche Gesellschaft fuer Erdoel, Erdgas und Kohle e.V., Hamburg (Germany), 2003. http://hdl.handle.net/10068/169974 (accessed October 29, 2015).

[207] N. Marcelino, S. Brünken, J. Cernicharo, D. Quan, E. Roueff, E. Herbst, P. Thaddeus, *A&A*, 2010, **516**, A105.

[208] T. A. Spiglanin, R. A. Perry, D. W. Chandler, *J. Phys. Chem.*, 1986, **90**, 6184–6189.

[209] T. A. Spiglanin, D. W. Chandler, *Chem. Phys. Lett.*, 1987, **141**, 428–432.

[210] D. W. Chandler, private communication, August 10, 2015.

[211] D. W. Chandler, Janssen, H. M. Maurice, S. Stolte, R. N. Strickland, J. W. Thoman, D. H. Parker, *J. Phys. Chem.*, 1990, **94**, 4839–4846.

[212] M. Zyrianov, T. Droz-Georget, A. Sanov, H. Reisler, *J. Chem. Phys.*, 1996, **105**, 8111–8116.

[213] A. Sanov, T. Droz-Georget, M. Zyrianov, H. Reisler, *J. Chem. Phys.*, 1997, **106**, 7013–7022.

[214] T. Droz-Georget, M. Zyrianov, H. Reisler, D. W. Chandler, *Chem. Phys. Lett.*, 1997, **276**, 316–324.

[215] H. Wang, S.-l. Liu, J. Liu, F.-y. Wang, B. Jiang, X.-m. Yang, *Chin. J. Chem. Phys.*, 2007, **20**, 388–394.

[216] Z. Zhang, Z. Chen, C. Huang, Y. Chen, D. Dai, D. H. Parker, X. Yang, *J. Phys. Chem. A*, 2014, **118**, 2413–2418.

[217] G. Herzberg, C. Reid, *Discuss. Faraday Soc.*, 1950, **9**, 92–99.

[218] K. Yamada, *J. Mol. Spectrosc.*, 1980, **79**, 323–344.

[219] D. A. Steiner, K. A. Wishah, S. R. Polo, T. K. McCubbin Jr., *J. Mol. Spectrosc.*, 1979, **76**, 341–373.

[220] C. G. Rowland, J. H. D. Eland., C. J. Danby, *Chem. Commun.*, 1968, pp. 1535–1536.

[221] G. T. Fujimoto, M. E. Umstead, M. C. Lin, *Chem. Phys.*, 1982, **65**, 197–203.

[222] W. S. Drozdoski, A. P. Baronavski, J. R. McDonald, *Chem. Phys. Lett.*, 1979, **64**, 421–425.

[223] S. Yu, S. Su, D. Dai, K. Yuan, X. Yang, *J. Phys. Chem. A*, 2013, **117**, 13564–13571.

[224] S. Yu, S. Su, Y. Dorenkamp, A. M. Wodtke, D. Dai, K. Yuan, X. Yang, *J. Phys. Chem. A*, 2013, **117**, 11673–11678.

[225] J. H. D. Eland, *Philos. Trans. R. Soc. London, Ser. A*, 1970, **268**, 87–96.

[226] S. Cradock, E. A. V. Ebsworth, J. D. Murdoch, *J. Chem. Soc., Faraday Trans. 2*, 1972, **68**, 86–100.

[227] S. Wilsey, S. E. Thomas, J. H. D. Eland, *Chem. Phys.*, 2000, **258**, 21–36.

[228] C. W. Hand, D. J. Bogan, *J. Phys. Chem.*, 1971, **75**, 1532–1536.

[229] B. Ruscic, J. Berkowitz, *J. Chem. Phys.*, 1994, **100**, 4498–4508.

[230] F. Holzmeier, M. Lang, I. Fischer, X. Tang, B. K. Cunha de Miranda, C. Romanzin, C. Alcaraz, P. Hemberger, *J. Chem. Phys.*, 2015, **142**, 184306.

[231] T. Oka, *J. Mol. Spectrosc.*, 1973, **48**, 503–507.

[232] M. Mladenović, M. Lewerenz, *Chem. Phys.*, 2008, **343**, 129–140.

[233] A. L. Sobolewski, W. Domcke, *Phys. Chem. Chem. Phys.*, 2010, **12**, 4897–4898.

[234] B. W. J. McNeil., N. R. Thompson, *Nat. Photon.*, 2010, **4**, 814–821.

[235] B. K. McFarland, J. P. Farrell, S. Miyabe, F. Tarantelli, A. Aguilar, N. Berrah, C. Bostedt, J. D. Bozek, P. H. Bucksbaum, J. C. Catagna, R. N. Coffee, J. P. Cryan, L. Fang, R. Feifel, K. J. Gaffney, J. M. Glownia, T. J. Martinez, M. Mucke, B. Murphy, A. Natan, T. Osipov, V. S. Petrović, S. Schorb, T. Schultz, L. S. Spector, M. Swiggers, I. Tenney, S. Wang, J. L. White, W. White, M. Gühr, Time Resolved Auger Probing of Molecular Fragmentation in Thymine, 2011, unpublished raw data.

[236] H.-W. Jochims, M. Schwell, H. Baumgärtel, S. Leach, *Chem. Phys.*, 2005, **314**, 263–282.

[237] M. Schwell, H.-W. Jochims, H. Baumgärtel, S. Leach, *Chem. Phys.*, 2008, **353**, 145–162.

[238] R. Improta, G. Scalmani, V. Barone, *Int. J. Mass. Spectrom.*, 2000, **201**, 321–336.

[239] A. Pietzsch, A. Föhlisch, M. Beye, M. Deppe, F. Hennies, M. Nagasono,

E. Suljoti, W. Wurth, C. Gahl, K. Döbrich, A. Melnikov, *New J. Phys.*, 2008, **10**, 033004.

[240] M. Oura, T. Wagai, A. Chainani, J. Miyawaki, H. Sato, M. Matsunami, R. Eguchi, T. Kiss, T. Yamaguchi, Y. Nakatani, T. Togashi, T. Katayama, K. Ogawa, M. Yabashi, Y. Tanaka, Y. Kohmura, K. Tamasaku, S. Shin, T. Ishikawa, *J. Synchrotron Radiat.*, 2013, **21**, 183–192.

[241] A. Fognini, G. Salvatella, T. U. Michlmayr, C. Wetli, U. Ramsperger, T. Bähler, F. Sorgenfrei, M. Beye, A. Eschenlohr, N. Pontius, C. Stamm, F. Hieke, M. Dell'Angela, S. d. Jong, R. Kukreja, N. Gerasimova, V. Rybnikov, H. Redlin, J. Raabe, A. Föhlisch, H. A. Dürr, W. Wurth, D. Pescia, A. Vaterlaus, Y. Acremann, *New J. Phys.*, 2014, **16**, 043031.

[242] A. Hiltunen, S. Aksela, G. Víkor, S. Ricz, Á. Kövér, B. Sulik, *Nucl. Instrum. Methods Phys. Res., Sect. B*, 1999, **154**, 267–271.

[243] G. R. Wight, C. E. Brion, *J. Electron Spectrosc. Relat. Phenom.*, 1974, **3**, 191–205.

[244] Y. Ma, C. T. Chen, G. Meigs, K. Randall, F. Sette, *Phys. Rev. A*, 1991, **44**, 1848–1858.

[245] J.-i. Adachi, N. Kosugi, E. Shigemasa, A. Yagishita, *J. Phys. Chem.*, 1996, **100**, 19783–19788.

[246] S. S. Prasad, W. T. Huntress, *Mon. Not. R. Astron. Soc.*, 1978, **185**, 741–744.

[247] R. N. Dixon, *Philos. Trans. R. Soc. London, Ser. A*, 1960, **252**, 165–192.

[248] A. Carrington, A. R. Fabris, B. J. Howard, N. J. D. Lucas, *Mol. Phys.*, 1971, **20**, 961–980.

[249] D. E. Milligan, M. E. Jacox, *J. Chem. Phys.*, 1967, **47**, 5157–5168.

[250] J. Yao, J. A. Fernandez, E. R. Bernstein, *J. Chem. Phys.*, 1997, **107**, 8813–8822.

[251] S. Gómez, H. M. Lambert, P. L. Houston, *J. Phys. Chem. A*, 2001, **105**, 6342–6352.

[252] A. A. Hoops, R. T. Bise, J. R. Gascooke, D. M. Neumark, *J. Chem. Phys.*, 2001, **114**, 9020–9027.

[253] X. Tan, P. J. Dagdigian, *Chem. Phys. Lett.*, 2003, **375**, 532–539.

[254] R. Prasad, *J. Chem. Phys.*, 2004, **120**, 10089–10100.

[255] O. Yazidi, H. Gritli, G. Chambaud, *Mol. Phys.*, 2005, **103**, 3321–3336.

[256] C. Léonard, H. Gritli, G. Chambaud, *J. Mol. Spectrosc.*, 2007, **243**, 90–98.

[257] J. M. Dyke, N. Jonathan, A. E. Lewis, J. D. Mills, A. Morris, *Mol. Phys.*, 1983, **50**, 77–89.

[258] E. Nachbaur, W. Gottardi, *Monatsh. Chemie*, 1966, **97**, 115–120.

[259] S. Mollet, F. Merkt, *J. Chem. Phys.*, 2013, **139**, 034302.

[260] D. C. Frost, H. W. Kroto, C. A. McDowell, N. P. C. Westwood, *J. Electron Spectrosc. Relat. Phenom.*, 1977, **11**, 147–156.

[261] R. F. Lake, H. Thompson, *Proc. R. Soc. Lond. A*, 1970, **317**, 187–198.

[262] D. M. P. Holland, D. A. Shaw, L. Karlsson, L. G. Shpinkova, L. Cooper, A. B. Trofimov, J. Schirmer, *Mol. Phys.*, 2000, **98**, 1939–1947.

[263] V. Butcher, J. M. Dyke, A. E. Lewis, A. Morris, A. Ridha, *J. Chem. Soc. Faraday Trans. 2*, 1988, **84**, 299–310.

[264] J. Berkowitz, *J. Chem. Phys.*, 1962, **36**, 2533–2539.

[265] R. Frey, B. Gotchev, O. F. Kalman, W. B. Peatman, H. Pollak, E. W. Schlag, *Chem. Phys.*, 1977, **21**, 89–100.

[266] T. Baer, P. M. Guyon, *J. Chem. Phys.*, 1986, **85**, 4765–4778.

[267] J. Liu, W. Chen, C.-W. Hsu, M. Hochlaf, M. Evans, S. Stimson, C. Y. Ng, *J. Chem. Phys.*, 2000, **112**, 10767–10777.

[268] J. M. Dyke, N. B. H. Jonathan, A. E. Lewis, A. Morris, *Mol. Phys.*, 1982, **47**, 1231–1240.

[269] E. Ikeda, P. Nicholls, J. C. Mackie, *Proc. Combust. Inst.*, 2000, **28**, 1709–1716.

[270] G. B. Bacskay, M. Martoprawiro, J. C. Mackie, *Chem. Phys. Lett.*, 1998, **290**, 391–398.

[271] O. Santos, A. C. Testa, M. O'Sullivan, *J. Photochem.*, 1983, **23**, 257–263.

[272] D. A. Blank, S. W. North, Y. T. Lee, *Chem. Phys.*, 1994, **187**, 35–47.

[273] J. Wei, A. Kuczmann, J. Riedel, F. Renth, F. Temps, *Phys. Chem. Chem. Phys.*, 2003, **5**, 315–320.

[274] J. Wei, J. Riedel, A. Kuczmann, F. Renth, F. Temps, *Faraday Discuss.*, 2004, **127**, 267–282.

[275] B. Cronin, M. G. D. Nix, R. H. Qadiri, M .N. R. Ashfold, *Phys. Chem. Chem. Phys.*, 2004, **6**, 5031–5041.

[276] A. J. Gianola, T. Ichino, R. L. Hoenigman, S. Kato, V. M. Bierbaum, Lineberger, W. Carl, *J. Phys. Chem. A*, 2004, **108**, 10326–10335.

[277] A. Motzke, Z. Lan, C. Woywod, W. Domcke, *Chem. Phys.*, 2006, **329**, 50–64.

[278] X. Zhu, D. R. Yarkony, *J. Phys. Chem. C*, 2010, **114**, 5312–5320.

[279] J. C. Mackie, K. R. Doolan, P. F. Nelson, *J. Phys. Chem.*, 1989, **93**, 664–670.

[280] A. V. Friderichsen, E.-J. Shin, R. J. Evans, M. R. Nimlos, D. C. Dayton, G. B. Ellison, *Fuel*, 2001, **80**, 1747–1755.

[281] A. M. Scheer, C. Mukarakate, D. J. Robichaud, G. B. Ellison, M. R. Nimlos, *J. Phys. Chem. A*, 2010, **114**, 9043–9056.

[282] T. Lister, R. H. Prager, M. Tsaconas, K. L. Wilkinson, *Aust. J. Chem.*, 2003, **56**, 913–916.

[283] H. J. Wörner, F. Merkt, *Angew. Chem. Int. Ed.*, 2006, **45**, 293–296.

[284] H. J. Wörner, F. Merkt, *J. Chem. Phys.*, 2007, **127**, 034303.

[285] M. Steinbauer, P. Hemberger, I. Fischer, M. Johnson, A. Bodi, *Chem. Phys. Lett.*, 2010, **500**, 232–236.

[286] K. B. Wiberg, G. B. Ellison, J. J. Wendoloski, C. R. Brundle, N. A. Kuebler, *J. Am. Chem. Soc.*, 1976, **98**, 7179–7182.

[287] P. J. Derrick, L. Åsbrink, O. Edqvist, B.-Ö. Jonsson, E. Lindholm, *Int. J. Mass. Spectrom. Ion Phys.*, 1971, **6**, 191–202.

[288] A. D. Baker, D. Betteridge, N. R. Kemp, R. E. Kirby, *Anal. Chem.*, 1970, **42**, 1064–1073.

[289] S. Olivella, A. Sole, A. Garcia-Raso, *J. Phys. Chem.*, 1995, **99**, 10549–10556.

[290] S. Liang, P. Hemberger, N. M. Neisius, A. Bodi, H. Grützmacher, J. Levalois-Grützmacher, S. Gaan, *Chem. Eur. J.*, 2015, **21**, 1073–1080.

[291] P. Hemberger, G. da Silva, Trevitt, A. J., T. Gerber, A. Bodi, *Phys. Chem. Chem. Phys.*, October 2015; [Epub ahead of print].

[292] J. Kreile, A. Schweig, W. Theil, *Chem. Phys. Lett.*, 1982, **87**, 473–476.

[293] S. T. Pratt, P. M. Dehmer, J. L. Dehmer, *J. Chem. Phys.*, 1993, **99**, 6233–6244.

[294] L. V. Moskaleva, M. C. Lin, *J. Comput. Chem.*, 2000, **21**, 415–425.

[295] S. J. Dunne, L. A. Summers, E. I. von Nagy-Felsobuki, *Org. Mass Spectrom.*, 1993, **28**, 316–320.

[296] J. Bouwman, B. Sztáray, J. Oomens, P. Hemberger, A. Bodi, *J. Phys. Chem. A*, 2015, **119**, 1127–1136.

[297] N. S. Shuman, A. Bodi, T. Baer, *J. Phys. Chem. A*, 2010, **114**, 232–240.

[298] M. W. Chase, *J. Phys. Chem. Ref. Data, Monograph 9*, 1998.

[299] L. M. P. F. Amaral, M. A. V. Ribeiro da Silva, *J. Chem. Thermodyn.*, 2012, **48**, 65–69.

[300] L. A. Curtiss, K. Raghavachari, P. C. Redfern, J. A. Pople, *J. Chem. Phys.*, 1997, **106**, 1063–1079.

[301] P. H. Kasai, D. McLeod, *J. Am. Chem. Soc.*, 1972, **94**, 720–727.

[302] A. Korte, A. Mardyukov, W. Sander, *Aust. J. Chem.*, 2014, **67**, 1324–1329.

[303] M. Lucas, J. Minor, J. Zhang, C. Brazier, *J. Phys. Chem. A*, 2013, **117**, 12138–12145.

[304] R. Liu, T. T.-S. Huang, J. Tittle, D. Xia, *J. Phys. Chem. A*, 2000, **104**, 8368–8374.

[305] S. Thorwirth, M. C. McCarthy, J. B. Dudek, P. Thaddeus, *J. Mol. Spectrosc.*, 2004, **225**, 93–95.

[306] T. Gilbert, T. L. Grebner, I. Fischer, P. Chen, *J. Chem. Phys.*, 1999, **110**, 5485–5488.

[307] I. Fischer, P. Chen, *J. Phys. Chem. A*, 2002, **106**, 4291–4300.

[308] D. Stefanović, H. F. Grützmacher, *Org. Mass Spectrom.*, 1974, **9**, 1052–1054.

[309] F. Holzmeier, M. Lang, I. Fischer, P. Hemberger, *Chem. Phys. Lett.*, 2015, **638**, 201–204.

[310] A. C. Parr, A. J. Jason, R. Stockbauer, K. E. McCulloh, *Int. J. Mass. Spectrom. Ion Phys.*, 1979, **30**, 319–330.

[311] K. Vasilatou, F. Merkt, *J. Chem. Phys.*, 2011, **135**, 124310.

[312] C. Baker, D. W. Turner, *Chem. Commun. (London)*, 1967, **16**, 797–799.

[313] G. Bieri, F. Burger, E. Heilbronner, J. P. Maier, *Helv. Chim. Acta*, 1977, **60**, 2213–2233.

[314] P. Masclet, D. Grosjean, G. Mouvier, J. Dubois, *J. Electron Spectrosc. Relat. Phenom.*, 1973, **2**, 225–237.

[315] A. Terentis, A. Doughty, J. C. Mackie, *J. Phys. Chem.*, 1992, **96**, 10334–10339.

[316] A. Doughty, J. C. Mackie, *J. Phys. Chem.*, 1992, **96**, 10339–10348.

[317] J. Jones, G. B. Bacskay, J. C. Mackie, *Isr. J. Chem.*, 1996, **36**, 239–248.

[318] J. S. Roberts, M. Szwarc, *J. Chem. Phys.*, 1948, **16**, 981–983.

[319] B. D. Barton, S. E. Stein, *J. Chem. Soc., Faraday Trans. 1*, 1981, **77**, 1755–1762.

[320] J. A. Bray, E. R. Bernstein, *J. Phys. Chem. A*, 1999, **103**, 2208–2213.

[321] T. F. Palmer, F. P. Lossing, *J. Am. Chem. Soc.*, 1963, **85**, 1733–1735.

[322] A. Stock, E. Pohland, *Ber. Dtsch. Chem. Ges.*, 1926, **59**, 2210–2215.

[323] M. Kranz, T. Clark, *J. Org. Chem.*, 1992, **57**, 5492–5500.

[324] M. Baranac-Stojanović, *Chem. Eur. J.*, 2014, **20**, 16558–16565.

[325] K. M. Davies, M. J. S. Dewar, P. Rona, *J. Am. Chem. Soc.*, 1967, **89**, 6294–6297.

[326] A. Marwitz, M. H. Matus, L. N. Zakharov, D. A. Dixon, S.-Y. Liu, *Angew. Chem. Int. Ed.*, 2009, **48**, 973–977.

[327] H. Braunschweig, K. Geetharani, J. O. C. Jimenez-Halla, M. Schäfer, *Angew. Chem. Int. Ed.*, 2014, pp. 3500–3504.

[328] H. Braunschweig, C. Hörl, L. Mailänder, K. Radacki, J. Wahler, *Chem. Eur. J.*, 2014, **20**, 9858–9861.

[329] H. Braunschweig, M. A. Celik, F. Hupp, I. Krummenacher, L. Mailänder, *Angew. Chem. Int. Ed.*, 2015, **54**, 6347–6351.

[330] P. M. Maitlis, *J. Chem. Soc.*, 1961, pp. 425–429.

[331] T. Agou, M. Sekine, J. Kobayashi, T. Kawashima, *Chem. Commun.*, 2009, **14**, 1894–1896.

[332] H. Braunschweig, A. Damme, J. O. C. Jimenez-Halla, B. Pfaffinger, K. Radacki, J. Wolf, *Angew. Chem. Int. Ed.*, 2012, **51**, 10034–10037.

[333] L. Weber, I. Domke, W. Greschner, K. Miqueu, A. Chrostowska, P. Baylère, *Organometallics*, 2005, **24**, 5455–5463.

[334] A. Chrostowska, M. Maciejczyk, A. Dargelos, P. Baylere, L. Weber, V. Werner, D. Eickhoff, H.-G. Stammler, B. Neumann, *Organometallics*, 2010, **29**, 5192–5198.

[335] A. Chrostowska, S. Xu, A. N. Lamm, A. Mazière, C. D. Weber, A. Dargelos, P. Baylère, A. Graciaa, S.-Y. Liu, *J. Am. Chem. Soc.*, 2012, **134**, 10279–10285.

[336] H. Heinz Karsch, G. Hanika, B. Huber, J. Riede, G. Müller, *J. Organomet. Chem.*, 1989, **361**, C25–C29.

[337] S. Mathur, T. Rügamer, H. Braunschweig, G. D'Andola, *Z. Anorg. Allg. Chem.*, 2007, **633**, 2459–2462.

[338] F. Holzmeier, M. Lang, P. Hemberger, A. Bodi, M. Schäfer, R. D. Dewhurst, H. Braunschweig, I. Fischer, *Chem. Eur. J.*, 2014, **20**, 9683–9692.

[339] X. Wang, Y. Li, Y. D. Wu, M. N. Paddon-Row, N. G. Rondan, K. N. Houk, *J. Org. Chem.*, 1990, **55**, 2601–2609.

[340] T. Schüßler, H.-J. Deyerl, S. Dümmler, I. Fischer, C. Alcaraz, M. Elhanine, *J. Chem. Phys.*, 2003, **118**, 9077–9080.

[341] F. A. Houle, J. L. Beauchamp, *J. Am. Chem. Soc.*, 1979, **101**, 4067–4074.

[342] U. Alkemade, K. H. Homann, *Z. Phys. Chem. (Muenchen, Ger.)*, 1989, **161**, 19–34.

[343] T. C. Zhang, L. D. Zhang, X. Hong, K. W. Zhang, F. Qi, C. K. Law, T. H. Ye, P. H. Zhao, Y. L. Chen, *Combust. Flame*, 2009, **156**, 2071–2083.

[344] N. J. Reilly, D. L. Kokkin, K. Nakajima, K. Nauta, S. H. Kable, T. W. Schmidt, *J. Am. Chem. Soc.*, 2008, **130**, 3137–3142.

[345] P. Hemberger, M. Steinbauer, M. Schneider, I. Fischer, M. Johnson, A. Bodi, T. Gerber, *J. Phys. Chem. A*, 2010, **114**, 4698–4703.

[346] L. I. Smith, J. S. Swenson, *J. Am. Chem. Soc.*, 1957, **79**, 2962–2966.

[347] J.-J. Lian, P.-C. Chen, Y.-P. Lin, H.-C. Ting, R.-S. Liu, *J. Am. Chem. Soc.*, 2006, **128**, 11372–11373.

[348] P. Hemberger, *Photoionisation an Radikalen und Carbenen mit VUV-Synchrotronstrahlung* PhD thesis, Julius-Maximilians Universität Würzburg, Würzburg, 2011.

[349] O. Krechkivska, C. Wilcox, G. D. O'Connor, K. Nauta, S. H. Kable, T. W. Schmidt, *J. Phys. Chem. A*, 2014, **118**, 10252–10258.

[350] F. Holzmeier, M. Lang, P. Hemberger, I. Fischer, *ChemPhysChem*, 2014, **15**, 3489–3492.

[351] K. H. Fischer, J. Herterich, I. Fischer, S. Jaeqx, A. M. Rijs, *J. Phys. Chem. A*, 2012, **116**, 8515–8522.

[352] M. W. Wong, L. Radom, *J. Am. Chem. Soc.*, 1993, **115**, 1507–1514.

[353] A. J. Yencha, A. J. Cormack, R. J. Donovan, A. Hopkirk, G. C. King, *Chem. Phys.*, 1998, **238**, 109–131.

[354] H.-J. Deyerl, I. Fischer, P. Chen, *J. Chem. Phys.*, 1999, **111**, 3441–3448.

[355] A. Bodi, N. S. Shuman, T. Baer, *Phys. Chem. Chem. Phys.*, 2009, **11**, 11013–11021.

[356] P. Hemberger, A. Bodi, T. Gerber, M. Würtemberger, U. Radius, *Chem. Eur. J.*, 2013, **19**, 7090–7099.

[357] A. Mardyukov, W. Sander, *Chem. Eur. J.*, 2009, **15**, 1462–1467.

[358] F. Holzmeier, M. Lang, I. Fischer, P. Hemberger, G. A. Garcia, X. Tang, J.-C. Loison, *Phys. Chem. Chem. Phys.*, 2015, **17**, 19507–19514.

[359] E. R. Lory, R. F. Porter, *J. Am. Chem. Soc.*, 1973, **95**, 1766–1770.

[360] Y. Kawashima, K. Kawaguchi, E. Hirota, *J. Chem. Phys.*, 1987, **87**, 6331–6333.

[361] C. A. Thompson, L. Andrews, *J. Am. Chem. Soc.*, 1995, **117**, 10125–10126.

[362] C. A. Thompson, L. Andrews, J. M. L. Martin, J. El-Yazal, *J. Phys. Chem.*, 1995, **99**, 13839–13849.

[363] F. Zhang, P. Maksyutenko, R. I. Kaiser, A. M. Mebel, A. Gregušová, Perera, S. Ajith, R. J. Bartlett, *J. Phys. Chem. A*, 2010, **114**, 12148–12154.

[364] P. Paetzold, C. V. Plotho, G. Schmid, R. Boese, B. Schrader, D. Bougeard, U. Pfeiffer, R. Gleiter, W. Schüfer, *Chem. Ber.*, 1984, **117**, 1089–1102.

[365] L. Szepes, T. Baer, *J. Am. Chem. Soc.*, 1984, **106**, 273–278.

[366] M. Linhard, *Z. Anorg. Allg. Chem.*, 1938, **236**, 200–208.

[367] R. A. Ashby, R. L. Werner, *J. Mol. Spectrosc.*, 1965, **18**, 184–201.

[368] G. Fischer, J. Geith, T. M. Klapötke, B. Krumm, *Z. Naturforsch.*, 2002, **57 b**, 19–24.

[369] W. H. Hocking, M. C. L. Gerry, *J. Mol. Spectrosc.*, 1972, **42**, 547–566.

[370] T. C. Devore, *J. Mol. Struct.*, 1987, **162**, 287–304.

[371] E. V. Brown, G. R. Granneman, *J. Am. Chem. Soc.*, 1975, **97**, 621–627.

[372] S. Thies, H. Sell, C. Schütt, C. Bornholdt, C. Näther, F. Tuczek, R. Herges, *J. Am. Chem. Soc.*, 2011, **133**, 16243–16250.

[373] S. K. Dey, D. A. Lightner, *J. Org. Chem.*, 2007, **72**, 9395–9397.

# Danksagung

Ich möchte mich an dieser Stelle bei all denjenigen bedanken, die mich während des Studiums und der Promotion unterstützt und somit zum Gelingen dieser Arbeit beigetragen haben.

Besonders hervorzuheben ist hierbei Prof. Dr. Ingo Fischer, der es mir ermöglicht hat in seiner Gruppe solch ein interessantes Thema zu bearbeiten. Dabei gewährte er viele wissenschaftliche Freiräume und zeigte sich stets offen für neue Ideen, was meine Begeisterung am wissenschaftlichen Arbeiten enorm steigerte. Durch seine unkomplizierte Art trägt er maßgeblich zum äußerst angenehmen Klima im Arbeitskreis bei. Die zahlreichen Auslandsaufenthalte an den Speicherringen in der Schweiz und in Frankreich sowie die Teilnahmen an internationalen Tagungen, die er mir ermöglichte, werden mir stets in Erinnerung bleiben und haben mir auch abseits der Wissenschaft wertvolle Kompetenzen gebracht. Vielen Dank dafür!

Ohne Dr. Melanie Lang wären die anstrengenden Messzeiten am Synchrotron sicherlich nur halb so erfolgreich gewesen. Gemeinsam konnten wir das Experiment (bis auf einmal) trotz wenig Schlafs unter Kontrolle halten und brachten von jeder Messzeit große Datensätze erfolgreicher Experimente mit, auch wenn wir dies manchmal erst hinterher bemerkten. Ich möchte mich bei Melanie für die intensiven, motivierenden, oft auch im Privaten durchgeführten, wissenschaftlichen Diskussionen bedanken und vor allem für die tolle Zeit, die wir abseits der Experimente verbracht haben. Du warst mehr als nur eine Kollegin!

Außerdem konnte ich bei den Messzeiten auf die Unterstützung von Engelbert Reusch und den Bachelor-Studenten und Praktikanten Isabella Wagner, Max Herbert, Martina Raschig, Kathrin Weiland und Christopher Schwarz zählen. Ich hoffe, ihr konntet auch von mir profitieren und habt dabei auch etwas gelernt.

Den Mitarbeitern an den Synchrotron Beamlines Dr. Patrick Hemberger, Dr. András Bödi, Dr. Xiaofeng Tang, und Dr. Saikat Nandi möchte ich für die hervorragenden Voraussetzungen danken, für die sie während unserer Experimente sorgten. Das große Engagement von Patrick und András bei der Datenauswertung, den Rechnungen und allen dazugehörigen Verständnisfragen ist besonders hervorzuheben. Vielen Dank auch für die netten Abenden bei euch zu Hause, die eine willkommene Abwechslung zu den Messzeiten waren.

Bei Dr. Christian Alcaraz möchte ich mich für die fruchtbringende Zusammenarbeit bei der Analyse des HNCO Spektrums und für die weiteren erfolgreichen Projekte bedanken. Außerdem seien Marius Schäfer und Benjamin Kiendl für die aufwändigen Synthesen gedankt und Prof. Dr. Markus Gühr und Dr. Markus Wolf für die gemeinsame Messzeit in Frankreich, die mir dabei ein weiteres sehr interessantes Themengebiet näher brachten.

Danke an Christof Walther und Kilian Hader für die Unterstützung bei Herausforderungen der theoretischen Chemie bzw. Programmierung.

Ich möchte mich außerdem bei meinen Arbeitskollegen des Ak Fischer für die tolle Atmosphäre in der Gruppe bedanken. Mit Dr. Jens Giegerich hatte ich, die erste Nacht in Potsdam ausgenommen, einen äußerst rücksichtsvollen Zimmerpartner auf den Tagungen, der offen für alle wissenschaftlichen Diskussionen war und sich stets äußerst interessiert zeigte. Auf die Hilfe von Philipp Constantinidis, Hans-Christian Schmitt, Dr. Thiemo Gerbich und Kai Pachner konnte ich immer zählen, wenn ich Vorexperimente im Laserla-

bor durchgeführt habe. Hervorzuheben sind auch die ehemaligen Mitarbeiter der Arbeitsgruppe, insbesondere Dr. Michael Steinbauer, der mir als Betreuer meiner Bachelorarbeit den Weg zu meiner Promotion bereitete, und Dr. Jörg-Viktor Herterich für seine konstanten Erinnerungen, dass der Spaß und das Leben abseits der Uni nicht zu kurz kommen darf.

Schließlich geht der Dank noch an meine familie, die mich während des kompletten Studiums bestmöglich unterstützt hat und mir in meinen Entscheidungen immer maximale Freiräume gewährt hat. Hier sei vor allem meine Schwester Christina erwähnt für ihre standhafte Positionen in unseren leidenschaftlichen Diskussionen über Homöopathie, Superfood und andere Scharlatanerien. Diese waren immer ein gutes Training für das Verteidigen von wissenschaftlichen Standpunkten.